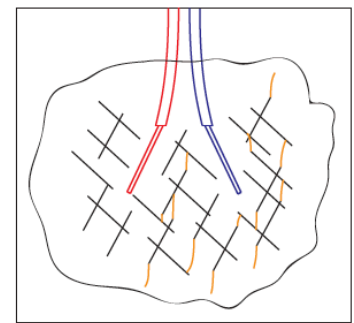
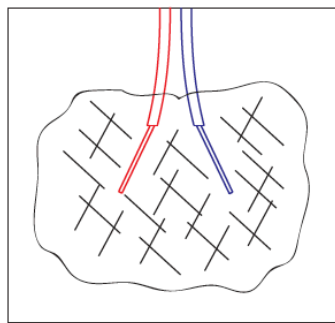
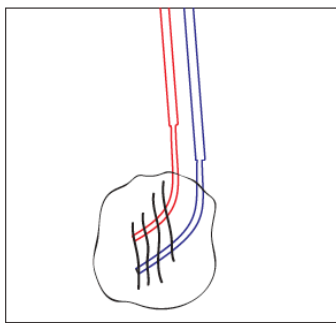




Final report

STIMDESIGN

Hydraulic stimulation design for deep geothermal reservoirs - a numerical approach





Date: 30/10/2018

Place: Lausanne

Publisher:

Swiss Federal Office of Energy SFOE
Research Programme Geothermal Energy
CH-3003 Bern
www.bfe.admin.ch
energieforschung@bfe.admin.ch

Agent:

École polytechnique fédérale de Lausanne
Geo-Energy Laboratory – Gaznat Chair on Geo-Energy
EPFL-ENAC-IIC-GEL
Station 18, CH-1015 Lausanne
gel.epfl.ch

Author:

Prof. Brice Lecampion, École polytechnique fédérale de Lausanne, brice.lecampion@epfl.ch
Federico Ciardo, École polytechnique fédérale de Lausanne, federico.ciardo@epfl.ch

SFOE head of domain: Gunter Siddiqi, gunter.siddiqi@bfe.admin.ch

SFOE programme manager: Céline Weber, cweber@focus-e.ch

SFOE contract number: SI/501354-01

The author of this report bears the entire responsibility for the content and for the conclusions drawn therefrom.



Summary

This report is the third intermediate report of the StimDesign project which will finish in June next year. The focus is here solely on our two dimensional numerical developments. We report advances on the different building blocks of our numerical model: fracture mechanics solver with frictional contacts and cohesive forces, finite volume discretization for fluid flow and fully coupled hydro-mechanical solvers. This reports documents in depth the mathematical formulation as well as the numerical discretization. Notably a new scheme to account for both frictional contact of shear crack as well as opening mode is presented and tested on a series of tests examples. Tests of our implementation of algorithms based on hierarchical matrices for the acceleration of the solution of linear systems arising in the boundary element methods is also documented. We report significant speedup and reduction in memory requirements. Finally, two studies which have or will soon be submitted for publication are put in appendix. The first study investigate the effect of shear induced dilatancy on the transition from aseismic to seismic in the context of fluid injection in a planar fault. The second study investigates the possibility of remote activation / nucleation (in a frictional weakening zone) due to the stress transfer associated with the propagation of a purely aseismic crack due to fluid injection in a friction neutral layer.





Date: October 8, 2019

Place: Lausanne

Publisher:

Swiss Federal Office of Energy SFoE
Research Programme Geothermal Energy
CH-3003 Bern
www.bfe.admin.ch
energieforschung@bfe.admin.ch

Agent:

École polytechnique fédérale de Lausanne
Geo-Energy Laboratory – Gaznat Chair on Geo-Energy
EPFL-ENAC-IIC-GEL
Station 18, CH-1015 Lausanne
gel.epfl.ch

Authors:

Prof. Brice Lecampion, École polytechnique fédérale de Lausanne, brice.lecampion@epfl.ch
Federico Ciardo, École polytechnique fédérale de Lausanne
Lisa Gordeliy, École polytechnique fédérale de Lausanne
Carlo Peruzzo, École polytechnique fédérale de Lausanne
Dmitry Nikolskiy, École polytechnique fédérale de Lausanne

SFOE head of domain:

Gunter Siddiqi, gunter.siddiqi@bfe.admin.ch

SFOE programme manager:

Céline Weber, cweber@focus-e.ch

SFOE contract number:

SI/501354-01

The authors of this report bear the entire responsibility for the content and for the conclusions drawn therefrom.



SUMMARY

This report describes the theory and numerical implementation of numerical models for the simulation of hydraulic stimulation in two and three dimensions. A C++ library for the solution of elasto-statics fracture problems via a hyper-singular collocation boundary element method has been developed in both two and three dimensions. The library also has specific routines for the construction and use of hierarchical matrices for the solution of any type of boundary integral equations - direct H-LU as well as iterative solvers are available. The use of a hierarchical matrix allows the solution of large boundary element problems, paving the way to the modeling of realistic geological conditions. A series of verification tests in both two and three dimensions validate the developed solver for fracture problems - very high accuracy at reasonable cost is obtained in all cases. In two dimensions, a one-way coupled hydro-mechanical solver allowing to model localized deformation along fractures (in the form of shear crack with frictional contact as well as open cracks) has been developed. The solver allows for weakening of frictional contact as well as cohesion. Besides verification tests, we show the capabilities of this solver in the context of hydraulic stimulation of a rock with randomly oriented pre-existing fractures. The importance of the initial stress state on the development of the hydraulically induced shear slip is notably highlighted. A fully coupled hydromechanical solver allowing to study the nucleation of dynamic rupture (i.e. the transition from seismic to aseismic slip) on a planar fault is then presented. Here again the code is successfully benchmarked against existing solutions. It is then used to study the effect of fault dilatancy on the transition from aseismic to seismic slip during fluid injection. The series of codes developed during this project provide a robust basis for the modeling of hydraulic stimulation.





Contents

1	Introduction	9
2	Elastic solver for fractures at depth	13
2.1	The elasto-static problem	13
2.1.1	Maxwell-Betti theorem	13
2.1.2	Fundamental Point force solution	14
2.1.2.1	Isotropic full-space - Kelvin solution	14
2.1.2.2	General properties for the point force fundamental solutions	15
2.1.3	Integral representation	16
2.1.4	Fracture(s) at depth	16
2.1.5	Integral representation for fracture problem	17
2.1.5.1	Interlude - link with a nuclei of strain	18
2.1.5.2	Back to the integral representation - link with the solution of a Volterra edge dislocation	19
2.1.5.3	Case of a planar crack in 2D - dislocation density	20
2.2	Numerical discretization - collocation - regularization after integration	21
2.2.1	Fracture Discretization	22
2.2.2	Choice of basis function / choice of collocation points	22
2.2.3	Analytical integration over an element	23
2.2.4	Assembly of the final system	25
2.2.4.1	Extension to Quasi-dynamic	26
2.2.5	Simple Examples in 2D	27
2.2.5.1	Griffith Crack	27
2.3	Acceleration - a brief introduction to \mathcal{H} -matrices	27
2.4	Our implementation	31
2.5	Two-dimensional Benchmarks	32
2.5.1	Circular arc crack	32
2.5.1.1	Geometry and reference solution	32
2.5.1.2	Numerical solution without or with \mathcal{H} -matrix approximation	32
2.5.2	Star crack	38
2.5.2.1	Geometry and reference solution	38
2.5.2.2	Numerical solution for stress intensity factor (dense matrix)	39
2.5.2.3	Numerical solution without or with \mathcal{H} -matrix approximation	41
2.5.3	Two parallel cracks	54
2.5.3.1	Geometry and reference solutions	54
2.5.3.2	Numerical solution for stress intensity factor (dense matrix)	55
2.5.3.3	Numerical solution without or with \mathcal{H} -matrix approximation	55
2.5.4	Array of parallel cracks	60
2.5.4.1	Geometry and reference solutions	60
2.5.4.2	Numerical solution without or with \mathcal{H} -matrix approximation	60
2.5.5	Performance of the GMRes iterative linear solver	62
2.6	Three dimensional benchmarks	69
2.6.1	A penny-shaped crack	69



2.6.1.1	Solution Verification	69
2.6.1.2	Mesh Refinement	69
2.6.1.3	Efficiency of the \mathcal{H} -matrix approximation	71
2.6.2	A bowl shaped crack	74
2.6.2.1	Solution Verification	74
2.6.3	Summary	74
3	Hydro-mechanical behavior of fractures	79
3.1	Mechanical behavior of joint/fracture interface	79
3.1.1	Kinematics description	79
3.1.2	Behavior when in contact	80
3.1.2.1	Frictional slip	80
3.1.3	Cohesive failure of potential 'slip' lines / fractures	81
3.1.3.1	Constitutive relations for the displacement discontinuity locus	81
3.1.4	LEFM with frictional contact	84
3.2	Fluid Flow in fractures	84
3.2.1	Permeability models	85
4	One-way coupled hydro-mechanical solver for the stimulation of fractured rock mass	87
4.1	Numerical solver description	88
4.1.1	Fluid flow solver	89
4.1.2	Mechanical solver	92
4.1.3	Preconditioning & solution of the tangent system	94
4.1.4	Adaptive time stepping	97
4.1.5	Implementation details	98
4.2	Verification tests	99
4.2.1	Test #1 : Branched fault subjected to compressive far field stress	99
4.2.2	Test #2 : Fluid injection into a frictional weakening planar fault	100
4.2.3	Test #3 : Loading/Unloading test	101
4.3	Fluid injection into a Discrete Fracture Network: critically stressed vs marginally pressurized case	103
4.3.1	Discrete Fracture Network generation	103
4.3.2	Scaling & dimensionless governing parameters	105
4.3.3	Fluid injection into a marginally pressurized DFN	108
4.3.4	Fluid injection into a critically stressed DFN	109
5	Fully coupled hydro-mechanical solver for planar fault -	
	Effect of dilatancy on the nucleation of dynamic rupture induced by fluid injection	117
5.1	Introduction	118
5.2	Problem formulation	119
5.2.1	Equilibrium, activation and dilatancy of slip-weakening fault	120
5.2.1.1	Activation and plasticity	120
5.2.1.2	Slip weakening and nucleation length-scale	122
5.2.2	Fluid flow	122
5.2.3	Initial and injection conditions	124
5.3	Activation and transition between aseismic and seismic slip	124
5.3.1	Case of a non-dilatant fault	124
5.3.2	Effect of dilatancy	125
5.3.2.1	Undrained fault response	125
5.3.2.2	Small scale yielding & stability condition	126
5.4	Numerical scheme description	128
5.4.1	Characteristic scales for dimensionless governing problem	129
5.5	Dilatant hardening effect on a fault characterized by constant permeability	130
5.5.1	Case of unstable fault without dilatancy $\tau_o > \tau_r$	130
5.5.2	Case of an ultimately stable fault even without dilatancy ($\tau_o < \tau_r$)	134



5.6	Effect of shear-induced permeability changes	135
5.7	Conclusions	138
5.8	Supporting Information	140
5.8.1	Fully implicit hydro-mechanical solver for frictional planar fault: algorithm description	140
5.8.2	Verification of the numerical scheme: benchmark for the non-dilatant case	143
5.8.3	Mesh convergence study	145
5.8.4	Case of otherwise unstable fault $\tau_o > \tau_r$ - Nucleation and Arrest	146
5.8.5	Approximated solution for quasi-static growth assuming $a \propto \sqrt{4\alpha t}$	147
5.8.6	Dilatancy effect on purely aseismic crack propagation	150
5.8.7	Effect of shear-induced permeability changes: case of effective stress-dependent permeability	150
6	Conclusions and perspectives	155





Chapter 1

Introduction

The ultimate goal at the impetus of this project is to develop robust numerical solvers for the simulation of hydraulic stimulation of fractured rock mass. The aim is to provide to the geothermal community a set of tools to help designing hydraulic stimulation treatment - similar to what is currently available for hydraulic fracturing in the oil and gas industry (Adachi et al. 2007, Lecampion et al. 2018). The problem calls for an approach allowing to properly model the mechanical behavior (reactivation and/or propagation) of fracture(s) in shear and opening deformation modes as well as fluid flow within the pre-existing and newly created fractures. These hydro-mechanical phenomena are strongly coupled and non-linear and exhibit a change of geometry in time (propagation of fractures). We refer to the review articles of Jung (2013), Ghassemi (2012), Cornet (2016) for the description of the key mechanisms involved in hydraulic stimulation. At minima, the numerical model must account for i) the mechanical deformation of the rock mass in presence of fractures, ii) the fluid flow within the fracture(s), iii) the reactivation of pre-existing fractures and their frictional behavior, and iv) the associated fracture permeability changes.

A large number of contributions have been made to develop numerical models for hydraulic stimulation since the early works of Cundall (1982), Asgian (1989). Different numerical techniques have been used:

- ad-hoc models not even satisfying the balance of momentum - e.g. Kohl & Mégel (2007),
- distinct element for mechanical deformation and finite difference for flow (Yoon et al. 2014)
- continuum domain methods:
 - combining boundary element and finite differences explicitly modeling the fractures (McClure & Horne 2011, Tao et al. 2011, McClure & Horne 2013, 2014, Verde & Ghassemi 2015, Kamali & Ghassemi 2018)
 - finite element or finite volume based schemes that may lump the presence of fracture in a continuum approach (e.g. Yoon et al. 2014, Dempsey et al. 2015) or model them explicitly (e.g. Fu et al. 2013, Ucar et al. 2017).

We refer to Hayashi et al. (1999) and White et al. (2017) for a review of currently available numerical tools.

Modeling choices

We make the following approximations from the onset: i) we assume the rock matrix to be impermeable (at the time-scale of injection), ii) we neglect thermally induced stresses¹, iii) the reservoir is assumed to be homogenous and its extent sufficient to be considered as infinite².

¹Note that these two approximations could be somehow relaxed but at the expense of significant computational cost (and some specific numerical developments).

²Finite boundaries can be taken into account (if any) meshing them via boundary element like the fractures. Piece-wise variations of elastic properties could be similarly taken into account by meshing the boundaries between material and enforcing proper continuity conditions.



We assume that initially, a set of pre-existing fractures exist with orientation, length, hydraulic and mechanical properties statistics known. We also assume that the initial stress field is known. Furthermore, we aim to rigorously account for the following phenomena:

- Elastic deformation of fractures under the action of both fluid pressurization, stress transfer between neighboring fractures
- Fluid flow in fractures with evolution of hydraulic conductivity due to mechanical opening but also slip
- Frictional contact on mechanically closed fractures with friction laws allowing to model the nucleation of dynamic rupture events
- Further growth of pre-existing fractures under mixed mode loading (shear and opening mode)

It is important to recall that these different hydro-mechanical phenomena are extremely non-linear (and fully coupled). Their numerical solution is challenging, and careful verification and validation of numerical is mandatory - although seldomly done by most research groups. We thus put a strong emphasis on code verification.

Numerical methods used

We have chosen to combine a displacement discontinuity boundary element method (for the solution of the balance of momentum in an elastic rock mass) with finite volume methods for the spatial discretization of the flow equations. Moreover, the time integration is performed in a fully implicit manner therefore allowing to take large time-steps accurately and robustly.

Our work, however, differs from the codes developed in Stanford and University of Oklahoma (which also used boundary element for mechanics and finite difference for flow). In particular, we use piece-wise linear (in 2D) and piece-wise quadratic (in 3D) displacement discontinuity elements compared to piece-wise constant elements. This notably allows us to use non-uniform without losing accuracy and treat fractures intersection accurately. The stresses computed around deforming fractures are also much more accurate. Additionally, we use a continuous linear interpolation for pore fluid pressure inside the fracture - and our vertex centered finite volume scheme (which is very similar to a finite element method) automatically capture the fluid flow partitioning between different fracture branches at fractures intersection. Finally, our scheme is fully coupled and implicit (compared to McClure & Horne (2013)).

Computer codes developed

We have developed two C++ codes for two respectively three dimensional configurations. We aim to have minimal dependencies to external libraries. Our numerical developments use a light-weight C++ library for scientific computing developed by InsideLoop³. This library allows to develop efficient / optimized numerical code in C++ for shared memory machines. Note that we prototype algorithms in Mathematica prior to coding them up in C++. We also use Mathematica for pre and post-processing. We have collaborated with Stéphanie Chaillat-Loiseuille (ENSTA, France) and F. Fayard (InsideLoop) to develop a kernel independent hierarchical matrices library for vectorial problems. All our codes are under version control and hosted on the <https://c4science.ch/> platform: an “infrastructure for scientific code co-creation, curation, sharing and testing. Available to the entire Swiss universities community and accessible to external collaborators”.

Organization of this report

We first present in details the boundary element solvers for mechanical deformation of fractures in 2D and 3D: its theoretical foundation, numerical discretization and verification. We also test and discuss the use of hierarchical matrices within our boundary element formulation in order to solve large scale problems (up to 10^6 unknowns) at reasonable computational cost.

In chapter 3, we review the hydro-mechanical constitutive behavior of closed fracture and discuss the chosen models. We also discuss the theoretical background for the modeling of fluid flow in fractures.

³available under Apache License 2.0 at <https://github.com/InsideLoop/InsideLoop>



An implicit one-way 2D hydro-mechanical solver for the simulation of hydraulic stimulation is presented in chapter 4 together with a series of verification tests as well as a series of simulation spanning marginally pressurized and critically stressed conditions in a rock mass containing a large number of randomly oriented fractures. This chapter will lead to two journal publications - one on the numerical scheme, one on hydraulic reactivation of fractured rock mass.

Chapter discuss a fully coupled implicit 2D hydro-mechanical solver for the re-activation of a planar fault due to fluid injection accounting for the stabilising effect of dilatancy on the nucleation of dynamic rupture. This chapter corresponds to a paper published in *J. Geophys. Res.- Solid Earth*.

Conclusions and perspectives close this report in chapter 6.





Chapter 2

Elastic solver for fractures at depth

The goal of this chapter is to summarize the fundamentals of boundary integral equations (BIE) for the solution of fracture problem in elasto-statics with an emphasis on the so-called displacement discontinuity formulation (also referred to as the distributed dislocation techniques in the literature), and present our implemented formulation. The theoretical basis mostly consists of a summary of the material described in more details in different textbooks, notably Bonnet (1999), Hills et al. (1996) and Mogilevskaya (2014). The emphasis is on the use of regularization of the BIE after integration which is the method that we use.

Let consider an elastic medium of domain Ω and boundary Γ with the stiffness tensor c_{ijkl} (with its usual symmetry). The unit normal \mathbf{n} is by convention taken positive toward the exterior of Ω . We denote as σ_{ij} and $\epsilon_{ij} = 1/2(u_{i,j} + u_{j,i})$ the stress and strain tensor under the hypothesis of small strain, while u_i denotes the displacement vector components. We use a Cartesian frame throughout defined by the basis vector \mathbf{e}_i , $i = 1, 2, 3$. We denote $\mathbf{x} = x_i \mathbf{e}_i$ ($\mathbf{y} = y_i \mathbf{e}_i$) as the coordinates vector. Einstein convention of summation over repeated indices is used otherwise specified. The stresses are taken positive in tension.

By convention, we will denote \mathbf{x} , respectively \mathbf{y} , the location of the source, respectively the field (receiver/observation) points. For a function $g(\mathbf{x}, \mathbf{y})$, we denote $g_{,\bar{j}}$ the derivatives with respect to the first argument (i.e. the source point) and $g_{,j}$ the derivatives with respect to the second argument (i.e. the field/observation point):

$$\begin{aligned} g_{,\bar{j}}(\mathbf{x}, \mathbf{y}) &= \partial_{x_j} g(\mathbf{x}, \mathbf{y}) \\ g_{,j}(\mathbf{x}, \mathbf{y}) &= \partial_{y_j} g(\mathbf{x}, \mathbf{y}) \end{aligned}$$

Note: Notations are only adapted slightly from Bonnet (1999). Stresses and tractions are taken positive in tension in this chapter.

2.1 The elasto-static problem

$$\begin{aligned} \sigma_{ij,j} + f_i &= 0 & \text{in } \Omega \\ t_i = \sigma_{ij} n_j &= t_i^g & \text{on } \Gamma_{t_i} \\ u_i &= u_i^g & \text{on } \Gamma_{u_i} \\ \Gamma_{u_i} \cap \Gamma_{t_i} &= \emptyset & \Gamma_{u_i} \cup \Gamma_{t_i} = \Gamma = \partial\Omega \end{aligned}$$

2.1.1 Maxwell-Betti theorem

Maxwell-Betti's reciprocal theorem states the equivalence of the cross elastic energy between two states belonging to the same material space (domain and elastic constants):

$$\sigma_{ij}^{(1)} \epsilon_{ij}^{(2)} = \sigma_{ij}^{(2)} \epsilon_{ij}^{(1)}$$



Another statement is obtained after integration over the domain Ω and use of the divergence theorem, i.e.:

$$\int_{\Gamma} \sigma_{ij}^{(1)} u_j^{(2)} n_i \, dS_y - \int_{\Omega} \sigma_{ij,j}^{(1)} u_i^{(2)} \, dV_y = \int_{\Gamma} \sigma_{ij}^{(2)} u_j^{(1)} n_i \, dS_y - \int_{\Omega} \sigma_{ij,j}^{(2)} u_i^{(1)} \, dV_y$$

2.1.2 Fundamental Point force solution

The fundamental solution for a point force in the direction k located at \mathbf{x} within Ω (often referred as the Green's function in elastostatics) is the solution to the following problem

$$\begin{aligned} \sigma_{ij,j} + \delta_{ik} \delta(\mathbf{y} - \mathbf{x}) &= 0 \\ \sigma_{ij} &= c_{ijkl} \epsilon_{kl} = c_{ijkl} \frac{1}{2} (u_{k,l} + u_{l,k}) = c_{ijkl} u_{k,l} \end{aligned}$$

with for the case of a full-space ($\Omega \equiv \mathbb{R}^3$), the following boundary conditions

$$\lim_{y \rightarrow \infty} \sigma_{ij} = 0 \quad \lim_{y \rightarrow \infty} u_i = 0$$

Note that point force Green function's are known for a number of domain (full, half-space, bi-material) for both isotropic elasticity as well as some form of anisotropy (e.g. transverse isotropy, orthotropy) in 2D and 3D. For now - we just have to remember that such a solution exist.

We will write $U_i^k(\mathbf{x}, \mathbf{y})$ the i th displacement component at \mathbf{y} (the field or observation point) due to a point force in the direction k located at \mathbf{x} (the source point). (This Green's function is sometimes written as G_{ij} in elasticity textbooks (Mura, T. 1982)). Note that the first argument of U_i^k denotes the source point while the second argument the field point.

Similarly we will write as $S_{ij}^k(\mathbf{x}, \mathbf{y})$ the ij component of the stress tensor σ_{ij} at \mathbf{y} due to a point force in the direction k located at \mathbf{x} . By definition of the elastic constitutive law, we have:

$$S_{ij}^k(\mathbf{x}, \mathbf{y}) = c_{ijmn} U_{m,n}^k(\mathbf{x}, \mathbf{y})$$

and $S_{ij}^k = S_{ji}^k$ by symmetry of the stress tensor.

We will also denote the traction solution vector T_i^k , defined as the traction vector in the direction \mathbf{n} associated with the fundamental solution

$$T_i^k(\mathbf{x}, \mathbf{y}) = S_{ij}^k(\mathbf{x}, \mathbf{y}) n_j(\mathbf{y})$$

For any fundamental solution in elasto-statics, the global equilibrium reads:

$$\kappa \delta_{ik} + \int_{\Gamma} T_i^k(\mathbf{x}, \mathbf{y}) \, dS_y = 0$$

$$\text{with } \kappa = \begin{cases} 1 & \mathbf{x} \in \Omega \\ 0 & \mathbf{x} \notin \Omega \end{cases}$$

2.1.2.1 Isotropic full-space - Kelvin solution

For an isotropic material,

$$\begin{aligned} c_{ijkl} &= G (\delta_{ik} \delta_{jl} + \delta_{il} \delta_{jk}) + (K - 2/3G) \delta_{ij} \delta_{kl} \\ 2G &= E/(1 + \nu) \quad 3K = E/(1 - 2\nu) \\ c_{ijkl} &= G (\delta_{ik} \delta_{jl} + \delta_{il} \delta_{jk}) + \frac{2G\nu}{1 - 2\nu} \delta_{ij} \delta_{kl} \end{aligned}$$

The balance of momentum can be transformed into Navier equations:

$$U_{i,ll}^k + \frac{1}{1 - 2\nu} U_{l,li}^k + \delta_{ik} \delta(\mathbf{y} - \mathbf{x})/G = 0$$



The displacement solution can be sought for in the following form:

$$U_i^k = 2(1 - \nu)g_{i,jj}^k - g_{j,ji}^k$$

where g_i^k is denoted the Galerkin tensor, which must be solution of the following fundamental bi-harmonic equation [Show that by introducing the previous form of U_i^k in Navier eq]:

$$g_{i,jjll}^k = -\frac{\delta_{ik}\delta(\mathbf{y} - \mathbf{x})}{2G(1 - \nu)}$$

The fundamental solution of the bi-Laplacian in 3D ($f_{,jjll} = \delta$) is $-r/8\pi$ where $r = \|\mathbf{y} - \mathbf{x}\|$, such that we obtain:

$$g_i^k = \frac{r}{16\pi G(1 - \nu)}\delta_{ik}$$

From this result, we can obtain the following form for the displacement solution due to a unit point force at \mathbf{x} in the direction k

$$U_i^k(\mathbf{x}, \mathbf{y}) = \frac{1}{16\pi G(1 - \nu)} \frac{1}{r} (r_{,i}r_{,k} + (3 - 4\nu)\delta_{ik})$$

where

$$r = \|\mathbf{y} - \mathbf{x}\|$$

$$r_{,i} = \frac{(y_i - x_i)}{r}$$

The stresses follows from the isotropic elastic law as:

$$S_{ij}^k(\mathbf{x}, \mathbf{y}) = -\frac{1}{8\pi(1 - \nu)} \frac{1}{r^2} (3r_{,i}r_{,j}r_{,k} + (1 - 2\nu)(\delta_{ik}r_{,j} + \delta_{jk}r_{,i} - \delta_{ij}r_{,k}))$$

It is important to note that the displacement and stresses are singular when $\mathbf{y} \rightarrow \mathbf{x}$, respectively as $\|\mathbf{y} - \mathbf{x}\|^{-1}$ and $\|\mathbf{y} - \mathbf{x}\|^{-2}$. This is a result of the fact that the traction are prescribed at a single point. All fundamental solutions are actually by nature singular when the observation and source point coincides.

2D plane elasticity Denoting $r(\mathbf{x}, \mathbf{y}) = \sqrt{(y_1 - x_1)^2 + (y_2 - x_2)^2}$ the Euclidian distance between \mathbf{y} and \mathbf{x} in 2d, the point force fundamental solution is given by:

$$U_i^k(\mathbf{x}, \mathbf{y}) = \frac{1}{8\pi G(1 - \nu)} [r_{,i}r_{,k} - (3 - 4\nu)\delta_{ik} \log r]$$

$$S_{ij}^k(\mathbf{x}, \mathbf{y}) = -\frac{1}{4\pi(1 - \nu)r} [2r_{,i}r_{,j}r_{,k} + (1 - 2\nu)(\delta_{ik}r_{,j} + \delta_{jk}r_{,i} - \delta_{ij}r_{,k})]$$

In 2D, the displacement is log singular when $\mathbf{y} \rightarrow \mathbf{x}$, and the stresses are singular as $\|\mathbf{y} - \mathbf{x}\|^{-1}$.

Note that the displacement point force fundamental solution is tending to infinity at infinity (log). This is due to the fact that the plane strain solution correspond to an infinite line of point force. In practice, integration is up to a constant (which can be disregarded).

2.1.2.2 General properties for the point force fundamental solutions

One can use the Maxell-Betti identity for 2 elastic states corresponding to i) a point force at \mathbf{x} in the direction k and ii) a point force at \mathbf{y} in the direction l . By doing so, one obtains the following symmetry for any point force solution:

$$U_l^k(\mathbf{x}, \mathbf{y}) = U_k^l(\mathbf{y}, \mathbf{x})$$

which further implies the following relations:

$$c_{ijkl}U_{a,l}^k(\mathbf{x}, \mathbf{y}) = S_{ij}^a(\mathbf{y}, \mathbf{x})$$

$$c_{ijkl}S_{ab,l}^k(\mathbf{x}, \mathbf{y}) = c_{abkl}S_{ij,l}^k(\mathbf{y}, \mathbf{x})$$



Note that more symmetrical relations hold in the case of an **infinite space** as the source and the observation point can be exchanged by simple coordinate translation (full symmetry of source and observation point). Notably:

$$\begin{aligned} S_{ij}^k(\mathbf{x}, \mathbf{y}) &= -S_{ij}^k(\mathbf{y}, \mathbf{x}) \\ U_{i,l}^k(\mathbf{x}, \mathbf{y}) &= -U_{i,l}^k(\mathbf{y}, \mathbf{x}) \\ S_{ij,l}^k(\mathbf{x}, \mathbf{y}) &= -S_{ij,l}^k(\mathbf{y}, \mathbf{x}) \end{aligned}$$

2.1.3 Integral representation

Let now apply the Maxwell-Betti theorem, taking for system (1), the solution for a point-force at \mathbf{x} in direction k and dropping subscript (2) for the other system. We finally obtain the well-known boundary integral representation for the displacement at any point \mathbf{x} in the domain from the knowledge of the stress and displacement on the boundary (plus a volume term in the presence of body forces):

$$\kappa u_k(\mathbf{x}) = \int_{\Gamma} [\sigma_{ij}(\mathbf{y}) U_{j,l}^k(\mathbf{x}, \mathbf{y}) - S_{ij}^k(\mathbf{x}, \mathbf{y}) u_j(\mathbf{y})] n_i(\mathbf{y}) dS_y + \int_{\Omega} f_i(\mathbf{y}) U_i^k(\mathbf{x}, \mathbf{y}) dV_y \quad (2.1)$$

where $\kappa = 1$ for $\mathbf{x} \in \Omega$ and 0 for $\mathbf{x} \notin \Omega$ (this definition comes from the integral of the Kronecker delta. This integral representation tells us that if we known the traction vector and the displacement on the boundary, then we can obtain the displacement at any point inside the body.

It is also important to note that the fundamental solution for displacement and stresses $S_{ij}^k(\mathbf{x}, \mathbf{y})$ tends to infinity when $\mathbf{x} \in \Gamma$ such that the above integral representation is singular and thus undefined for $\mathbf{x} \in \Gamma$. It requires to be handled properly either by a regularization prior or after integration. We will come back to that later.

Introducing, the traction vector ($t_i = \sigma_{ij} n_j$) and its fundamental counterpart T_i^k , we can re-write the previous equation as:

$$\kappa u_k(\mathbf{x}) = \int_{\Gamma} [t_i(\mathbf{y}) U_i^k(\mathbf{x}, \mathbf{y}) - T_i^k(\mathbf{x}, \mathbf{y}) u_i(\mathbf{y})] dS_y + \int_{\Omega} f_i(\mathbf{y}) U_i^k(\mathbf{x}, \mathbf{y}) dV_y$$

A similar integral representation can be obtained for strain and stresses. For $\mathbf{x} \in \Omega$, and not belonging to Γ , the previous integral representation can be differentiated, denoting $g_{i,j}$ the derivatives of $g_i(\mathbf{x}, \mathbf{y})$ with respect to its first argument (here x_j):

$$u_{k,l}(\mathbf{x}) = \int_{\Gamma} [\sigma_{ij}(\mathbf{y}) U_{j,l}^k(\mathbf{x}, \mathbf{y}) - S_{ij,l}^k(\mathbf{x}, \mathbf{y}) u_j(\mathbf{y})] n_i(\mathbf{y}) dS_y + \int_{\Omega} f_i(\mathbf{y}) U_{i,l}^k(\mathbf{x}, \mathbf{y}) dV_y$$

wich in turn, provide the following representation for the stress tensor

$$\begin{aligned} \sigma_{ij}(\mathbf{x}) &= \int_{\Gamma} [\sigma_{ab}(\mathbf{y}) c_{ijkl} U_{b,l}^k(\mathbf{x}, \mathbf{y}) - c_{ijkl} S_{ab,l}^k(\mathbf{x}, \mathbf{y}) u_a(\mathbf{y})] n_b(\mathbf{y}) dS_y \\ &+ \int_{\Omega} f_a(\mathbf{y}) c_{ijkl} U_{a,l}^k(\mathbf{x}, \mathbf{y}) dV_y \end{aligned} \quad (2.2)$$

2.1.4 Fracture(s) at depth

In geomechanics we are interested in changes with respect to an initial state - noting σ_{ij}^o the corresponding initial state (which is a solution of the balance of momentum when accounting for gravity and tectonic loading etc.), we can re write the balance of momemtun as

$$\sigma_{ij,j} - \sigma_{ij,j}^o = 0 = (\sigma_{ij} - \sigma_{ij}^o)_{,j}$$

Moreover - here - we are interested in the case of fracture(s) deformation at depth - such that the domain of interest Ω will be either the full space ($\Omega \equiv \mathbb{R}^3$) or the half-space ($\Omega \equiv \mathbb{R}^2 \times \mathbb{R}^+$). For simplicity,



in the following, we restrict to fractures in a full space. Extensions to account for other boundaries such as a wellbore or a tunnel are possible - we refer to Bonnet (1999) for more details.

Several boundary element methods have been developed for fracture problem, notably the dual-BEM or the multi-region approach which model the two opposite fracture surfaces. Here we solely restrict to the so-called displacement discontinuity method (also sometimes named the distributed dislocations technique). In that method, the primary kinematic variables are the displacement jump across the fracture. We will denote Γ the mid-plane fracture surface having a unit normal n_i and we denote n_i^+ the normal of the top surface Γ^+ , respectively $n_i^- = n_i$ the normal of the bottom surface, we have $n_i^+ = -n_i^- = -n_i$.

We write the displacement discontinuity d_i across the fracture as positive in overlap [consistent with convection used for dislocation]

$$d_i = u_i^- - u_i^+ (= -\Delta u_i)$$

The traction vector may also possibly be discontinuous between the two crack surfaces (that can be the case when accounting for the effect of a fluid shear stress - but this is typically small and can be neglected). We write ρ_i as such a traction discontinuity

$$\rho_i = (\sigma_{ij}^- - \sigma_{ij}^+) n_j = t_i^+ + t_i^-$$

However, expect in peculiar case (e.g. when accounting for a fluid shear stress), the traction is continuous across the fracture surfaces, such that

$$\rho_i = 0$$

The fracture is self-equilibrated in such cases. We will assume this is the case from now on.

2.1.5 Integral representation for fracture problem

Restricting to the case of a full space with fracture surface Γ , the boundary integral representation for the stress tensor reads (accounting for an initial state of stress):

$$\begin{aligned} \sigma_{ij}(\mathbf{x}) - \sigma_{ij}^o(\mathbf{x}) &= \int_{\Gamma^+} \left[(\sigma_{ab}^+(\mathbf{y}) - \sigma_{ab}^o(\mathbf{y})) c_{ijkl} U_{b,l}^k(\mathbf{x}, \mathbf{y}) - c_{ijkl} S_{ab,l}^k(\mathbf{x}, \mathbf{y}) u_a^+(\mathbf{y}) \right] n_b^+(\mathbf{y}) dS_y \\ &+ \int_{\Gamma^-} \left[(\sigma_{ab}^-(\mathbf{y}) - \sigma_{ab}^o(\mathbf{y})) c_{ijkl} U_{b,l}^k(\mathbf{x}, \mathbf{y}) - c_{ijkl} S_{ab,l}^k(\mathbf{x}, \mathbf{y}) u_a^-(\mathbf{y}) \right] n_b^-(\mathbf{y}) dS_y \end{aligned}$$

which with the notation for the jump of displacement and traction previously introduced becomes:

$$\sigma_{ij}(\mathbf{x}) - \sigma_{ij}^o(\mathbf{x}) = \int_{\Gamma} \rho_i(\mathbf{y}) c_{ijkl} U_{b,l}^k(\mathbf{x}, \mathbf{y}) - \int_{\Gamma} c_{ijkl} S_{ab,l}^k(\mathbf{x}, \mathbf{y}) d_a(\mathbf{y}) n_b(\mathbf{y}) dS_y$$

Restricting to the case of continuous traction ($\rho_i = 0$) which is the typical case, we obtain the following integral representation for the traction vector:

$$t_i(\mathbf{x}) - t_i^o(\mathbf{x}) = -n_j(\mathbf{x}) \int_{\Gamma} c_{ijkl} S_{ab,l}^k(\mathbf{x}, \mathbf{y}) d_a(\mathbf{y}) n_b(\mathbf{y}) dS_y$$

In the case of a infinite space, we can use the relation $S_{ab,l}^k(\mathbf{x}, \mathbf{y}) = -S_{ab,l}^k(\mathbf{x}, \mathbf{y})$ such that

$$\sigma_{ij}(\mathbf{x}) - \sigma_{ij}^o(\mathbf{x}) = \int_{\Gamma} c_{ijkl} S_{ab,l}^k(\mathbf{x}, \mathbf{y}) d_a(\mathbf{y}) n_b(\mathbf{y}) dS_y \quad (2.3)$$

$$t_i(\mathbf{x}) - t_i^o(\mathbf{x}) = n_j(\mathbf{x}) \int_{\Gamma} c_{ijkl} S_{ab,l}^k(\mathbf{x}, \mathbf{y}) d_a(\mathbf{y}) n_b(\mathbf{y}) dS_y \quad (2.4)$$



2.1.5.1 Interlude - link with a nuclei of strain

It is interesting for a moment to pause, and have a look at the integral $\int_{\Gamma} c_{ijkl} S_{ab,l}^k(\mathbf{x}, \mathbf{y}) d_a(\mathbf{y}) n_b(\mathbf{y}) dS_y$. It corresponds to the stress at point \mathbf{x} due a distribution of displacement discontinuity $d_a(\mathbf{y})$ located along the fracture surface Γ of normal $n_b(\mathbf{y})$. $d_a(\mathbf{y}) n_b(\mathbf{y})$ is akin to a point dislocation dipole.

It is interesting to make the link with a nuclei of strain in an infinite medium. A nuclei of strain $\epsilon_{ij}^*(\mathbf{y})$ is as its name suggest a strain located at \mathbf{y} (can model a defect or when distributed a thermal strain, plastic strain etc.). The elastic constitutive relation - when accounting for a distributed eigenstrain is given by

$$\sigma_{ij} = c_{ijkl}(\epsilon_{kl} - \epsilon_{kl}^*)$$

In the absence of other body forces, the balance of momentum becomes:

$$\sigma_{ij,j} - c_{ijkl} \epsilon_{kl,j}^* = 0$$

in other word the effect of a distributed eigenstrain is thus akin to a body force of intensity $-c_{ijkl} \epsilon_{kl,j}^*$.

For a DD on a plane of normal n , the eigenstrain becomes:

$$\left(\frac{1}{2} (d_a(\mathbf{y}) n_b(\mathbf{y}) + d_b(\mathbf{y}) n_a(\mathbf{y})) \right)$$

The moment tensor in seismology is directly this quantity integrated on the slipping patch.

In a full space, the integral representation for displacement (2.1) without any other boundaries (hole, fractures etc.) therefore reduces to

$$u_k(\mathbf{x}) = \int_{\Omega} -c_{ijmn} \epsilon_{mn,j}^*(\mathbf{y}) U_i^k(\mathbf{x}, \mathbf{y}) dV_y$$

where we have dropped the κ (full-space). Integrating by parts assuming ϵ_{mn}^* goes to zero at infinity (localized eigenstrain)

$$\begin{aligned} u_k(\mathbf{x}) &= \int_{\Omega} c_{ijmn} \epsilon_{mn}^*(\mathbf{y}) U_{i,j}^k(\mathbf{x}, \mathbf{y}) dV_y \\ &= \int_{\Omega} \epsilon_{ij}^*(\mathbf{y}) S_{ij}^k(\mathbf{x}, \mathbf{y}) dV_y \end{aligned}$$

we therefore see that the fundamental solution for the displacement u_k at \mathbf{x} due to a nuclei of strain ϵ_{ij}^* at \mathbf{y} (i.e. $\epsilon_{ij}^*(\mathbf{y}) = \epsilon_{ij}^* \delta(\mathbf{y})$) is nothing else than the stresses tensor given by a point force in the direction k contracted with the eigenstrain. Similarly, the stress integral representation (2.2) in the absence of other boundaries and body forces for the full-space reduces to

$$\begin{aligned} \sigma_{ij}(\mathbf{x}) &= - \int_{\Omega} c_{abmn} \epsilon_{mn,b}^*(\mathbf{y}) c_{ijkl} U_{a,l}^k(\mathbf{x}, \mathbf{y}) dV_y = \int_{\Omega} c_{abmn} \epsilon_{mn,b}^*(\mathbf{y}) c_{ijkl} U_{a,l}^k(\mathbf{x}, \mathbf{y}) dV_y \\ &= \int_{\Omega} c_{ijkl} \epsilon_{ab}^*(\mathbf{y}) S_{ab,l}^k(\mathbf{x}, \mathbf{y}) dV_y \end{aligned}$$

i.e. the fundamental stress tensor solution at \mathbf{x} due to a point eigenstrain (nuclei of strain) at \mathbf{y} can be obtained by simple differentiation of the point force stress solution. Moreover, we also see that it is completely similar to the previously obtained integral representation in the case of a fracture with displacement discontinuity (2.3) - with difference that the term $d_a n_b$ does not have the symmetric properties of a strain tensor. However, due to the symmetric properties of the stress tensor, we can rewrite:

$$\begin{aligned} c_{ijkl} S_{ab,l}^k(\mathbf{x}, \mathbf{y}) d_a(\mathbf{y}) n_b(\mathbf{y}) &= c_{ijkl} S_{ab,l}^k(\mathbf{x}, \mathbf{y}) \left(\frac{1}{2} (d_a(\mathbf{y}) n_b(\mathbf{y}) + d_b(\mathbf{y}) n_a(\mathbf{y})) \right) \\ &= c_{ijkl} S_{ab,l}^k(\mathbf{x}, \mathbf{y}) \left(\frac{1}{2} (\delta_{am} \delta_{bn} + \delta_{bm} \delta_{an}) \right) d_a(\mathbf{y}) n_b(\mathbf{y}) \end{aligned}$$

i.e. $c_{ijkl} S_{ab,l}^k(\mathbf{x}, \mathbf{y}) \times \frac{1}{2} (\delta_{am} \delta_{bn} + \delta_{bm} \delta_{an})$ is the fundamental stress solution due to a displacement discontinuity tensor $d_a n_b$.



2.1.5.2 Back to the integral representation - link with the solution of a Volterra edge dislocation

Let's now return to the traction representation for a fracture (2.4) in order to make the link with dislocation.

After integration by parts - assuming that $d_a = 0$ at the crack tips (note - be careful for example when modelling a surface breaking crack). One obtain for the stress tensor and traction vector

$$\begin{aligned}\sigma_{ij}(\mathbf{x}) - \sigma_{ij}^o(\mathbf{x}) &= - \int_{\Gamma} c_{ijkl} S_{ab}^k(\mathbf{x}, \mathbf{y}) [d_a(\mathbf{y}) n_b(\mathbf{y})]_{,l} dS_y \\ t_i(\mathbf{x}) - t_i^o(\mathbf{x}) &= - n_j(\mathbf{x}) \int_{\Gamma} c_{ijkl} S_{ab}^k(\mathbf{x}, \mathbf{y}) [d_a(\mathbf{y}) n_b(\mathbf{y})]_{,l} dS_y\end{aligned}\quad (2.5)$$

Note that $[d_a(\mathbf{y}) n_b(\mathbf{y})]_{,l}$ is the **surface gradient** of $d_a(\mathbf{y}) n_b(\mathbf{y})$, i.e. the gradient with the component normal to the surface removed. It is given by for a scalar function f

$$\nabla_S f = f_{,i} - (f_{,j} n_j) n_i$$

here as:

$$\begin{aligned}[d_a(\mathbf{y}) n_b(\mathbf{y})]_{,l} &= d_{a,l}(\mathbf{y}) n_b(\mathbf{y}) - n_l(\mathbf{y}) (d_{a,i}(\mathbf{y}) n_i(\mathbf{y})) n_b(\mathbf{y}) \\ &= d_{a,l}(\mathbf{y}) n_b(\mathbf{y}) - n_l(\mathbf{y}) d_{a,b}(\mathbf{y})\end{aligned}\quad (2.6)$$

as $n_i n_b = \delta_{ib}$.

Edge dislocation Now image the particular case of an edge dislocation: a semi-infinite constant displacement discontinuity along the plane Γ of (constant) normal n_b . In the dislocation literature the displacement discontinuity is referred to as the Burgers vector (and written b_a).

For example - in 2D taking $n_b = e_2$ in that case $d_a(\mathbf{y}) = d_a H(y_1)$ where H is the Heaviside function. Hence, the surface gradient becomes

$$[d_a(\mathbf{y}) n_b(\mathbf{y})]_{,l} = \delta(y_1) [\delta_{l1} \delta_{b2} d_a e_2 - e_2 \delta_{b1} \delta_{l2} d_a]$$

and the stress at point \mathbf{x} due to such a dislocation are given by:

$$\sigma_{ij}(\mathbf{x}) - \sigma_{ij}^o(\mathbf{x}) = - [c_{ijk1} S_{2a}^k(\mathbf{x}, \mathbf{0}) - c_{ijk2} S_{1a}^k(\mathbf{x}, \mathbf{0})] d_a$$

One can introduce the following notation for such a fundamental kernel (stress tensor induced by an edge dislocation centered on the origin for a unit displacement jump)

$$s_{ijk}(\mathbf{x}) = - [c_{ijm1} S_{2k}^m(\mathbf{x}, \mathbf{0}) - c_{ijm2} S_{1k}^m(\mathbf{x}, \mathbf{0})] \quad (2.7)$$

such that the stresses induced by an edge dislocation with a Burgers vector b_k

$$\sigma_{ij}(\mathbf{x}) - \sigma_{ij}^o(\mathbf{x}) = s_{ijk}(\mathbf{x}) b_k$$

It is interesting to note that the dislocation solution is a combination of a number of point-forces, contracted with the stiffness tensor.

2D Plane-strain case Using the 2D plane-strain point force solution, it is possible to obtain the analytical expression for the different component of s_{ijk} ($i, j, k = 1, 2$)

$$\begin{aligned}s_{ijk} &= \frac{2G}{\pi(\kappa + 1)} h_{ijk} = \frac{E'}{4\pi} g_{ijk} \\ h_{111} &= \frac{-x_2(3x_1^2 + x_2^2)}{r^4} & h_{112} &= \frac{x_1(x_1^2 - x_2^2)}{r^4} \\ h_{221} &= \frac{x_2(x_1^2 - x_2^2)}{r^4} & h_{222} &= \frac{x_1(x_1^2 + 3x_2^2)}{r^4} \\ h_{121} &= \frac{x_1(x_1^2 - x_2^2)}{r^4} & h_{122} &= \frac{x_2(x_1^2 - x_2^2)}{r^4} \\ r^2 &= x_1^2 + x_2^2\end{aligned}\quad (2.8)$$

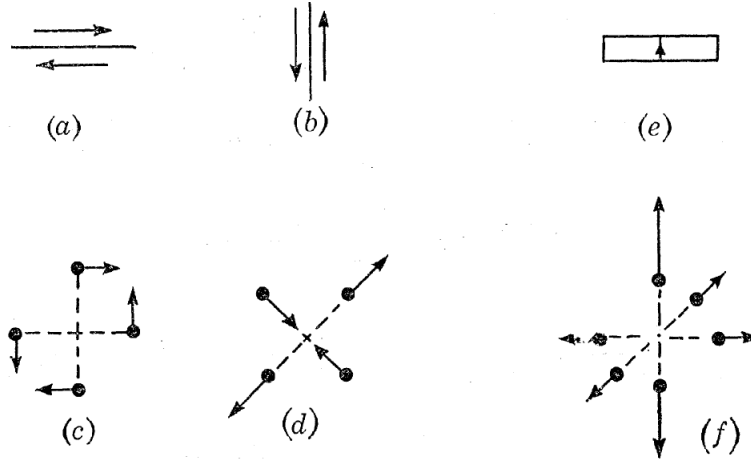


FIGURE 2. Equivalence between elementary dislocated areas and point-force clusters.

Figure 2.1: Schematic representation of elementary dislocated area as combination of point forces- taken from Eshelby (1973).

We of course obtain the exact same expressions than the ones obtained from a direct solution of the plane elasticity problem for a dislocation (see appendix 6).

Dislocation dipole Now, it is possible to combine two edge dislocation of opposite sign, one at the origin and the other at Δx_1 , taking the limiting $\Delta x_1 \rightarrow 0$, we obtain a dislocation dipole, and the corresponding stress is related to the derivatives of s_{ijk} . For example,

$$\frac{\pi(\kappa + 1)}{2G} \sigma_{22}^{dipole 2}(x_1 - \xi, x_2 = 0) = b_2 \left(\frac{1}{x_1 - \xi - d\xi} - \frac{1}{x_1 - \xi} \right) \approx b_2 \frac{d\xi}{(x_1 - \xi)^2} = b_2 \frac{\partial s_{222}(x_1 - \xi)}{\partial \xi}$$

, in general

$$\sigma_{ij}^{ab} = c_{ijkl} S_{ab,l}^k(\mathbf{x}, \mathbf{y})$$

for a dislocation dipole of normal n_b and dd vector d_a . Note that we in fact recover the displacement discontinuity tensor (see above) - prior to the integration by parts. [In 3D the dislocation dipole is replaced by an infinitesimal dislocation loop.]

2.1.5.3 Case of a planar crack in 2D - dislocation density

Similarly than for the dislocation, we can particularize the traction integral representation (2.5) for a planar crack in 2D located along the \mathbf{e}_1 axis (normal \mathbf{e}_2) of the infinite space. Similarly than for the dislocation, the surface gradient reduce to

$$[d_a(\mathbf{y})n_b]_{,l} = d_{a,l}\delta_{l1}\delta_{b2} - \delta_{l2}\delta_{b1}d_{a,b}$$

and the integral representation for the traction vector becomes (in the case of the full space where the point force solution is function of $\mathbf{x} - \mathbf{y}$

$$\begin{aligned} t_i(\mathbf{x}) - t_i^o(\mathbf{x}) &= -n_j(\mathbf{x}) \int_{\Gamma(y_2=0)} [c_{ijk1} S_{2a}^k(\mathbf{x}, \mathbf{y}) - c_{ijk2} S_{1a}^k(\mathbf{x}, \mathbf{y})] d_{a,1}(\mathbf{y}) dS_y \\ &= n_j(\mathbf{x}) \int_{\Gamma(y_2=0)} s_{ijk}(\mathbf{x} - \mathbf{y}) d_{k,1}(\mathbf{y}) dS_y \end{aligned}$$

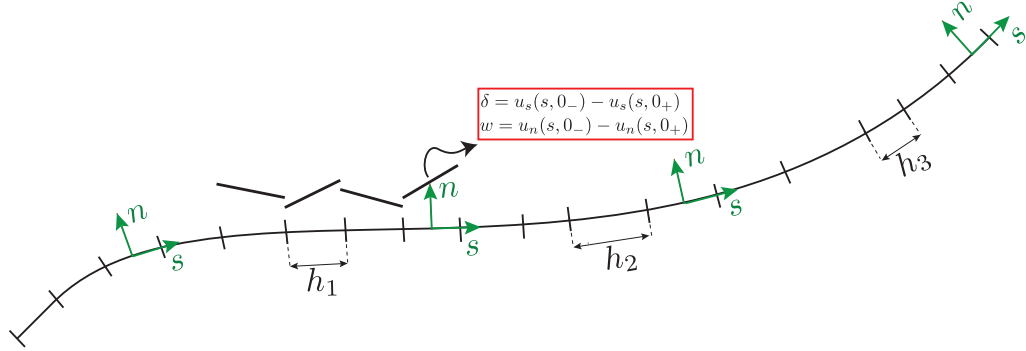


Figure 2.2: A fracture in 2D discretized with linear segments. The jump of displacement across the fracture (displacement discontinuity) are the primary unknowns, and are approximately linearly along a linear segment. Note that we don't enforce continuity between the elements (which is beneficial when modeling intersections between fractures). The elements used are so-called piece-wise linear element P1 elements. The code also has P0 elements (piece-wise constant) implemented. Note that two conventions are possible: i) positive stress in traction / positive DD in overlap, or ii) positive stress in compression / positive DD in opening.

i.e. the contribution is therefore the one of distributed dislocations. For a planar crack of length $2a$ on $y_2 = 0$ for $n_j(\mathbf{x}) = e_2$, we obtain

$$t_1(x_1, x_2) - t_1^0(x_1, x_2) = \frac{G}{2\pi(1-\nu)} \int_{-a}^a h_{121}(x_1 - y_1, x_2) \frac{\partial d_1}{\partial y_1} dy_1 + \frac{G}{2\pi(1-\nu)} \int_{-a}^a h_{122}(x_1 - y_1, x_2) \frac{\partial d_2}{\partial y_1} dy_1$$

$$t_2(x_1, x_2) - t_2^0(x_1, x_2) = \frac{G}{2\pi(1-\nu)} \int_{-a}^a h_{221}(x_1 - y_1, x_2) \frac{\partial d_1}{\partial y_1} dy_1 + \frac{G}{2\pi(1-\nu)} \int_{-a}^a h_{222}(x_1 - y_1, x_2) \frac{\partial d_2}{\partial y_1} dy_1$$

which can further be specified for the case where \mathbf{x} is on the crack plane ($x_2 = 0$), using the previously derived expressions of h_{ijk} (2.8):

$$t_1(x_1, x_2 = 0) - t_1^0(x_1, x_2 = 0) = \frac{G}{2\pi(1-\nu)} \int_{-a}^a \frac{1}{x_1 - y_1} \frac{\partial d_1}{\partial y_1} dy_1 \quad (2.9)$$

$$t_2(x_1, x_2 = 0) - t_2^0(x_1, x_2 = 0) = \frac{G}{2\pi(1-\nu)} \int_{-a}^a \frac{1}{x_1 - y_1} \frac{\partial d_2}{\partial y_1} dy_1 \quad (2.10)$$

We notably see that for a planar crack, the shear and opening tractions boundary integral equations decouples - a shear DD does not induce any normal stress on the crack plane, and vice versa an opening DD does not induce any shear stress on the plane. This is of course only the case for a planar crack. Interestingly, the same results is also obtained for anisotropic material.

The integral representation (2.9)-(2.10) are singular integral equations when x_1 is inside the fracture. Knowing the tractions applied on the fracture plane, they can be solved to obtain the corresponding normal / shear DD. Due to their singular nature (Cauchy singular to be precise), special care needs to be used for their solution. The same singular nature extends to the case of non-planar cracks. In the case of planar cracks, specific quadrature can be used to solve these boundary integral equations with spectral accuracy. In the following, we focus on devising a collocation method based on the discretization of the fracture with linear segment elements (in 2D) and triangular element (in 3D).

2.2 Numerical discretization - collocation - regularization after integration

We now turn to the solution of the general boundary integral equation (BIE) eq.(2.5) which link the tractions to the displacement discontinuities along the fracture. From the knowledge of the tractions t_i along the



fracture, our aim is to determine the displacement discontinuities. We recall that when \mathbf{x} is inside the fracture, the integral representation is singular, i.e. combining (2.5) and (2.6), we have the following singular systems of BIE ($i = 1, 2$ in 2D, $i = 1, 2, 3$ in 3D):

$$t_i(\mathbf{x}) - t_i^o(\mathbf{x}) = -n_j(\mathbf{x}) \int_{\Gamma} c_{ijkl} S_{ab}^k(\mathbf{x}, \mathbf{y}) [d_{a,l}(\mathbf{y}) n_b(\mathbf{y}) - n_l(\mathbf{y}) d_{a,b}(\mathbf{y})] dS_y \quad \mathbf{x} \in \Gamma$$

We focus in the following in the solution of this system of equations using the so-called displacement discontinuity method (aka distributed dislocations techniques) - which is a collocation method.

2.2.1 Fracture Discretization

The first step is to discretize the fracture surface Γ into a set of elements / cells e.g. segments in 2D, triangles or polygons in 3D. We only consider planar elements here (locally, the fracture curvature is approximated by planar elements).

The surface mesh of Γ consists of N of such planar elements of surface Γ_e , i.e.

$$\Gamma \approx \sum_{e=1, N} \Gamma_e$$

[note that even for large curvature the tessellation converges toward Γ for a sufficiently large number of elements]. The discretize BIE therefore becomes

$$t_i(\mathbf{x}) - t_i^o(\mathbf{x}) = -n_j(\mathbf{x}) \sum_{e=1, N} \int_{\Gamma_e} c_{ijkl} S_{ab}^k(\mathbf{x}, \mathbf{y}) [d_{a,l}(\mathbf{y}) n_b^e - n_l^e d_{a,b}(\mathbf{y})] dS_y \quad (2.11)$$

with n_i^e the normal to element Γ_e . Note that we could also use directly the original BIE (2.4) (prior to integration by parts), i.e.

$$t_i(\mathbf{x}) - t_i^o(\mathbf{x}) = n_j(\mathbf{x}) \sum_{e=1, N} \int_{\Gamma_e} c_{ijkl} S_{ab,l}^k(\mathbf{x}, \mathbf{y}) d_a(\mathbf{y}) n_b^e dS_y \quad (2.12)$$

2.2.2 Choice of basis function / choice of collocation points

We now turn to the choice of the interpolation of the displacement discontinuity vector d_i over the discretized surface. One could think of using familiar continuous interpolation similar to what is typically done in finite elements. Using continuous interpolation for such a Cauchy singular BIE is possible - but discontinuous interpolation are also often used (and we will mostly discussed discontinuous interpolation in what follow). It is important to note that due to singular nature of the BIE, collocation can not be performed at a point either located along an edge of the element (3D) or at one of the vertex (in 2D and 3D) of the element.

Piece-wise constant element The lowest possible order of interpolation is the piece-wise constant approximation. It implies that the displacement discontinuity are constant within one element. Such interpolation is intrinsically discontinuous between elements. As a result, we have two respectively three displacement discontinuities unknowns in 2D respectively 3D problems. We will therefore need to collocate the BIEs at one point within the element - the natural (and actually optimal) choice is to collocate the BIEs at the element center.

Piece-wise polynomial element A straightforward generalization is to use a discontinuous polynomial interpolation of the DD vector within one element - without enforcing continuity between elements. For example, in 2D a segment with linear or quadratic interpolation for d_i can be easily built. As the order of the polynomial increase, the BIEs needs to be collocated at $p + 1$ points (where p is the order of the polynomial). Example of elements are:



- Piece-wise linear element (2D) - 4 unknowns per element (2 shear and 2 opening dd) - 2 collocation points
- Piece-wise quadratic element (2d) - 6 unknowns per element (3 shear and 3 opening dd) - 3 collocation points
- Piece-wise linear triangular element (3D) - 9 unknowns per element - 3 collocation points
- Piece-wise quadratic triangular element (3D) - 18 unknowns per element - 6 collocation points (see Nikolskiy et al. (2015))

Even cubic triangular elements have been used (30 unknowns per element - 10 collocation points) ! see e.g. Napier & Malan (2007). It is important to note that as the interpolation is discontinuous between elements, the total number of unknowns is directly $N_e \times N_{\text{dof},e}$: number of elements times number of unknowns (i.e. dofs) per elements.

Continuous polynomial element It is also possible to use continuous interpolation of the displacement discontinuities between elements. In doing this, the total number of unknowns is of course less than when using discontinuous interpolation. However, careful choice of the collocation points is required (as the BIE can not be collocated at the nodes without further regularization). Moreover, discontinuous interpolation between elements is a nice feature when dealing with fracture intersections notably (as well as sharp corner boundaries).

2.2.3 Analytical integration over an element

We now restrict the discussion to piece-wise constant or piece-wise linear element in 2D for sake of illustration. We see that equation (2.12) is a sum of integration over each element Γ_e . We therefore need to evaluate the following integrals

$$I_i^e(\mathbf{x}) = n_j(\mathbf{x}) \int_{\Gamma_e} c_{ijkl} S_{ab,l}^k(\mathbf{x}, \mathbf{y}) d_a(\mathbf{y}) n_b^e dS_y$$

As the element Γ_e is planar, we can re-use what we have derived for the planar crack case and moreover, perform a change of coordinates and perform the integration for a reference segment centered in the origin of length 2 along the e_1 axis. Denoting by $'$ the coordinates of the source and receiver point in that local reference system, the element integral becomes

$$I_i^{e=R}(\mathbf{x}') = n_j(\mathbf{x}') \int_{-1}^1 s_{ijk}(\mathbf{x}' - \mathbf{y}') d_{k,1}(\mathbf{y}') dy_1'$$

Piece-wise constant element For the piece-wise constant case this reduces to the simple expression,

$$\begin{aligned} I_i^e(\mathbf{x}') &= -n_j(\mathbf{x}') d_k \int_{-1}^1 s_{ijk,1}(x_1' - y_1', x_2') [\delta(y_1 - 1) - \delta(y_1 + 1)] dy_1 \\ &= -n_j(\mathbf{x}') d_k \times [s_{ijk}(x_1' - 1, x_2) - s_{ijk}(x_1' + 1, x_2')] \end{aligned}$$

Note that a self-effect correction for elements located near the fracture tip has been proposed by Ryder & Napier (1985)- It consists in adding to the tip element self-effect (normal-normal & shear-shear) the quantity $\alpha E'/(4h)$ where h is the corresponding element size and α a pre-factor taken as $1/3$ - see also Gordeliy & Detournay (2011). We will refer to it as the “tip” correction. (it works well in both 2 and 3D).

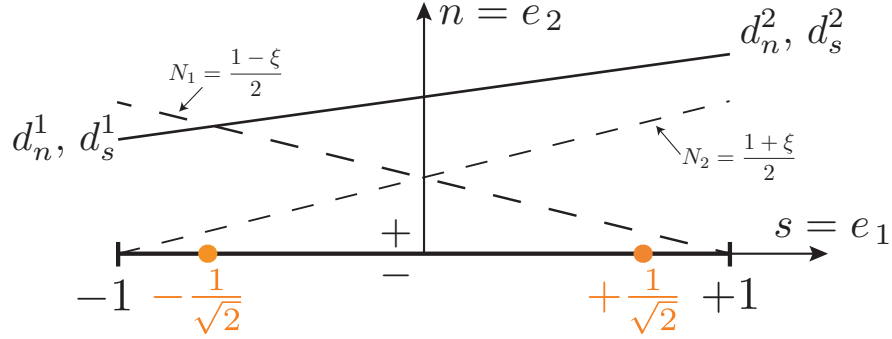


Figure 2.3: Reference displacement discontinuity segment - Piece-wise linear DD (so-called P1 element). The normal $d_n = u_n^- - u_n^+$ and shear displacement discontinuity $d_s = u_s^- - u_s^+$ (positive in overlap) are linearly evolving within an element. The normal n is n^- with the classical convention of outward normal to the elastic body. The integral equation is enforced at the collocation points (orange points): for a piece-wise linear element at $[-1/\sqrt{2}, 1/\sqrt{2}]$, at 0 for a piece-wise constant element. For a piece-wise linear element, the unknowns dofs are located at the nodes $(-1, 1)$.

Piece-wise linear element Here again it is easier to perform the integration for a unit segment along the e_1 axis centered in the origin and of size 2, i.e. segment defined by $y_1' \in [-1, 1]$ (see Fig. 2.3). The case of any segment orientation, size and position (of the segment as well as of the observation point) can be deduced easily by a change of coordinates. Moreover, it is customary to denote in that local frame of the element d_1 as d_s (s for shear) and d_2 as d_n (n for normal). Dropping the $'$ for clarity.

The shear and normal component of the displacement discontinuity thus varies as:

$$\begin{aligned} d_s(\xi) &= N_1(\xi)d_s^1 + N_2(\xi)d_s^2 \\ d_n(\xi) &= N_1(\xi)d_n^1 + N_2(\xi)d_n^2 \end{aligned}$$

with the usual 1D linear shape functions

$$N_1(\xi) = \frac{1 - \xi}{2} \quad N_2(\xi) = \frac{1 + \xi}{2}$$

We thus have the stress at x_i due to the shear, respectively normal, linear variation of displacement discontinuity over the reference element as:

$$\begin{aligned} \sigma_{ij}^s(x'_1, x'_2) &= - \underbrace{\int_{-1}^1 \frac{\partial s_{ij1}}{\partial \xi} N_1(\xi) d\xi}_{\sigma_{ij}^{s1}} \times d_s^1 - \underbrace{\int_{-1}^1 \frac{\partial s_{ij1}}{\partial \xi} N_2(\xi) d\xi}_{\sigma_{ij}^{s2}} \times d_s^2 \\ \sigma_{ij}^n(x'_1, x'_2) &= - \underbrace{\int_{-1}^1 \frac{\partial s_{ij2}}{\partial \xi} N_1(\xi) d\xi}_{\sigma_{ij}^{n1}} \times d_n^1 - \underbrace{\int_{-1}^1 \frac{\partial s_{ij2}}{\partial \xi} N_2(\xi) d\xi}_{\sigma_{ij}^{n2}} \times d_n^2 \end{aligned}$$

such that

$$I_i^e(x'_1, x'_2) = n_j(x'_1, x'_2) \sigma_{ij}^s(x'_1, x'_2) + n_j(x'_1, x'_2) \sigma_{ij}^n(x'_1, x'_2)$$

The different integrals σ_{ij}^{n1} etc. (there is a total of $4 \times 3 = 12$ integrals for the piece-wise linear DD element) can be obtained analytically (note that the principal value should be taken when $x'_2 = 0$). Note however, that the integrals (e.g. σ_{xx}^{s1} etc.) are still singular for $x'_1 = \pm 1, x'_2 = 0$. This is why when solving a fracture problem using N displacement discontinuity segment, we collocate the integral equations for shear and normal tractions at points inside of the DD segments, i.e. located at $\pm 1/\sqrt{2}$ in the unit segment (a choice argued to be optimal - see discussion in Crawford & Curran (1982)).

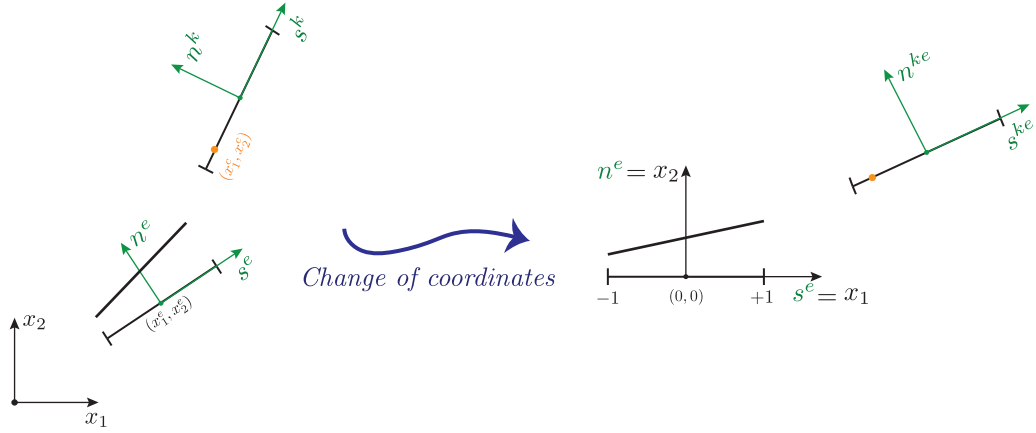


Figure 2.4: Influence of segment DD element e on element k . We perform a change of coordinates to compute the influence of the element e displacement discontinuities on the normal and shear tractions at the collocation points of element k . This change of coordinates is such that element e corresponds to the reference unit element.

It is worthwhile to note that due to the symmetries of s_{ijk} , we have the following relations, which helps reducing computational cost:

$$\sigma_{xx}^n = \sigma_{xy}^s \quad \sigma_{xy}^n = \sigma_{yy}^s$$

instead of 12 integrals, we therefore only need to evaluate 6. These integrals can be obtained easily using for example Mathematica. Recall that they are expressed in the coordinate system of the reference element.

2.2.4 Assembly of the final system

Let's now come back to the case of a plane-strain fracture (e.g. Fig.2.2) in an in-situ stress field σ_{ij}^o (in the absence of a crack) with given normal and shear tractions t_n and t_s applied inside the fracture. To construct the equations for shear and normal tractions at a given collocation point (x_1^k, x_2^k) in element k of normal n_i^k (and tangent vector s_i^k), we use the stress field induced by a piece-wise linear dd element e of normal n^e centered in $(\bar{x}_1^e, \bar{x}_2^e)$ in the global reference frame. Changing of coordinates such that the element e corresponds to the unit reference element centered in the origin with normal along e_2' (as discussed previously), and denoting as R the rotation matrix to switch from the local element e system to the global system of coordinates, the normal and tangential unit vector for element k in that system will be denoted as n_i^{ke} and s_i^{ke} :

$$n_i^{ke} = R_{ij}^T n_j^k \quad s_i^{ke} = R_{ij}^T s_j^k$$

and the collocation point x_i^k is $x_i'^k$ in the reference frame of element e :

$$x_i'^k = R_{ij}^T \cdot (x_j^k - \bar{x}_j^e)$$

such that the induced shear $t_s^{ek}(x^k)$ and normal $t_n^{ek}(x^k)$ tractions by the linear variation of displacement discontinuity over element e at the collocation point x_m^k located in element k are

$$\begin{aligned} t_s^e(x_m^k) &= s_i^{ke} \sigma_{ij}^{s1}(x_m^k) n_j^{ke} d_s^1 + s_i^{ke} \sigma_{ij}^{s2}(x_m^k) n_j^{ke} d_s^2 + s_i^{ke} \sigma_{ij}^{n1}(x_m^k) n_j^{ke} d_n^1 + s_i^{ke} \sigma_{ij}^{n2}(x_m^k) n_j^{ke} d_n^2 \\ t_n^e(x_m^k) &= n_i^{ke} \sigma_{ij}^{s1}(x_m^k) n_j^{ke} d_s^1 + n_i^{ke} \sigma_{ij}^{s2}(x_m^k) n_j^{ke} d_s^2 + n_i^{ke} \sigma_{ij}^{n1}(x_m^k) n_j^{ke} d_n^1 + n_i^{ke} \sigma_{ij}^{n2}(x_m^k) n_j^{ke} d_n^2 \end{aligned}$$



To simplify the notation, we re-write

$$\begin{aligned} s_i^{ke} \sigma_{ij}^{sl}(x_m^k) n_j^{ke} &= K_{ss}^{el}(x_m^k) & l = 1, 2 \\ s_i^{ke} \sigma_{ij}^{nl}(x_m^k) n_j^{ke} &= K_{sn}^{el}(x_m^k) & l = 1, 2 \\ n_i^{ke} \sigma_{ij}^{sl}(x_m^k) n_j^{ke} &= K_{ns}^{el}(x_m^k) & l = 1, 2 \\ n_i^{ke} \sigma_{ij}^{nl}(x_m^k) n_j^{ke} &= K_{nn}^{el}(x_m^k) & l = 1, 2 \end{aligned}$$

Finally, we can sum up the contributions of all elements in the mesh to the induced shear and normal tractions at the collocation point \mathbf{x}^k located in element k in order to balance the in-situ tractions t_i^o and applied normal and shear tractions t_n and t_s inside the fracture at \mathbf{x}^k :

$$\begin{aligned} t_s(\mathbf{x}^k) - t_s^o(\mathbf{x}^k) &= \sum_{e=1}^N \sum_{l=1}^2 (K_{ss}^{el}(\mathbf{x}^k) d_s^{el} + K_{sn}^{el}(\mathbf{x}^k) d_n^{el}) \\ t_n(\mathbf{x}^k) - t_n^o(\mathbf{x}^k) &= \sum_{e=1}^N \sum_{l=1}^2 (K_{ns}^{el}(\mathbf{x}^k) d_s^{el} + K_{nn}^{el}(\mathbf{x}^k) d_n^{el}) \end{aligned}$$

where in the previous equation there are no summation on repeated indices, i.e. d_s^{e1} denotes the shear displacement discontinuity at nodes 1 of element e , and K_{ss}^{el} correspond to the corresponding contribution on the shear traction at \mathbf{x}^k etc. We write the previous equations for shear and normal tractions at $2N$ collocations point to obtain a system of $4N$ equations with $4N$ unknowns related to the shear and normal displacement discontinuities in each piece-wise linear element DD.

Introducing the total vector of displacement discontinuity \mathbf{d} (of size $4N$) obtained by stacking the unknown as:

$$\mathbf{d} = (d_s^{e=1,l=1}, d_n^{e=1,l=1}, \dots, d_s^{e,l=1}, d_n^{e,l=1}, d_s^{e,l=2}, d_n^{e,l=2} \dots)$$

and the total vector of applied tractions (and similarly in-situ tractions) at all the collocation points (2 per elements)

$$\mathbf{t} = (t_s^{e=1,l=1}, t_n^{e=1,l=1}, \dots, t_s^{e,l=1}, t_n^{e,l=1}, t_s^{e,l=2}, t_n^{e,l=2} \dots)$$

we can schematically re-writte the elastic system of equations as:

$$\mathbf{t} - \mathbf{t}^o = \mathbb{E} \mathbf{d} \quad (2.13)$$

where \mathbb{E} is a $4N \times 4N$ matrix (in the case of P1 elements) containing the corresponding entries $K_{ss}^{el}(\mathbf{x}^k)$, etc. It is in general a fully populated (dense) matrix which is not symmetric. However, it is worth to note that for the particular case of a straight crack the shear and normal component uncouples ($K_{sn} = K_{ns} = 0$).

2.2.4.1 Extension to Quasi-dynamic

The boundary element method presented previously is restricted to quasi-static elasticity. Upon the nucleation of a dynamic rupture, inertial effects are no more negligible. Rigorously, one would need to switch to fully elastodynamic formulation. However, a quasi-dynamic approximation - originally proposed by Rice (1993) - can be used to account for radiation of seismic waves in a simplified manner and avoid unrealistic unbounded slip rates. It consists in adding a term related to slip and opening rates and multiplied by the ratio between elastic modulus and wave-speeds on the right-hand side elasto-static boundary integral equations (2.12) and () in the end, i.e. a so-called radiation damping term:

$$-\frac{1}{2} \begin{bmatrix} G/c_s & 0 \\ 0 & G/c_p \end{bmatrix} \cdot \frac{\partial}{\partial t} \begin{bmatrix} d_s \\ d_n \end{bmatrix}$$

where c_s and c_p denote the shear and compressional wave speeds: $c_s = \sqrt{G/\rho}$ and $c_p = \sqrt{(K + 4/3G)/\rho}$. Such a quasi-dynamic approximation results in an additional diagonal term in the final elasticity equation. Note that as discussed in Rice (1993), mass scaling can be performed to relax time-step restrictions when integrating through instabilities.



2.2.5 Simple Examples in 2D

We focus on 2 simple examples: a griffith crack (uniformly pressurized crack) and a series of intersecting crack - aka star-crack

2.2.5.1 Griffith Crack

The solution of a crack of length $2a$ centered of the origin of a 2D elastic infinite space in plane-strain under remote far-field tension p or similarly uniformly pressurized is well known (see e.g. Sneddon, I. N. (1946) and references therein). The fracture width $w = -d_y$ is notably given by:

$$w(x) = \frac{4p}{E'} \sqrt{a^2 - x^2} \quad |x| \leq a$$

and the mode I stress intensity factor is given by

$$K_I = p\sqrt{\pi a}$$

We can compare thus the numerical results obtained either with P0 or P1 element - first for the case of an uniform mesh (see Fig. 2.5). We see that P0 element with tip correction outperform P1 element in that case. Interestingly, P1 element do not exhibit a larger convergence rate than P0 element (w.o tip correction) but are always more precise- this is because even P1 element do not capture well the near-tip square-root behavior which control convergence.

Local tip refinement - Piece-wise constant versus linear element It is interesting to test the case where the mesh is refined near the fracture tip (in the last 25% of the crack) with either P0 (with tip correction) or P1 element. The local relative error on the fracture width along the fracture is displayed in fig. 2.6. One observe that P0 element (even with tip correction) perform really badly on such a non-uniform mesh, whereas P1 element actually benefit from such a mesh refinement. P0 elements can really be used only with uniform mesh (and with the Napier-Ryder tip correction). P1 elements are more versatile mesh wise. Note that the same results are observed in 3D.

2.3 Acceleration - a brief introduction to \mathcal{H} -matrices

The boundary element method described previously -like all BEM - allows to reduce the problem dimension by one. However, the resulting matrices are fully populated - which is a striking difference compared to domain based method such as the finite element method (for which the number of unknowns is significantly larger but the final matrix is very sparse). The fact that the final BEM matrix is fully populated has two negative consequences:

- The memory requirements are in $O(N^2)$ and become large to the point that the system can not fit in memory even for not so large cases- e.g. $N = 10^5$ unknowns requires 80GB of RAM (using 64 bits(8 Bytes)- i.e. $8 * (10^5)^2$)
- A solution of the system via a direct solver scales in $O(N^3)$ and a solution via an iterative solver as $O(kN^2)$ - where k is the number of iterations.

Profile of $t_y(x)$ in front of the fracture / approximation as $\mathcal{V}_{crack} \times t_y^{dd}$.

A number of different techniques have therefore emerged to address these limitations intrinsic to BIE with the aim to solve problem of large size. All these techniques rely on the observation that for elliptic operator, the fundamental kernel decays as the distance between the source and observation points increases- such that the integral representation “smooth” out details for far-enough observation points. As a result one can “lump” the influence of sources far from an observation points. The first technique to use such an idea was coined as the panel clustering method (see e.g. Hackbusch & Nowak (1989)) which provide a fast way to perform matrix-vector product of the collocation matrix). Along similar lines, but in

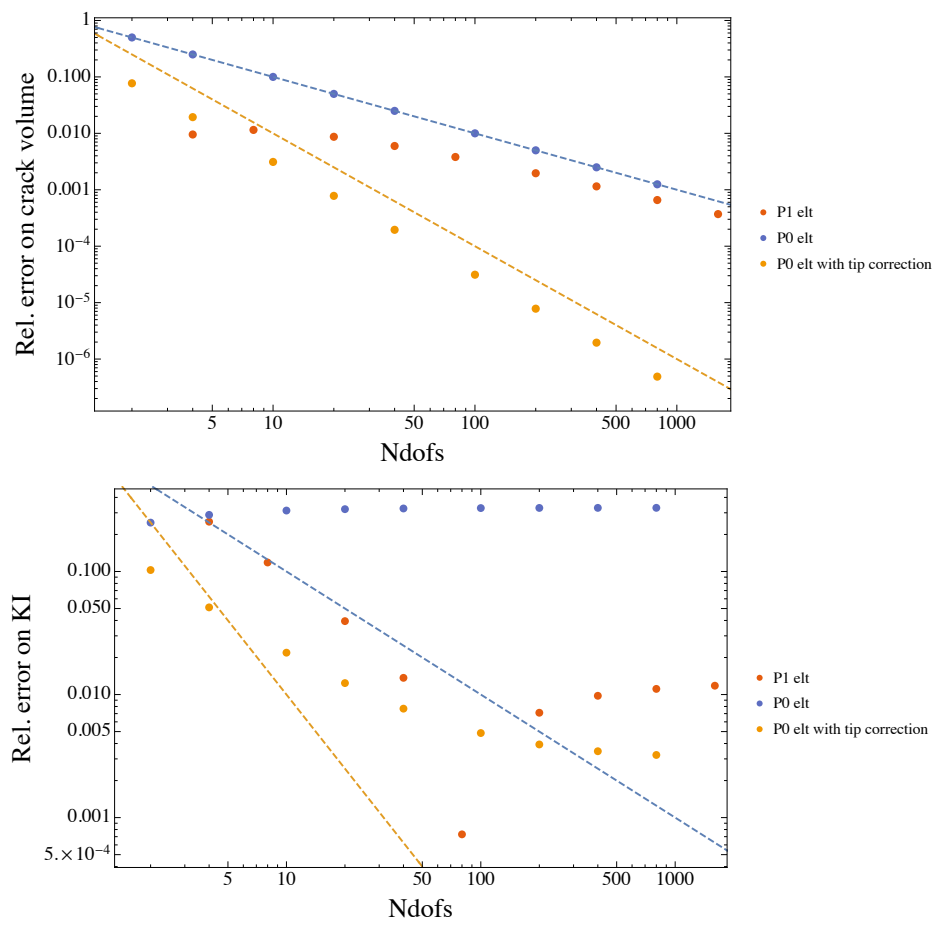


Figure 2.5: Griffith crack example - uniform mesh case. The dashed blue line correspond to a convergence in N^{-1} while the yellow dashed line corresponds to N^{-2} .

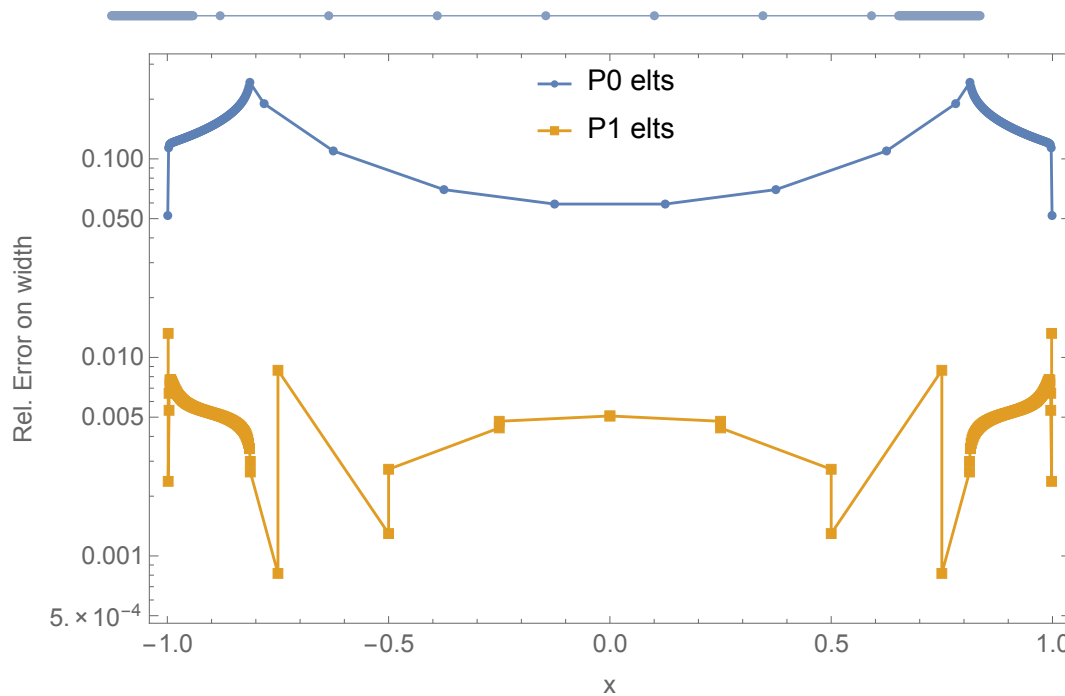


Figure 2.6: Griffith crack (uniformly pressurized) - Local relative error on the fracture width - case of a constant mesh refinement at the tip. The P0 elements fails miserably (even with tip correction) for such a non-uniform mesh, whereas the P1 elements properly captured the width everywhere in the domain (maximum of 2% of relative error compared to the analytical solution).

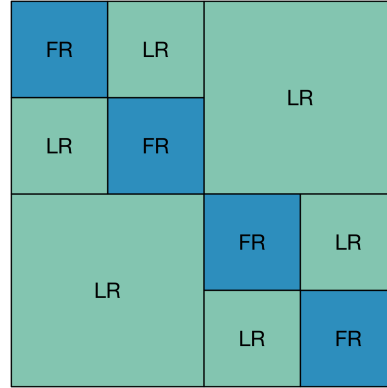


Figure 2.7: Simple example of a hierarchical matrix of a BIE operator - the near-field contribution are computed exactly (full-rank block), whereas the far-field contribution are stored as low-rank approximant of the original matrix. this in a hierarchical way based on a geometric cluster tree. Sketch from François Fayard (Inside Loop).

a more formal manner, the fast multipole method first derived by Rokhlin (1985) has been developed in different context (e.g. Yoshida, K. et al. (2001), Margonari, M. & Bonnet M. (2005) among many others). It is based on a tree structure of sources / collocations points distances and a multipole moment expansion of the integral equation. As such it requires specific development for each type of integral equations. In parallel, hierarchical matrices have gained popularity - their are also based on a cluster tree of sources / collocations points distances in order to if the far-field effect can be approximated or the near effect kept evaluated as usual. This is based on a solely geometric admissibility conditions. Then the far-field “blocks” cluster of the collocation matrix are approximated using a low rank approximation - cheaper to compute than a truncated SVD - a so-called adaptive cross approximation (see Hackbusch (2015), Bebendorf (2005)). This is a purely algebraic technique that can be applied to any type of BIE (provided that the kernel exhibit a smooth decay with distance). Hierarchical matrices allow a very significant condensation of the memory required. Moreover, fast product vector algebra as well as so-called H-LU decomposition have been developed which allow to either be used as direct solver or as pre-conditionner when using iterative solvers.

Typically the construction of the hierarchical matrix scales in $O(n \log n)$, similarly for its dot product and an iterative solver thus scales in $O(k \times n \log n)$.

Admissibility condition The decision to store the influence either has full or low-rank block is based on a geometrical admissibility condition with a dimensionless parameter η controlling the “aggressivity” of the approach. I.e. for two clusters of points A and B which satisfy

$$\max(\text{diam}(A), \text{diam}(B)) \leq \eta \text{dist}(A, B)$$

the 2 cross influence of the 2 clusters are deemed admissible and are thus approximated with a low-rank approximation. In the previous, we have

$$\begin{aligned} \text{diam}(A) &= \max_{i,j \in A} \|\mathbf{x}^i - \mathbf{x}^j\| \\ \text{dist}(A, B) &= \min_{i \in A, j \in B} \|\mathbf{x}^i - \mathbf{x}^j\| \end{aligned}$$

[i.e. larger η result in more aggressive approximation]. Practically, when doing the cluster tree - which is purely based on geometry - another parameter is the depth of the tree - the maximum number of leaf (`max_leaf_size`). The smaller is the `max_leaf_size` the finer is the cluster tree and as a result finer/better is the resulting the hierarchical matrix.

Our current implementation of the construction of the cluster tree is not very optimal from a memory point of view - such that for very large number of unknowns, `max_leaf_size` must be increased (to minimize the memory required to build the cluster tree).



Low rank approximation Another parameter of the algorithm is the tolerance ϵ of the low-rank approximation of the admissible matrix block performed via the Adaptive Cross Approximation algorithm (see Hackbusch (2015), Bebendorf (2005) for details). This \mathcal{H} – LU algorithm has in addition another tolerance ϵ_{LU} controlling the precision of the final LU approximation obtained.

2.4 Our implementation

In collaboration with Inside Loop (F. Fayard) and S. Chaillat-Loiseuille (from ENSTA), we have developed an efficiency multithreaded C++ library implementing all the necessary algorithms for the use of hierarchical matrices in the context of the boundary element method. The method is BIE agnostic and can thus be used in different context easily. We have also developed in C++ a collocation based BIE solver for quasi-static elasticity with either piece-wise linear and piece-wise constant displacement discontinuity element in 2D plane-strain configuration. We present in the subsequent section - a series of verification tests and discuss the efficiency of the hierarchical matrix acceleration techniques. We have also developed in C++, a collocation based BIE solver for quasi-static elasticity using triangular piece-wise quadratic displacement discontinuity elements. We also present in what follow some verification tests for this 3D solver.



2.5 Two-dimensional Benchmarks

In this section, we present validation of our 2D plane-strain displacement discontinuity solver for fracture problems. We also present a series of tests on the performance of the \mathcal{H} -matrix approach. All the simulations reported here have been performed on a personal laptop.

2.5.1 Circular arc crack

2.5.1.1 Geometry and reference solution

A crack in the form of a circular arc in an infinite plane is considered, under the assumption of plane strain. The crack is defined by $x = R \cos \phi$, $y = R \sin \phi$, where R is the radius of the arc, $\phi \in [-\theta, \theta]$ is the angle defining the location on the crack, and $[-\theta, \theta]$ is the arc's angular extent (Figs. 2.8 and 2.9). The infinite plane is subjected to a hydrostatic far-field tensile stress P . The plane strain Young's modulus of the medium is E' .

An analytical reference solution for the displacement jump (crack opening $w(\phi)$, ride $v(\phi)$) is given by Piva (1982):

$$w(\phi) = \frac{PR}{E'} \operatorname{Re} \left[4\sqrt{2} \frac{e^{-\frac{1}{2}i(2\theta+\phi)} (e^{i\phi} - e^{i\theta}) (e^{i(\theta+\phi)} - 1)}{(3 - \cos \theta) \sqrt{\cos \phi - \cos \theta}} \right] \quad (2.14)$$

$$v(\phi) = \frac{PR}{E'} \operatorname{Im} \left[4\sqrt{2} \frac{e^{-\frac{1}{2}i(2\theta+\phi)} (e^{i\phi} - e^{i\theta}) (e^{i(\theta+\phi)} - 1)}{(3 - \cos \theta) \sqrt{\cos \phi - \cos \theta}} \right] \quad (2.15)$$

The analytical expressions for the stress intensity factors (SIFs) are given in ?:

$$\begin{Bmatrix} K_I \\ K_{II} \end{Bmatrix} = \frac{P\sqrt{\pi R} \sin \theta}{1 + \sin^2 \left(\frac{\theta}{2} \right)} \times \begin{Bmatrix} \cos \left(\frac{\theta}{2} \right) \\ \sin \left(\frac{\theta}{2} \right) \end{Bmatrix} \quad (2.16)$$

2.5.1.2 Numerical solution without or with \mathcal{H} -matrix approximation

We consider two arc crack configurations, corresponding to $\theta = 85^\circ$, and $\theta = 175^\circ$. P1 displacement discontinuity (DD) elements have been used to discretize the circular arc crack. Figs. 2.8 and 2.9 show the discretized crack, as well as a comparison of the DD solutions, obtained using the full (dense) DD influence matrix, with the analytical solution (2.14) - (2.16). The mode I SIF has been obtained in the DDM solution from the crack width at the inner edge of the tip element, averaged from the two DD elements containing that edge.

The DDM solutions, obtained with the full (dense) influence matrix and with the H-mat low-rank approximation of the influence matrix, are compared in the following to investigate the efficiency and the accuracy of the H-mat approach. Tables 2.1 and 2.2 list the relative errors of the DD solutions with respect to the analytical solution (2.14) - (2.16) and the computational efficiency for the circular arc crack problem with $\theta = 85^\circ$. The H-mat parameters η and ε are varied to show its effects on the relative errors, the storage requirements and the computation time. Similarly, tables 2.3 and 2.4 list the relative errors and the computational efficiency for the circular arc crack problem with $\theta = 175^\circ$, for varying H-mat parameters η and ε . For these examples, the maximum leaf size 32 was used for the H-mat approximation. The results in tables 2.1 - 2.4 are listed for the case $N_{dof} = 4 \times 10^4$, corresponding to 10^4 P1 elements used to discretize the crack.

Figures 2.10 and 2.11 show the relative errors, the matrix assembly time and the total solver time for $\theta = 175^\circ$, vs. the number of the degrees of freedom (DOFs). An example of the matrix compression ratios is shown for $\eta = 0.3$ and $\eta = 0.0001$ in Fig. 2.12.

Several observations can be noted from these results:

- The example with $\theta = 175^\circ$ is more severe than that with $\theta = 85^\circ$, due to the fact that in the former case, the two crack tips are close to each other. The geometry with $\theta = 175^\circ$ is placing more stringent requirements for the H-mat parameters η and ε .

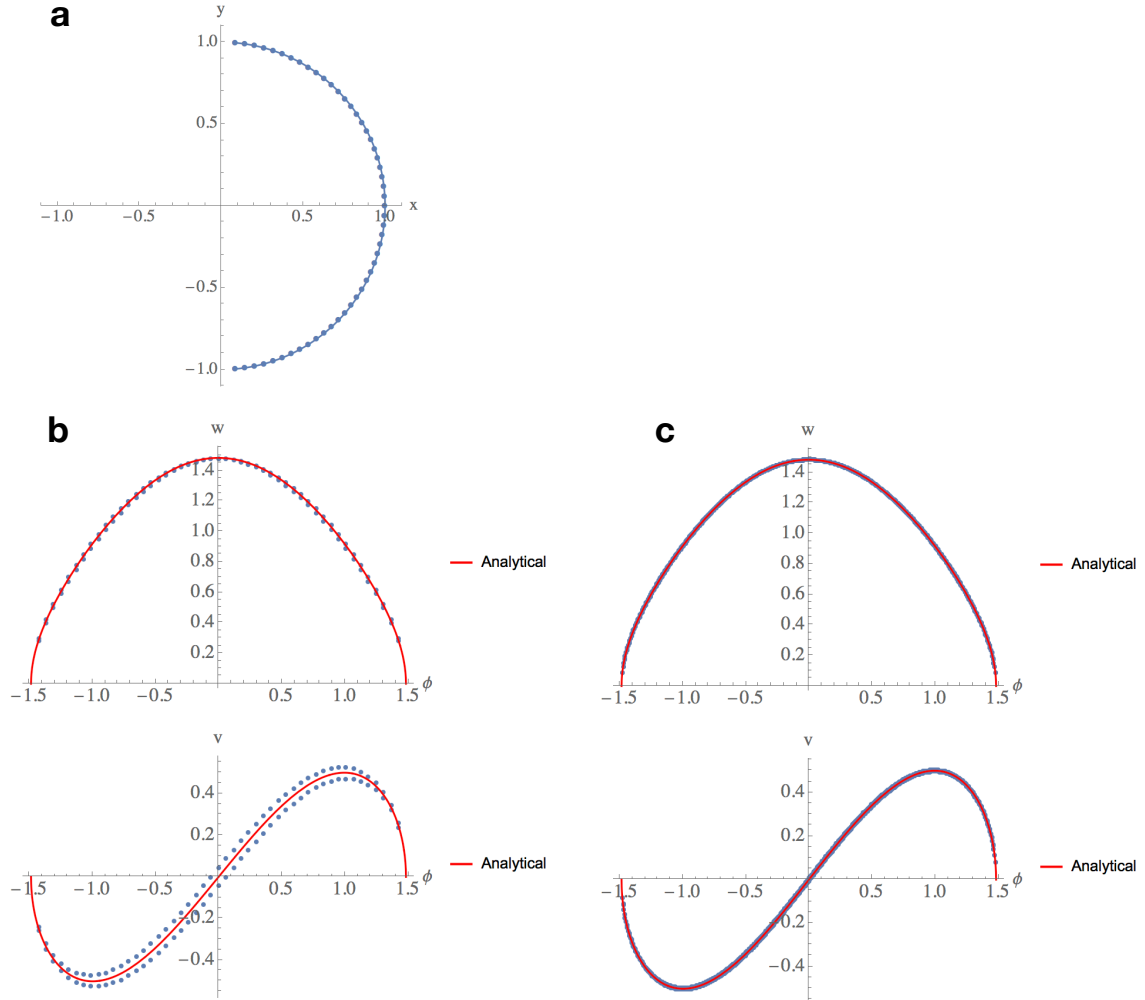


Figure 2.8: A numerical DD solution for the circular arc crack corresponding to $\theta = 85^\circ$: (a) the circular arc crack discretized with 50 DD P1 elements, (b) a comparison of the DD solution with 50 P1 elements to the analytical solution, and (c) a comparison of the DD solution with 500 P1 elements to the analytical solution.

type	η	ε	Mean rel error in w	Mean rel error in v	Rel error in K_I	H-mat compr. ratio	Matrix constr. time (s)	Total solver time (s)
Dense			8.5×10^{-5}	1.8×10^{-3}	1.3×10^{-2}		57.0	1275.3
H-mat	0.1	10^{-4}	8.5×10^{-5}	1.8×10^{-3}	1.3×10^{-2}	6.5×10^{-2}	22.1	143.5
H-mat	0.3	10^{-4}	8.5×10^{-5}	1.8×10^{-3}	1.3×10^{-2}	3.1×10^{-2}	11.5	42.7
H-mat	1.0	10^{-4}	8.5×10^{-5}	1.8×10^{-3}	1.3×10^{-2}	1.7×10^{-2}	7.8	18.1
H-mat	2.0	10^{-4}	8.5×10^{-5}	1.8×10^{-3}	1.3×10^{-2}	1.5×10^{-2}	6.7	13.6
H-mat	5.0	10^{-4}	8.5×10^{-5}	1.8×10^{-3}	1.3×10^{-2}	1.5×10^{-2}	6.4	14.6

Table 2.1: Effect of the H-mat parameter η on relative errors and computational efficiency for the DDM solution of a circular arc crack problem, $\theta = 85^\circ$. Maximum leaf size 32 was used for the H-mat. The results are listed for the case $N_{dof} = 4 \times 10^4$. P1 elements were used.



type	η	ε	Mean rel error in w	Mean rel error in v	Rel error in K_I	H-mat compr. ratio	Matrix constr. time (s)	Total solver time (s)
H-mat	0.3	10^{-4}	8.5×10^{-5}	1.8×10^{-3}	1.3×10^{-2}	3.1×10^{-2}	11.5	42.7
H-mat	0.3	10^{-3}	8.5×10^{-5}	1.8×10^{-3}	1.3×10^{-2}	2.9×10^{-2}	10.9	40.0
H-mat	0.3	10^{-2}	1.2×10^{-4}	1.9×10^{-3}	1.3×10^{-2}	2.7×10^{-2}	9.9	39.1
H-mat	0.3	10^{-1}	8.1×10^{-4}	3.9×10^{-3}	1.2×10^{-2}	2.3×10^{-2}	7.8	35.0
H-mat	1.0	10^{-4}	8.5×10^{-5}	1.8×10^{-3}	1.3×10^{-2}	1.7×10^{-2}	7.8	18.1
H-mat	1.0	10^{-3}	8.3×10^{-5}	1.8×10^{-3}	1.3×10^{-2}	1.5×10^{-2}	6.5	15.2
H-mat	1.0	10^{-2}	3.5×10^{-4}	1.9×10^{-3}	1.3×10^{-2}	1.3×10^{-2}	5.7	14.0
H-mat	1.0	10^{-1}	1.2×10^{-2}	4.8×10^{-2}	8.7×10^{-3}	1.1×10^{-2}	4.6	12.0

Table 2.2: Effect of the H-mat parameter ε on relative errors and computational efficiency for the DDM solution of a circular arc crack problem, $\theta = 85^\circ$. Maximum leaf size 32 was used for the H-mat. The results are listed for the case $N_{dof} = 4 \times 10^4$. P1 elements were used.

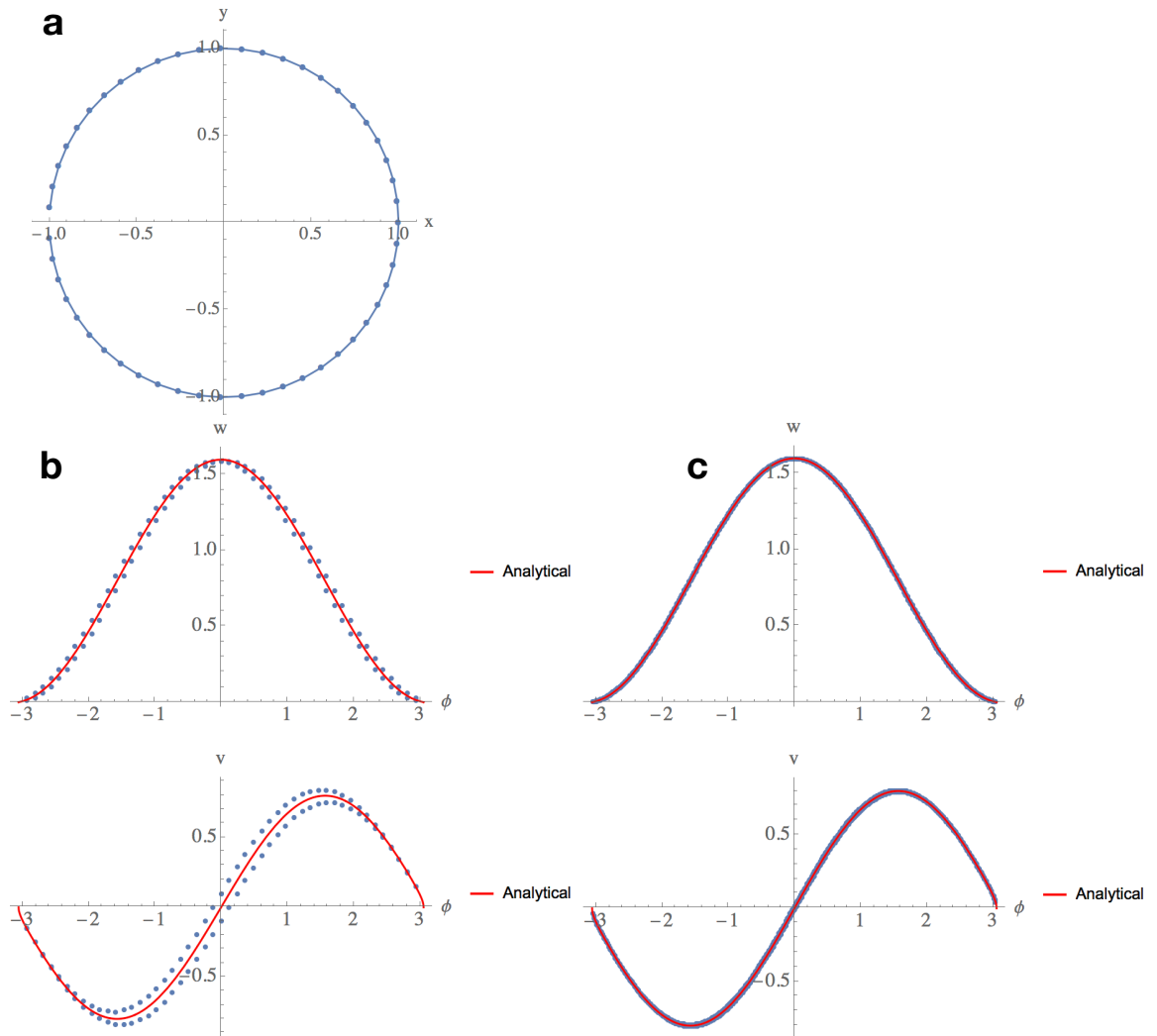


Figure 2.9: A numerical DD solution for the circular arc crack corresponding to $\theta = 175^\circ$: (a) the circular arc crack discretized with 50 DD P1 elements, (b) a comparison of the DD solution with 50 P1 elements to the analytical solution, and (c) a comparison of the DD solution with 500 P1 elements to the analytical solution.



type	η	ε	Mean rel error in w	Mean rel error in v	Rel error in K_I	H-mat compr. ratio	Matrix constr. time (s)	Total solver time (s)
Dense			6.3×10^{-4}	1.8×10^{-3}	2.1×10^{-2}		56.8	1646.2
H-mat	0.1	10^{-4}	6.3×10^{-4}	1.8×10^{-3}	2.7×10^{-2}	7.3×10^{-2}	25.1	203.6
H-mat	0.3	10^{-4}	1.2×10^{-3}	3.4×10^{-3}	3.7×10^{-2}	3.4×10^{-2}	13.2	56.1
H-mat	1.0	10^{-4}	1.0×10^{-3}	2.9×10^{-3}	3.4×10^{-2}	1.8×10^{-2}	8.4	21.6
H-mat	2.0	10^{-4}	6.3×10^{-4}	1.8×10^{-3}	2.9×10^{-2}	1.6×10^{-2}	6.9	15.0
H-mat	5.0	10^{-4}	6.3×10^{-4}	1.8×10^{-3}	2.4×10^{-2}	1.6×10^{-2}	7.0	14.7

Table 2.3: Effect of the H-mat parameter η on relative errors and computational efficiency for the DDM solution of a circular arc crack problem, $\theta = 175^\circ$. Maximum leaf size 32 was used for the H-mat. The results are listed for the case $N_{dof} = 4 \times 10^4$. P1 elements were used.

type	η	ε	Mean rel error in w	Mean rel error in v	Rel error in K_I	H-mat compr. ratio	Matrix constr. time (s)	Total solver time (s)
H-mat	0.1	10^{-4}	6.3×10^{-4}	1.8×10^{-3}	2.7×10^{-2}	7.3×10^{-2}	25.1	203.6
H-mat	0.1	10^{-3}	6.3×10^{-4}	1.8×10^{-3}	1.6×10^{-2}	7.1×10^{-2}	23.7	191.6
H-mat	0.1	10^{-2}	5.7×10^{-3}	1.6×10^{-2}	4.6×10^{-2}	6.0×10^{-2}	18.8	182.3
H-mat	0.1	10^{-1}	5.8×10^{-3}	1.6×10^{-2}	4.6×10^{-2}	5.9×10^{-2}	18.5	181.2
H-mat	0.3	10^{-4}	1.2×10^{-3}	3.4×10^{-3}	3.7×10^{-2}	3.4×10^{-2}	13.2	56.1
H-mat	0.3	10^{-3}	2.3×10^{-3}	6.3×10^{-3}	5.0×10^{-2}	3.2×10^{-2}	11.8	54.0
H-mat	0.3	10^{-2}	3.9×10^{-2}	1.1×10^{-1}	4.5×10^{-1}	2.9×10^{-2}	10.7	54.2
H-mat	0.3	10^{-1}	4.2×10^{-1}	1.2	5.0	2.5×10^{-2}	9.4	49.9
H-mat	2.0	10^{-4}	6.3×10^{-4}	1.8×10^{-3}	2.9×10^{-2}	1.6×10^{-2}	6.9	15.0
H-mat	2.0	10^{-3}	4.0×10^{-3}	1.1×10^{-2}	5.8×10^{-2}	1.4×10^{-2}	6.7	14.4
H-mat	2.0	10^{-2}	5.8×10^{-2}	1.6×10^{-1}	6.6×10^{-1}	1.2×10^{-2}	5.0	12.5
H-mat	2.0	10^{-1}	2.2×10^{-1}	5.1×10^{-1}	1.5	1.0×10^{-2}	4.2	11.1

Table 2.4: Effect of the H-mat parameter ε on relative errors and computational efficiency for the DDM solution of a circular arc crack problem, $\theta = 175^\circ$. Maximum leaf size 32 was used for the H-mat. The results are listed for the case $N_{dof} = 4 \times 10^4$. P1 elements were used.

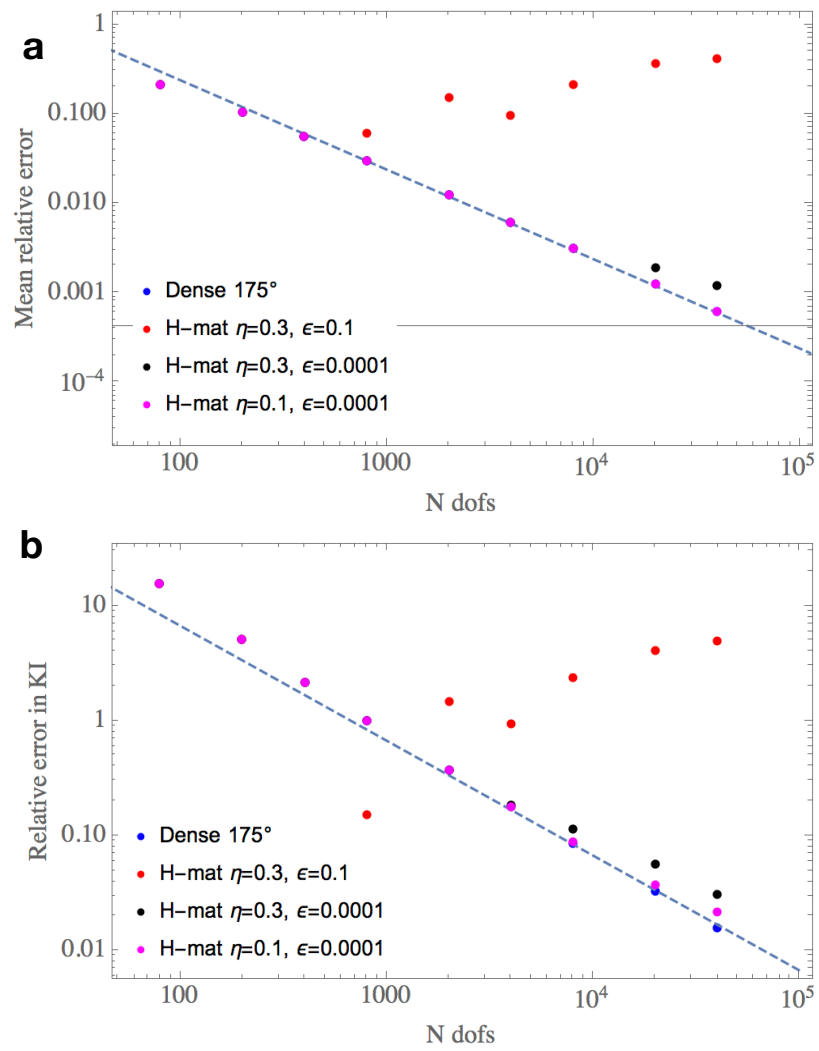


Figure 2.10: Circular arc crack example ($\theta = 175^\circ$, P1 elements): (a) mean relative error, and (b) relative error in the mode I SIF, vs number of DOFs. H-mat parameters (η , ϵ) are listed for each data series.

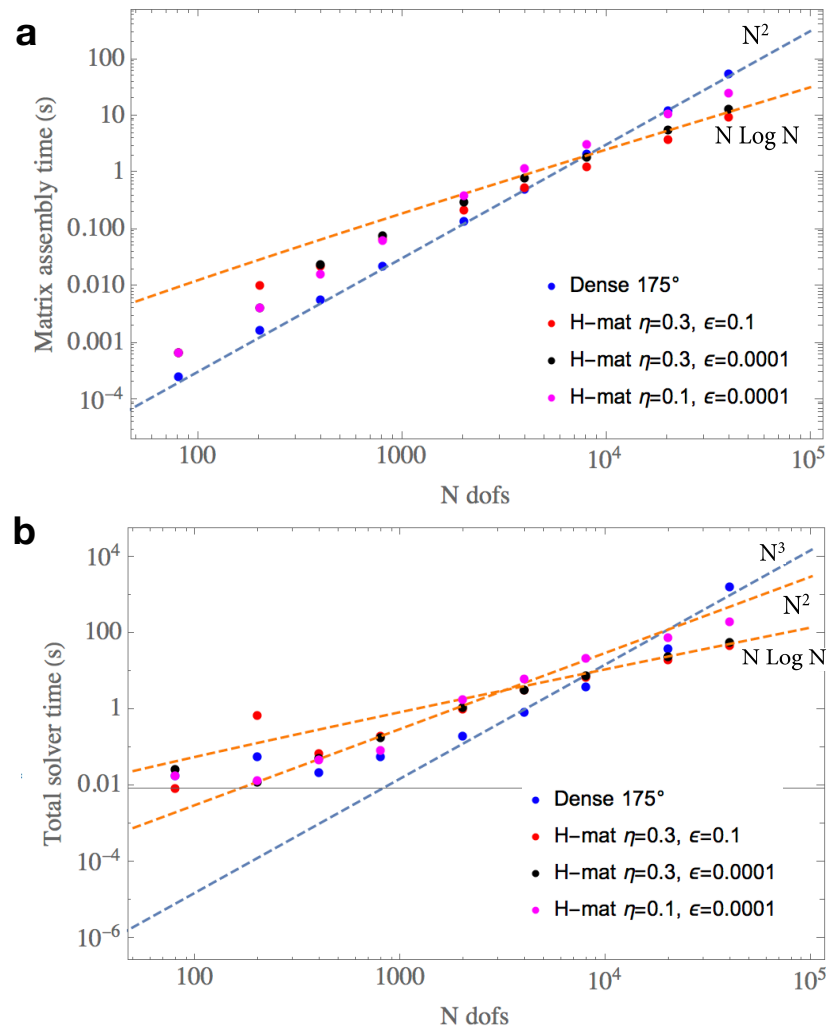


Figure 2.11: Circular arc crack example ($\theta = 175^\circ$, P1 elements): (a) matrix assembly cost in sec., and (b) total solver cost in sec., vs number of DOFs. H-mat parameters (η , ϵ) are listed for each data series.

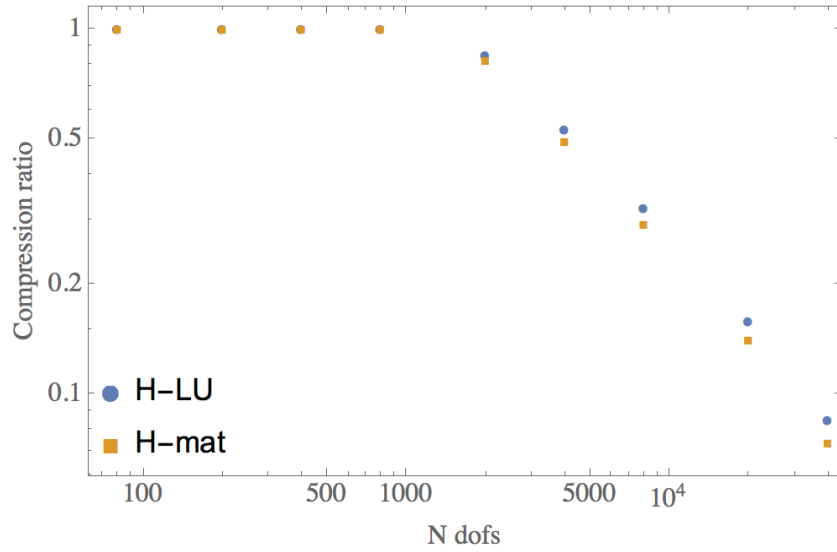


Figure 2.12: Circular arc crack example ($\theta = 175^\circ$, P1 elements): H-matrix compression ratios vs number of DOFs, for $\eta = 0.3$ and $\epsilon = 0.0001$.

- One can find suitable values of η and ϵ to significantly reduce the storage (required for the influence matrix) and the solver time, while keeping the solution accuracy at a level similar to that of the solution with the dense influence matrix.
- The effect of decrease of parameter ϵ (for a fixed η) is consistent for both $\theta = 85^\circ$, 175° : it leads to the increased accuracy of the solution, and to the increased solver time and the storage requirement (via the increase in the H-matrix compression ratio).
- Choosing a too large value of ϵ can lead to divergent solutions, see Fig. 2.10. The solution for the large numbers of DOFs diverges from the analytical solution for $\eta = 0.3$ and $\eta = 0.1$, and the errors increase. On the other hand, for $\eta = 0.3$ and $\eta = 0.0001$, the numerical errors continue to decrease.
- The effect of increase of parameter η (for a fixed ϵ) on the solution accuracy is less straightforward. E.g. for $\theta = 175^\circ$, table 2.3 shows a nonmonotone behavior of the relative errors for increasing η and $\epsilon = 10^{-4}$. The efficiency of the solution (solver time and storage requirement, corresponding to the H-matrix compression ratio) is consistently improved with increasing η for all cases.

2.5.2 Star crack

2.5.2.1 Geometry and reference solution

A crack in the form of a star in an infinite plane is considered, under the assumption of plane strain. The crack is composed of n ($n \geq 2$) straight crack segments of length a (crack wings) with one end at the origin and the other end oriented radially from the origin, with an equal angle between the neighbour crack segments. The crack is pressurized with a uniform pressure P . The plane strain Young's modulus of the medium is E' .

An analytical reference solution for the mode I SIF K_I , the crack opening w_o at the mouth of each crack wing, and the work W done in opening the crack is given by Stallybrass (1970), ? in the following form:

$$\frac{K_I^{ref}}{P\sqrt{a}} = \sqrt{2\pi}\mathcal{K}(n) \quad (2.17)$$



$$\frac{w_o^{ref}}{(P a/E')} = \frac{4\sqrt{n} \sin\left(\frac{\pi}{n}\right)}{\sqrt{1 + \frac{n}{2\pi} \sin\left(\frac{2\pi}{n}\right)}} \mathcal{K}(n) \quad (2.18)$$

$$\frac{W^{ref}}{(P^2 a^2/E')} = n\pi (\mathcal{K}(n))^2 \quad (2.19)$$

where

$$\mathcal{K}(n) = 2^{1-\frac{2}{n}} \frac{1}{\sqrt{n}} \exp\left(-\frac{1}{\pi} I(n)\right) \quad (2.20)$$

$$I(n) = \int_0^{\pi/2} \log \left[1 + \tan(y) \sin\left(\frac{2\pi}{n}\right) \operatorname{csch}\left(\frac{2\pi}{n}\right) \tan(y) \right] dy \quad (2.21)$$

For this report, the integral in Eq. (2.21) is computed numerically using software Mathematica.

2.5.2.2 Numerical solution for stress intensity factor (dense matrix)

First, we investigate the accuracy of the stress intensity factor computation in comparison to the analytical solution (2.17). Three formulas have been used to compute the mode I SIF from the DDM solution, obtained with the P1 displacement discontinuity elements:

$$K_I^{(1)} = E' \sqrt{\frac{\pi}{32}} \frac{w_{aver}(a - \Delta s)}{\sqrt{\Delta s}} \quad (2.22)$$

$$K_I^{(2)} = E' \sqrt{\frac{\pi}{32}} \frac{w_{aver}(a - 2\Delta s)}{\sqrt{2\Delta s}} \quad (2.23)$$

$$K_I^{(3)} = \sqrt{\frac{2WE'}{a n}} \quad (2.24)$$

$$W = \frac{P}{2} \int_{crack} w(s) ds \quad (2.25)$$

where Δs is the length of a single DD element. Above, $K_I^{(i)}$ for $i = 1, 2$ is the SIF computed using the local near-tip crack width at the distance $i \times \Delta s$ from the crack tip. In Eqs. (2.22) and (2.23), the crack width $w_{aver}(a - i\Delta s)$ for $i = 1, 2$ is the average of the two values of the crack width at the node $s = (a - i\Delta s)$, resulting from the P1 DD approximation.

The formula (2.24) computes the SIF from the integral of the crack width over the complete crack (with n wings). This formula is obtained via the following relationships between the strain energy release rate G and the work W done to open the crack (the strain energy of the system) (Stallybrass 1970, 1969, Rooke & Sneddon 1969, ?): $K_I^2 = E'G = E' \frac{1}{n} \frac{dW}{da}$.

Table 2.5 shows a comparison of the mode I SIF computed from Eqs. (2.22) - (2.24), for the star-crack problem with $n = 3$. P1 DD elements were used to discretize the star crack. The full (dense) DDM influence matrix was used. It is seen that the SIF computed from the local near-tip crack width ($K_I^{(i)}$ for $i = 1, 2$) is less accurate than the SIF computed from the integral of the crack width over the complete crack. Eq. (2.23) provides a more accurate approximation than Eq. (2.22). Note that the accuracy in $K_I^{(1)}$ and $K_I^{(2)}$ relates to the accuracy of the DDM solution in the crack tip, while the accuracy in $K_I^{(3)}$ relates to the overall accuracy of the DDM solution over the crack since it involves integration of the crack width over the complete crack (Eqs. (2.24) and (2.25)).



# DD elts (total)	$\frac{K_I^{(1)}}{P\sqrt{a}}$	$\frac{K_I^{(2)}}{P\sqrt{a}}$	$\frac{K_I^{(3)}}{P\sqrt{a}}$	Rel error in $K_I^{(1)}$	Rel error in $K_I^{(2)}$	Rel error in $K_I^{(3)}$
300	1.68407	1.65562	1.66785	9.2×10^{-3}	7.9×10^{-3}	5.5×10^{-4}
3000	1.68905	1.66541	1.66863	1.2×10^{-2}	2.0×10^{-3}	8.2×10^{-5}
9000	1.68943	1.66615	1.66871	1.2×10^{-2}	1.6×10^{-3}	3.2×10^{-5}
12000	1.68948	1.66624	1.66872	1.2×10^{-2}	1.5×10^{-3}	2.5×10^{-5}

Table 2.5: Comparison of the mode I SIF computed from the DDM solution of a star crack problem, $n = 3$, from Eqs. (2.22) - (2.24). The full (dense) DDM influence matrix was used. The first column shows the total number of P1 DD elements used to discretize the star crack. The relative errors are computed with respect to the reference value given by Eq. (2.17), which for this problem is $\frac{K_I^{ref}}{P\sqrt{a}} = 1.66876....$

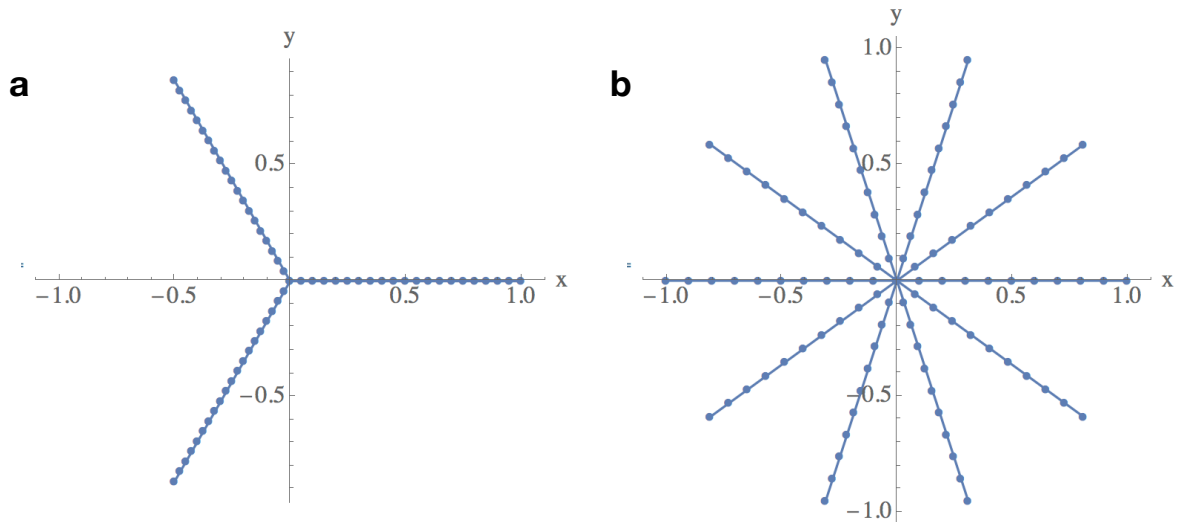


Figure 2.13: A DD discretization of the star crack: (a) the star crack with $n = 3$ wings discretized with the total of 60 DD P1 elements, (b) the star crack with $n = 10$ wings discretized with the total of 100 DD P1 elements. Circles denote the locations of the end-nodes of the DD elements.



type	η	ε	Rel error in w_o	Rel error in $K_I^{(2)}$	Rel error in $K_I^{(3)}$	H-mat compr. ratio	Matrix constr. time (s)	Total solver time (s)
Dense			3.6×10^{-5}	1.6×10^{-3}	3.2×10^{-5}		42.0	729.2
H-mat	0.1	10^{-4}	3.6×10^{-5}	1.6×10^{-3}	3.2×10^{-5}	8.1×10^{-2}	22.8	212.9
H-mat	0.3	10^{-4}	3.6×10^{-5}	1.6×10^{-3}	3.2×10^{-5}	3.9×10^{-2}	12.1	58.0
H-mat	1.0	10^{-4}	3.6×10^{-5}	1.6×10^{-3}	3.2×10^{-5}	1.9×10^{-2}	6.6	20.1
H-mat	2.0	10^{-4}	3.7×10^{-5}	1.6×10^{-3}	3.2×10^{-5}	1.7×10^{-2}	6.0	14.4
H-mat	5.0	10^{-4}	3.7×10^{-5}	1.6×10^{-3}	3.2×10^{-5}	1.7×10^{-2}	5.6	12.7
H-mat	0.1	10^{-1}	3.2×10^{-4}	1.8×10^{-3}	1.9×10^{-4}	6.3×10^{-2}	15.9	183.8
H-mat	0.3	10^{-1}	3.4×10^{-4}	3.5×10^{-4}	2.0×10^{-4}	2.8×10^{-2}	8.2	49.2
H-mat	1.0	10^{-1}	1.2×10^{-2}	7.2×10^{-3}	4.3×10^{-3}	1.3×10^{-2}	4.4	15.6
H-mat	2.0	10^{-1}	1.4×10^{-2}	7.2×10^{-3}	3.8×10^{-3}	1.2×10^{-2}	4.0	12.1
H-mat	5.0	10^{-1}	4.6×10^{-3}	6.1×10^{-3}	3.5×10^{-3}	1.1×10^{-2}	3.7	10.7

Table 2.6: Effect of the H-mat parameter η on relative errors and computational efficiency for the DDM solution of a star crack problem, $n = 3$. Maximum leaf size 32 was used for the H-mat. The results are listed for the case $N_{dof} = 3.6 \times 10^4$. P1 elements were used (9000 DD elements total).

type	η	ε	Rel error in w_o	Rel error in $K_I^{(2)}$	Rel error in $K_I^{(3)}$	H-mat compr. ratio	Matrix constr. time (s)	Total solver time (s)
H-mat	0.3	10^{-4}	3.6×10^{-5}	1.6×10^{-3}	3.2×10^{-5}	3.9×10^{-2}	12.1	58.0
H-mat	0.3	10^{-3}	3.8×10^{-5}	1.6×10^{-3}	3.3×10^{-5}	3.6×10^{-2}	10.6	50.5
H-mat	0.3	10^{-2}	2.1×10^{-5}	1.5×10^{-3}	3.8×10^{-6}	3.4×10^{-2}	10.1	53.1
H-mat	0.3	10^{-1}	3.4×10^{-4}	3.5×10^{-4}	2.0×10^{-4}	2.8×10^{-2}	8.2	49.2
H-mat	2.0	10^{-4}	3.7×10^{-5}	1.6×10^{-3}	3.2×10^{-5}	1.7×10^{-2}	6.0	14.4
H-mat	2.0	10^{-3}	2.1×10^{-5}	1.6×10^{-3}	2.3×10^{-5}	1.6×10^{-2}	5.2	13.5
H-mat	2.0	10^{-2}	1.3×10^{-4}	1.5×10^{-3}	2.5×10^{-5}	1.3×10^{-2}	4.4	12.4
H-mat	2.0	10^{-1}	1.4×10^{-2}	7.2×10^{-3}	3.8×10^{-3}	1.2×10^{-2}	4.0	12.1

Table 2.7: Effect of the H-mat parameter ε on relative errors and computational efficiency for the DDM solution of a star crack problem, $n = 3$. Maximum leaf size 32 was used for the H-mat. The results are listed for the case $N_{dof} = 3.6 \times 10^4$. P1 elements were used (9000 DD elements total).

2.5.2.3 Numerical solution without or with \mathcal{H} -matrix approximation

We consider three star crack configurations, corresponding to $n = 3, 4, 10$. P1 displacement discontinuity (DD) elements have been used to discretize the crack. Fig. 2.13 shows examples of discretized cracks. For the H-mat low-rank approximation of the DD influence matrix, the maximum leaf size was set to 32 for $n = 3$ and to 320 for $n = 4, 10$.

The DDM solutions, obtained with the full (dense) influence matrix and with the H-mat low-rank approximation of the influence matrix, are compared in the following to investigate the efficiency and the accuracy of the H-mat approach. See Tables 2.6 - 2.11 and Figs. 2.14 - 2.25 for a detailed study of the effects of the H-mat parameters (η, ε) on the accuracy of the solution for $w_o, K_I^{(2)}$ and $K_I^{(3)}$, on the computational time spent to assemble the influence matrix or its H-mat approximation, on the computational time spent to solve the linear system, and on the compression ratio achieved by using the low-rank H-mat approximation.

Several observations can be made from these results:

- For all the star cracks tested ($n = 3, 4, 10$), the values $\eta = 2, 5$ and $\varepsilon = 10^{-4}$ provide: convergence to the analytical solution for the crack width and the stress intensity factor $K_I^{(3)}$ (Figs. 2.14, 2.15, 2.20, 2.23; Tables 2.6 - 2.11), and a significant reduction in the storage required to store the influence matrix (Figs. 2.19, 2.22, 2.25; Tables 2.6 - 2.11).
- For $n = 3$, the use of the H-mat with $\eta = 2, 5$ and $\varepsilon = 10^{-4}$ also leads to a significant reduction



type	η	ε	Rel error in w_o	Rel error in $K_I^{(2)}$	Rel error in $K_I^{(3)}$	H-mat compr. ratio	Matrix constr. time (s)	Total solver time (s)
Dense			3.4×10^{-5}	1.6×10^{-3}	3.1×10^{-5}		74.1	75486.8
H-mat	1.0	10^{-4}	3.3×10^{-5}	1.6×10^{-3}	3.1×10^{-5}	1.1×10^{-1}	29.6	3483.19
H-mat	2.0	10^{-4}	3.2×10^{-5}	1.6×10^{-3}	3.1×10^{-5}	6.9×10^{-2}	20.9	1528.9
H-mat	5.0	10^{-4}	3.4×10^{-5}	1.6×10^{-3}	3.1×10^{-5}	5.4×10^{-2}	17.3	766.1
H-mat	10.0	10^{-4}	3.4×10^{-5}	1.6×10^{-3}	3.1×10^{-5}	5.4×10^{-2}	16.6	800.4

Table 2.8: Effect of the H-mat parameter η on relative errors and computational efficiency for the DDM solution of a star crack problem, $n = 4$. Maximum leaf size 320 was used for the H-mat. The results are listed for the case $N_{dof} = 4.8 \times 10^4$. P1 elements were used (12000 DD elements total).

type	η	ε	Rel error in w_o	Rel error in $K_I^{(2)}$	Rel error in $K_I^{(3)}$	H-mat compr. ratio	Matrix constr. time (s)	Total solver time (s)
H-mat	5.0	10^{-4}	3.4×10^{-5}	1.6×10^{-3}	3.1×10^{-5}	5.4×10^{-2}	17.3	766.1
H-mat	5.0	10^{-3}	9.3×10^{-5}	1.6×10^{-3}	3.3×10^{-5}	5.3×10^{-2}	15.7	801.4
H-mat	5.0	10^{-2}	2.2×10^{-4}	1.8×10^{-3}	1.0×10^{-4}	5.1×10^{-2}	14.8	817.6
H-mat	5.0	10^{-1}	3.7×10^{-3}	6.9×10^{-4}	9.5×10^{-5}	5.0×10^{-2}	14.0	810.3

Table 2.9: Effect of the H-mat parameter ε on relative errors and computational efficiency for the DDM solution of a star crack problem, $n = 4$. Maximum leaf size 320 was used for the H-mat. The results are listed for the case $N_{dof} = 4.8 \times 10^4$. P1 elements were used (12000 DD elements total).

type	η	ε	Rel error in w_o	Rel error in $K_I^{(2)}$	Rel error in $K_I^{(3)}$	H-mat compr. ratio	Matrix constr. time (s)	Total solver time (s)
Dense			7.0×10^{-5}	3.9×10^{-3}	6.7×10^{-5}		53.1	948.6
H-mat	0.1	10^{-4}	7.0×10^{-5}	3.9×10^{-3}	6.7×10^{-5}	9.5×10^{-1}	142.0	1065.8
H-mat	0.3	10^{-4}	7.0×10^{-5}	3.9×10^{-3}	6.7×10^{-5}	7.5×10^{-1}	112.5	3827.0
H-mat	2.0	10^{-4}	8.9×10^{-5}	3.9×10^{-3}	6.7×10^{-5}	1.3×10^{-1}	25.3	2028.7
H-mat	5.0	10^{-4}	5.6×10^{-5}	3.9×10^{-3}	6.7×10^{-5}	8.4×10^{-2}	17.8	599.3
H-mat	0.3	10^{-1}	2.0×10^{-3}	3.4×10^{-3}	4.0×10^{-5}	7.5×10^{-1}	111.1	3965.9
H-mat	2.0	10^{-1}	1.6×10^{-1}	1.3×10^{-3}	1.0×10^{-3}	1.2×10^{-1}	21.3	2029.8
H-mat	5.0	10^{-1}	2.0	5.5×10^{-2}	2.5×10^{-3}	7.6×10^{-2}	13.8	637.5

Table 2.10: Effect of the H-mat parameter η on relative errors and computational efficiency for the DDM solution of a star crack problem, $n = 10$. Maximum leaf size 320 was used for the H-mat. The results are listed for the case $N_{dof} = 4 \times 10^4$. P1 elements were used (10000 DD elements total).

type	η	ε	Rel error in w_o	Rel error in $K_I^{(2)}$	Rel error in $K_I^{(3)}$	H-mat compr. ratio	Matrix constr. time (s)	Total solver time (s)
H-mat	2.0	10^{-4}	8.9×10^{-5}	3.9×10^{-3}	6.7×10^{-5}	1.3×10^{-1}	25.3	2028.7
H-mat	2.0	10^{-3}	2.7×10^{-3}	3.8×10^{-3}	6.6×10^{-5}	1.3×10^{-1}	23.0	2006.0
H-mat	2.0	10^{-2}	1.2×10^{-2}	3.7×10^{-3}	1.0×10^{-4}	1.3×10^{-1}	21.9	2031.9
H-mat	2.0	10^{-1}	1.6×10^{-1}	1.3×10^{-3}	1.0×10^{-3}	1.2×10^{-1}	21.3	2029.8
H-mat	5.0	10^{-4}	5.6×10^{-5}	3.9×10^{-3}	6.7×10^{-5}	8.4×10^{-2}	17.8	599.3
H-mat	5.0	10^{-3}	7.4×10^{-3}	3.7×10^{-3}	7.1×10^{-5}	8.1×10^{-2}	17.0	622.9
H-mat	5.0	10^{-2}	1.5×10^{-1}	1.1×10^{-2}	1.3×10^{-4}	7.9×10^{-2}	15.3	629.6
H-mat	5.0	10^{-1}	2.0	5.5×10^{-2}	2.5×10^{-3}	7.6×10^{-2}	13.8	637.5

Table 2.11: Effect of the H-mat parameter ε on relative errors and computational efficiency for the DDM solution of a star crack problem, $n = 10$. Maximum leaf size 320 was used for the H-mat. The results are listed for the case $N_{dof} = 4 \times 10^4$. P1 elements were used (10000 DD elements total).

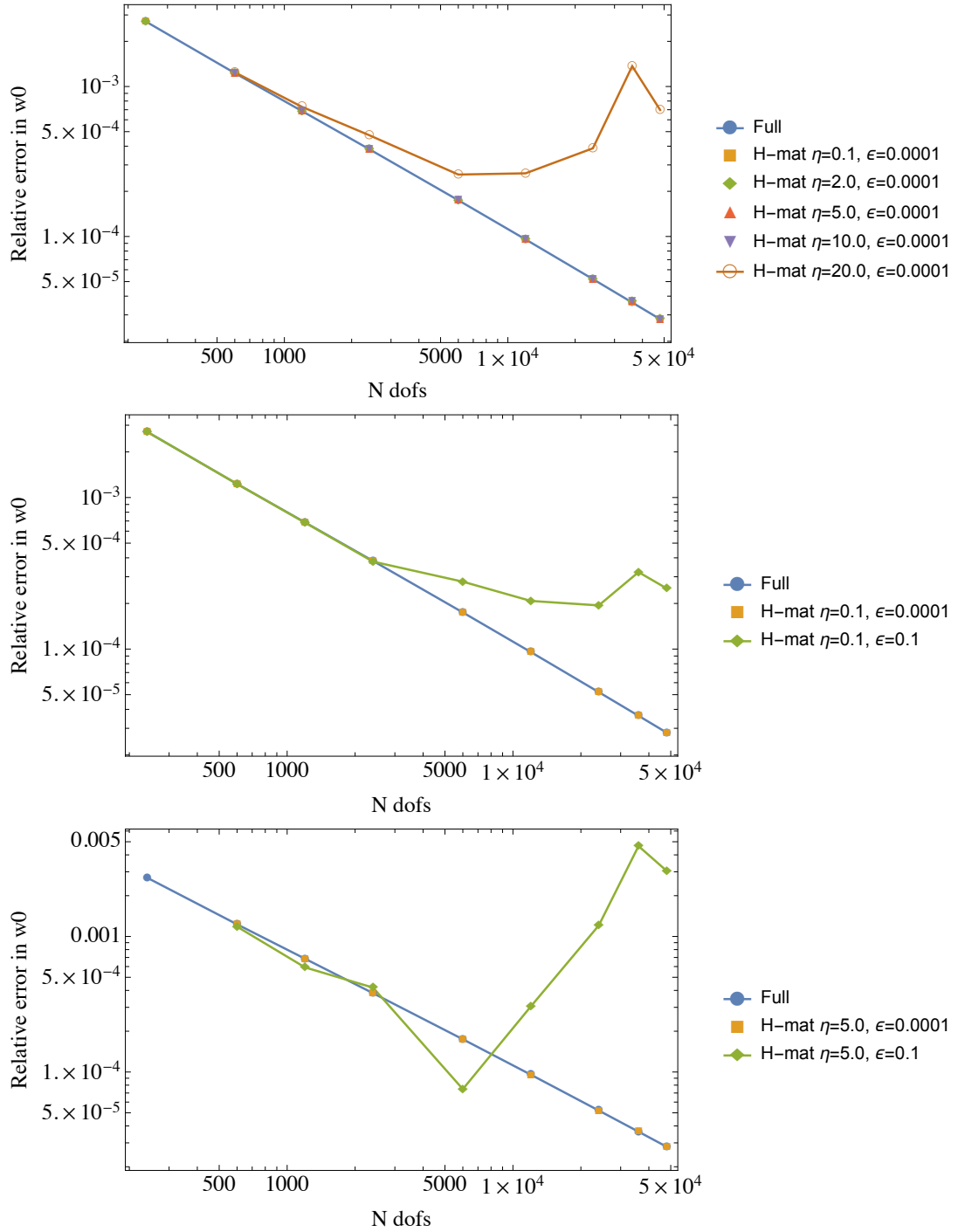


Figure 2.14: Star crack example ($n = 3$, P1 elements): relative error in crack opening at the center, vs number of DOFs: effect of parameter η (top) and parameter ϵ (middle, bottom). H-mat parameters (η , ϵ) are listed for each data series.

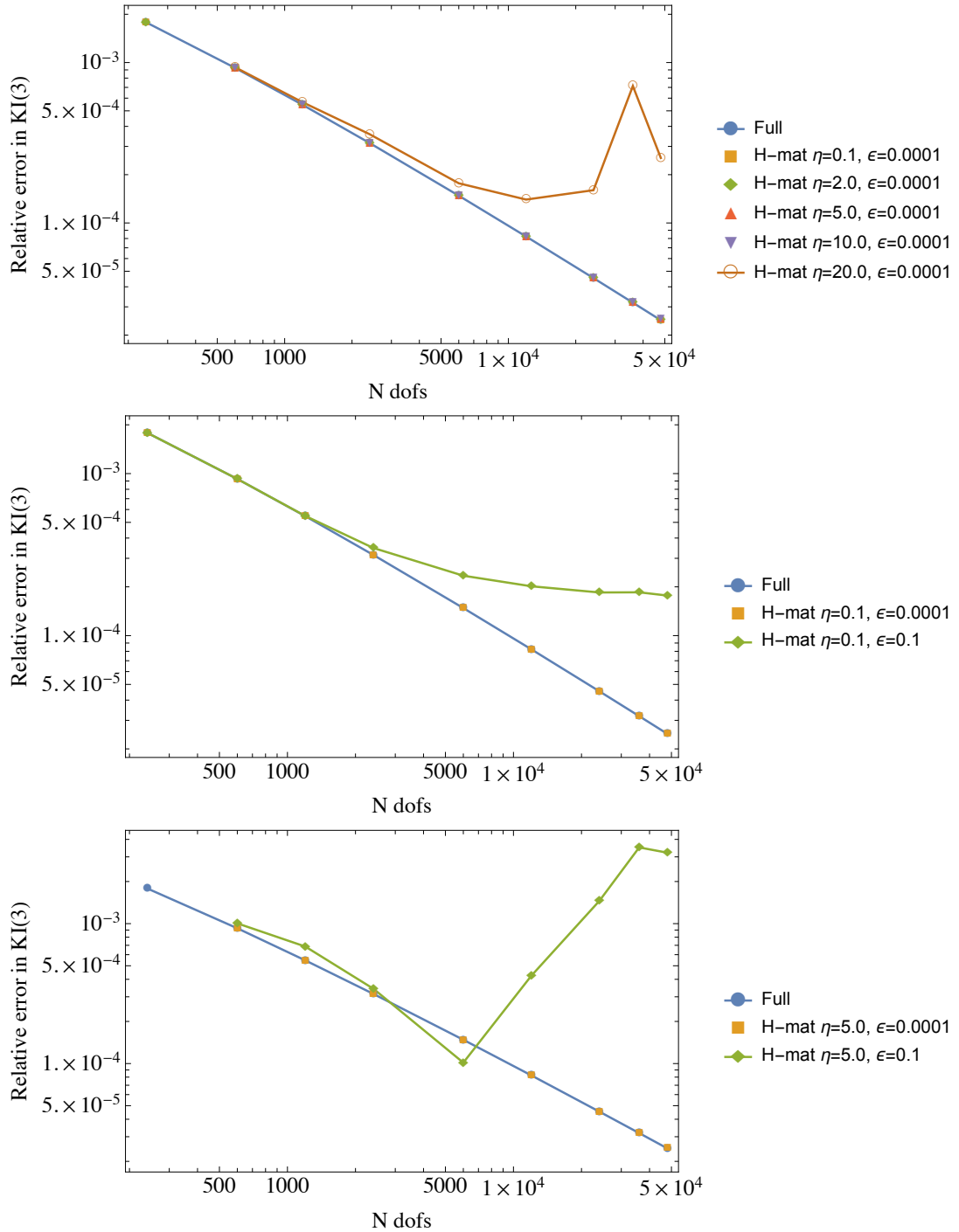


Figure 2.15: Star crack example ($n = 3$, P1 elements): relative error in the SIF $K_I^{(3)}$ computed using Eqs. (2.24) and (2.25), vs number of DOFs: effect of parameter η (top) and parameter ϵ (middle, bottom). H-mat parameters (η, ϵ) are listed for each data series.

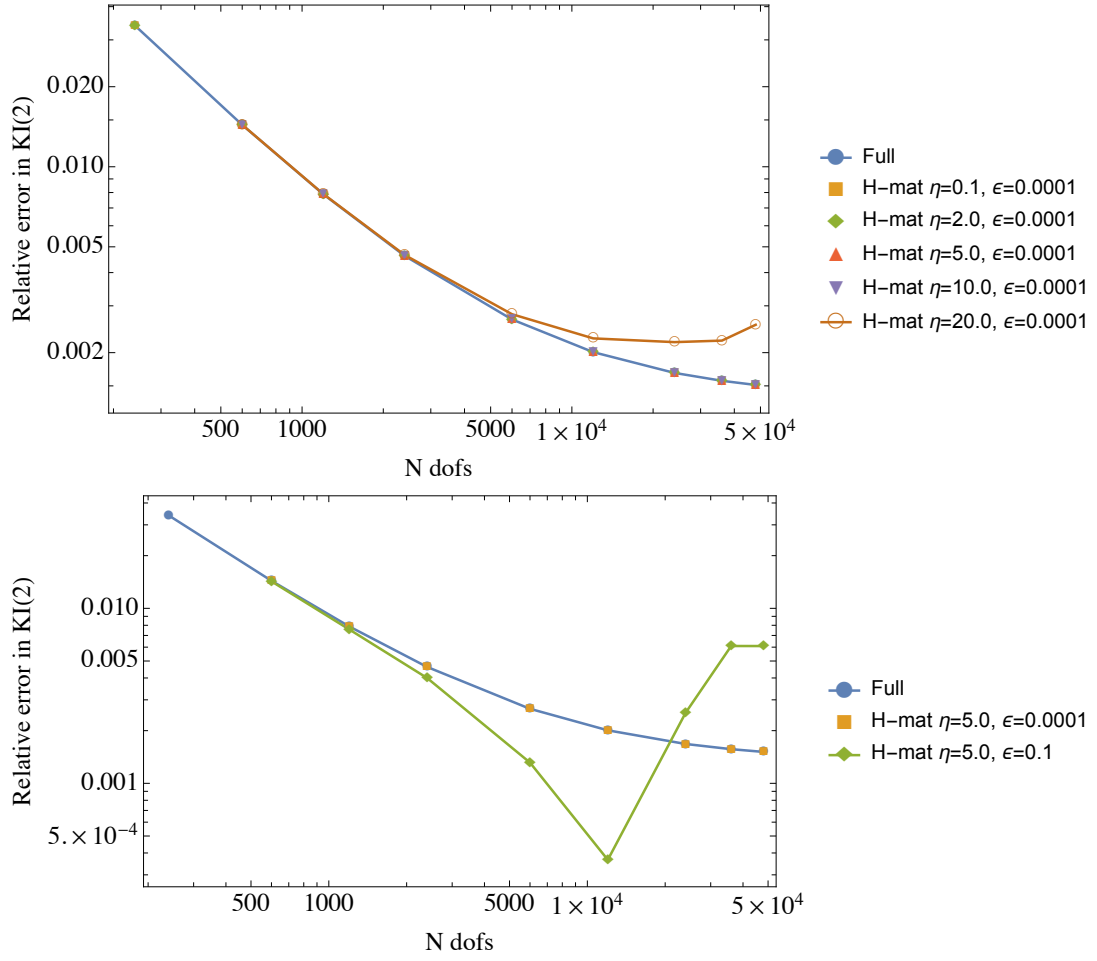


Figure 2.16: Star crack example ($n = 3$, P1 elements): relative error in the SIF $K_I^{(2)}$ computed using Eq. (2.23), vs number of DOFs: effect of parameter η (top) and parameter ϵ (bottom). H-mat parameters (η, ϵ) are listed for each data series.

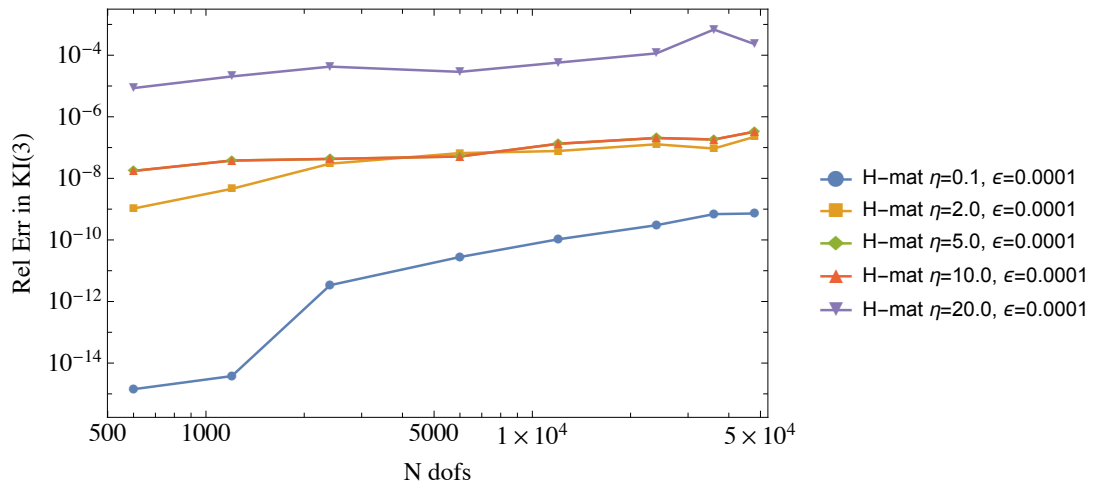


Figure 2.17: Star crack example ($n = 3$, P1 elements): the relative errors in the SIF $K_I^{(3)}$ obtained from the H-matrix solutions with respect to the values of $K_I^{(3)}$ obtained using the full DDM matrix, vs number of DOFs. H-mat parameters (η, ϵ) are listed for each data series.

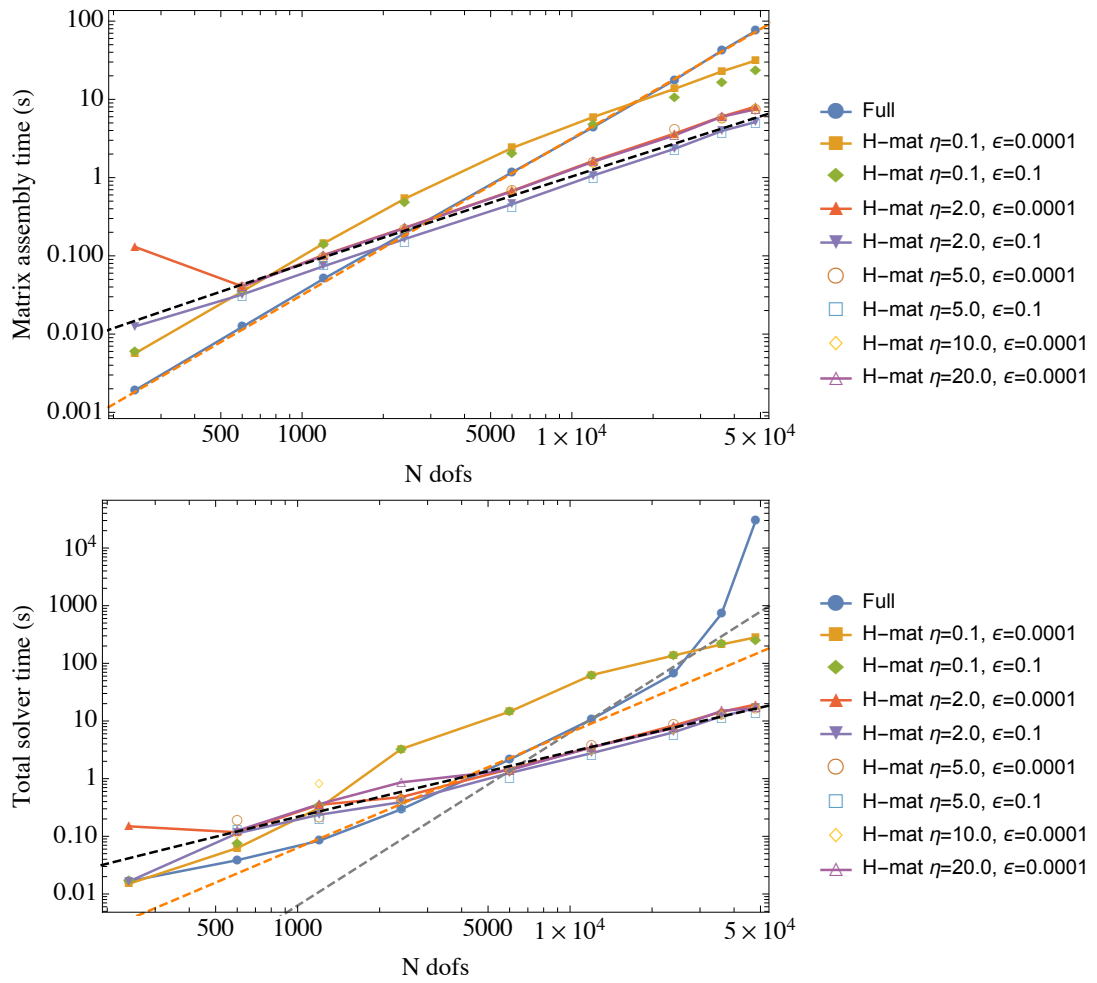


Figure 2.18: Star crack example ($n = 3$, P1 elements): matrix assembly cost in sec. (top), and total solver cost in sec. (bottom), vs number of DOFs. Dashed lines correspond to N^3 (gray), N^2 (orange) and $N \log N$ (black) growth rates. H-mat parameters (η , ϵ) are listed for each data series.

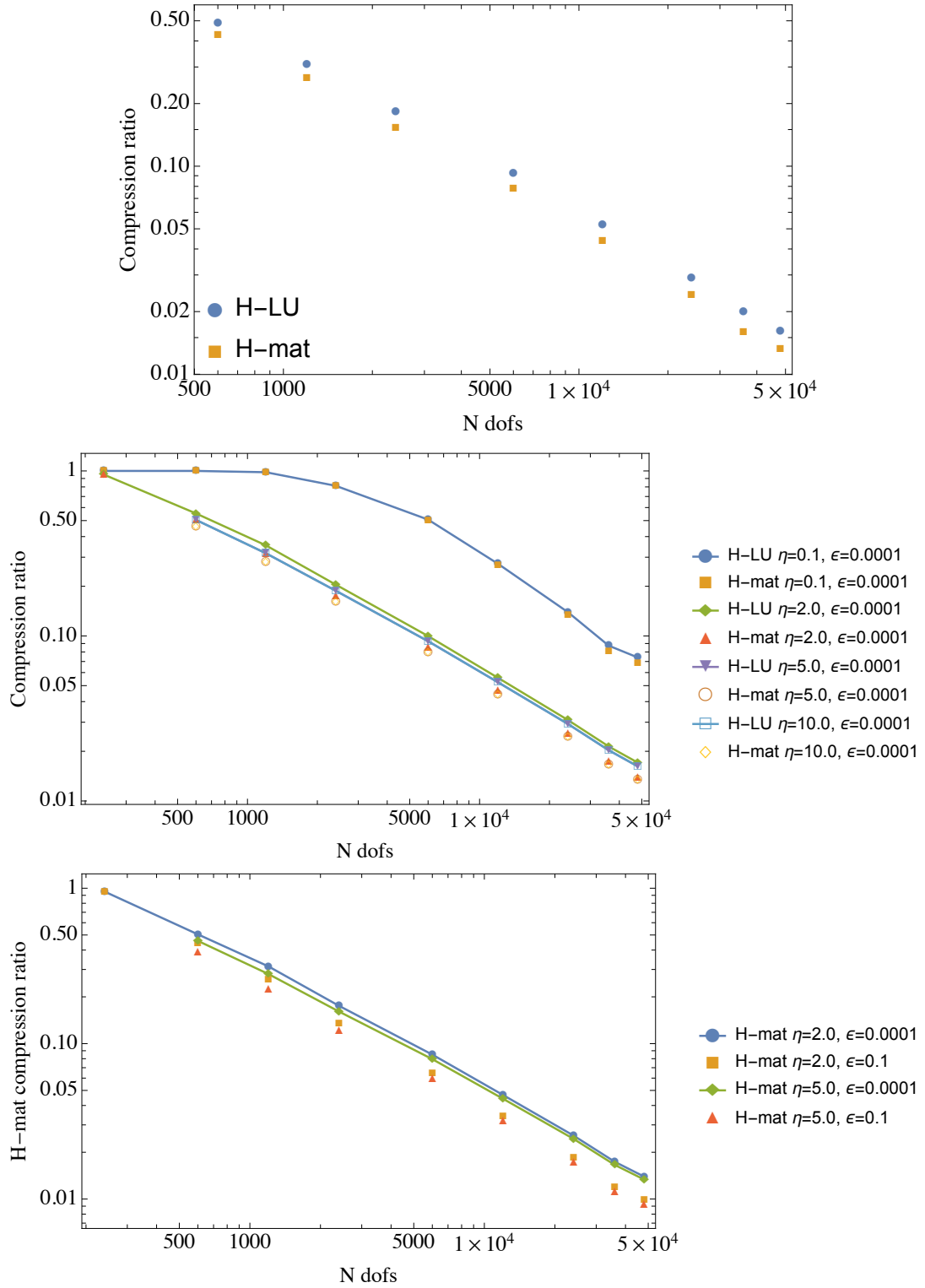


Figure 2.19: Star crack example ($n = 3$, P1 elements): H-matrix compression ratios vs number of DOFs for $\eta = 5.0$ and $\epsilon = 0.0001$ (top), and H-matrix compression ratios vs number of DOFs for several values of parameters η and ϵ (middle, bottom).

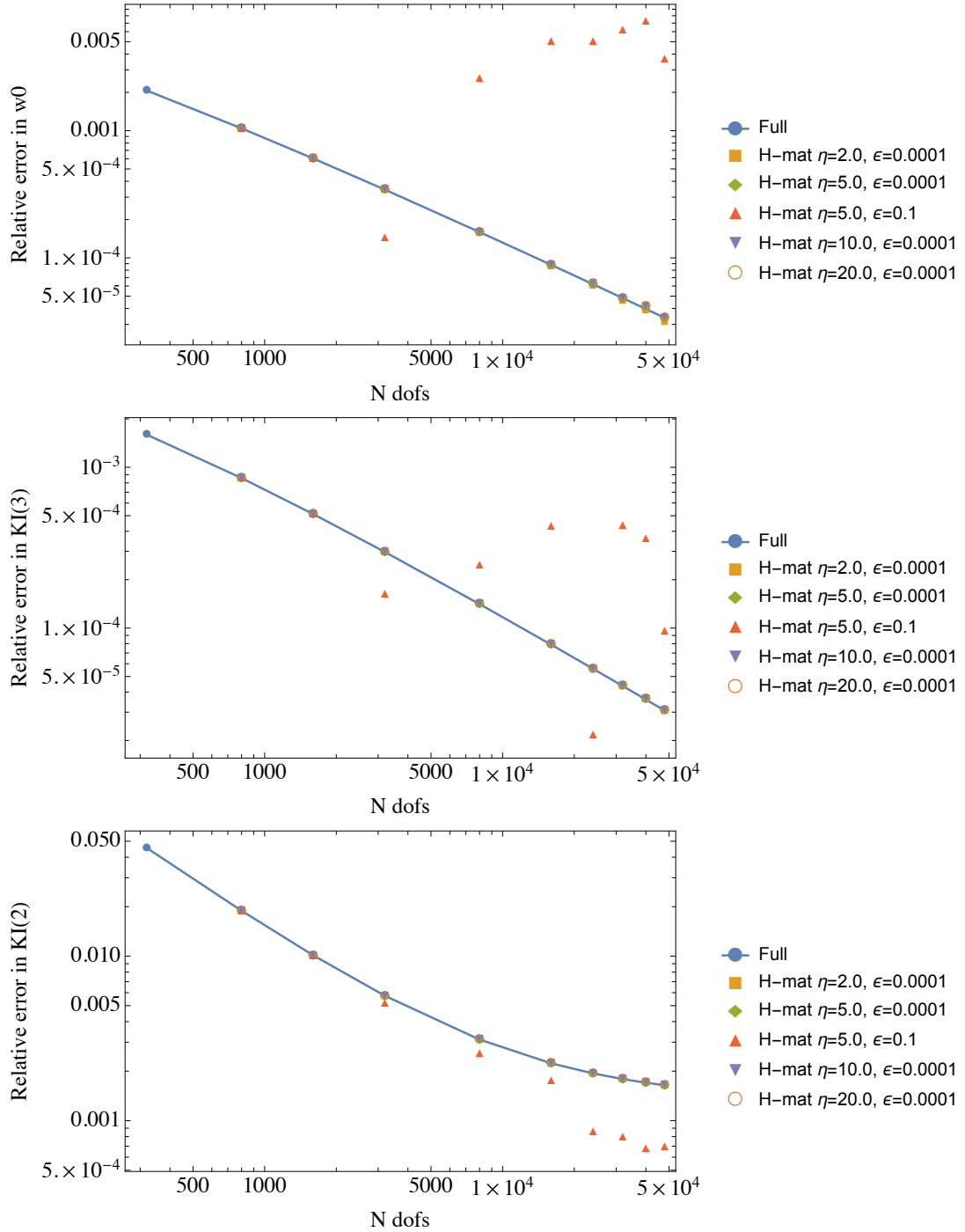


Figure 2.20: Star crack example ($n = 4$, P1 elements), relative errors vs number of DOFs for: crack opening at the center (top), SIF $K_I^{(3)}$ computed using Eqs. (2.24) and (2.25) (middle), and SIF $K_I^{(2)}$ computed using Eq. (2.23) (bottom). H-mat parameters (η, ϵ) are listed for each data series.

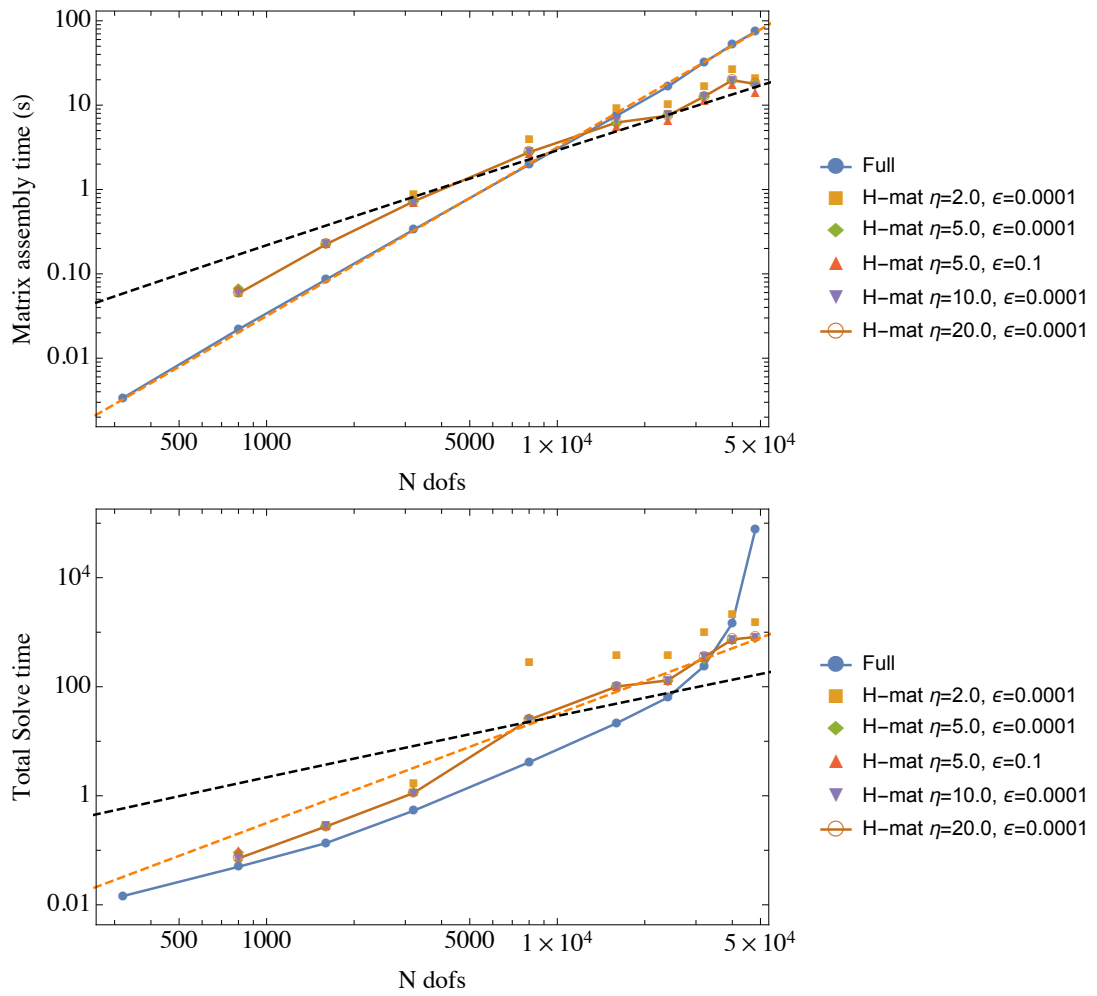


Figure 2.21: Star crack example ($n = 4$, P1 elements): matrix assembly cost in sec. (top), and total solver cost in sec. (bottom), vs number of DOFs. Dashed lines correspond to N^2 (orange) and $N \log N$ (black) growth rates. H-mat parameters (η, ϵ) are listed for each data series.

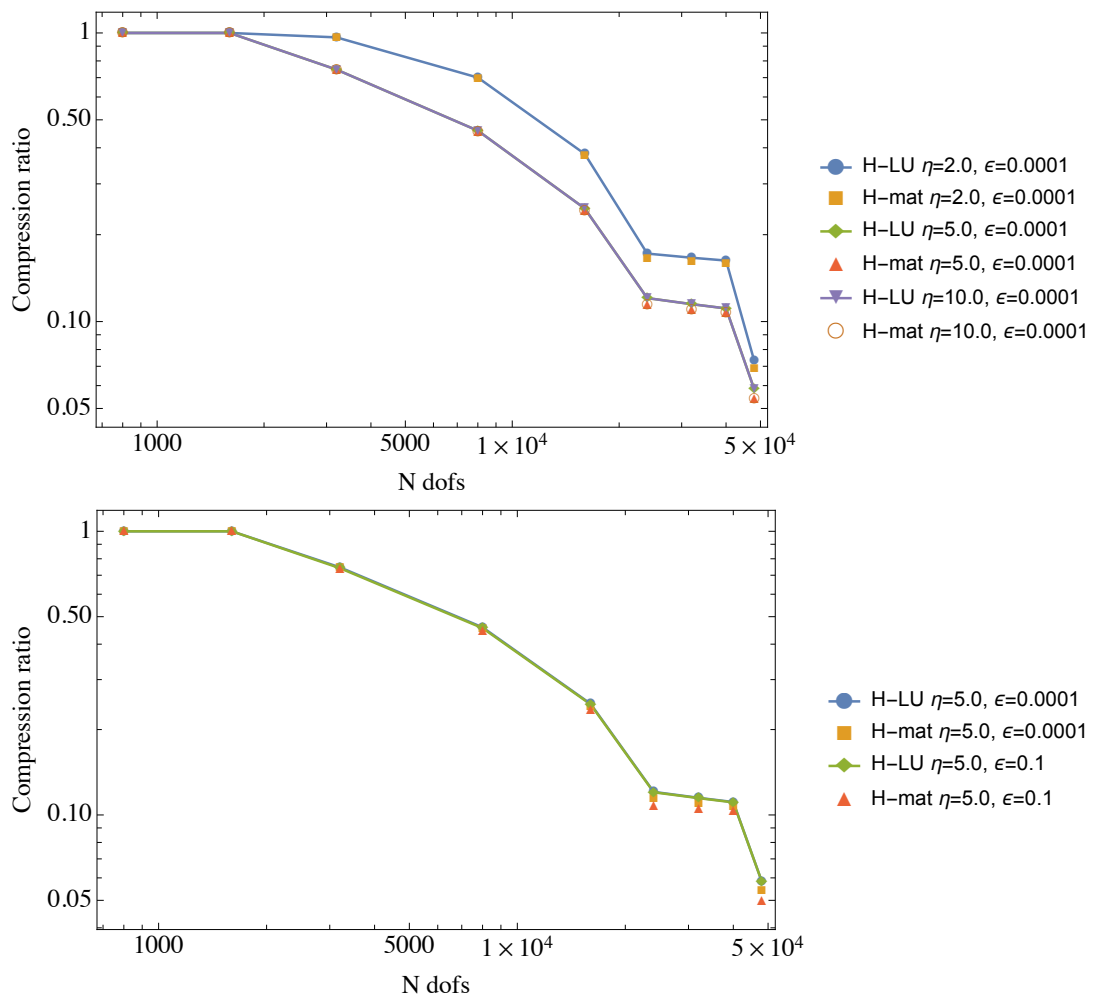


Figure 2.22: Star crack example ($n = 4$, P1 elements): H-matrix compression ratios vs number of DOFs. H-mat parameters (η, ϵ) are listed for each data series.

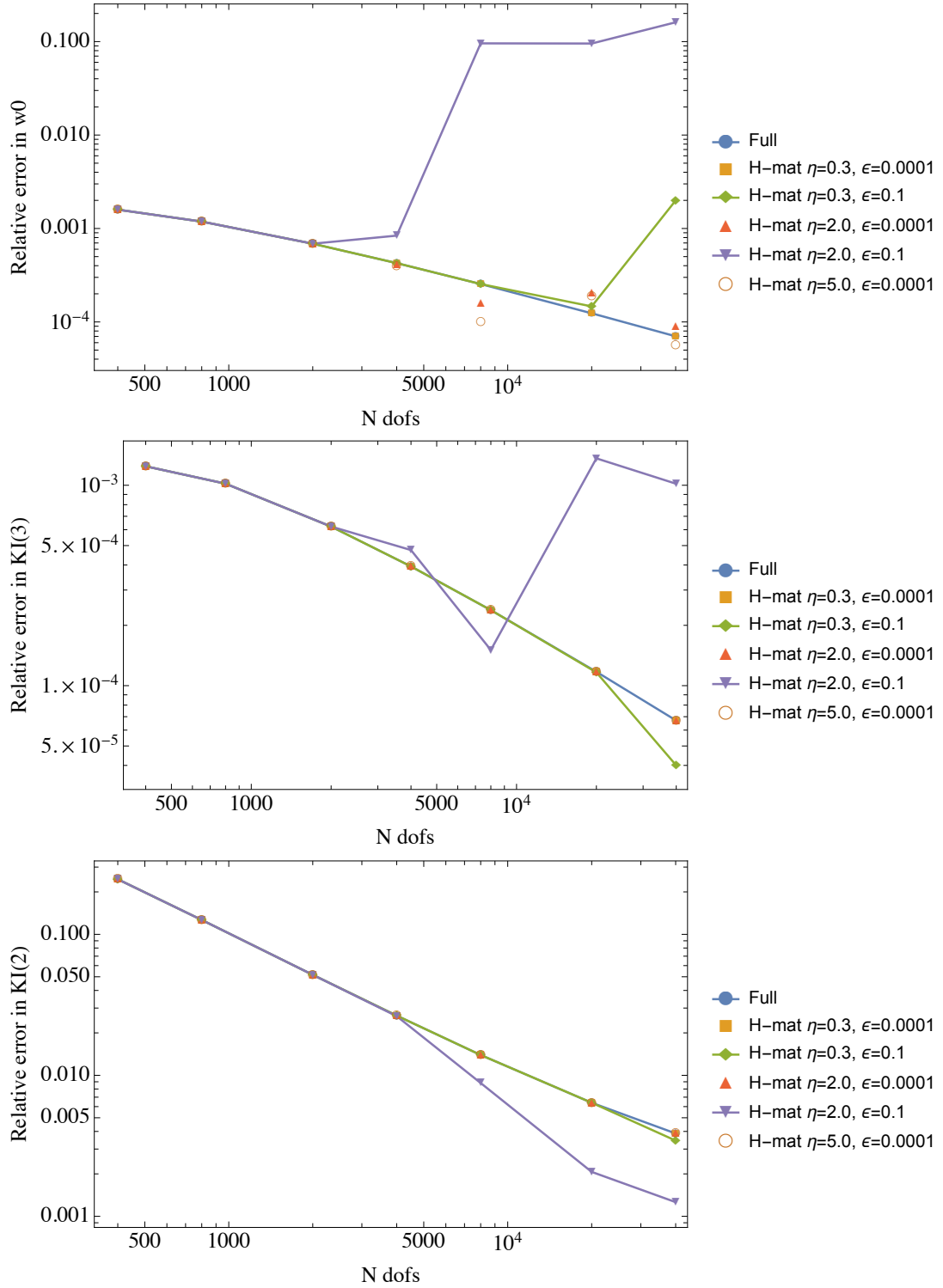


Figure 2.23: Star crack example ($n = 10$, P1 elements), relative errors vs number of DOFs for: crack opening at the center (top), SIF $K_I^{(3)}$ computed using Eqs. (2.24) and (2.25) (middle), and SIF $K_I^{(2)}$ computed using Eq. (2.23) (bottom). H-mat parameters (η, ϵ) are listed for each data series.

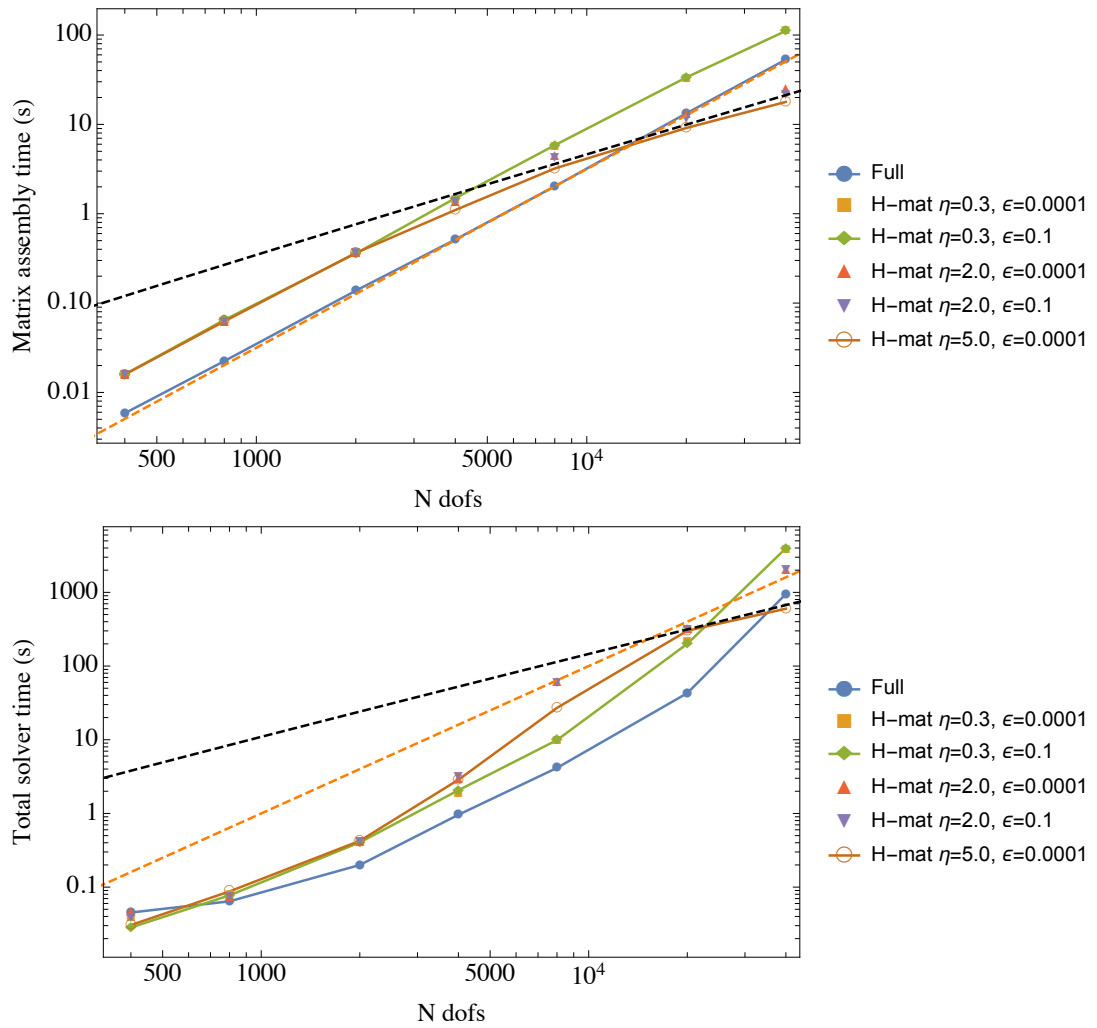


Figure 2.24: Star crack example ($n = 10$, P1 elements): matrix assembly cost in sec. (top), and total solver cost in sec. (bottom), vs number of DOFs. Dashed lines correspond to N^2 (orange) and $N \log N$ (black) growth rates. H-mat parameters (η , ϵ) are listed for each data series.

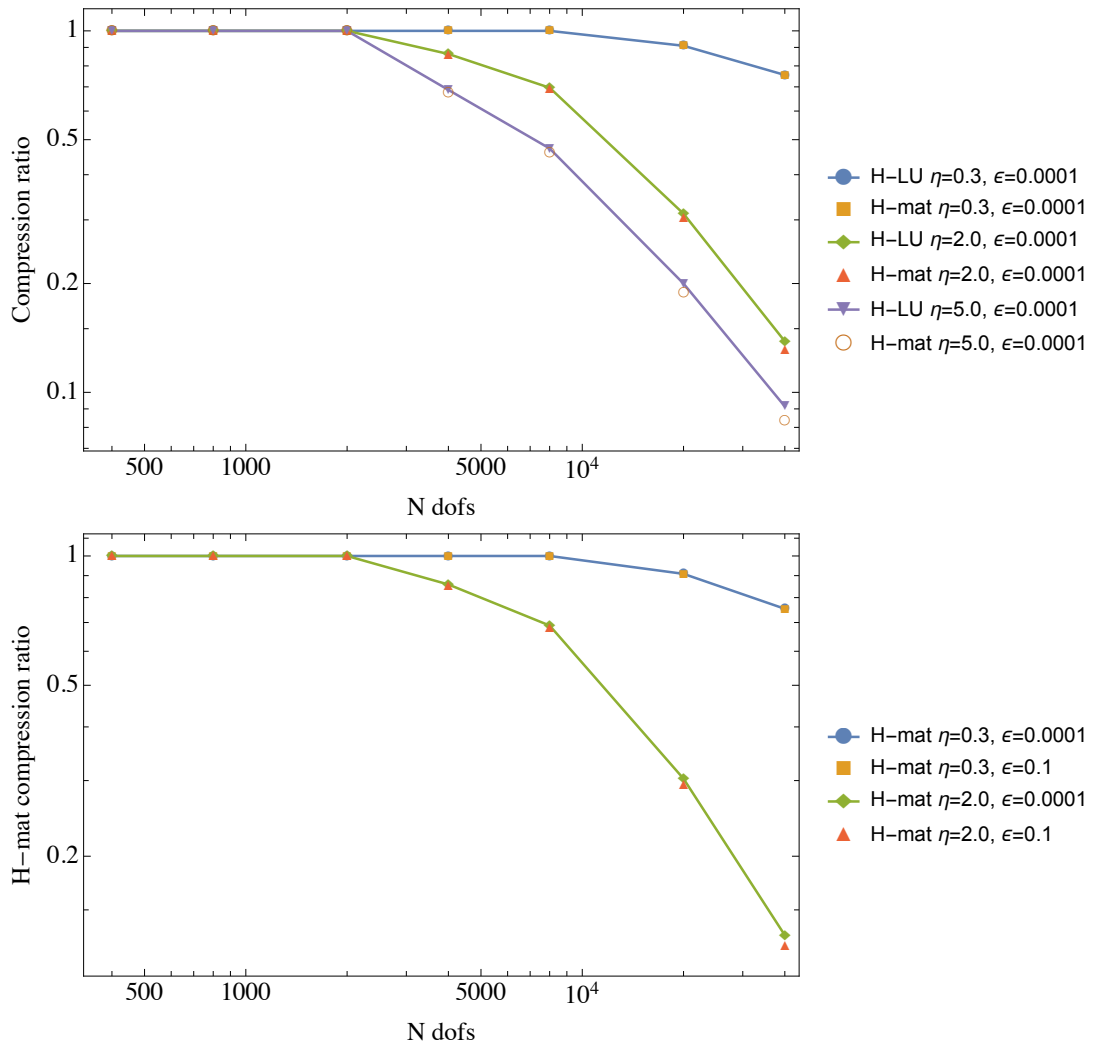


Figure 2.25: Star crack example ($n = 10$, P1 elements): H-matrix compression ratios vs number of DOFs. H-mat parameters (η, ϵ) are listed for each data series.



in the computation time (Fig. 2.18). For $n = 4$ and $n = 10$, the advantage of the use of H-mat in the solver time is only seen at larger number of the degrees of freedom, i.e. for $N_{dof} \geq 4 \times 10^4$ (Figs. 2.21 and 2.24). It is possible that for $n = 4, 10$, the advantage could be observed for even larger numbers of the degrees of freedom, which however were not feasible to use in the present computations due to the memory limit.

- Fig. 2.17 shows the relative errors in the SIF $K_I^{(3)}$ obtained from the H-matrix solutions with respect to the values of $K_I^{(3)}$ obtained using the full DDM matrix, vs the number of the degrees of freedom. The results correspond to $n = 3$. These relative errors represent the error due to the H-matrix approximation of the DDM influence matrix. (i.e. these errors do not include the approximation error due to the DDM discretization of the crack.) For all numbers of the degrees of freedom tested, these relative errors are below 10^{-6} for $\eta = 0.1, 2, 5, 10$ and $\varepsilon = 10^{-4}$. Naturally, the relative errors due to the H-matrix approximation increase with increasing η for a fixed $\varepsilon = 10^{-4}$, since the H-matrix approximation becomes more aggressive. These relative errors slightly grow as the size of the linear system increases, within the limits for the numbers of degrees of freedom in the tested cases.
- By increasing η (for a fixed $\varepsilon = 10^{-4}$), the efficiency of the solution (solver time and storage requirement, corresponding to the H-matrix compression ratio) is improved. At some threshold value of η , however, the efficiency no longer shows a significant improvement, and there is no significant advantage in a further increase of η . For example, for $n = 3$, there is a significant improvement in the solver time and the compression ratio due to the increase from $\eta = 0.1$ to $\eta = 2$, but no such a significant improvement due to the increase from $\eta = 2$ to $\eta = 10$ (Figs. 2.18 and 2.19). Similarly, for $n = 4$, there is an improvement in the solver time and the compression ratio due to the increase from $\eta = 2$ to $\eta = 5$, but no significant improvement due to the increase from $\eta = 5$ to $\eta = 20$ (Figs. 2.21 and 2.22). For this problem it is optimal to use the values around $\eta = 2, 5$ (for $\varepsilon = 10^{-4}$), for accuracy and efficiency.
- Choosing a too large value of η (e.g. $\eta = 20$) can lead to a divergent solution at large numbers of DD elements, see Figs. 2.14, 2.15.
- By decreasing ε (for a fixed η), the accuracy of the solution is increased. At the same time, in this problem, the solver time and the H-mat compression ratio do not grow significantly by decreasing from $\varepsilon = 0.1$ to $\varepsilon = 10^{-4}$, for all n tested. Therefore, for this problem it is optimal to use $\varepsilon = 10^{-4}$, for accuracy and efficiency.
- Choosing a too large value of ε (e.g. $\varepsilon = 0.1$) can lead to a divergent solution at large numbers of DD elements, see Figs. 2.14, 2.15, 2.20, 2.23.
- In summary, one can find suitable values of η and ε to significantly reduce the storage (required for the influence matrix) and the solver time, while keeping the solution accuracy at a level similar to that of the solution with the dense influence matrix.

2.5.3 Two parallel cracks

2.5.3.1 Geometry and reference solutions

Two parallel cracks of length $2a$ at the distance h in an infinite plane are considered, under the assumption of plane strain. The infinite plane is subjected to a far-field tensile stress P acting orthogonal to the traction-free cracks. The plane strain Young's modulus of the medium is E' .

No exact solution is available for this problem. An approximate reference solution for the mode I SIF is given in Tada et al. (2000):

$$\frac{K_I}{P\sqrt{\pi a}} = F_I(s) \quad (2.26)$$

$$s = \frac{a}{a + \frac{h}{2}}, \quad F_I(s) = 1 - 0.293 s \left[1 - (1 - s)^4 \right] \quad (2.27)$$



# DD elts (total)	$\frac{K_I^{(1)}}{P\sqrt{\pi a}}$	$\frac{K_I^{(2)}}{P\sqrt{\pi a}}$
16000	0.8533	0.8414
24000	0.8534	0.8416
40000	0.8535	0.8417

Table 2.12: Comparison of the mode I SIF computed from the DDM solution for the problem of two parallel cracks, $h/a = 2$, from Eqs. (2.22) and (2.23). The full (dense) DDM influence matrix was used. The first column shows the total number of P1 DD elements used to discretize the two cracks.

The accuracy of the approximation for F_I is stated to be better than 1% Tada et al. (2000). There are also tabulated numerical values for the case of two cracks in Gorbatiikh et al. (2007), including reference numerical results from two other works. The difference between the results from Tada et al. (2000) and Gorbatiikh et al. (2007) is of the order of few percent for $h/a \geq 1$ and is larger for $h/a < 1$. For studying the efficiency and convergence properties of the H-mat approach for this problem, we will use the solution from the present method obtained with the full (dense) DDM matrix and the finest tested mesh.

2.5.3.2 Numerical solution for stress intensity factor (dense matrix)

First, we investigate the accuracy of the stress intensity factor computation in comparison to available reference solutions, see Table 2.12. Similarly to the case of the star crack, Eqs. (2.22) and (2.23) have been used to compute the mode I SIF from the DDM solution, obtained with the P1 displacement discontinuity elements. P1 DD elements were used to discretize the cracks. The full (dense) DDM influence matrix was used. For the case $h/a = 2$, the reference values are: $\frac{K_I}{P\sqrt{\pi a}} \approx 0.8627$ (Tada et al. 2000), $\frac{K_I}{P\sqrt{\pi a}} \approx 0.8374$ (Gorbatiikh et al. 2007). The obtained values from the present method are in agreement with the reference values.

It was observed for the star crack problem, that Eq. (2.23) provides a more accurate approximation than Eq. (2.22). In the following, we use Eq. (2.23) to compute the mode I stress intensity factor.

2.5.3.3 Numerical solution without or with \mathcal{H} -matrix approximation

We consider the two cracks corresponding to $h/a = 2$. P1 displacement discontinuity (DD) elements have been used to discretize the cracks. First, the problem has been solved using $\eta = 1, 5$; $\varepsilon = 10^{-4}, 10^{-1}$; and the maximum leaf size for the H-mat low-rank approximation set to 32. Then, to show the effect of the maximum leaf size on the compression of the influence matrix, the problem was solved using $\eta = 5$, $\varepsilon = 10^{-4}$, and the maximum leaf size set to 320. The numbers of degrees of freedom were increased from 160 to 4×10^5 (for the maximum leaf size 32) and to 10^6 (for the maximum leaf size 320). The results of these simulations are shown in Figs. 2.26 - 2.29.

Fig. 2.26 shows the computed mode I SIF $K_I^{(2)}$, the relative error in $K_I^{(2)}$ with respect to the numerical value obtained for $K_I^{(2)}$ using the present DDM with the full (dense) matrix, and the mean relative error in the crack width computed with respect to the solution obtained with the present DDM with the full (dense) matrix. Fig. 2.27 shows the effects of the H-mat parameters on the computational time spent to assemble the influence matrix or its H-mat approximation, and on the computational time spent to solve the linear system. Figs. 2.28 and 2.29 show the effects of the H-mat parameters on the compression ratio achieved by using the low-rank H-mat approximation, including the effect of the maximum leaf size.

Several observations can be made from these results:

- For the case tested ($h/a = 2$), the values $\eta = 1, 5$ and $\varepsilon = 10^{-4}$ provide convergence in the stress intensity factor $K_I^{(2)}$, while the same values of η with $\varepsilon = 10^{-1}$ lead to divergence of the results (Fig. 2.26).
- Fig. 2.27 shows a significant reduction in computational time due to the use of the H-matrix approximation. For the simulations with the full matrix, the time spent for matrix assembly grows as

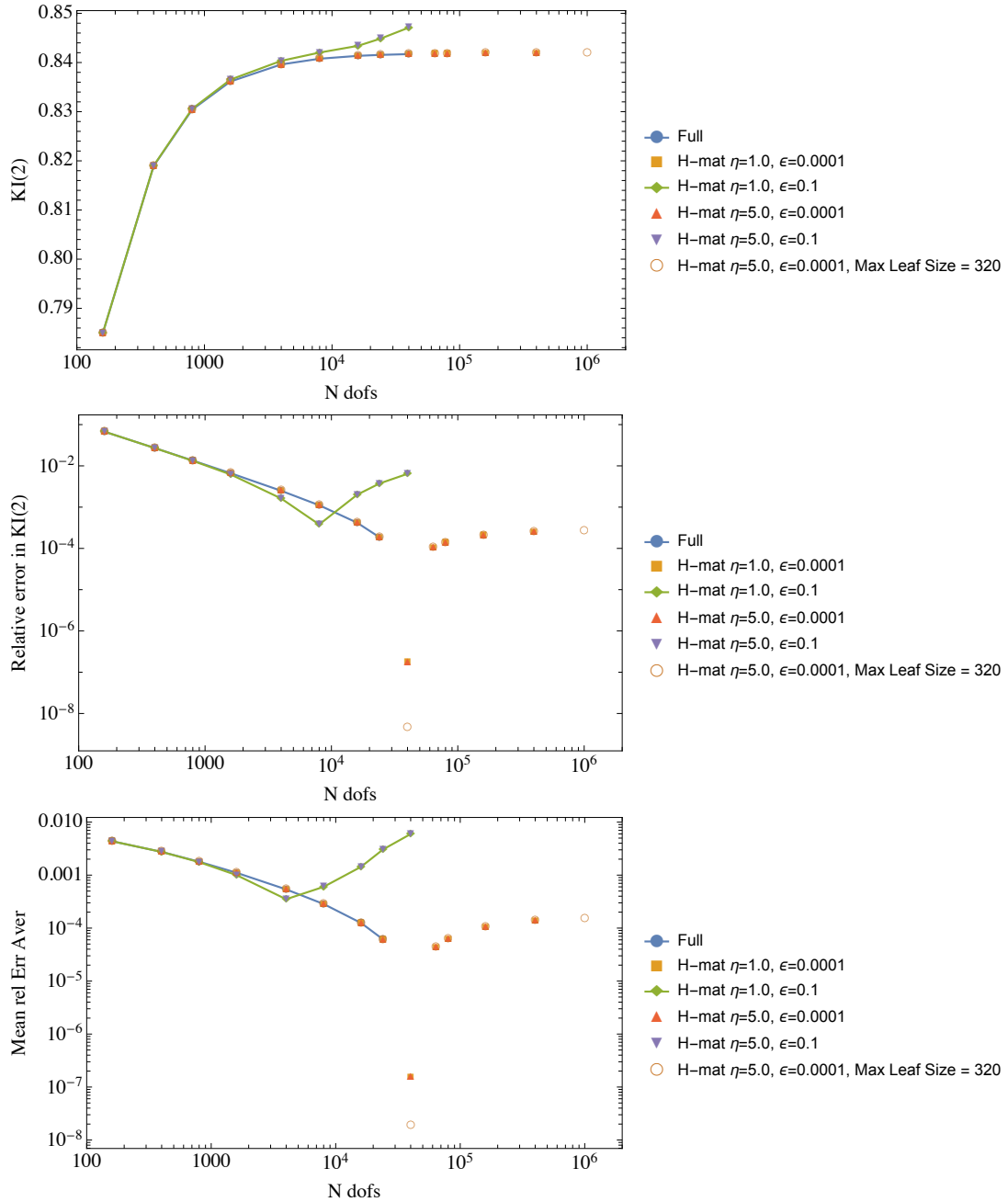


Figure 2.26: Two parallel cracks ($h/a = 2$, P1 elements), numerical results vs number of DOFs for: mode I SIF $K_I^{(2)}$ (top), the relative error in $K_I^{(2)}$ with respect to the numerical value obtained with the full matrix and $N_{dofs} = 5 \times 10^3$ (middle), and the mean relative error in crack width with respect to the solution obtained with the full matrix and $N_{dofs} = 5 \times 10^3$ (bottom). H-mat parameters (η, ϵ) are listed for each data series. The maximum leaf size for H-mat simulations was set to 32, unless noted otherwise.

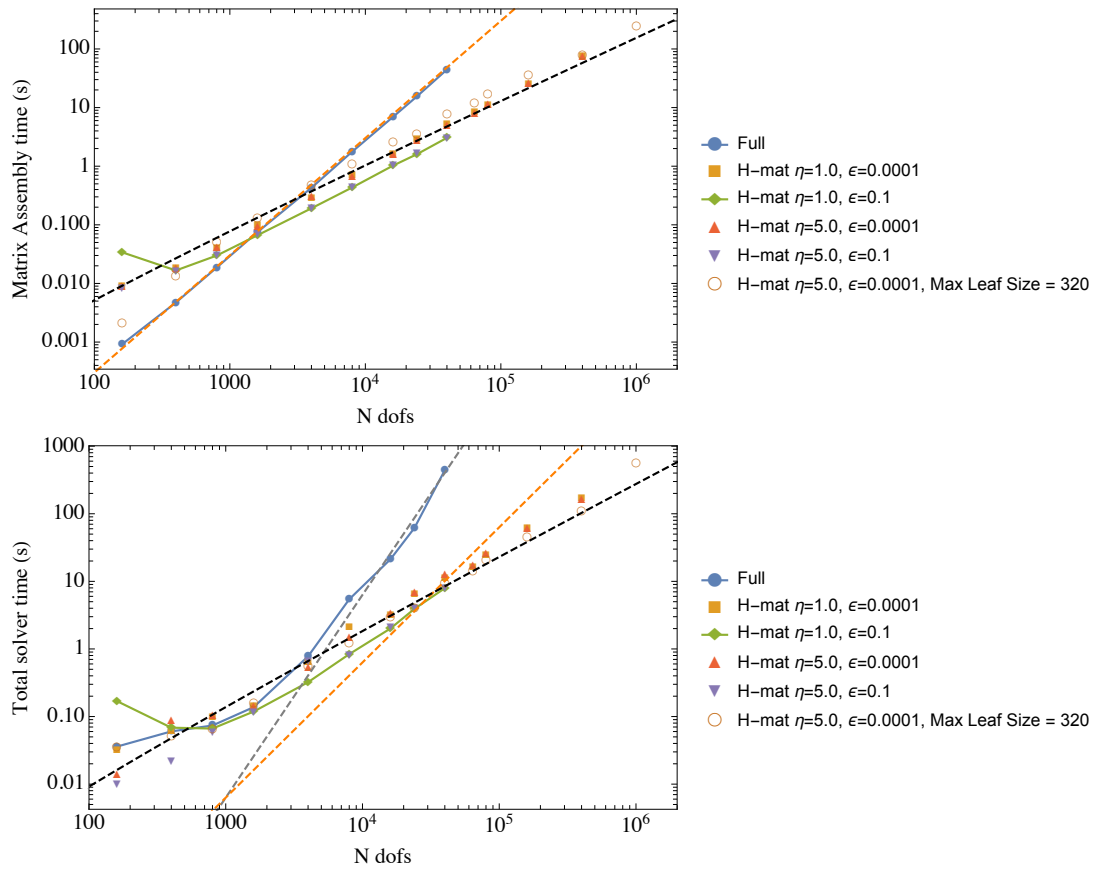


Figure 2.27: Two parallel cracks ($h/a = 2$, P1 elements): matrix assembly cost in sec. (top), and total solver cost in sec. (bottom), vs number of DOFs. Dashed lines correspond to N^3 (gray), N^2 (orange) and $N \log N$ (black) growth rates. H-mat parameters (η, ϵ) are listed for each data series. The maximum leaf size for H-mat simulations was set to 32, unless noted otherwise.

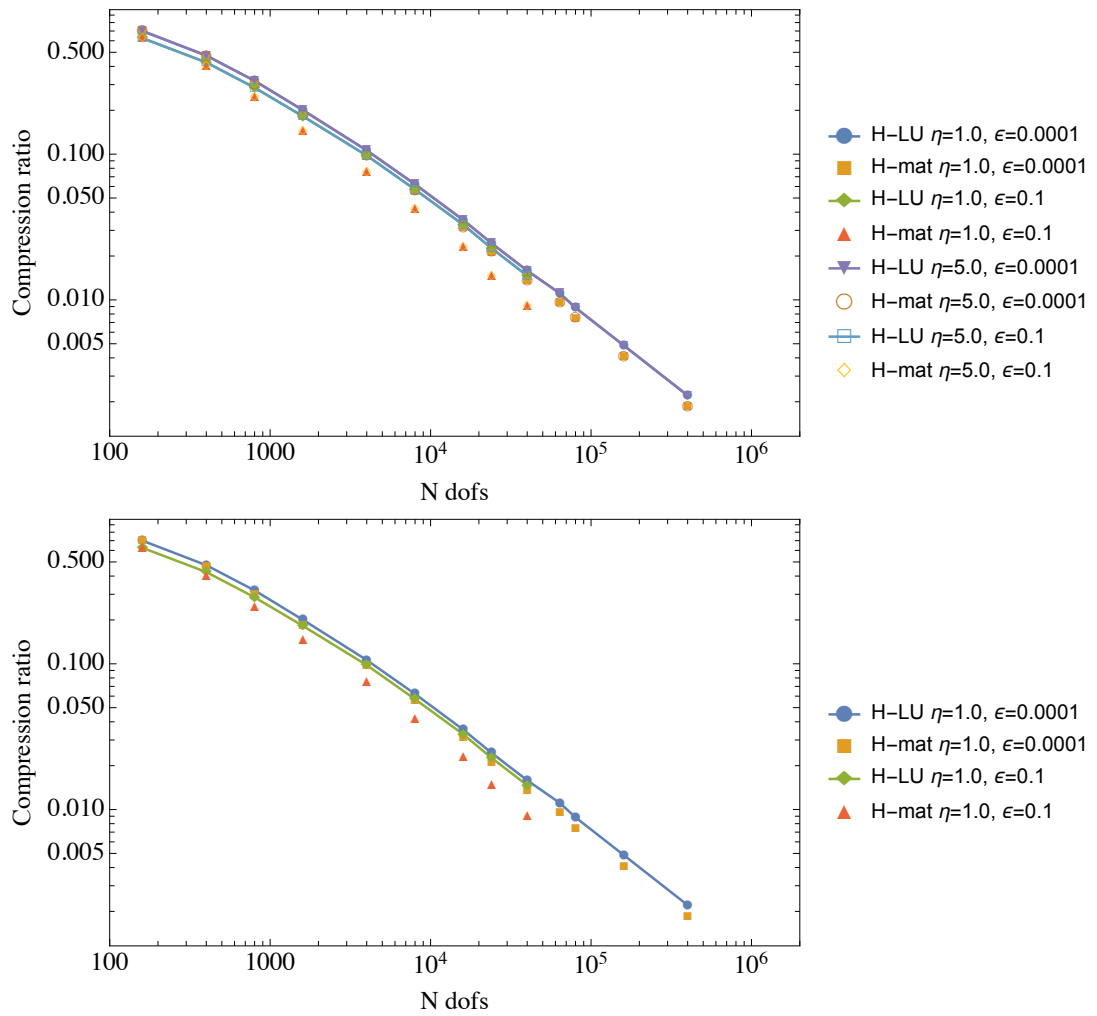


Figure 2.28: Two parallel cracks ($h/a = 2$, P1 elements): H-matrix compression ratios vs number of DOFs. H-mat parameters (η, ϵ) are listed for each data series. The maximum leaf size for H-mat simulations was set to 32.

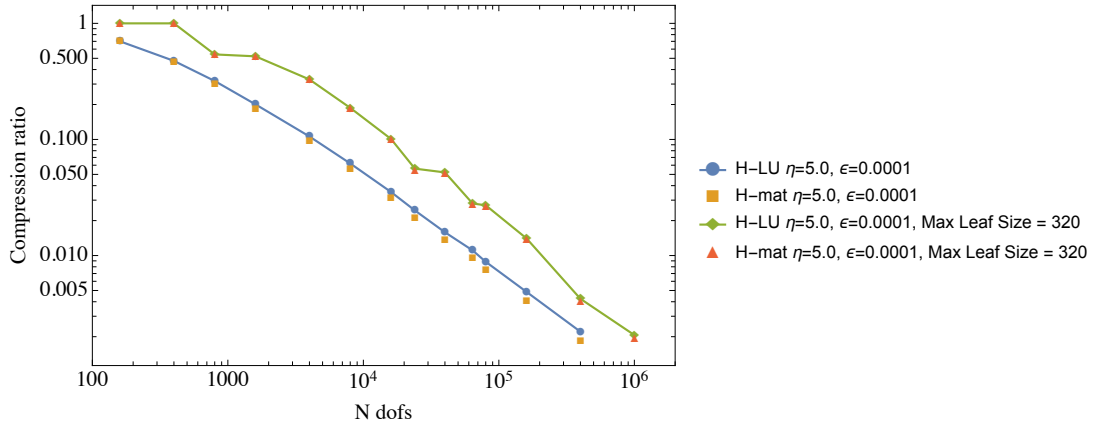


Figure 2.29: The effect of the maximum leaf size on the H-mat compression ratios for two parallel cracks ($h/a = 2$, P1 elements): H-matrix compression ratios vs number of DOFs. H-mat parameters (η , ϵ) are listed for each data series. The maximum leaf size for H-mat simulations was set to 32, unless noted otherwise.

N^2 , and the total solution time (including time in the linear solver) grows roughly as N^3 for large numbers of degrees of freedom N . For the simulations with H-matrix approximation, the time spent for matrix assembly grows roughly as $N \log N$, and the growth rate for the total solution time for large N is between N^2 to $N \log N$. In particular, the total solution time for $N = 4 \times 10^4$ (i.e. 5×10^3 P1 elements per crack) is 442 sec. with the full matrix and 13 sec. with the H-matrix with $\eta = 5$, $\epsilon = 10^{-4}$, and the maximum leaf size set to 32.

- Fig. 2.28 shows a significant reduction in storage required for the influence matrix. E.g. for $N = 4 \times 10^4$ (i.e. 5×10^3 P1 elements per crack), the compression ratio of the influence matrix for all tested values of η and ϵ is around 1-2%.
- The use of the H-matrix approximation allowed for using much larger numbers of degrees of freedom in the problem, i.e. much finer meshes on the cracks. E.g., the largest number of degrees of freedom that was used with the full matrix was $N = 4 \times 10^4$ (i.e. 5×10^3 P1 elements per crack). With the H-matrix, it was possible to run the simulations using $N = 4 \times 10^5$ (i.e. 50×10^3 P1 elements per crack) when the maximum leaf size was set to 32, and using $N = 10^6$ (i.e. 125×10^3 P1 elements per crack) when the maximum leaf size was set to 320.
- The effect of the maximum leaf size of the H-matrix is shown in Figs. 2.26, 2.27 and 2.29. By increasing the maximum leaf size from 32 to 320 (with $\eta = 5$, $\epsilon = 10^{-4}$), there was no significant change of the accuracy of the solution (Fig. 2.26) and no significant change in the computational time (Fig. 2.27). Naturally, the compression ratio of the H-matrix increased with the larger maximum leaf size. On the other hand, by setting the maximum leaf size to 320, it was possible to run the simulation with $N = 10^6$, while a simulation with the maximum leaf size set to 32 and $N = 10^6$ could not proceed due to the memory limit.
- There is no significant difference in the total solution time between the H-matrix simulations with $\eta = 1$ and $\eta = 5$, and no difference in the accuracy of the SIF. In fact, the values of SIF $K_I^{(2)}$ computed using $\eta = 1$, 5 and $\epsilon = 10^{-4}$ are found to be exactly the same, see Fig. 2.30 (top). In a further test with $N = 400$, 16×10^3 , it was found that the values of the SIF $K_I^{(2)}$ computed using $\eta = 1$, 5, 10 and $\epsilon = 10^{-4}$, 10^{-1} are exactly the same, see Fig. 2.30 (middle, bottom).
- Fig. 2.31 shows the relative errors in the SIF $K_I^{(2)}$ obtained from three H-matrix solutions with respect to the values of $K_I^{(2)}$ obtained using the full DDM matrix, vs the number of the degrees of freedom. These relative errors represent the error due to the H-matrix approximation of the DDM influence matrix. For all numbers of the degrees of freedom tested, these relative errors are below



10^{-6} . Naturally, the relative errors due to the use of H-matrix are lower when the maximum leaf size is larger (320), since in this case the H-matrix approximation is less aggressive.

- In summary, one can find suitable values of η and ε to significantly reduce the storage (required for the influence matrix) and the solver time, while keeping the solution accuracy at a level similar to that of the solution with the dense influence matrix.

2.5.4 Array of parallel cracks

2.5.4.1 Geometry and reference solutions

An array of n ($n \geq 2$) parallel cracks of length $2a$ in an infinite plane is considered, under the assumption of plane strain. The spacing between the neighbour cracks is h . The infinite plane is subjected to a far-field tensile stress P acting orthogonal to the traction-free cracks. The plane strain Young's modulus of the medium is E' .

We consider below the case when $h/a = 4$. As the number of cracks increases, the SIF of the middle crack should approach the SIF value for an infinite stack of parallel cracks. A relevant reference numerical solution (not restricted to large or small values of h/a) can be found in Sih (1973) (p. 1.2.6-16) as a tabulated value:

$$\frac{K_I^{ref}}{P\sqrt{\pi a}} = 0.7896 \quad (h/a = 4) \quad (2.28)$$

2.5.4.2 Numerical solution without or with \mathcal{H} -matrix approximation

We consider an increasing number of parallel cracks: $n = 21, 41, 81$, with $h/a = 4$. P1 displacement discontinuity (DD) elements have been used to discretize the cracks. The maximum leaf size for the H-matrix low-rank approximation has been set to 320. Eq. (2.23) was used to compute the mode I stress intensity factor.

First, the problem has been solved for $n = 21$ using the full DDM matrix and the H-matrix approximation with several values of η and ε . Fig. 2.32(top) shows the computed mode I SIF $K_I^{(2)}$ for the middle crack of the array, vs the number of the degrees of freedom. Fig. 2.32(bottom) shows the relative error in $K_I^{(2)}$ for the middle crack, obtained using H-matrix, with respect to the numerical value of $K_I^{(2)}$ for the middle crack, obtained using the full DDM matrix with the same mesh. These relative errors represent the error due to the H-matrix approximation of the DDM influence matrix. Fig. 2.33 shows the effects of the H-mat parameters on the computational time spent to assemble the influence matrix or its H-mat approximation, and on the computational time spent to solve the linear system. Fig. 2.34 shows the effect of the H-mat parameters on the compression ratio achieved by using the low-rank H-mat approximation.

Several observations can be made from these results for 21 cracks ($n = 21$):

- For the case tested ($h/a = 4$), the values $\eta = 1, 5, 10$ and $\varepsilon = 10^{-4}$ provide convergence in the stress intensity factor $K_I^{(2)}$ (Fig. 2.32).
- The relative errors due to the H-matrix approximation decrease with decreasing η for a fixed $\varepsilon = 10^{-4}$ (Fig. 2.32(bottom)). These relative errors do not grow as the size of the linear system increases, for the tested cases. For all numbers of the degrees of freedom tested, these relative errors are below 10^{-5} for $\varepsilon = 10^{-4}$. The relative errors due to the use of the H-matrix increase for the increase from $\varepsilon = 10^{-4}$ to $\varepsilon = 10^{-1}$, for a fixed $\eta = 5$.
- Fig. 2.33 shows a significant reduction in computational time due to the use of the H-matrix approximation. For the simulations with the full matrix, the total solution time (including time in the linear solver) grows roughly as N^3 for large numbers of degrees of freedom N . For the simulations with H-matrix approximation, the growth rate for the total solution time for large N is between N^2 to $N \log N$. In particular, the total solution time for $N = 4.2 \times 10^4$ (i.e. 500 P1 elements per crack) is approximately 43 minutes with the full matrix and about 8 sec. with the H-matrix with $\eta = 5$,

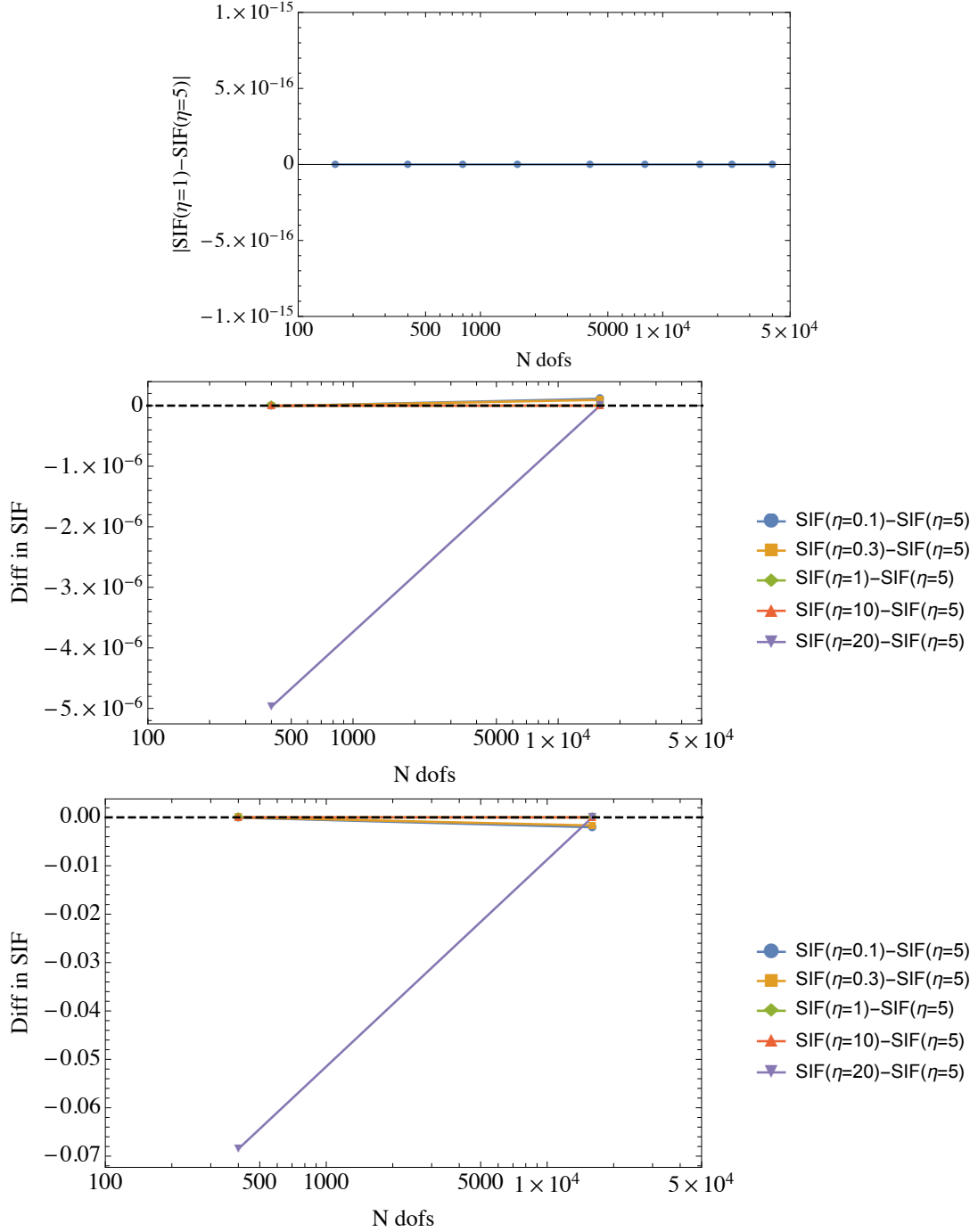


Figure 2.30: Two parallel cracks ($h/a = 2$, P1 elements), numerical results vs number of DOFs for: difference in mode I SIF $K_I^{(2)}$ between the solutions computed with $\eta = 1, 5$ and $\varepsilon = 10^{-4}$ (top), difference in mode I SIF $K_I^{(2)}$ between the solutions computed with $\eta = 0.1, 0.3, 1, 10, 20$ and $\eta = 5$, using $\varepsilon = 10^{-4}$ (middle), and difference in mode I SIF $K_I^{(2)}$ between the solutions computed with $\eta = 0.1, 0.3, 1, 10, 20$ and $\eta = 5$, using $\varepsilon = 10^{-1}$ (bottom). The maximum leaf size for H-mat simulations was set to 32. In the middle and bottom figures, only the simulations with $N = 400$ and $N = 16 \times 10^3$ are shown.

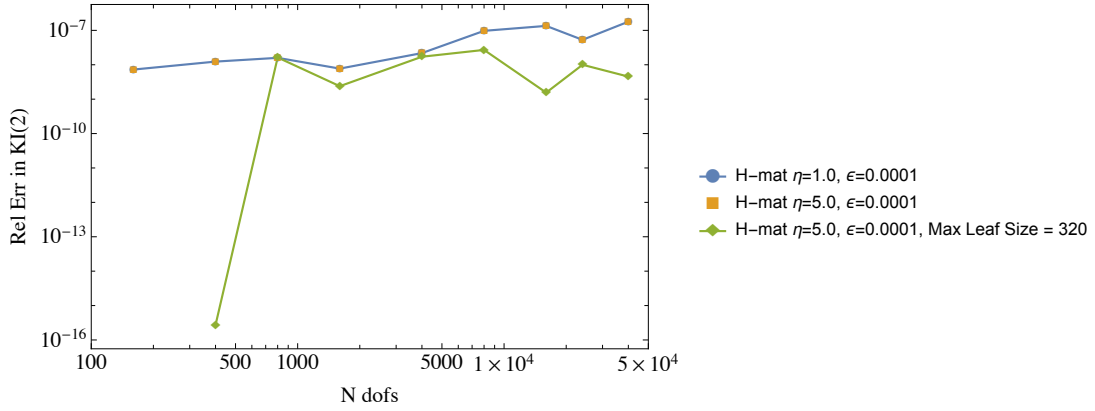


Figure 2.31: Two parallel cracks ($h/a = 2$, P1 elements): the relative errors in the SIF $K_I^{(2)}$ obtained from the H-matrix solutions with respect to the values of $K_I^{(2)}$ obtained using the full DDM matrix, vs number of DOFs. H-mat parameters (η , ϵ) are listed for each data series. The maximum leaf size for H-mat simulations was set to 32, unless noted otherwise.

$\epsilon = 10^{-4}$. There is no significant difference in the time spent for matrix assembly between the simulations with the full matrix and with the H-matrix, for this test case.

- Fig. 2.34 shows a significant reduction in storage required for the influence matrix. E.g. for $N = 4.2 \times 10^5$ (i.e. 5×10^3 P1 elements per crack), the compression ratio of the influence matrix for all tested values of η and ϵ is around 0.5%.
- The use of the H-matrix approximation allowed for using much larger numbers of degrees of freedom in comparison to those feasible with the full matrix simulations. I.e., much finer meshes on the cracks can be used with the H-matrix approximation. E.g., the largest number of degrees of freedom that was used with the full matrix corresponded to 500 P1 elements per crack. With the H-matrix, it was possible to run the simulations using 10^4 P1 elements per crack, i.e. with the total size of the linear system equal to $N = 8.2 \times 10^5$.
- There is no significant difference in the total solution time between the H-matrix simulations with the tested values of η and ϵ .
- In summary, one can find suitable values of η and ϵ to significantly reduce the storage (required for the influence matrix) and the solver time, while keeping the solution accuracy at a level similar to that of the solution with the dense influence matrix.

Finally, Fig. 2.35 shows the mode I SIF for each crack in the array computed for the arrays with 21, 41 and 81 cracks, using fine meshes. It can be seen that, as the number of cracks increases, the SIF for the middle crack in the array, corresponding to $(\text{crack number})/n \approx 0.5$, approaches the SIF for an infinite array of cracks from Eq. (2.28).

2.5.5 Performance of the GMRes iterative linear solver

In this section we investigate the performance of the generalized minimal residual method (GMRes), an iterative linear solver. It is tested on the example of two parallel cracks with $h/a = 2$, discretized with P1 DD elements. The problem formulation follows that of Section 2.5.3. The two-crack problem is solved using the DDM with the H-matrix approximation of the DD influence matrix. The H-matrix has been constructed using $\eta = 5$, $\epsilon = 10^{-4}$, and the maximum leaf size set to 32. To solve the resulting linear system, the GMRes is used.

A preconditioner for the GMRes solver is chosen between the LU preconditioner and the Jacobi preconditioner. The creation of the LU preconditioner involves additional parameters ($\eta_{prec}, \epsilon_{prec}$). The

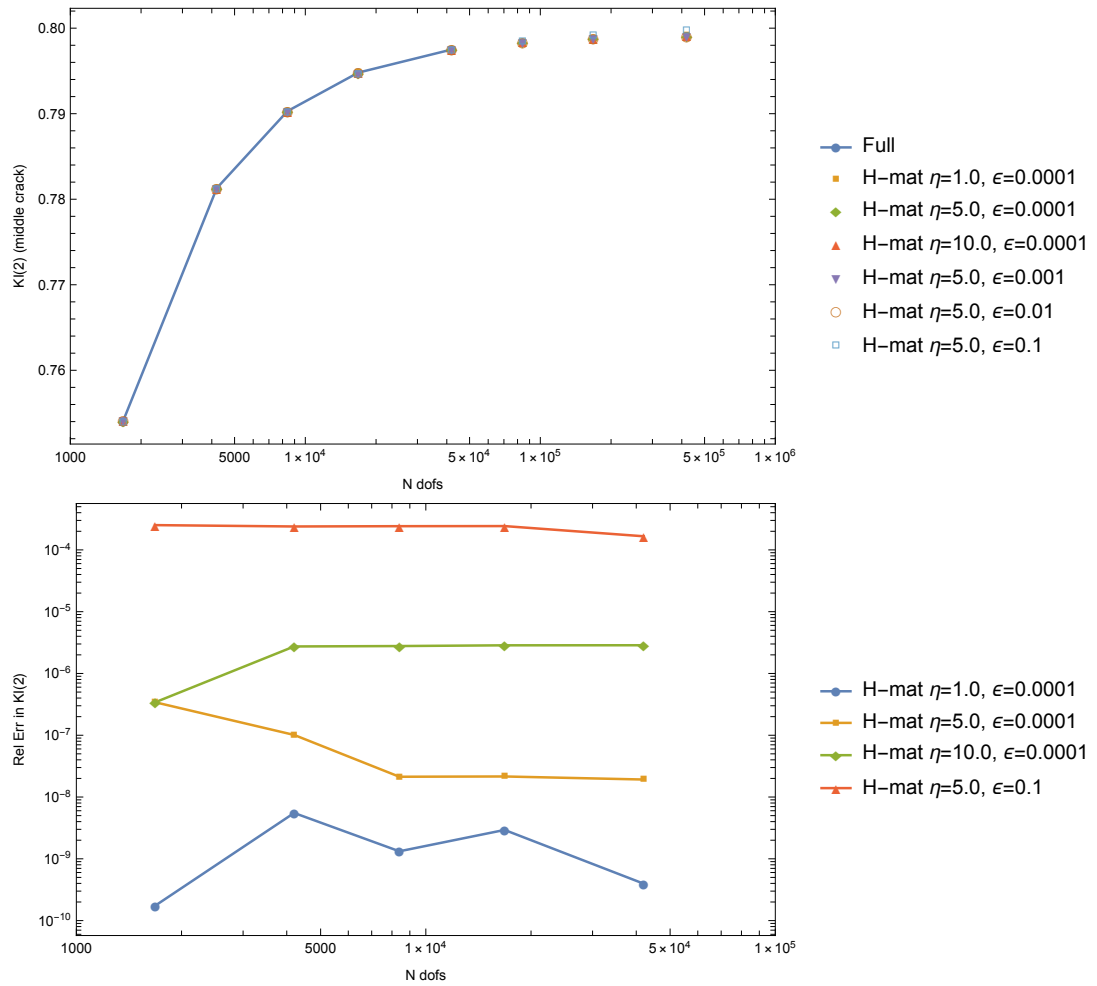


Figure 2.32: Array of 21 parallel cracks ($n = 21$, $h/a = 4$, P1 elements), numerical results vs number of DOFs for: mode I SIF $K_I^{(2)}/(P\sqrt{\pi a})$ for the middle crack (top), the relative error in $K_I^{(2)}$ for the middle crack with respect to the corresponding numerical value obtained with the full matrix (bottom). H-mat parameters (η , ϵ) are listed for each data series.

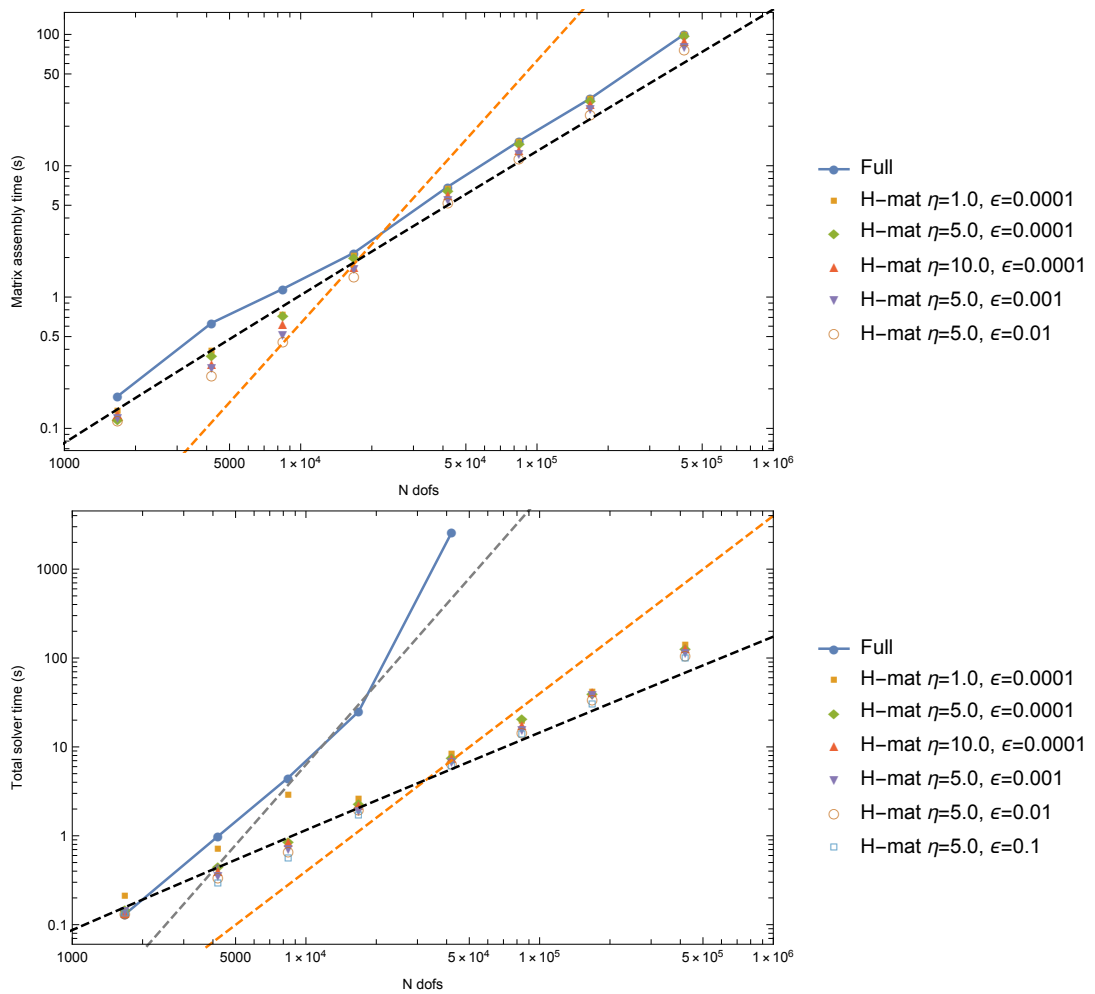


Figure 2.33: Array of 21 parallel cracks ($n = 21$, $h/a = 4$, P1 elements): matrix assembly cost in sec. (top), and total solver cost in sec. (bottom), vs number of DOFs. Dashed lines correspond to N^3 (gray), N^2 (orange) and $N \log N$ (black) growth rates. H-mat parameters (η , ϵ) are listed for each data series.

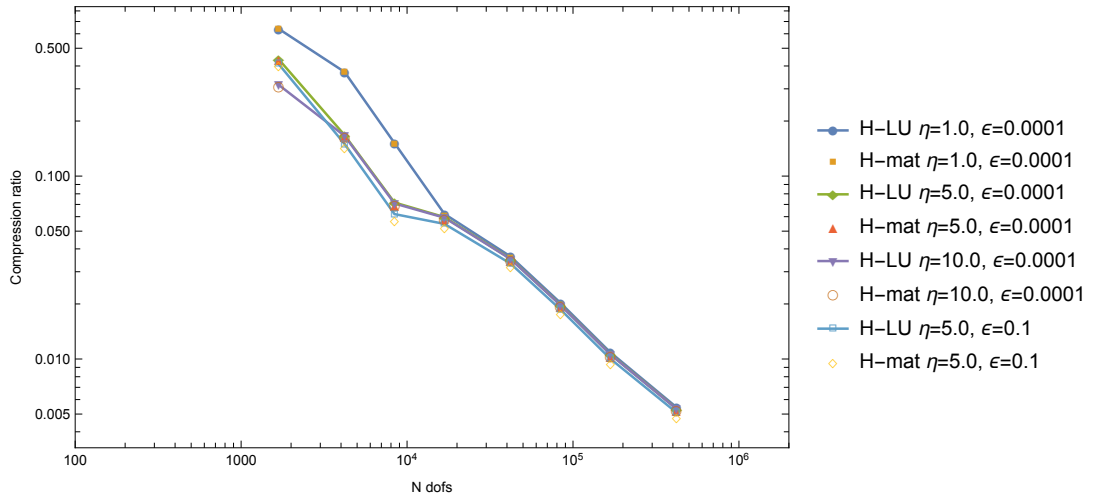


Figure 2.34: Array of 21 parallel cracks ($n = 21$, $h/a = 4$, P1 elements): H-matrix compression ratios vs number of DOFs. H-mat parameters (η , ϵ) are listed for each data series. The maximum leaf size for H-mat simulations was set to 320.

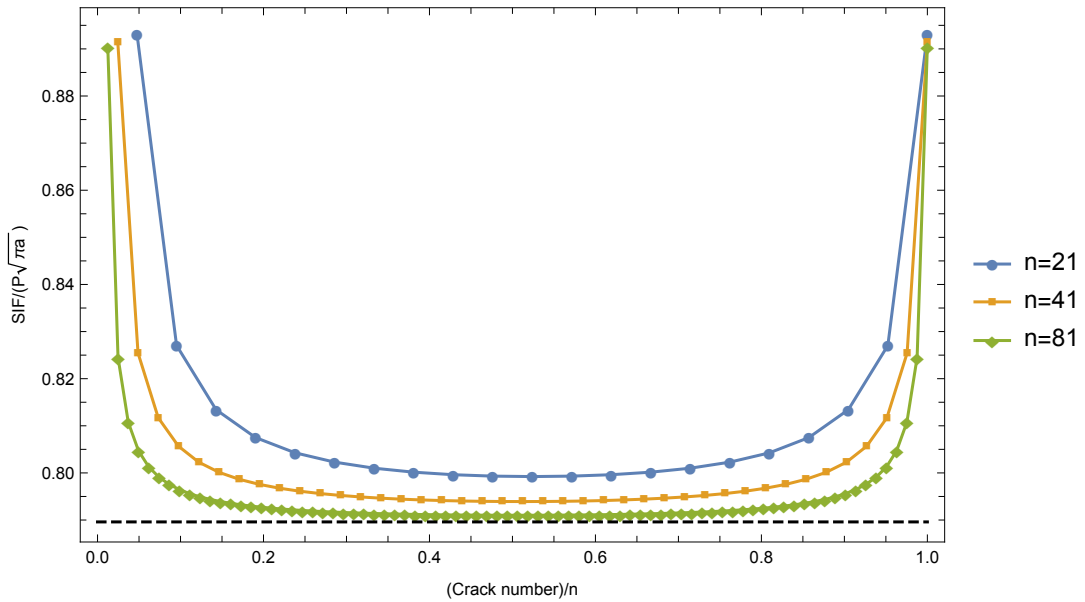


Figure 2.35: Array of n parallel cracks ($h/a = 4$, P1 elements): mode I SIF for each crack in the array, vs the crack number. The results are shown for the arrays with 21, 41 and 81 cracks. The results were obtained using H-matrix with $\eta = 5$, $\epsilon = 10^{-4}$ and the total number of degrees of freedom equal to 84×10^4 (for $n = 21$), 82×10^4 (for $n = 41$), and 81×10^4 (for $n = 81$). The dashed black line corresponds to the reference value for an infinite array of cracks from Sih (1973), Eq. (2.28).



LU preconditioner is based on a crude H-matrix approximation of the original DDM influence matrix, corresponding to the pair $(\eta_{prec}, \varepsilon_{prec})$. We construct such an H-LU preconditioner using

$$\eta_{prec} = \eta, \quad \varepsilon_{prec} \geq \varepsilon.$$

In the following examples, the H-LU preconditioner is constructed using $\varepsilon_{prec} = 10^{-3}$ and 10^{-1} .

Two additional parameters in the GMRes are the maximum number of iterations (set to 10^3) and the maximum number of restarts of iterations (set to 200).

The observations are summarized as follows:

- Fig. 2.36 shows the relative error in $K_I^{(2)}$ with respect to the corresponding numerical value obtained with the full matrix. The figure includes the results from four H-matrix simulations: one with the direct linear solver, two with the GMRes solver and the H-LU preconditioner, and one with the GMRes solver and the Jacobi preconditioner. These results represent the error in the solution due to the use of the H-matrix (for the simulation with the direct linear solver), and a combined approximation error due to the use of the H-matrix and the GMRes solver (for the simulations with the GMRes solver). It can be seen that the approximation error due to the use of the GMRes solver is negligible in comparison to the approximation error due to the H-matrix approximation itself, in this example.
- Fig. 2.37 shows the number of the GMRes iterations used in the simulations. It is seen that with the H-LU preconditioner, the GMRes converges within a few iterations for moderate numbers of degrees of freedom. For the GMRes-HLU simulations with the two largest numbers of the degrees of freedom, the solution may have not converged since the GMRes reached the maximum preset number of iterations, 10^3 . The number of iterations with the Jacobi preconditioner steadily grows as the size of the linear system grows. However, simulations with the Jacobi preconditioner were only run with moderate numbers of degrees of freedom, due to the memory limit and a large computational time required for larger numbers of the degrees of freedom.
- Fig. 2.38 shows the total solver time and the time spent for preconditioner creation. For this example, the solutions with the H-matrix and the GMRes solver with the H-LU preconditioner took similar times as the solutions with the H-matrix and the direct linear solver, except for those simulations in which the GMRes reached the maximum number of iterations. For the largest numbers of degrees of freedom, for which the GMRes may have not converged, the solution with the H-matrix and the direct linear solver is the fastest.
- The GMRes simulations with the Jacobi preconditioner took more time than the GMRes simulations with the H-LU preconditioner, for this example.

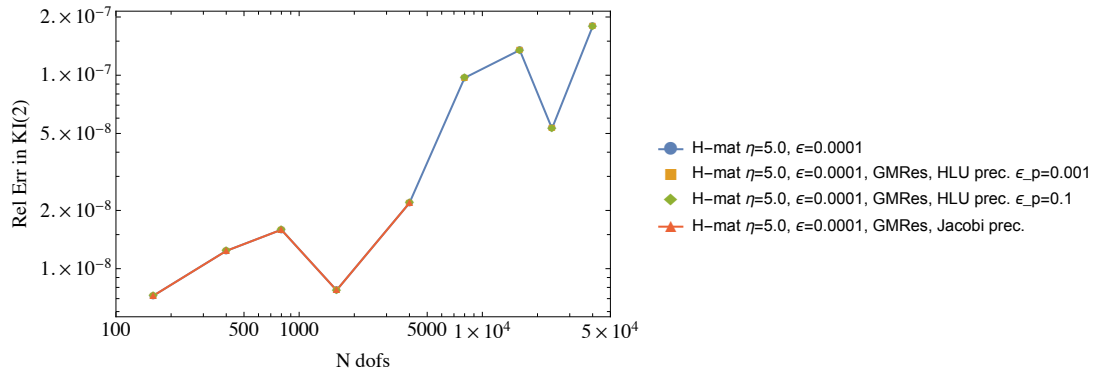


Figure 2.36: Two parallel cracks ($h/a = 2$, P1 elements): the relative error in $K_I^{(2)}$ with respect to the corresponding numerical value obtained with the full matrix and the same number of DOFs, vs number of DOFs. H-mat parameters (η, ϵ) are listed for each data series. The maximum leaf size for H-mat simulations was set to 32.

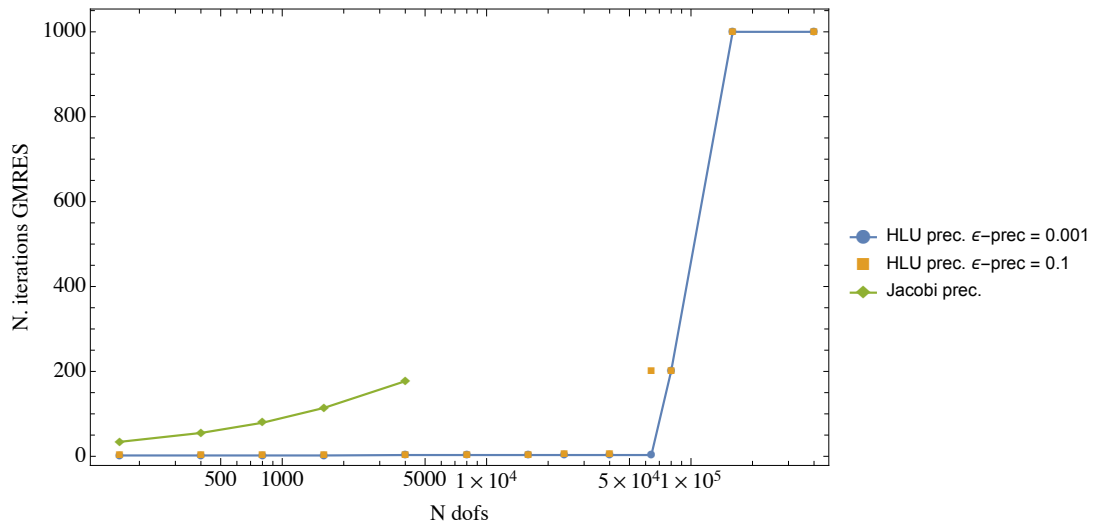


Figure 2.37: Two parallel cracks ($h/a = 2$, P1 elements): the number of iterations of the GMRes solver, vs number of DOFs. H-mat parameters were set to $\eta = 5$, $\epsilon = 10^{-4}$; the maximum leaf size was set to 32.

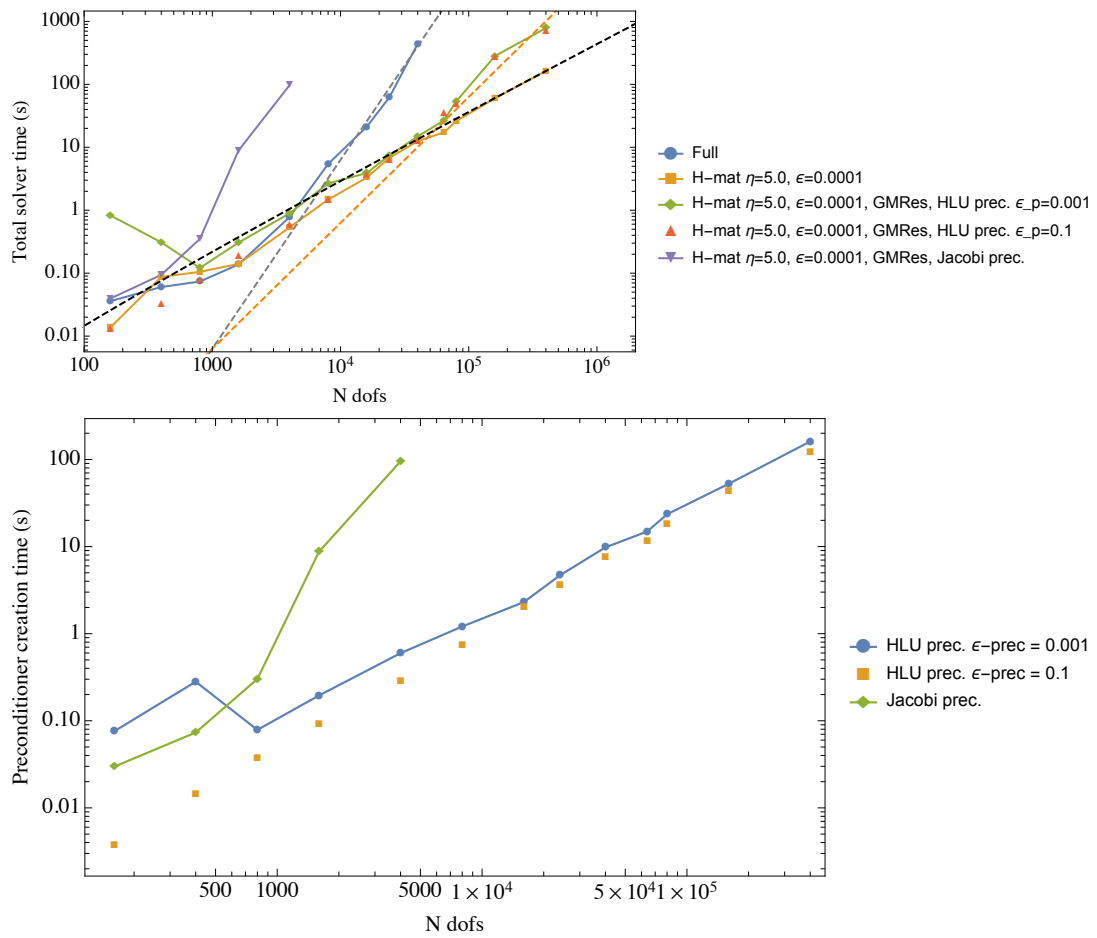


Figure 2.38: Two parallel cracks ($h/a = 2$, P1 elements): total solver cost in sec. (top), and preconditioner creation cost in sec. (bottom), vs number of DOFs. Dashed lines correspond to N^3 (gray), N^2 (orange) and $N \log N$ (black) growth rates.



2.6 Three dimensional benchmarks

In this section, we present two verification tests of our three-dimensional displacement discontinuity solver based on quadratic triangular elements. We also discuss the performance of the \mathcal{H} -matrix approximation for these two tests.

It is important to point out that the field of displacement discontinuities are interpolated by a quadratic polynomial over each element but are discontinuous between element - similar to the interpolation used in two dimensions. Although more computationally expensive, the use of piece-wise quadratic element has obvious advantage when dealing with fractures intersection. Finally, we recall that the influence integrals for such a quadratic displacement discontinuity element have been obtained analytically for isotropic material (Mogilevskaya & Nikolskiy 2014, Nikolskiy et al. 2015)- hence the numerical error is solely function of the mesh discretization and the location of the collocation points where the elasticity equation is enforced in a strong manner.

Two different benchmarks are presented: 1) a penny-shaped crack under uniform tensile loading and 2) a bowl-shaped crack under uniform normal pressure. Both tests consider a infinite linear elastic isotropic medium. The numerical and analytical solutions are compared for the crack opening displacements, the stresses ahead of the crack front and the Stress Intensity Factor.

In order to reduce its memory requirement, the coefficient matrix of the system can be replaced by its hierarchical approximation (HMat). The gain in terms of performance of memory is shown for the two benchmarks as well as the relationship between the level of approximation and the quality of the solution.

The numerical solution of the linear system can be obtained using either a direct or an iterative solver. The first employs the LU decomposition while the latter, is the generalized minimal residual method (GMRes). The convergence of this solver is accelerated by preconditioning the coefficient matrix of the system. Two preconditioners are tested: the LU decomposition of the HMat and the Jacobi preconditioner. All the numerical results that are presented below are obtained by using a GMRes with a Jacobi preconditioner because the results obtained with all these solvers are equivalent up to the chosen convergence tolerance of GMRes (10^{-12}).

2.6.1 A penny-shaped crack

2.6.1.1 Solution Verification

Fracture width For a radial planar (penny-shaped) crack of radius R , loaded with an uniform pressure p , the crack width w , equal to the normal displacement jump d_n , is given by (Sneddon, I. N. 1946, Green & Sneddon 1950):

$$\frac{E'}{pR}w(r) = \sqrt{1 - \left(\frac{r}{R}\right)^2}$$

where $E' = E/(1 - \nu^2)$ is the plane strain Young's modulus, E is the Young's modulus, ν is the Poisson's ratio and r is the radius of the computational point at which the crack width is computed.

We present first the numerical solution for the crack opening obtained with non structured mesh made of 1276 elements. Figure 2.39 shows the comparison between the numerical and analytical solutions as a function of the normalized distance x/R from the crack front. For $x/R \rightarrow 0$ the analytical solution is zero while its derivative is singular of order $O(1/\sqrt{x})$. The quadratic interpolation of the displacement discontinuities over the element at the front can not capture such singularity in the first derivative and this results in a larger error also in the crack opening. For $x/R \rightarrow 1$, the analytical solution and its derivative are finite and numerical solution show the same behaviour (w_{center} is the crack width at the center of the domain).

2.6.1.2 Mesh Refinement

A better description of the elastic field closer to the crack front can be reached by refining the mesh. We compare in Fig. 2.40 the solution for the crack opening for two distinct unstructured meshes: i) a mesh with a uniform mesh size and ii) a mesh with a refinement near the crack front. The two meshes have

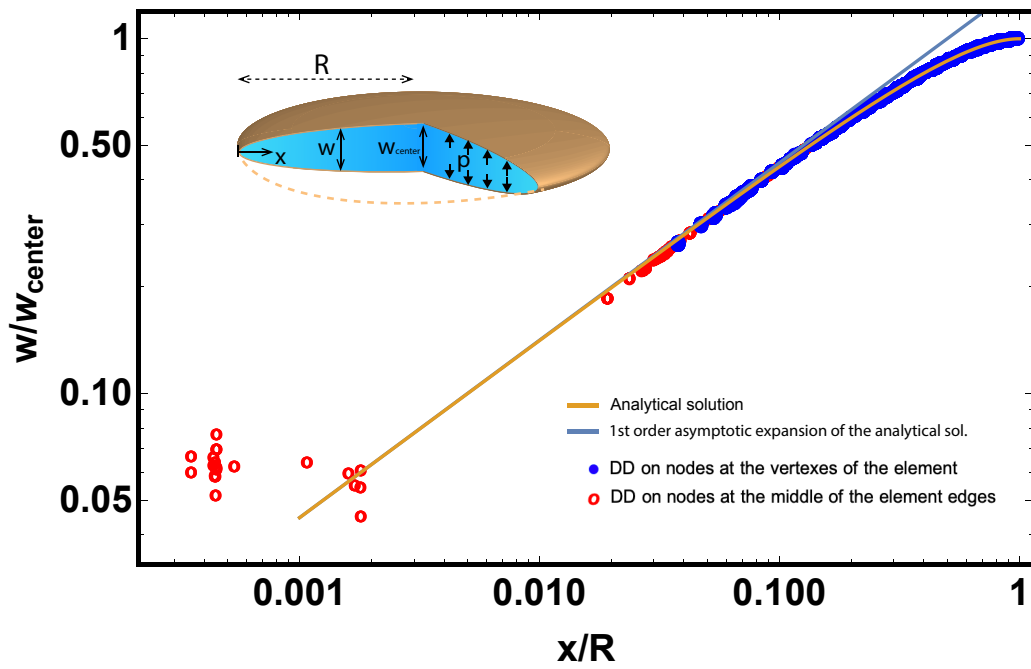


Figure 2.39: Penny-shaped crack example: normalized crack width w/w_{center} , as a function of the normalized distance from the crack front x/R . The continuous orange curve represents the analytical solution. The blue line represents its asymptotic expansion for $x/R \rightarrow 0$.

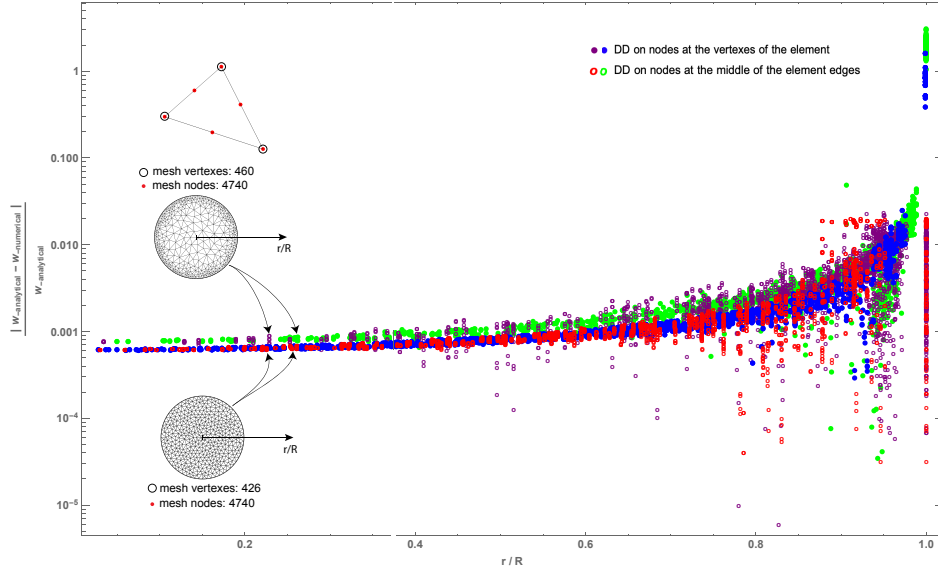


Figure 2.40: Penny-shaped crack example: relative error of the crack width, obtained using a uniform and a non-uniform mesh refined at the crack front. The size of the linear system is the same for both meshes

the same total number of unknowns (14220) but have different number of vertices. We do not see the benefit of using a refined mesh near the crack front - for the same number of unknowns, except for a slightly lower relative error near the crack front.

Stresses ahead of the crack tip The numerical solution for the stresses has been verified against the analytical solution in the surrounding of the crack (Green & Sneddon 1950). The relative error for the stress component σ_{xx} is computed at a series of points. These observation points are located along a line ahead of the crack tip. Their positions are represented by blue dots in Figure 2.41a. The results are shown in Figure 2.41b. The reference system is such that the z axis is orthogonal to the crack plane and the y axis is parallel to the axis r/R in the Figure 2.41 b). The analytical solution in terms of stresses is singular at the crack front and the relative error is increasing as it approaches $r/R = 0$ in the reference system to the Figure 2.41b. The vertical lines in Figure 2.41 b) are placed at the normalized distances S_r and S_u from the front. Considering as “element at the front” each element that have two vertices at the front, we estimate the size of each of them as the difference between the radial position of the node not at the front and the radius R of the crack. After normalization with the crack radius, we take the average value between all the elements at the front. For the refined mesh at the front such a value is $S_r = 0.047$ and for the uniform mesh $S_u = 0.082$ (2.41b). The figure shows that the mesh refined at the crack front provides a slightly less error closer to the crack front while the uniform mesh has a slightly lower error for $r/R \gtrsim S_u$.

2.6.1.3 Efficiency of the \mathcal{H} -matrix approximation

Numerical solutions are obtained using a series of unstructured uniform meshes shown on the Figure 2.43. The elastic parameters used are $G = 1000$ (shear modulus) and $\nu = 0.1$ and a crack radius $R = 1.5$. The \mathcal{H} -matrix parameters $\varepsilon = 10^{-5}$ (and a max_leaf_size of 500 to construct the cluster tree) has been used for all the simulations whereas the admissibility parameter η has been varied. Figure 2.44 a) shows the compression ratio achieved for each simulation vs. number of degrees of freedom. The larger η , the lower the compression ratio, e.g. the lower is the memory requirement for the storage of the system

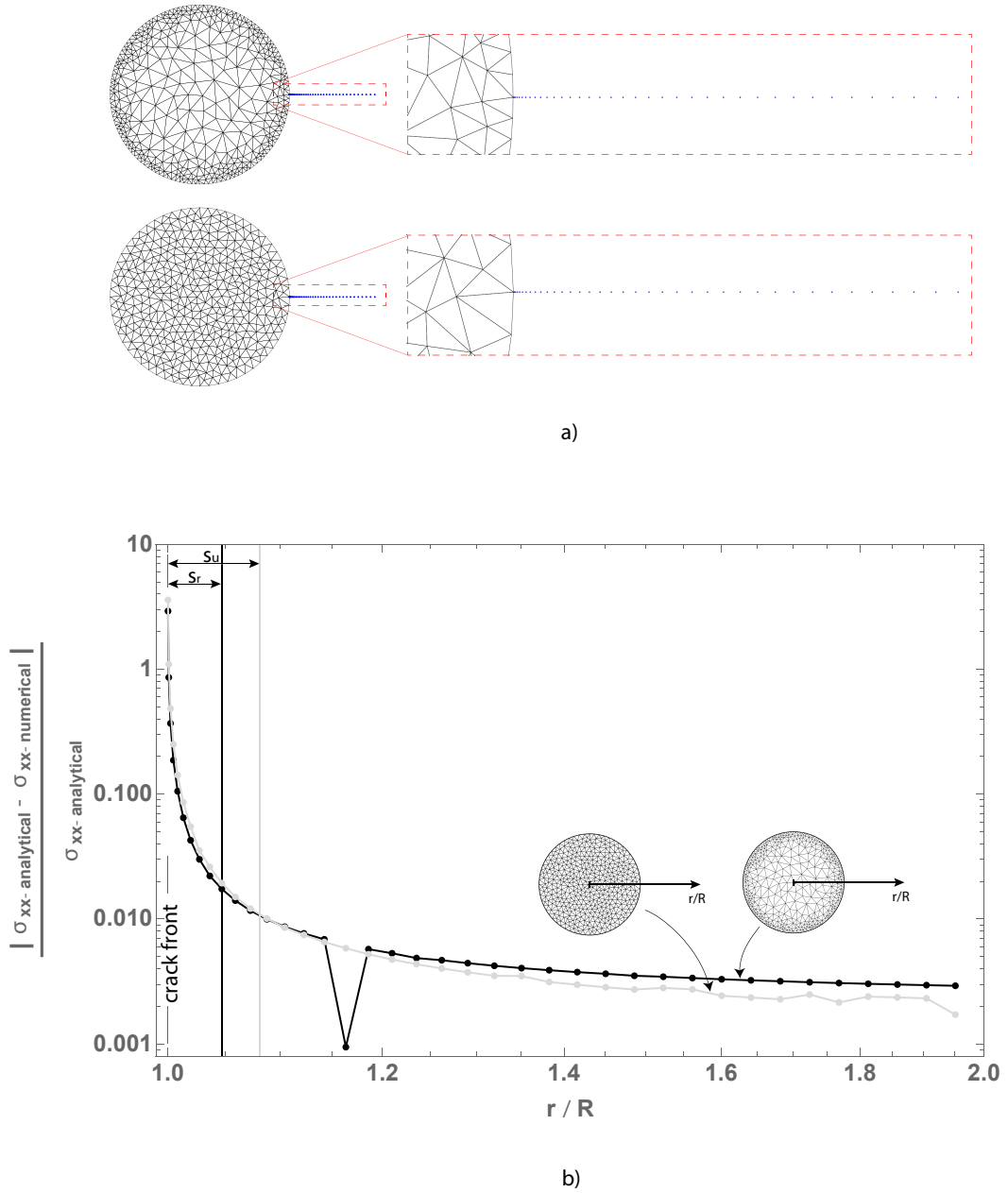


Figure 2.41: Penny-shaped crack example: The location of the observation points at which the stresses are estimated is equal for the two meshes and they are displayed by blue dots. a) Relative error for the stress component σ_{xx} (compared against the analytical solution of Green & Sneddon (1950)) for the two unstructured meshes considered previously. b) The values S_1 and S_2 are the average size of the elements at the front.

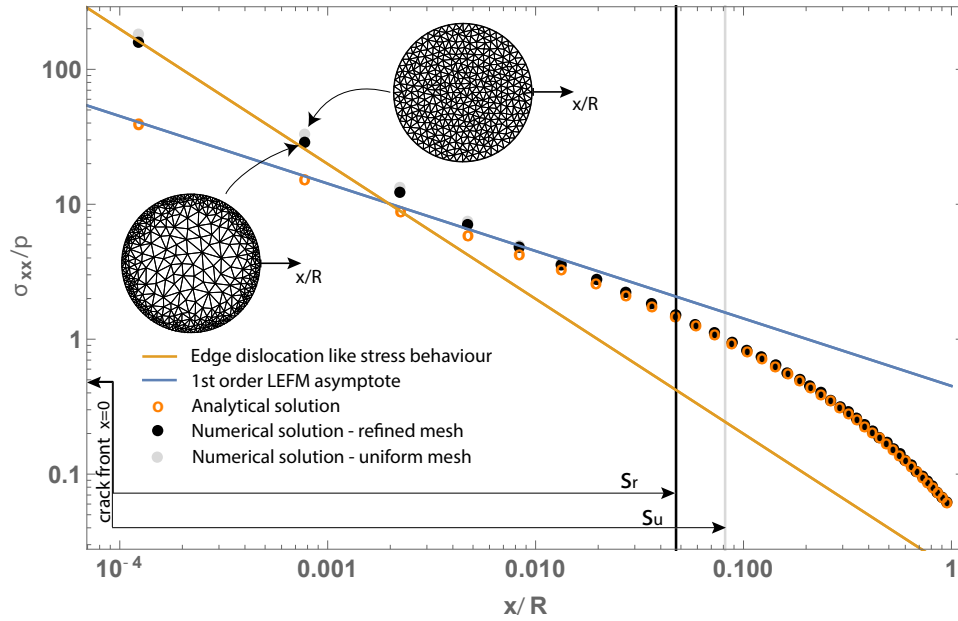


Figure 2.42: Penny-shaped crack example: Normalized stresses σ_{xx}/p ahead of the crack front are compared against the analytical solution of Green & Sneddon (1950). The stresses are computed at the same locations ahead of the crack tip for an uniform mesh and a refined mesh. The two meshes have the same number of unknowns.

of equations. On the other hand, a larger value of η leads to a coarser approximation of the boundary integral equations. It is important to control quantitatively how η affects the accuracy of the solution. Figure 2.44 b) and c) are showing respectively the L2 norm of the absolute error in the crack width and the relative error of the Stress Intensity Factor (SIF) K_I . The first is computed as follows:

$$L_2 (\text{Relative error on } w) = \frac{1}{\sum_{p=1}^{NoP} p} \sqrt{\sum_{p=1}^{NoP} \left(\frac{w_p - w_{analytical}}{w_{center}} \right)^2}$$

where NoP is the total number of nodes, $NoP = 6 NoE$, (NoE is the total number of elements). The mode I SIF is computed using the asymptotic solution for the crack width at the crack front:

$$w(r) = \left(\frac{32}{\pi} \right)^{1/2} \frac{K_I}{E'} \sqrt{R-r} \quad R-r \ll 1$$

Then the mode I SIF is obtained from the crack width near the crack front as:

$$\left(\frac{32}{\pi} \right)^{1/2} K_I = \lim_{r \rightarrow R} \frac{w(r) E'}{\sqrt{R-r}} \approx \frac{w_p(r) E'}{\sqrt{R-r_p}}$$

where r_p is the orthogonal distance from the designated node p to the front, w_p is the numerical nodal value of the crack width. The optimal position of p is a-priori unknown. The asymptotic solution suggest that p should be chosen as the limit at the crack front. However, the closer is the point to the front, the higher is the error on w_p . If p is chosen as the barycenter of the triangular element, as for the triangle IJK in figure 2.45 the estimation of K_I is affected by the higher error of the solution at the front. A better estimation is achieved by choosing the node for the estimatio of K_I as the node the of the element the furthest away from the front. Figure 2.45 shows the chosen node and the chosen distance to the front for elements ELF, ELH, and ABC respectively. Finally, for a given mesh the relative error of K_I is computed as follows:



$$\max \left\{ \frac{w_p(r) E'}{\sqrt{R - r_p}} \sqrt{\frac{\pi}{32}} - K_{I-\text{analytical}} \right\}$$

where:

$$K_{I-\text{analytical}} = 2p \sqrt{\frac{R}{\pi}}$$

Figure 2.44d shows that by increasing the number of unknowns (N) as well as η , the creation time of the H matrix approximation follows the $N \log(N)$ asymptote while for small values of N or for small values of η , the complexity is $\mathcal{O}(N^2)$ and the time needed for solving the linear system is shown in Figure 2.44e. This result show that one can use a large value of η (e.g. $\eta = 10$) without any reduction in the accuracy of the numerical solution. Beside the reduction in memory requirements, the computational cost is also reduced.

2.6.2 A bowl shaped crack

We now turn to the case of a non-planar 3D crack. Although under uniform pressure, this example activate elastic coupling between shear and normal displacement discontinuities.

2.6.2.1 Solution Verification

A bowl-shaped crack of radius $R = 1.5$ and $\alpha = 60^\circ$ (see 2.46) has been discretized with 890 triangular elements, leading to a final system of 14760 unknowns. The parameters that characterize the isotropic linear elastic medium are taken as $G = 1000$ (Shear modulus) and $\nu = 0.1$. The crack is subjected to a uniform unit pressure. The solution has been compared against a numerical solution obtained with an axisymmetric displacement discontinuity code (Gordeliy & Detournay 2011). The comparison between the analytical and numerical solution in terms of crack opening is shown in Figure 2.47 while Figure 2.48 shows the the relative difference of the opening as a function of the distance r from the center of the crack. The relative difference is larger at the crack front because the mesh is relatively coarse and the aspect ratio of some of the triangle is large (see Fig. 2.46b).

2.6.3 Summary

The two verification examples presented above validate the (very) good accuracy of our three dimensional elastic solver for fracture. We also see the benefit in term of computation cost of using a \mathcal{H} -matrix approximation. It is important to point out that all the simulations reported above have been performed on a laptop with 8Gb of RAM (mac book Pro late 2017).

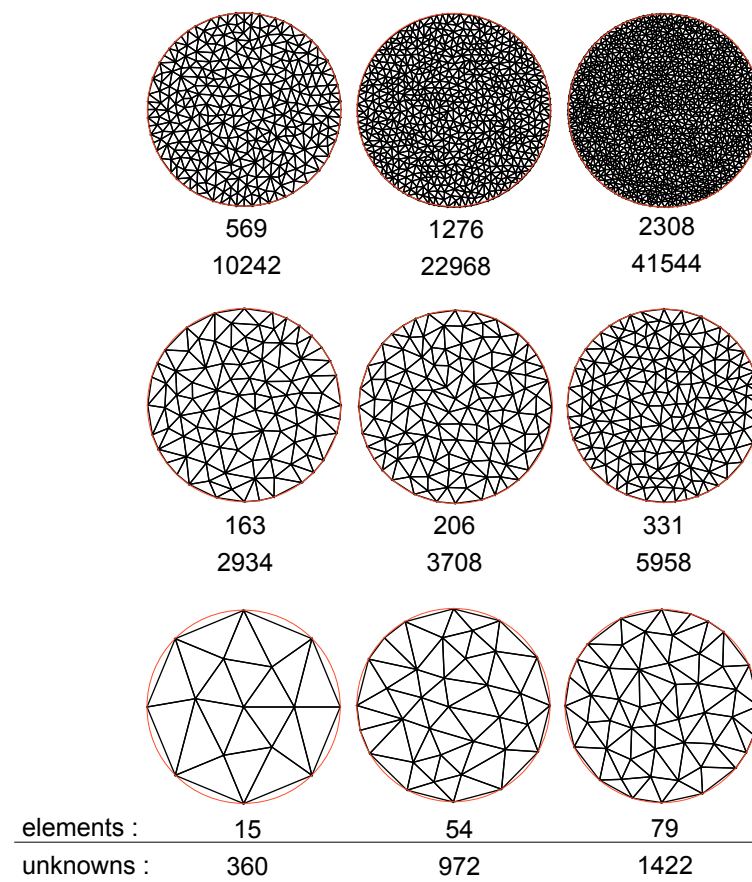


Figure 2.43: Penny-shaped crack example: series of uniformly unstructured meshes with increasing resolution (from bottom to top).

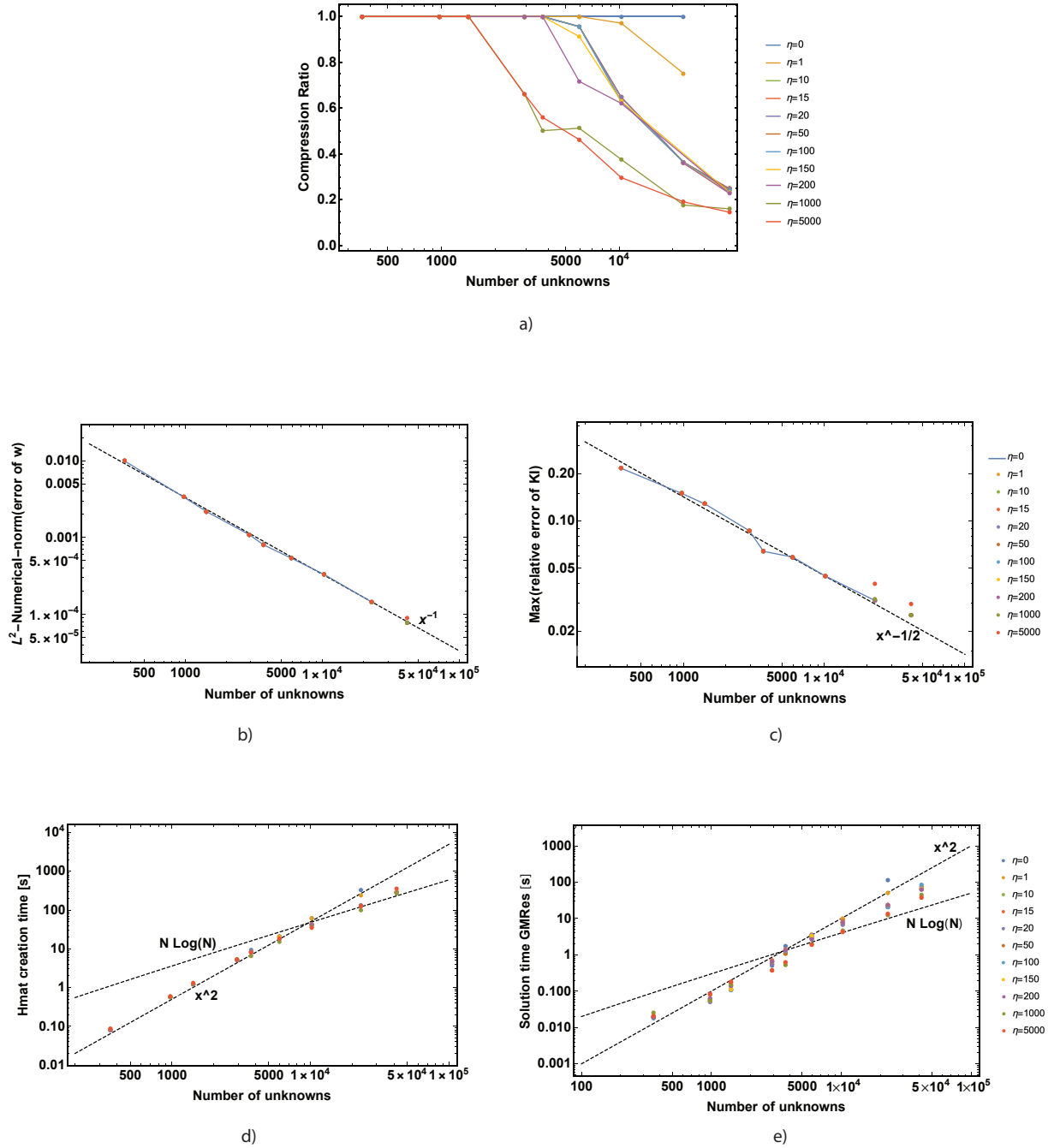


Figure 2.44: Penny-shaped crack example: a) Compression ratio of the hierarchical matrix, b) L_2 numerical norm of the absolute error of the crack opening w , c) maximum relative error on the SIF K_I , d) \mathcal{H} -matrix creation time vs. number of unknowns, e) time required for the solution of the linear system using GMRes. Results for different number of unknowns (see Fig. 2.43 for the different meshes), and different values of the admissibility condition parameter η .

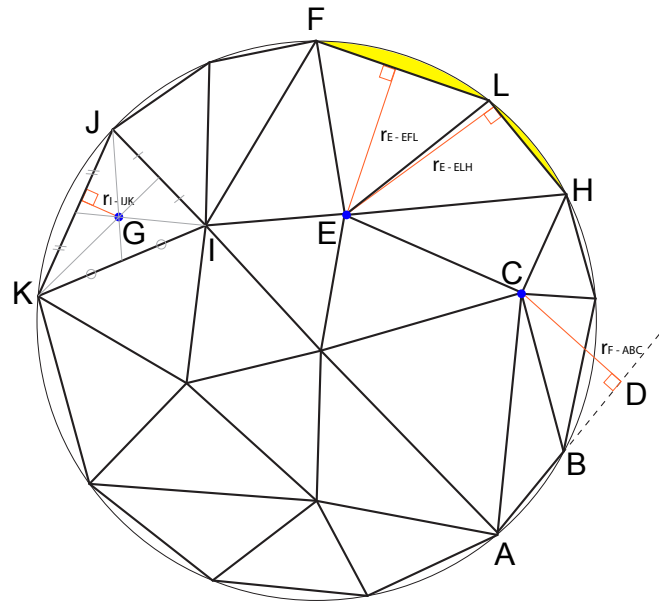


Figure 2.45: Mesh of a radial crack. The error due to the discretization of the geometry is shown in yellow for elements EFL and ELH. The computation of K_I is done for each element at the crack front (e.g. each element with two nodes at the front). The distance from the designated point used for computing K_I is taken orthogonal to the edge at the front. This will lead to 2 different values of K_I for elements EFL and ELH. The distance from point E to the front and the crack opening at this point lead to a better estimation of the Stress Intensity Factor K_I than the same quantities evaluated at the barycenter of each element (e.g. point G for the triangle IJK). Elements with large aspect ratio (e.g. element ABC) should be avoided.

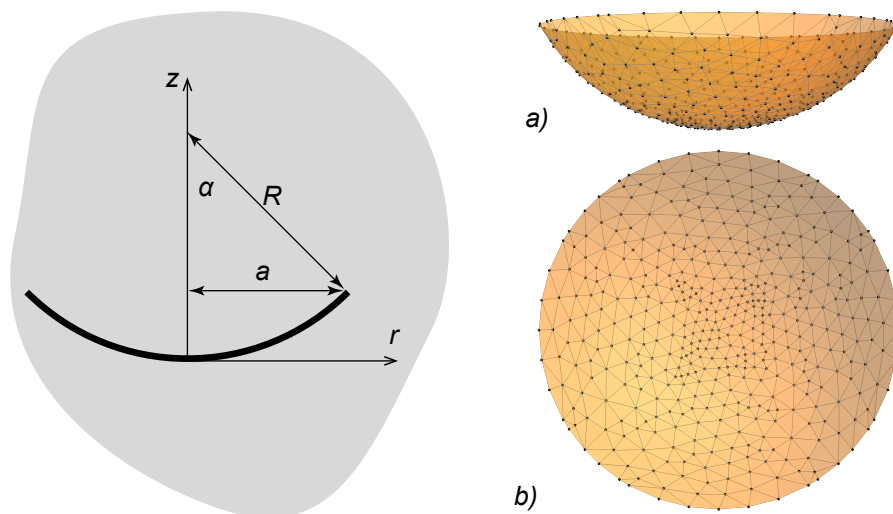


Figure 2.46: Cross-section of a bowl-shaped crack in an infinite space (left), a) lateral view and b) top view of the discretized bowl-shaped crack.

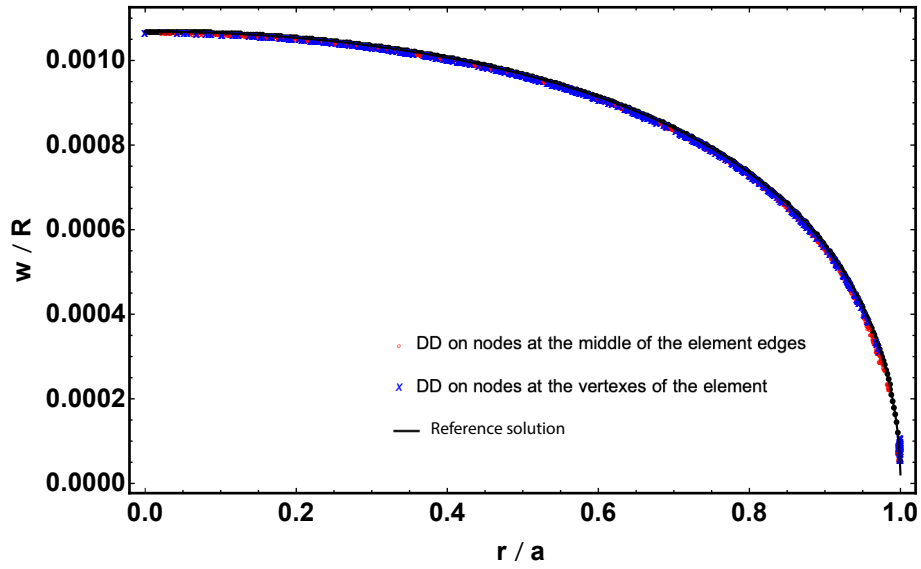


Figure 2.47: Bowl-shaped crack example: comparison of the crack normal opening w scaled with the crack radius R with a numerical solution obtained with an axisymmetric Displacement Discontinuity code (Gordeliy & Detournay 2011).

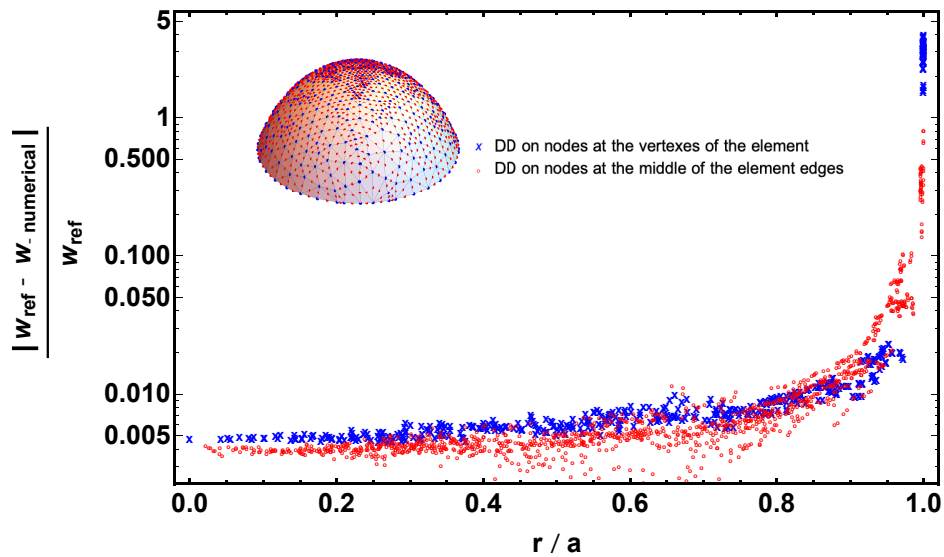


Figure 2.48: Bowl-shaped crack example. Relative difference between the crack widths w obtained with the axisymmetric displacement discontinuity code of Gordeliy & Detournay (2011) and the present code Hfp-3D.



Chapter 3

Hydro-mechanical behavior of fractures

Convention

It is important to recall that if the stresses are taken positive in tension, the displacement discontinuity d_i are then positive in overlap ($d_i = u_i^- - u_i^+$) in the elasticity equation. On the other hand, if the stresses are taken positive in compression, the displacement discontinuity d_i is then positive in opening ($d_i = u_i^+ - u_i^-$). We use this second convention in the subsequent section: stress positive in compression and displacement discontinuity positive in opening (and the shear displacement discontinuity is positive in a clock-wise rotation). Moreover, in some cases, we will use the following notation for the normal and shear components of traction and displacement discontinuity:

$$\begin{aligned} t_n &= \sigma & t_s &= \tau \\ d_n &= w & d_s &= \delta \end{aligned}$$

3.1 Mechanical behavior of joint/fracture interface

3.1.1 Kinematics description

We do not model the micro-scale details of the interface (surface roughness), the macroscopic kinematic variable is locally the displacement discontinuity

$$d_i = u_i^+ - u_i^-$$

taken positive in opening. Such a displacement jump can be taken from the mid-plane of the top and bottom fracture surfaces (which may exhibit roughness). Contact will therefore first occur between the top and bottom asperities when d_n has a positive (albeit small) value - i.e. $w_{c,m}$.

The (Signorini) contact conditions can thus be written as: [We need to choose another notation than w_c - to differentiate with critical width during debonding]

$$d_n - w_c \geq 0 \quad t'_n \geq 0 \quad (d_n - w_c)t'_n = 0$$

However, when in contact, under increasing compressive stress, the fracture / joint close further. In lab experiments of joint closure, a non-linear relation between joint closure, i.e. w_c and effective normal stress is typically observed. This can be accounted for via making the fracture closure w_c decreases from its initial (maximum) value $w_{c,m}$ when the asperities becomes first in contact to zero at infinitely large compressive effective normal stress.

Note that such a “closure” below $w_{c,m}$ is somehow reversible upon reversal of effective normal stress - hence the idea to treat the closure / contact behavior via a non-linear spring. This choice is prominent in the rock mechanics literature. However, there seems to be confusion with respect to the initial opening



of the joint - and some authors do appear to allow for a degree of interpenetrability - i.e. letting d_n to become slightly negative and contact to be activated at $d_n = 0$ (somehow taking the distance between the greatest asperities of the 2 surfaces to define the displacement jump).

Here, to be consistent with a flow model within the fracture and associate permeability change with d_n , we do not allow for any interpenetrability - i.e. $d_n \geq 0$ but do activate contact when $d_n = w_{c,m}$ upon closure. Moreover $w_{c,m}$ may be taken as a history variable dependent on how the fracture was created (and may have evolved). Notably for fresh / new fractures $w_{c,m}$ should follow the maximum opening displacement below encounter during decohesion and be equal to w_c at full de-cohesion.

3.1.2 Behavior when in contact

The contact is therefore first obtained when $d_n = w_{c,m}$, then d_n can fall all the way to zero (but can not become negative). The effective normal/contact stress (pressure) is then necessarily compressive.

Most if not all joint/fracture model in the literature account for both a elastic \dot{d}_i^e (often non-linear) deformation of the fracture (under compressive stress) and inelastic/slip deformation¹. Such models are typically developed to formulate joint element in finite element code, the rate of the displacement discontinuity vector \dot{d}_i is decomposed in an elastic and “slip” component (which will be related to slip and dilatancy linking to Mohr-Coulomb frictional contact):

$$\dot{d}_i = \dot{d}_i^e + \dot{d}_i^s$$

and the rate of effective contact traction are related to the rate of dd

$$\dot{t}'_i = -\mathbf{D}\dot{d}_i^e \quad \mathbf{D} = \begin{pmatrix} k_s(t'_n) & 0 \\ 0 & k_n(t'_n) \end{pmatrix}$$

where the minus comes from the convention of positive DD in opening, and positive stress in compression, such that an increase in compressive stress results in a decrease of the displacement discontinuity (i.e. the displacement discontinuity goes into overlap). The normal stiffness is highly normal effective stress dependent, and a well accepted model is due to Bandis et al. (1981), Nguyen & Selvadurai (1998)

$$k_n = k_{ni} \left(\frac{k_{ni}w_{c,m} + t'_n}{k_{ni}w_{c,m}} \right)^2$$

where $w_{c,m}$ is the maximum fracture closure and k_{ni} the stiffness at zero effective normal stress. For uncorrelated fracture, the evolution of stiffness appears linear with t'_n instead of quadratic (Cornet 2015b, Bandis et al. 1983). Similarly, the shear stiffness k_s is also function of effective tractions - typically shear stiffness is much lower than normal stiffness at low effective stress, and becomes of the same order at large compressive effective stress.

It is important to note that these contact stiffness tends to zero when contact is “lost” i.e. when $d_n > w_{c,m}$ and $t'_n \leq 0$

3.1.2.1 Frictional slip

When in contact, where

$$d_n \leq w_{c,m} \quad (d_n \geq 0) \quad t'_n > 0$$

Frictional slip can occur. We use a Mohr-Coulomb criteria for the onset of non-reversible slip

$$F_2(t_s, t'_n) = |t_s| - c(\kappa, \kappa_m) - f(\eta, \eta_m)t'_n \leq 0$$

where typically for pre-existing joint / fractures in contact, cohesion is null. Using a non-associative flow rule in order to account for a dilation angle lower than the friction angle (as typically observed), one has if $F_2 = 0$

$$\dot{d}_s^s = \lambda \times \text{sign}(t_s) \quad \dot{d}_n^s = \lambda \tan \psi(\eta)$$

¹The term elastoplastic is not appropriate for frictional contact as shear slip is reversible via load reversal.



and we can write $\lambda = |\dot{d}_s^s|$. Note that $F_2|\dot{d}_s^s| = 0$ (i.e. if $|\dot{d}_s^s| > 0$, $F_2 = 0$ and if $F_2 < 0$ then $|\dot{d}_s^s| = 0$). and the “consistency condition”

$$\dot{F}_2|\dot{d}_s^s| = 0$$

which states that if $|\dot{d}_s^s| > 0$ then the state of traction remains on the yield surface.

3.1.3 Cohesive failure of potential ‘slip’ lines / fractures

Note that in the following, we neglect elastic deformation of the fracture and write \dot{d}_i^s instead of \dot{d}_i .

3.1.3.1 Constitutive relations for the displacement discontinuity locus

Our aim is to combine Coulomb friction on pre-existing fractures with the possibility of having the creation of new fractures using a mixed mode cohesive zone type approach. For quasi-brittle materials like rocks, the energy dissipation associated with the creation of new fractures surfaces or frictional weakening tend to concentrate in a narrow region (process zones) - such processes are often modeled by reducing the process zone to a surface where displacement discontinuity are permitted and a softening traction-separation law constitutively relates traction to displacement discontinuity. Such a cohesive zone approach is very popular in fracture mechanics in both mode I and II (Barenblatt 1962, Dugdale 1960, Elices et al. 2002, Needleman 2014, Camacho & Ortiz 1996, Snozzi & Molinari 2013). In parallel, frictional contact laws (with or without associated dilatancy, with or without softening) are also commonly used (Ida 1972, Palmer & Rice 1973, Maier et al. 1993, Plesha et al. 1989, Carol et al. 1997, Stupkiewicz & Mróz 2001).

Here, in the context of the displacement discontinuity methods, we use a cohesive interface “yield” criteria combining a Mohr-Coulomb criteria with a tensile cut-off - allowing for softening/hardening - expressed in terms of the effective normal $t'_n = t_n - p$ and shear t_s tractions acting on the displacement discontinuity segment:

$$F_1(t_s, t'_n) = -\sigma_c(\kappa, \kappa_m) - t'_n \leq 0, \quad F_2(t_s, t'_n) = |t_s| - c(\kappa, \kappa_m) - f(\eta, \eta_m)t'_n \leq 0, \quad (3.1)$$

where $f(\eta, \eta_m)$ is the friction coefficient function of a softening variable η (and its maximum value obtained during the loading history η_m), $\sigma_c(\kappa, \kappa_m)$ and $c(\kappa, \kappa_m)$ are the tensile strength and cohesion respectively, both function of another softening variable κ (and its maximum value obtained during the loading history κ_m). A graphical Mohr-like representation of such yield criteria is given in Figure 3.1.

In order to define uniquely which yield function the tractions must satisfy in the vicinity of the corner point ($F_1 = F_2$) of this composite yield surface, we introduce a function $h(t_s, t'_n)$ in the traction space (see Figure 3.1) defined as (e.g. following an approach to the one used in Flac Itasca Consulting Group (2010))

$$h(t_s, t'_n) = |t_s| - \beta\sigma_c(\kappa) - \alpha^c(\eta)(\sigma_c(\kappa) + t'_n), \quad (3.2)$$

where $\beta\sigma_c$ and $\alpha^c(\eta)$ are two scalars (which evolve with softening) defined as

$$\beta\sigma_c = c(\kappa, \kappa_m) - f(\eta, \eta_m)\sigma_c(\kappa, \kappa_m)$$

$$\alpha^c(\eta) = \sqrt{1 + f(\eta, \eta_m)^2} - f(\eta, \eta_m)$$

In the case where the trial tractions violate both criteria simultaneously ($F_1(t_s, t'_n) > 0$ and $F_2(t_s, t'_n) > 0$), tensile failure ($F_1 = 0$) is chosen to occur if $h(t_s, t'_n) < 0$ while shear failure ($F_2 = 0$) is chosen if $h(t_s, t'_n) > 0$. Note that if $h(t_s, t'_n) = 0$, we enforce both criteria and compute the corresponding shear and opening displacement. Importantly, in the case where the cohesion and tensile strength are equal to zero, then we strictly enforce both criteria $F_1 = F_2 = 0$ and let both shear and normal displacement discontinuity evolves to ensure zero shear and normal effective stress.

Another simpler choice to choose which criteria to use is to simply to always enforce tensile failure if $F_1(t_s, t'_n) > 0$ and $F_2(t_s, t'_n) > 0$.

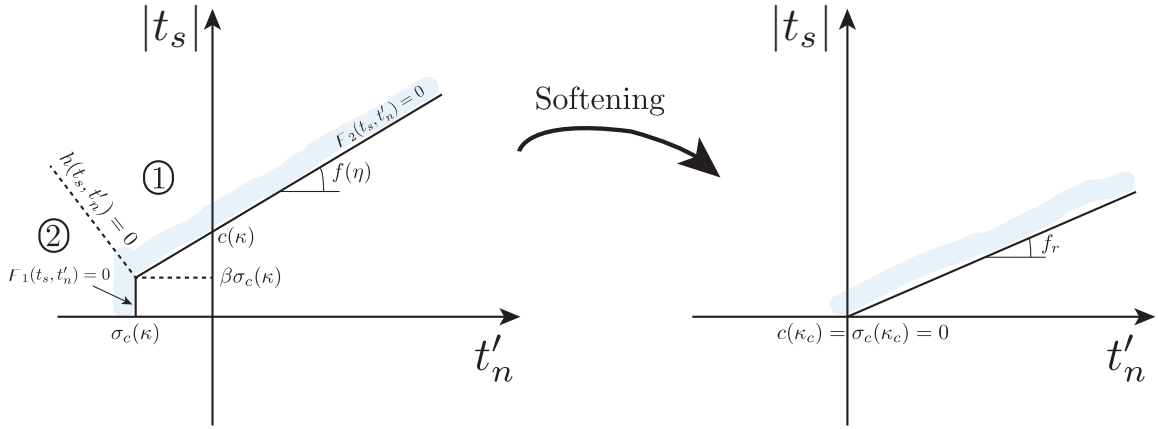


Figure 3.1: Yield limit composed of a cohesive-frictional line and a tensile cut-off (left). After ultimate softening, the interface is purely frictional (zero cohesion/tensile strength) with a residual friction coefficient (left).

Evolution of displacement discontinuities

Mode I prior complete softening If $F_1 > 0$, we must enforce $F_1(t_s, t'_n) = 0$, using the concept of an associate flow rule - but allowing for crack unloading/closure, we obtain the following constraints in the case where the *sole* mode I criteria is active:

$$F_1 = 0 \quad |\dot{d}_n| \geq 0 \quad |\dot{d}_s| = 0 \quad (3.3)$$

which just state that if $F_1 = 0$, the interface can open or close $|\dot{d}_n| > 0$, but the rate of shear displacement discontinuity is zero. Moreover, if $F_1 = 0$, we also write a consistency condition $\dot{F}_1|\dot{d}_n| = 0$ stating that if $|\dot{d}_n| > 0$, the traction state should remain on the yield surface F_1 , while if the traction moves away from the yield surface one has $|\dot{d}_n| = 0$. It is important at this stage to note that the evolution of the critical tensile strength with softening variable will in fact dictate a traction separation law as $F_1 = 0$ imply $t'_n = -\sigma_c(\kappa, \kappa_m)^2$. In fact, the evolution of $\sigma_c(\kappa, \kappa_m)$ will model both softening and reversible unloading /re-loading when $\kappa < \kappa_m$. The simplest evolution of σ_c is one of linear softening from $\kappa = 0$ to κ_c , and a linear reversible unloading/reloading branch, i.e.:

$$\frac{\sigma_c(\kappa, \kappa_m)}{\sigma_{c,p}} = \begin{cases} 1 - \kappa/\kappa_c & \kappa < \kappa_c \text{ \& } \kappa = \kappa_m \\ (1 - \kappa_m/\kappa_c)\kappa/\kappa_m & \kappa < \kappa_c \text{ \& } \kappa < \kappa_m \\ 0 & \kappa \geq \kappa_c \end{cases} \quad (3.4)$$

where κ_m correspond to the maximum value of the internal softening variable κ , and κ_c is a critical value above which the tensile strength is zero. $\sigma_{c,p}$ correspond to the initial / peak tensile strength. In the pure mode I case, κ is typically taken as the opening displacement discontinuity (Another less common choice is the accumulated irreversible work (Carol et al. 1997)). Such a simple linearly softening traction separation law is often used in cohesive zone models.

Mode I at full softening: corner mode It is important to point that if the tensile strength and the cohesion is zero, if both yield criteria are active, then one must set

$$F_1 = 0 \quad |\dot{d}_n| \geq 0 \quad F_2 = 0 \quad |\dot{d}_s| \geq 0 \quad (3.5)$$

²the minus sign is due to convention of positive stress in compression



Mode II / frictional In this case where the trial state may exhibit $F_2 > 0$, the softening Mohr-coulomb model must be enforced $F_2(t_s, t'_n) = 0$. Similarly, accounting for the fact that the dilation angle is typically less than the friction angle, using the concept of a non-associated flow rule for dilatancy, we obtain the following constraints

$$F_2 = 0 \quad |\dot{d}_s| > 0 \quad |\dot{d}_n| = |\dot{d}_s| \tan \psi(\eta) \quad (3.6)$$

which just state that if $F_2 = 0$, the interface will exhibit shear slip and an associated dilation. Similarly if $F_2 = 0$, we also write a consistency condition $\dot{F}_2 |\dot{d}_s| = 0$ stating that if $|\dot{d}_s| > 0$, the traction state should remain on the yield surface F_2 .

Softening First, let's assume the case of a constant friction coefficient and focus on the softening of cohesion. The simplest choice is to evolve the cohesion in a similar way than the tensile strength, i.e. keeping the ratio c/σ_c constant. Such a choice makes physically sense.

$$\frac{c(\kappa, \kappa_m)}{c_p} = \begin{cases} 1 - \kappa/\kappa_c & \kappa < \kappa_c \text{ \& } \kappa = \kappa_m \\ (1 - \kappa_m/\kappa_c)\kappa/\kappa_m & \kappa < \kappa_m \\ 0 & \kappa \geq \kappa_c \end{cases} \quad (3.7)$$

where c_p is the original peak cohesion. We obtain a similar traction-separation law than a number of proposed cohesive zone models (Camacho & Ortiz 1996, Snozzi & Molinari 2013). It is important to note that under shear traction controlled loading (and constant effective normal stress), upon un-loading shear slip will revert as long as $F_2 = 0$ which will be the case until one reach $c(\kappa = 0, \kappa_m) = 0$ along the unloading branch.

Now turning to the weakening of friction, we use here a simple linear weakening of friction with the absolute value of shear slip - i.e. $\eta = |d_s|$. However, if unloading (or load reversal) occurs prior to having reaches residual friction, we assume that the friction coefficient does not further evolve if the absolute value of slip falls below the maximum experienced value of slip during the loading history $\eta_m = |d_s|_m = \delta_m$,

$$f(|d_s|, \delta_m) = \begin{cases} f_p - \frac{f_p - f_r}{\delta_c} |d_s| & |d_s| \leq \delta_c \text{ \& } |d_s| = \delta_m \\ f_p - \frac{f_p - f_r}{\delta_c} \delta_m, & |d_s| \leq \delta_c \text{ \& } |d_s| < \delta_m \\ f_r, & |d_s| > \delta_c \end{cases} \quad (3.8)$$

where δ_c is the critical length for frictional weakening which is typically in the order of the surface asperities size. More complex evolution of friction under cyclic loading have been proposed (Stupkiewicz & Mróz 2001) but are not considered here as reverseal of shear stress is unlikely to happen in geothermal reservoir. We expect that the weakening of friction occurs over a lengthscale larger than the one associated with tensile or purely cohesive shear strength κ_c . Similarly than the friction coefficient, the dilatancy angle also decreases with shear slip and goes to zero above critical slip (i.e. critical state of the surface with no more induced dilation). Here again, cyclic loading is unlikely, and we therefore use a similar law than for the evolution of the friction coefficient

$$\tan \psi(|d_s|, \delta_m) = \begin{cases} \tan \psi_p \times (1 - |d_s|/\delta_c) & |d_s| \leq \delta_c \text{ \& } |d_s| = \delta_m \\ \tan \psi_p \times (1 - \delta_m/\delta_c), & |d_s| \leq \delta_c \text{ \& } |d_s| < \delta_m \\ 0 & |d_s| > \delta_c \end{cases} \quad (3.9)$$

Arguably, one expectes a reversal of dilation upon slip reversal - which is not captured by the evolution chosen here (see Stupkiewicz & Mróz (2001) for more discussion).

Softening variable κ The softening variable κ reduces either to d_n respectively $|d_s|$ in pure mode I, respectively mode II. In mixed mode, the normal and shear displacement discontinuity are combined

$$\kappa = \sqrt{\zeta^2 d_s^2 + d_n^2}$$

where ζ is a phenomological variable accounting for the relative intensity of shear and normal displacement discontinuity on softening. Physically $\zeta > 1$, such that pure shear slip more strongly reduces tensile strength and cohesion of the interface as compared as to an opening.



3.1.4 LEFM with frictional contact

In this model cohesive forces are neglected, the propagation of fractures follow the principle of linear elastic fracture mechanics combined with a Coulomb friction law for contact.

3.2 Fluid Flow in fractures

We assume that the rock matrix is much less permeable than the fractures present in the medium. The flow is thus confined inside the fractures and is akin to thin-film lubrication flow (Szeri 2010). The mass conservation can be width averaged over the “hydraulic” aperture w_h (which is equal to the fracture width when the fracture is open), one obtains

$$\frac{\partial \rho w_h}{\partial t} + \nabla_{x,y} \cdot \rho w_h \mathbf{\bar{v}} + 2\rho v_{leak} = \delta(x_{inj}) \rho Q_{inj}(t)$$

where ρ is the fluid density, $\bar{\mathbf{v}}$ the average fluid velocity across the gap, v_{leak} the rate of fluid leaking out in the matrix, Q_{inj} is the injection rate and x_{inj} the location of the injection point. The operator $\nabla_{x,y}$ is the divergence in the 2D curvilinear coordinate of the fracture surface: it reduces to $\partial/\partial x$ in 2D. Note that for a weakly compressible liquid (i.e. water in liquid form), one can use the following simplified equation of state for density in the iso-thermal case:

$$\rho \approx \rho_o(1 + \beta(p - p_o))$$

where ρ_o is the fluid density at pressure p_o and β is the fluid compressibility (i.e. in the order $5 \times 10^{-10} \text{ Pa}^{-1}$ for water). We therefore see that because pressure variation are at most in MPa, the term $\beta(p - p_o)$ is in the order of 10^{-3} . Such that $\rho \approx \rho_o$, but $\partial_t \rho = \rho_o c_f \partial_t p$ may not be necessarily negligible compared to $\rho \partial_t w_h / w_h$. On the other hand, we neglect the spatial variation of density compared to spatial variation of velocity, i.e. $\nabla_{x,y} \cdot \rho w_h \mathbf{\bar{v}} \approx \rho_o \nabla_{x,y} \cdot w_h \mathbf{\bar{v}}$, i.e. $\beta(p - p_o) \ll 1$, such that $\rho \mathbf{\bar{v}} \approx \rho_o \mathbf{\bar{v}}$ - a condition always met for liquid for which $\beta = O(10^{-10}) \text{ Pa}^{-1}$ and $(p - p_o) = O(10^6) \text{ Pa}$. Note that more generally, for closed fracture, the term β is akin to a storage coefficient of a porous material and is the sum of the pore-compressibility and the fluid compressibility times the porosity.

Neglecting leak-off in the surrounding rock mass, we therefore rewrite the width averaged isothermal conservation of mass as

$$w_h c_f \frac{\partial p}{\partial t} + \frac{\partial w_h}{\partial t} + \nabla_{x,y} \cdot w_h \mathbf{\bar{v}} = \delta(x_{inj}) Q_{inj}(t)$$

In the previous formulation, w_h is the hydraulic aperture of the fracture / fault. It is equal to the mechanical aperture when the fracture is fully open, but when the fracture is mechanically closed, a residual aperture for fluid flow still exists (related to contact between asperities). See e.g. (Witherspoon 1980) etc. In a sense, one can write:

$$w_h = w_o + w \tag{3.10}$$

with w the mechanical opening and w_o a hydraulic opening at closure, i.e. $w_o \approx O(10^{-4}) \text{ m}$.

Darcy / Poiseuille like flow Similarly, one can width averaged the momentum equation and under the assumption of small Reynolds number, for flow between parallel plates (fracture of width w , i.e. open fracture), one recover the well-known Poiseuille like law.

$$\bar{\mathbf{v}} = -\frac{w^2}{12\mu} (\nabla p + \rho \mathbf{g})$$

where \mathbf{g} is the standard Earth's gravity vector (9.8066). Note that in the case where the pore-pressure is initially under hydrostatic conditions ($p^o = -\rho g y$ in a frame where e_y is directed against the gravity vector), we can rewrite $p + \rho g \cos \alpha = p - p^o$. Similarly, if the pore-pressure is initially over-pressured



(still with a vertical gradient, i.e. $p^o = -G_p y$), assuming there is no fluid flow initially, the driving pressure gradient is also $p - p^o$. We therefore write

$$\bar{\mathbf{v}} = -\frac{w^2}{12\mu} \nabla(p - p_o)$$

A number of extension exist when the width is small and of the level of the aperture roughness. One can also generalize that law to the mechanically closed state easily by writing Darcy's law for the closed fracture / fault:

$$\bar{\mathbf{v}} = -\frac{k_f}{\mu} \nabla(p - p_o)$$

where k_f is the fracture permeability. When mechanically closed, decrease of permeability with normal stress is typically observed and is highly non-linear. It is associated with increase of contact area with closure. Similarly, shear slip along closed fracture may increase fracture permeability (or in some time decrease it). This shear-induced permeability increase is typically associated with dilatancy - while decreases is often related to compaction.

3.2.1 Permeability models

A constant fracture permeability model would be - assuming Poiseuille's law

$$k = \frac{\omega_o^2}{12}$$

where ω_o is the initial hydraulic aperture.

The fracture permeability k is known to strongly evolve as function of mechanical deformation (opening, slip etc.). The simplest model choice is to assume Poiseuille's law and use the the current width hydraulic aperture, i.e.

$$k = \frac{w_h^2}{12} \quad (3.11)$$

such that the evolution of mechanical opening are directly reflected in permeability increases. Such an approximation is clearly valid for open fractures Witherspoon (1980) - and used in all Hydraulic Fracturing simulators. For mechanically closed fracture (i.e. under compressive stress), shear-induced dilation will also increase fracture permeability. Note that for small mechanical aperture, additional "friction" is observed such that Poiseuille's law is often corrected (Zimmerman & Bodvarsson 1996, Renshaw 1995, Witherspoon 1980, Lomize 1951, Louis 1969) to lower the fracture permeability due to surface roughness.

Note that some authors takes the fracture permeability as function of effective normal stresses (usually via an decreasing exponential) for the case of mechanically closed fracture (e.g. Rice (1992a))

$$k = k_* e^{-\sigma' / \sigma_*}$$

Such a dependence can actually be recovered using a non-linear elastic relation between effective stress and opening - e.g. Bandis-type model which is valid in the realm of mechanically closed fractures e.g. Nguyen & Selvadurai (1998):

$$\sigma' = k_{ni} \frac{v}{1 - v/v_m}$$

where v denotes the fracture/ 'closure' (zero when $\sigma' = 0$) and v_m the maximum joint closure - in such a notation 'the aperture' taken from full closure is $v_m - v$, such that using the lubrication law, the fracture permeability reads

$$k = \frac{1}{12} v_m^2 \left(\frac{k_{ni} v_m}{k_{ni} v_m + \sigma'} \right)^2$$

which actually has a very similar form than a decaying exponential as can be seen on Figure 3.2.

At the current stage, we neglect mechanically the elastic joint/fracture deformation under compressive stress. We thus do not model the non-linear elastic response of the fracture/joint under closure stress,

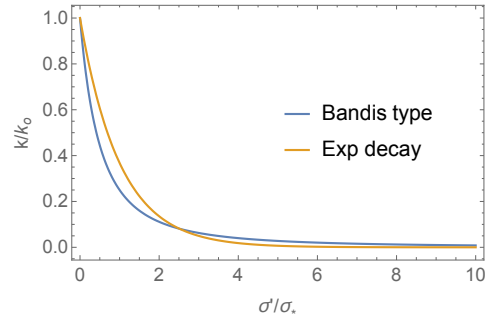


Figure 3.2: Permeability evolution with effective normal stress (case of closed fractures)- Exponential decay models (with $\kappa_o = \kappa_*$) - and Bandis type relation (with $\kappa_o = v_m^2/12$, and $\sigma_* = k_{ni}v_m$).

and as such the evolution of permeability with increasing closure stress. One possibility to account for such effect is to assimilate ω_o as $v_m - v$ and uses a Bandis-like dependence of ω_o with closure stress. Note that our numerical scheme allows for extremely strong non-linearity of permeability with opening and slip, and as such any type of law could be implemented besides eq.(3.11).



Chapter 4

One-way coupled hydro-mechanical solver for the stimulation of fractured rock mass



The upper crust of the Earth is essentially composed of fractured rock (Seeburger & Zoback 1982, Zoback 2010). A combination of chemical and mechanical processes at depth leads to a complex pattern of discontinuities. Pre-existing faults and fractures are commonly found on all scales, from microscopic scale, e.g. microfractures, to continental scale (Cornet 2015b). In the geological literature, fractures (also denoted joints) are distinguished from faults depending on the type of deformation they have withstood in the past. It is well known that the presence of these discontinuities exerts a profound effect on the physical properties of the hosting rock (Brace 1960, Hadley 1976, Budiansky B. & O'Connell R. 1976). Their presence and behavior is also of great importance for many engineering applications (e.g. deep geothermal energy extraction, hydrocarbons recovery to cite a few). We present in the following a robust numerical solver for the simulation of 2-dimensional hydraulic stimulation of fractured rock mass with the capability of accounting for a large number of pre-existing fractures, possible weakening of fracture properties with deformation, and to nucleate seismic slip. We report hereunder the details of this solver, present a number of verification tests and then discuss some preliminary simulation results for the stimulation of a randomly set of fractures in both marginally pressurized and critically stressed conditions.

4.1 Numerical solver description

This numerical solver is capable of modeling mixed mode driven fractures propagation along pre-existing cohesive material discontinuities/interfaces - either driven by fluid injection or mechanical loading. These discontinuities represent the locus of deformations (irreversible or reversible) and their positions as well as their lengths and orientations in the infinite, isotropic, homogeneous and linear elastic medium is supposed to be known a priori (through a statistical probability distribution, for instance, in the case of Discrete Fracture Network). In addition to this, we suppose the permeability of the host elastic medium is considerably smaller than the longitudinal permeability of the pre-existing discontinuities (reasonable assumption for very fine materials such as granite). As a result, fluid flow can only occur within such discontinuities (which implies that a given distribution of their initial hydraulic apertures must be known a priori).

We model the fracture(s) behavior within the framework of continuum mechanics. Stresses and deformations along such interfaces are related between each other through plane elasticity equations (see chapter 2) combined with cohesive interface constitutive laws (yield criteria - see chapter 3). This modeling perspective is valid for quasi-brittle materials (like rocks) where irreversible deformation is known to be localized in fractures and shear bands. The subsequent evolution of these fractures can be modeled using softening traction-separation constitutive laws which are valid (Maier et al. 1993).

In the following, we focus on the case of shear and opening fractures driven by fluid injection.

Upon fluid injection in a specific pre-existing discontinuity, fluid flow changes the local effective normal stress (through Terzaghi's principle). If the pore pressure increase is such to activate a crack (i.e. violating locally the fracture/joint yield criteria), then the crack starts to propagate paced by fluid flow diffusion.

In this solver, however, we assume that elastic deformations occurring during crack propagation do not affect fluid flow (i.e. fracture flow transmissivity are assumed constant), leading to a one way coupled modeling approach. Traction along pre-existing discontinuities thus change in response to i) change of far field/remote stresses, ii) stress interactions between multiple propagating fractures and iii) local changes of effective normal stress due to fluid flow.

We couple a displacement discontinuity method for elasticity with a finite volume scheme for fluid flow. Upon discretization of the pre-existing discontinuities into N_{elts} straight elements, the elasticity equations that relate tractions to displacement discontinuities reduce to a $4N_{elts} \times 4N_{elts}$ linear system of equations (for piecewise linear approximation of displacement discontinuities). Traction is expressed at collocation points, whereas displacement discontinuities are evaluated at mesh nodes (for N_{elts} finite elements, we have $N = N_{elts} + 1$ number of nodes). Fluid flow is interpolated via linear and continuous shape functions over each element. A finite volume scheme is used to solve numerically the width averaged fluid mass conservation equation. For stability issues, a backward Euler (implicit) scheme is used for time-integration.

The algorithm devised marches in time, from t^n to $t^{n+1} = t^n + \Delta t$. For sake of compactness, we use the notation of $X^{n+1} = X^n + \Delta X$ for referring to a generic time and space dependent variable $X(x, t)$ at current time t^{n+1} . Starting from a known solution at time n , the primary unknowns over a time step

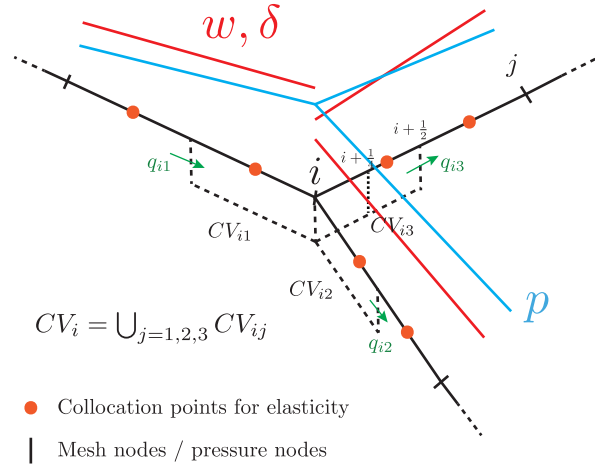


Figure 4.1: Sketch of displacement discontinuities and fluid pressure variation along three mesh elements converging in one generic node i . The former vary linearly and discontinuously between adjacent elements, whereas the latter is continuous at mesh node i . The control volume for finite volume scheme is centred at pressure node i inside which the fluid is conserved. Note that this numerical scheme can be easily extended to the case in which more than three elements intersect at node i (and obviously to the case in which only two elements converge at pressure node).

are the current pressure \mathbf{p}^{n+1} , the current tractions \mathbf{t}_i^{n+1} along the pre-existing discontinuities and the corresponding displacement discontinuities \mathbf{d}_i^{n+1} (or increment of displacement discontinuities $\Delta \mathbf{d}_i$ for incremental type of solution).

Since this hydro-mechanical numerical solver is one-way coupled, we solve first the fluid flow problem for the current pore pressure \mathbf{p}^{n+1} , and then use it to solve the mechanical problem for the corresponding current tractions and displacement discontinuities.

4.1.1 Fluid flow solver

Starting from an initial condition denoted by the subscript o , the increment of pore pressure $\Delta \mathbf{p}$ is calculated on N mesh nodes via a finite volume scheme. For sake of completeness, we recall here the discretization of the width averaged fluid mass conservation equation that govern the fluid flow within the pre-existing conductive fractures (here supposed way more permeable than the hosting rock mass). Restricting to the 2-dimensional case, the one-dimensional width averaged fluid mass conservation equation in absence of any source terms reads (see e.g. 3 for details)

$$w_h \beta \frac{\partial p}{\partial t} + \frac{\partial w}{\partial t} + \frac{\partial q}{\partial x} = 0, \quad (4.1)$$

where w_h is the fracture hydraulic width, β is the fluid compressibility, w the fracture aperture and q is the uni-dimensional Darcy's flux given by

$$q = -\frac{w_h \cdot k_f}{\mu} \frac{\partial (p - p_o)}{\partial x} \quad (4.2)$$

In equation (4.2), k_f is the longitudinal fracture permeability and μ is the fluid viscosity.

Upon discretization of the fracture with linear elements, pore pressure is supposed to vary linearly and continuously between adjacent elements, with pressure nodes located at the vertexes of the displacement discontinuity elements (see Figure 4.1).

Equation (4.1) is integrated over each control volume centred on pressure nodes (see Figure 4.1). The generic control volume centred on pressure node i is denoted as CV_i . This control volume can then



be subdivide into n_{ei} sub-control volumes, being n_{ei} the number of mesh elements connected to node i , i.e.

$$CV_i = \bigcup_{j=1}^{n_{ei}} CV_{ij}$$

Upon application of integral conservation law for CV_i combined with divergence theorem, fluid mass conservation equation reads

$$\underbrace{\int_{CV_i} \frac{\partial w}{\partial t} dx}_1 + \underbrace{\int_{CV_i} w_h \beta \frac{\partial p}{\partial t} dx}_2 + \sum_{j=1}^{n_{ei}} q_{ij} = 0, \quad (4.3)$$

where the fluxes q_{ij} entering the control volume CV_i via sub-control CV_{ij} are easily obtained from the Poiseuille law, knowing that the pressure gradient is constant over each mesh element:

$$q_{ij} = w_{h,CV_{ij}} \frac{k_{CV_{ij}}}{\mu} \frac{(p_j - p_j^o) - (p_i - p_i^o)}{h_{ij}} \quad w_{h,CV_{ij}} = (w_i + w_j)/2 \quad (4.4)$$

In equation (4.4), $w_{h,CV_{ij}}$ and $k_{CV_{ij}}$ are respectively the opening and permeability at the ends of each sub-control volume CV_{ij} , p_i and p_j are the nodal pressure values at i and j and finally h_{ij} is the euclidean distance between node i and node j . The fluxes therefore enter into each control volume from the middle of each mesh element.

When aggregating the conservation over all the control volumes (their total number coincides with mesh nodes N), the effect of fluxes entering the different control volume results in a banded matrix \mathbb{L} whose components are given by

$$\begin{aligned} \mathbb{L}_{ij}(\mathbf{w}) &= -w_{h,CV_{ij}} \frac{k_{CV_{ij}}}{\mu \cdot h_{ij}}, \quad i \neq j \\ \mathbb{L}_{ij}(\mathbf{w}) &= \sum_{j=1, \dots, n_{ei}} w_{h,CV_{ij}} \frac{k_{CV_{ij}}}{\mu \cdot h_{ij}}, \quad i = j \end{aligned} \quad (4.5)$$

In the case of one planar fracture, the matrix \mathbb{L} is a 4-banded diagonal matrix, whose size corresponds to the number of nodes in the mesh, i.e. $N \times N$. The integrals 1 and 2 of equation 4.3 over CV_i can be split over each sub-control volumes CV_{ij} , i.e.

$$\int_{CV_i} \frac{\partial w}{\partial t} dx = \bigcup_{j=1}^{n_{ei}} \int_{CV_{ij}} \frac{\partial w}{\partial t} dx \quad (4.6)$$

$$\int_{CV_i} w_h \beta \frac{\partial p}{\partial t} dx = \bigcup_{j=1}^{n_{ei}} \int_{CV_{ij}} w_h \beta \frac{\partial p}{\partial t} dx \quad (4.7)$$

By applying a Cavalieri-Simpson rule for space integration and backward Euler scheme for the time derivative (finite difference), the integral in (4.7) reduces to

$$\int_{CV_{ij}} w_h \beta \frac{\partial p}{\partial t} dx \rightarrow \int_0^{h_{ij}/2} w_h \beta \frac{\partial p}{\partial t} dx \approx \frac{h_{ij}}{12} \beta \left[\left(w_{h_i} + 3w_{h_{i+\frac{1}{4}}} + \frac{1}{2}w_{h_{i+\frac{1}{2}}} \right) \Delta p_i + \left(w_{h_{i+\frac{1}{4}}} + \frac{1}{2}w_{h_{i+\frac{1}{2}}} \right) \Delta p_j \right] \quad (4.8)$$

where the subscript i refers to value at node i , $i + 1/2$ refers to values at the ends to each sub-control volume (i.e. middle of each element), $i + 1/4$ refers to values at middle of each sub-control volume and finally j refers to values at next node j . For instance, the pressure values at $i + 1/2$ and $i + 1/4$ are respectively given by

$$\Delta p_{i+\frac{1}{2}} = \frac{\Delta p_i + \Delta p_j}{2}, \quad \Delta p_{i+\frac{1}{4}} = \frac{3\Delta p_i + \Delta p_j}{4}$$

By combining the integral (4.8) over each sub-control volume CV_{ij} of each mesh nodes, a pressure matrix of size $N \times N$ can be assembled, i.e. the second term of equation 4.3 can be rewritten as



$$\mathbb{V}_p(\mathbf{w}) \cdot \frac{\Delta \mathbf{p}}{\Delta t}$$

By applying the same procedure, the integral (4.6) reduces to

$$\int_{CV_{ij}} \frac{\partial w}{\partial t} dx \rightarrow \int_0^{h_{ij}/2} \frac{\partial w}{\partial t} dx \approx \frac{h_{ij}}{12} [\Delta w_i + 4\Delta w_{i+\frac{1}{4}} + \Delta w_{i+\frac{1}{2}}] = \frac{h_{ij}}{24} [9\Delta w_i + 3\Delta w_j], \quad (4.9)$$

which leads to a mass matrix of size $N \times 2N$ due to piecewise nature of linear displacement discontinuities over each element. The first term of equation 4.3 can thus be rewritten as

$$\mathbb{V}_w \cdot \frac{\Delta \mathbf{w}}{\Delta t}$$

Since we use an implicit scheme in time, we are not restricted by the Courant-Friedrichs-Lewy conditions (typically denoted as CFL condition), which otherwise would lead to a critical time step above which the numerical solution loose its stability. Upon discretization, the fluid mass balance conservation equation in absence of dilatancy term reads

$$\mathbb{V}_p(\mathbf{d}_n^{n+1}) \cdot \Delta \mathbf{p} + \Delta t \times \mathbb{L}(\mathbf{d}_n^{n+1}) \cdot \Delta \mathbf{p} = \Delta t \mathbf{S} - \Delta t \times \mathbb{L}(\mathbf{d}_n^{n+1}) \cdot (\mathbf{p}^n - \mathbf{p}_o), \quad (4.10)$$

which can be re-written in the form of a system of equations for the vector of nodal unknowns $\Delta \mathbf{p}$

$$\mathbb{A}_p \cdot \Delta \mathbf{p} = \mathbf{b}_p \quad (4.11)$$

where $\mathbb{A}_p = \mathbb{V}_p(\mathbf{d}_n^{n+1}) + \Delta t \times \mathbb{L}(\mathbf{d}_n^{n+1})$ is the matrix of coefficient, whereas $\mathbf{b}_p = \Delta t \mathbf{S} - \Delta t \times \mathbb{L}(\mathbf{d}_n^{n+1}) \cdot (\mathbf{p}^n - \mathbf{p}_o)$ is the right hand side vector that contains the source term \mathbf{S} in case of continuous injection. Note that the matrices \mathbb{V}_p and \mathbb{L} in equation 4.10, both function of the current value of fractures widths $\mathbf{d}_n = \mathbf{w}$, are sparse matrices (specifically tri-banded diagonal matrices). For this reason they are stored in memory as such. We solve the system (4.11) for the increment of pore pressure $\Delta \mathbf{p}$ over a given time step using the Pardiso solver shipped with the intel MKL¹ to Once the numerical solution of system 4.11 is obtained, the new pore pressure $\mathbf{p}^{n+1} = \mathbf{p}^n + \Delta \mathbf{p}$ can be calculated at all mesh nodes. This current pore pressure is then used to solve the mechanical problem, i.e. elasticity combined with yield criteria. As previously mentioned, elasticity is collocated at points whose locations lie inside the displacement discontinuity element (collocation points), whereas pore pressure is discretized at mesh nodes. Since we use linear and continuous shape functions for pore pressure, we can always move the nodal pore pressure values p_i to collocation points $p(\xi_i)$ via a simple linear transformation

$$p(\xi_i) = \sum_{i=1,2} N_i(\xi_i) p_i, \quad (4.12)$$

where N_i are the linear shape functions on the reference element

$$N_1(\xi) = \frac{1-\xi}{2} \quad N_2(\xi) = \frac{1+\xi}{2},$$

with $\xi_j = \pm \frac{\sqrt{2}}{2}$ the position of the collocation points in the reference element. Equation 4.12 can be expressed in matrix form as

$$\mathbf{p}_{coll} = \mathbf{N}_{pc} \mathbf{p},$$

where \mathbf{N}_{pc} is a $2N_{elts} \times N_{nodes}$ matrix for the transfer of the value of pressure from node to collocation points.

¹The Pardiso solver is a specific direct solver for the numerical solution of large sparse symmetric and unsymmetric linear systems of equations.



4.1.2 Mechanical solver

Once the fluid flow problem is solved at the beginning of each time step, the algorithm moves to the mechanical problem in order to obtain the current tractions \mathbf{t}_i^{n+1} and the corresponding displacement discontinuities \mathbf{d}_i^{n+1} .

The algorithm that we have devised is composed of two nested loops. The outer loop iterates to check i) yielding criteria with current softening variables at every collocation points of the mesh (implicit tracking of cracks' fronts) and ii) the inter-penetrability constraint at every mesh nodes. For a given iteration of the outer loop, the non-linear mechanical problem is solved using a fixed point iterative scheme for the effective tractions \mathbf{t}_i' and increment of displacement discontinuities $\Delta \mathbf{d}_i$. Note that we solve the mechanical problem in term of effective tractions and not total tractions. This simplifies the implementation of the scheme, as the constraints dictated by the yield criteria are already written in terms of effective tractions. The current total tractions \mathbf{t}_i^{n+1} are then calculated by simply adding the current pore pressure p^{n+1} to the obtained current effective tractions.

The outer loop allows to define which elements of the mesh are yielded (either in mode I or in mode II) and which elements do not satisfy the inter-penetrability condition, whereas the inner loop solves iteratively the equilibrium elastic problem accounting for the possible softening of failure properties of the fractures.

Tractions and displacement discontinuities are related to each others through the quasi-static elasticity equation, which can be expressed in discretized form as

$$\mathbf{t}_i^n + \Delta \mathbf{t}_i = \mathbf{t}_i^o + \mathbb{E}_{\mathcal{H}}(\mathbf{d}_i^n + \Delta \mathbf{d}_i), \quad (4.13)$$

where $\mathbb{E}_{\mathcal{H}}$ is the hierarchical representation of the elasticity matrix (possibly using a hierarchical matrix representation). Note that one can always recover the fully populated elasticity matrix by simply setting $\eta_{\mathcal{H}} = 0$ before the construction of the hierarchical matrix (such that the admissibility condition is never satisfied).

Since we solve the mechanical problem in terms of effective tractions \mathbf{t}_i' , we rewrite the discretized elasticity equations 4.13 as

$$\mathbf{t}_i'^{n+1} = \mathbf{t}_i^o + \mathbb{E}_{\mathcal{H}}(\mathbf{d}_i^n + \Delta \mathbf{d}_i) - p_{coll}^{n+1}, \quad (4.14)$$

where the effective tractions are evaluated at collocation points, whereas displacement discontinuities are evaluated at mesh nodes. Since we use piecewise linear displacement discontinuities, the number of unknowns is $8N_{elts}$ (half related to effective tractions and half related to increment of displacement discontinuities), for $4N_{elts}$ elasticity equations. In order to solve the mechanical problem, additional equations must be taken into account. These equations are given by the cohesive interface constitutive relations for the displacement discontinuities locus as they dictate the constraints for the primary unknowns of the mechanical problem. At each iteration of the outer loop, the algorithm identifies a set of elements $N_{a,I}$ (or collocation points) that are active in mode I, a set of elements $N_{a,II}$ (or collocation points) that are active in mode II, a set of inactive elements N_{inact} (or collocation points) and finally a set of elements that violate the inter-penetrability constraint N_{interp} . For each set of elements, different constraints have to be set, either in terms of tractions or in terms of deformations. We report hereunder the different constraints that must be applied to one node (for constraints in terms of deformations) or to one collocation point (for constraints in terms of effective tractions) of one mesh element. This element may belong to one of each previously discussed set of elements.

- Active set of elements $N_{a,I}$ - mode I

If the local tractions at current time are such that $F_1(\mathbf{t}_s^{n+1}, \mathbf{t}_n^{n+1}) > 0$ along $N_{a,I}$ elements (and mode I failure occur), then the algorithm enforces $F_1(\mathbf{t}_s^{n+1}, \mathbf{t}_n^{n+1}) = 0$ and $|\dot{d}_s| = 0$. The set of discretized equations for one node or collocation point of an active tensile element are

$$t_n'^{n+1} = -\sigma_c(\kappa^{n+1}, \kappa_m^{n+1}), \quad |\Delta d_s| = 0,$$

which can be rewritten in matrix form as



$$\begin{bmatrix} 0 & 0 \\ 0 & 1 \end{bmatrix} \begin{bmatrix} |t_s^{n+1}| \\ t_n^{\prime, n+1} \end{bmatrix} = \begin{bmatrix} 0 \\ -\sigma_c(\kappa^{n+1}, \kappa_m^{n+1}) \end{bmatrix}, \quad \begin{bmatrix} 1 & 0 \\ 0 & 0 \end{bmatrix} \begin{bmatrix} |\Delta d_s| \\ |\Delta d_n| \end{bmatrix} = \begin{bmatrix} 0 \\ 0 \end{bmatrix}$$

- Active set of elements $N_{a,II}$ - mode II

If the local tractions at current time are such that $F_2(\mathbf{t}_s^{n+1}, \mathbf{t}_n^{\prime, n+1}) > 0$ along $N_{a,II}$ elements (and mode II failure occur), then the algorithm enforces $F_2(\mathbf{t}_s^{n+1}, \mathbf{t}_n^{\prime, n+1}) = 0$ and $|\dot{d}_n| = |\dot{d}_s| \tan \psi(\eta, \eta_m)$. The set of discretized equations for one node or collocation point of an active shear element is

$$t_s^{n+1} = c(\kappa^{n+1}, \kappa_m^{n+1}) + f(\eta^{n+1}, \eta_m^{n+1}) t_n^{\prime, n+1}, \quad |\Delta d_n| = |\Delta d_s| \tan(\psi(\eta^{n+1}, \eta_m^{n+1})),$$

which can be rewritten in matrix form as

$$\begin{bmatrix} 1 & -f(\eta^{n+1}, \eta_m^{n+1}) \\ 0 & 0 \end{bmatrix} \begin{bmatrix} |t_s^{n+1}| \\ t_n^{\prime, n+1} \end{bmatrix} = \begin{bmatrix} c(\kappa^{n+1}, \kappa_m^{n+1}) \\ 0 \end{bmatrix}, \quad \begin{bmatrix} 0 & 0 \\ -\tan(\psi(\eta^{n+1}, \eta_m^{n+1})) & 1 \end{bmatrix} \begin{bmatrix} |\Delta d_s| \\ |\Delta d_n| \end{bmatrix} = \begin{bmatrix} 0 \\ 0 \end{bmatrix}$$

- Inactive set of elements N_{inact}

If the local tractions at current time are such that both yielding criteria are strictly satisfied, i.e. $F_1(\mathbf{t}_s^{n+1}, \mathbf{t}_n^{\prime, n+1}) < 0$ and $F_2(\mathbf{t}_s^{n+1}, \mathbf{t}_n^{\prime, n+1}) < 0$, along N_{inact} elements, then the rate of displacement discontinuities must be zero. In discretized form, this reads

$$|\Delta d_i| = 0, \quad i = s, n$$

or equivalently in matrix form

$$\begin{bmatrix} 1 & 0 \\ 0 & 1 \end{bmatrix} \begin{bmatrix} |\Delta d_s| \\ |\Delta d_n| \end{bmatrix} = \begin{bmatrix} 0 \\ 0 \end{bmatrix}$$

- Elements that violate the inter-penetrability condition

Inter-penetration of matter is physically not admissible. If the normal displacement discontinuity on one node is lower than the minimum admissible value \bar{w}_m , then the following constraint has to be applied

$$d_n^{n+1} = \bar{w}_m \quad (4.15)$$

Since we solve the mechanical problem in terms of increment of displacement discontinuities, equation 4.15 can be rewritten in matrix forms as

$$\begin{bmatrix} 1 & 0 \\ 0 & 1 \end{bmatrix} \begin{bmatrix} |\Delta d_s| \\ |\Delta d_n| \end{bmatrix} = \begin{bmatrix} 0 \\ \bar{w}_m - d_n^n \end{bmatrix} \quad (4.16)$$

By considering all the nodes as well as all the collocation points of the mesh and knowing that the displacement discontinuities vary discontinuously between adjacent elements, these constraints provide a set of $4N_{elts}$ equations that can be used to solve the mechanical problem. Gathering together the $4N_{elts}$ elasticity equations written in terms of effective tractions 4.14 with the constraints in terms of effective tractions and displacement discontinuities previously discussed, we can assemble the following $8N_{elts} \times 8N_{elts}$ system of equations

$$\begin{bmatrix} \mathbb{E}_{\mathcal{H}} & \mathbb{I} \\ \mathbb{A}_4 & \mathbb{A}_3 \end{bmatrix} \begin{bmatrix} \Delta \mathbf{d}_i \\ \mathbf{t}_i^{\prime, n+1} \end{bmatrix} = \begin{bmatrix} \mathbf{t}_i^o + \mathbb{E} \mathbf{d}_i^n - \mathbf{p}_{coll}^{n+1} \\ \bar{\mathbf{a}} \end{bmatrix} \quad (4.17)$$

where \mathbb{I} is a $4N_{elts} \times 4N_{elts}$ identity matrix, $\bar{\mathbf{a}}$ is a $4N_{elts} \times 1$ null vector that contains the current strength parameters (cohesion $c(\kappa^{n+1}, \kappa_m^{n+1})$ and tensile strength $\sigma_c(\kappa^{n+1}, \kappa_m^{n+1})$) on active elements and eventually the inter-penetrability constraint 4.16, and finally \mathbb{A}_4 and \mathbb{A}_3 are sparse block matrices that contain the constraints in term of displacement discontinuities and effective tractions, respectively. The pattern of these block matrices is not known a priori, but evolves in time based on yielding evolution during cracks propagation. Note that the system of equations 4.17 is non linear since the softening parameters (and



hence the yielding properties) depend on current deformations. Furthermore, its matrix of coefficient is not diagonal dominant as well as it is non-symmetric. Since all the sub-blocks composing the matrix of coefficient are square matrices, the system (4.17) is a square system of equations. Although the blocks \mathbb{A}_4 and \mathbb{A}_3 are singular sparse matrices, the inverse of the final matrix exist, i.e. the final matrix has always full rank.

It is worth mentioning that the hierarchical decomposition of the mesh domain involved in the \mathcal{H} -matrix construction may lead to a permutation of the degrees of freedom, which consequently leads to a feedback on the other blocks composing the matrix of coefficient as well as on the right hand side. Therefore, the proper permutations or back-permutations must be applied during its resolution.

The non-linear system of equations (4.17) can be solved via direct or iterative method. The former requires the inversion of the matrix of coefficient, which we want to avoid as the computational complexity scales as $O(n^3)$ (being n the dofs of the problem), whereas the latter requires at most k matrix-vector multiplication, i.e. $O(k \cdot n^2)$ with k the number of iterations (generally $k \ll n$). We solve such a non-linear system of equations with generalized minimal residual method (GMRES) iterative solver, which is one of the Krylov subspace iterative method. This iterative solver is part of the InsideLoop C++11 library (via an API to the intel MKL).

Since the matrix of coefficient that arise from gathering together the four sub-blocks is highly sparse and non-symmetric, a good preconditioner must be considered during the iterative resolution of (4.17). In the next section, we discuss in full details the block preconditioning we have developed for a faster solution of system (4.17).

4.1.3 Preconditioning & solution of the tangent system

The final linear system of equations 4.17 is unfortunately ill-conditioned. Its matrix of coefficient, in fact, is very sparse and highly non-symmetric. For sake of simplicity and compactness, we rewrite the system 4.17 as

$$\underbrace{\begin{bmatrix} \mathbb{E}_{\mathcal{H}} & \mathbb{I} \\ \mathbb{A}_4 & \mathbb{A}_3 \end{bmatrix}}_{\mathcal{A}} \underbrace{\begin{bmatrix} \mathbf{x}_1 \\ \mathbf{x}_2 \end{bmatrix}}_{\mathbf{x}} = \underbrace{\begin{bmatrix} \mathbf{y}_1 \\ \mathbf{y}_2 \end{bmatrix}}_{\mathbf{y}} \quad (4.18)$$

where \mathbf{x} is the vector of current unknowns (increment of displacement discontinuities and effective tractions) and \mathbf{y} is the right hand side vector. We denote the matrix of coefficient as \mathcal{A} .

In Figure 4.2, we show an example of spectral properties of \mathcal{A} arising from the following case: a planar fracture is discretized with 100 equal-sized elements, 6 of them are active in mode II while the others are inactive and they satisfy inter-penetrability constraint.

As one can see, the eigenvalues of \mathcal{A} are spread over a wide range on the complex plane, both in the real and in the imaginary axis. The spectral radius for such an example is indeed $\rho(\mathcal{A}) \sim 56.3$, implying slow convergence properties during iterative solution of system 4.18. In order to improve the spectral properties of matrix \mathcal{A} , i.e. clustering its eigenvalues around unity in the spectral plane, we need to introduce a preconditioning matrix \mathcal{P} such that the product $\mathcal{P}^{-1}\mathcal{A}$ (left preconditioner) or $\mathcal{A}\mathcal{P}^{-1}$ (right preconditioner) is as much closed to identity matrix \mathbb{I} as possible. Because of the block nature of the final matrix \mathcal{A} , the preconditioning matrix \mathcal{P} (or its inverse) is also composed by blocks, each of them properly chosen such to improve the conditioning of the final system of equations. We will thus talk about block preconditioners.

The choice of a good preconditioner may or may not stem from the nature of the problem under investigation. Preconditioners based on algebraic techniques, for instance, require little knowledge of the problem and can be used in a black-box fashion. Examples of these preconditioners are incomplete LU factorization of the system matrix or algebraic multilevel methods. These preconditioners, however, are not robust for system matrices that are far from being diagonally dominant (see Benzi (2002)), which is the case of the matrix \mathcal{A} . The incomplete lower-upper factorization (ILU) of the system matrix, for instance, may require storing many fill-ins that are small in absolute value and, therefore, contribute little to the quality of the preconditioner itself, while making it expensive to compute and to use. The preconditioner for the linear system 4.18, therefore, must be tailored based on the nature's knowledge

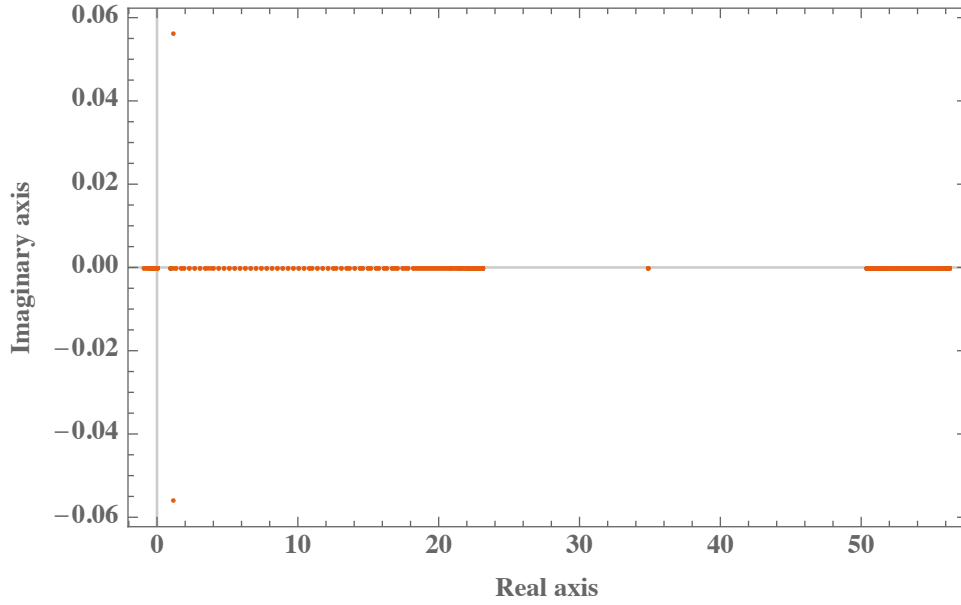


Figure 4.2: Example of spectral properties of the matrix of coefficient \mathcal{A} . This matrix results from a discretization of a planar fracture with 100 equal-sized elements, 6 of them active in mode II, while the others are inactive (and satisfy the inter-penetrability condition).

of the problem as well as on the pattern of the final matrix \mathcal{A} , similar to what is done for saddle point problems (see Benzi et al. (2005), Cao (2008, 2009), Li et al. (2010) among others).

Starting from the observation that if the sub-block matrix \mathbb{A}_3 is null, then the system of equations 4.18 is exactly equivalent to the one that arise from non-symmetric saddle point problem (for which several preconditioner are available in literature), we developed an ad-hoc preconditioner that suites our mechanical problem. Note that the block \mathbb{A}_3 is null only when all the elements of the mesh are inactive in both modes, i.e. when there are no deformations along computational mesh, and at the same time they satisfy the inter-penetrability condition. Beside this specific scenario, the matrix \mathbb{A}_3 is not null and it is typically characterized by an high level of sparsity.

We adapt a preconditioner that is tailored for saddle point problems to our specific problems. We introduce an upper-triangular block preconditioner applied on right side. The system of equations 4.18 can thus be rewritten as

$$\mathcal{A}\mathcal{P}_{up}^{-1}\mathbf{u} = \mathbf{y}, \quad \mathbf{u} = \mathcal{P}_{up}\mathbf{x} \quad (4.19)$$

where \mathcal{P}_{up}^{-1} is an upper-triangular block preconditioning matrix defines as

$$\mathcal{P}_{up}^{-1} = \begin{bmatrix} \mathcal{D}_e^{-1} & -\mathcal{D}_e^{-1}\mathcal{S}^{-1} \\ 0 & \mathcal{S}^{-1} \end{bmatrix}, \quad (4.20)$$

where \mathcal{D}_e is the diagonal of the hierarchical elastic matrix $\mathbb{E}_{\mathcal{H}}$ and $\mathcal{S} = \mathbb{A}_3 - \mathbb{A}_4\mathcal{D}_e^{-1}$ is the Schur complement of system 4.18 with respect to $\mathbb{E}_{\mathcal{H}}$. As far as the matrix \mathcal{P}_{up} is concerned, it can be easily obtained from the relation $\mathcal{P}_{up}^{-1}\mathcal{P}_{up} = \mathbb{I}$ (which comes from the definition of right preconditioning), which leads to

$$\mathcal{P}_{up} = \begin{bmatrix} \mathcal{D}_e & \mathbb{I} \\ 0 & \mathcal{S} \end{bmatrix} \quad (4.21)$$

Although the problem is reduced to solve two systems of equations instead of one (with respect to the non-preconditioning case), the effect of preconditioner is such that their resolutions is way faster than the resolution of system 4.18. Note that if $\mathcal{D}_e = \mathbb{E}_{\mathcal{H}}$, then the spectrum of $\mathbb{P}_{up}^{-1}\mathcal{A}$ is $\rho(\mathbb{P}_{up}^{-1}\mathcal{A}) = \{1\}$ and the preconditioned matrix has minimum polynomial of degree 2, so that the GMRES would converge in at most 2 iterations. In practice, however, we do not want to compute the inverse of the elasticity matrix



($\sim O(n^3)$ in case of fully populated elasticity matrix), so we make use of the non-local property of the elastic kernel to approximate \mathcal{D}_e as $\text{diag}(\mathbb{E}_{\mathcal{H}})$. The diagonal of the elasticity matrix (or its hierarchical approximation) contains the elastic self-effects, which are certainly the most relevant (and for this reason they are never approximated by the hierarchical matrix). By taking the diagonal of the elasticity matrix, the inverse of \mathcal{D}_e is relatively cheap and thus fast to compute. This choice is motivated by the fact that for saddle point problems, it has been mathematically proved that if the upper-left block (1,1) of the final matrix of coefficient is diagonal dominant, then taking its diagonal as (1,1) block of preconditioning matrix would lead to a good clustering of the eigenvalues around 1, $\frac{1}{2}(1 + \sqrt{5})$ and $\frac{1}{2}(1 - \sqrt{5})$. This, however, does not prevent the preconditioned matrix from having its eigenvalues on both sides of the imaginary axis (see Benzi (2002) for details).

Note that, in case of hierarchical approximation of elasticity matrix is used, its diagonal is never approximated (i.e. it is always stored), as the self-effects are the most meaningful terms for non-local elasticity.

Upon application of the preconditioners 4.20 and 4.21, the systems of equation 4.19 reduce to

$$\underbrace{\begin{bmatrix} \mathbb{E}_{\mathcal{H}}\mathcal{D}_e^{-1} & -\mathbb{E}_{\mathcal{H}}\mathcal{D}_e^{-1}\mathcal{S}^{-1} + \mathcal{S}^{-1} \\ \mathbb{A}_4\mathcal{D}_e^{-1} & -\mathbb{A}_4\mathcal{D}_e^{-1}\mathcal{S}^{-1} + \mathbb{A}_3\mathcal{S}^{-1} \end{bmatrix}}_1 \begin{bmatrix} \mathbf{u}_1 \\ \mathbf{u}_2 \end{bmatrix} = \begin{bmatrix} \mathbf{y}_1 \\ \mathbf{y}_2 \end{bmatrix}, \quad \underbrace{\begin{bmatrix} \mathcal{D}_e & \mathbb{I} \\ 0 & \mathcal{S} \end{bmatrix}}_2 \begin{bmatrix} x_1 \\ x_2 \end{bmatrix} = \begin{bmatrix} u_1 \\ u_2 \end{bmatrix} \quad (4.22)$$

As one can notice from system 1 of equation 4.22, the inverse of the Schur complement is needed for its resolution, setting thus a tight computational constraint. We overcome it by using the following change of variable

$$z_2 = \mathcal{S}^{-1}\mathbf{u}_2$$

such that the system 1 of 4.22 can be rewritten as

$$\underbrace{\begin{bmatrix} \mathbb{E}_{\mathcal{H}}\mathcal{D}_e^{-1} & -\mathbb{E}_{\mathcal{H}}\mathcal{D}_e^{-1} + \mathbb{I} \\ \mathbb{A}_4\mathcal{D}_e^{-1} & -\mathbb{A}_4\mathcal{D}_e^{-1} + \mathbb{A}_3 \end{bmatrix}}_{\mathcal{A}_p} \begin{bmatrix} \mathbf{u}_1 \\ \mathbf{z}_2 \end{bmatrix} = \begin{bmatrix} \mathbf{y}_1 \\ \mathbf{y}_2 \end{bmatrix} \quad (4.23)$$

We define the matrix of coefficients of system 4.23 as \mathcal{A}_p . In order to highlight the effect of preconditioner, we show in Figure 4.3 the spectral properties of the preconditioned matrix \mathcal{A}_p that arises from the same example previously reported.

As one can see from Figure 4.3, upon application of the right preconditioner to matrix \mathcal{A} , the resulting preconditioned matrix \mathcal{A}_p is characterized by better spectral properties. Its eigenvalues, in fact, are spread over a more narrow range (compared to the non-preconditioned case) and more importantly all the eigenvalues lay on the real axis, i.e. they are all real values. The spectral radius in this particular case is $\rho(\mathcal{A}_p) \sim 1.64$, roughly 3% compared to the one of \mathcal{A} . A faster convergence during the iterative solution of system 4.23 is thus expected.

Note again that the system 4.23 does not include the permutations and back-permutations that eventually must be applied if hierarchical representation of elasticity matrix is used.

Once the preconditioned system 4.23 is solved via GMRES iterative solver in terms of \mathbf{u}_1 and \mathbf{z}_2 , the solution of the system 2 of 4.22, which represent the final solution of the mechanical problem, can be easily obtained by performing the proper block matrix-vector multiplication:

$$\mathbf{x}_2 = \mathbf{z}_2, \quad \mathbf{x}_1 = \mathcal{D}_e^{-1}(\mathbf{u}_1 - \mathbf{z}_2)$$

Note that the numerical resolution of the preconditioned mechanical problem does never involve any matrix inversions, allowing a faster convergence of the GMRES, while keeping the computational cost relatively low. Once the convergence of the GMRES in terms of increment of displacement discontinuities Δd_i and effective tractions $t_i^{',n+1}$ is achieved within a given tolerance, the current deformations and total tractions can be easily calculated via

$$d_i^{n+1} = d_i^n + \Delta d_i, \quad t_i^{n+1} = t_i^{',n+1} + p_{coll}^{n+1}$$

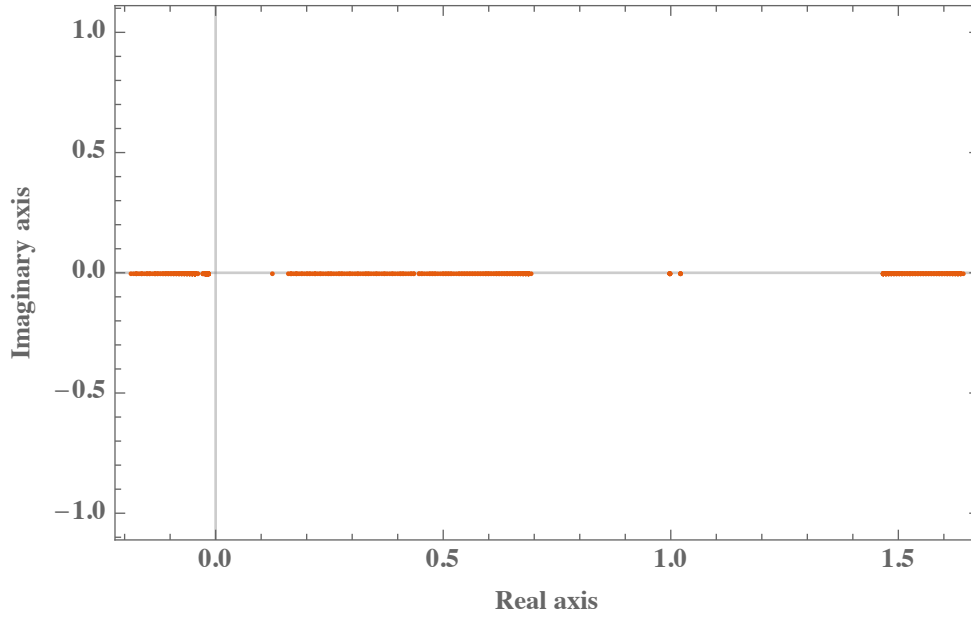


Figure 4.3: Example of spectral properties of the preconditioned matrix of coefficient \mathcal{A}_p . This matrix results from exactly the same example of Figure 4.2, but it has been applied the right block preconditioner.

The algorithm then checks again the yielding criteria and the inter-penetrability condition and it moves to the next time step if all the elements of the computational mesh satisfy simultaneously all constraints.

4.1.4 Adaptive time stepping

When dealing with the modeling of crack(s) propagation in isotropic or anisotropic material, an adaptive time stepping is a numerical technique of great importance. The combination of in-situ stress, frictional properties and loading conditions might lead to very fast (seismic) or very slow (aseismic) cracks propagation. Being able to adapt the time stepping such to minimize the run time of the numerical solver and at the same time ensuring the stability of the numerical solution is a must. Typically time step adaptation has not an unique recipe for every numerical solver, but it must be calibrated based on physical phenomena that take place in the problem under investigation.

In this specific context, we can identify two main physical governing phenomena: i) fluid flow within the pre-existing fractures and ii) mechanical problem (elasticity). Starting from the physics of these two phenomena, we can build the time step adaptation that suit our problems as well as we can identify the maximum and the minimum time step among which the new time step must fall between, i.e.

$$\Delta t_{min} \leq \Delta t_{new} \leq \Delta t_{max}$$

For a forward Euler time integration scheme (explicit scheme), the numerical solution of the width averaged fluid mass conservation equation is constrained by the CFL condition, i.e. the numerical solution is stable if and only if the time step is smaller than a critical value defined as

$$\Delta t_c = \min \left(\frac{h_i^2}{2\alpha} \right), \quad i = 1, \dots, N_{elts}, \quad (4.24)$$

where h is the mesh element size and α is the hydraulic diffusivity of the fracture.

Since we use a backward Euler time integration scheme (implicit scheme), we do not have to strictly satisfy condition 4.24. However, we can certainly imagine that the time step can not be three (or more) orders of magnitude larger than the critical one. We can thus introduce the following criterion for the maximum time step



$$\Delta t_{max} = \eta_t \Delta t_c,$$

where η_t is a user-defined constant parameter (typically $5 < \eta_t < 100$). The new time step Δt_{new} , therefore, must always be smaller than Δt_{max} .

As far as the minimum time step Δt_{min} is concerned, typically it is related to the wave speed in the material, i.e.

$$\Delta t_{min} \sim \max \left(\frac{h_i}{V_p} \right), \quad i = 1, \dots, N_{elts}$$

where V_p is the p -wave velocity of the medium. For granite, for instance, a typical value of V_p is ~ 6 Km/s. The new time step Δt_{new} , therefore, must always be larger than Δt_{min} .

Since the main purpose of this numerical solver is the modeling of fractures propagation, the time step must be adapted based on current crack(s) velocity. For each potential fracture propagation, indeed, we can calculate the current increment of velocity $\Delta v_{frac,i}$ over a given time step, that in turn can be used to calculate the theoretical new time step suited to each fracture

$$\Delta t_{new,frac,i} = \xi_t \frac{h_{m,i}}{\Delta v_{frac,i}}, \quad i = 1, \dots, N_{fracs}$$

where ξ_t is another user-defined constant parameter ($\xi_t \geq 1$) and $h_{m,i}$ is the minimum element size of the generic fracture i . The new time step is then given by the mean value of all the new time steps related to each fracture, i.e.

$$\Delta t_{new} = \left(\sum_i \Delta t_{new,frac,i} \right) / N_{fracs}$$

If no fracture propagation occurs, then the new time step Δt_{new} is set to its maximum value Δt_{max} .

With this adaptive time stepping, we expect that when cracks start to accelerate, for instance due to friction weakening along cohesive interfaces, the time step decreases (up to its minimum value), capturing thus the dynamic cracks propagation accurately. Vice-versa, when cracks propagation occur slowly, for instance during aseismic crack propagation, the time step increases. As one can notice, this time stepping adaptation technique depends only on two parameters, η_t and ξ_t , which allow a generic user to be more (or less) aggressive in the time step adaptation.

4.1.5 Implementation details

This numerical scheme has been coded up in C++. A combination of run-time polymorphism and class hierarchy brings flexibility and allows a generic user to easily specify a new softening law or friction models if needed. The code architecture has been designed with the purpose of fulfilling both functional (i.e. the code has to do what it is supposed to do) and non functional requirements (e.g. reliability, scalability, maintainability and performance), without going into deep abstraction solutions (mainly for a better readability). Classes and interfaces have been designed in a way to make the code easier to maintain and at the same time easier to generalise.

Upon generation of a .json configuration file in which the solver name must be provided (among other input data), the code calls the specific solver, reads all the input data and then starts the computations. Thanks to the usage of matID² and fracID³, heterogeneous material properties can be easily set, even when multiple pre-existing fractures are considered.

All the sparse matrices described in the previous sections are stored in memory as such. As far as the storage of the hierarchical elasticity matrix, the entries of inadmissible blocks are stored in memory, whereas the ones of admissible blocks are stored in low rank format.

²matID is an array of integers that must be input in the configuration file. One entry of it represents the mapping of one element of the computational mesh to a specific material property.

³fracID is an array of integers that must be input in the configuration file. One entry of it represents the mapping of one element of the computational mesh to a specific fracture.

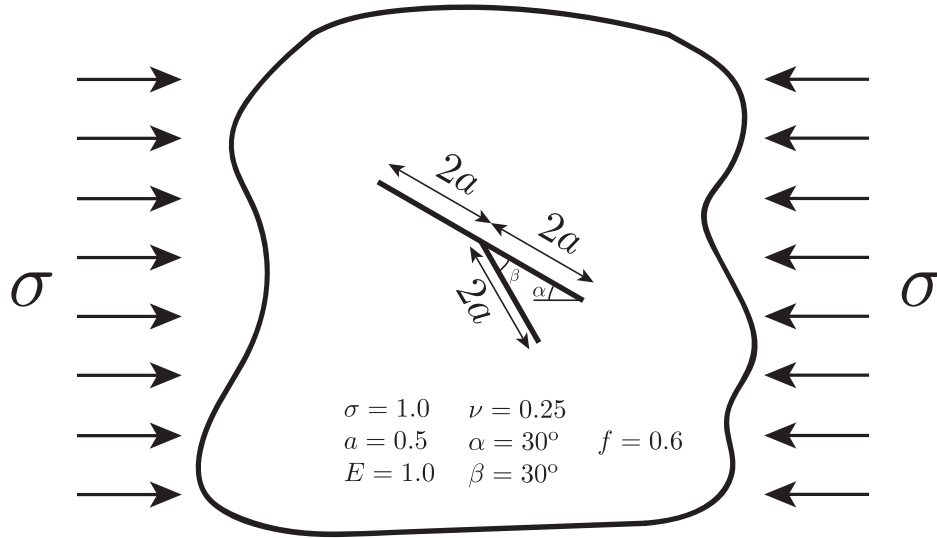


Figure 4.4: Sketch of verification test 1: a branched fault is embedded in an infinite, homogenous, isotropic and linear elastic material and it is subjected to a compressive remote stress σ . The fault is frictional neutral, with friction coefficient $f = 0.6$. All the input data related to geometry and material are reported in the figure.

The solution of the final preconditioned system of equations is obtained via GMRES, which uses an ad-hoc functor written for this specific block partitioned solver.

Before moving to the next time step, the algorithm writes a binary json file (.ubjson format) with the current solution and then it moves to the time stepping adaptation to identify the next time step.

4.2 Verification tests

When developing numerical solvers for addressing physical problems, it is of great importance to reproduce existing problems whose solution is available in closed form or whose solution has already been verified with other numerical solvers.

We report hereunder some tests we have performed with the one-way coupled hydro-mechanical solver previously discussed. These tests allow to verify the numerical solver, testing all its capabilities as well as its performance.

4.2.1 Test #1 : Branched fault subjected to compressive far field stress

This test consists in determining the distribution of tractions and slip on a branched fault under remote compressive stress (see Figure 4.4). The fault is located in an infinite, homogenous, isotropic and linear elastic medium, with neutral frictional properties (i.e. the friction coefficient f is constant all along the fault). Although this static problem is purely frictional and dry, it is a good test for the algorithm devised and its convergence in terms of fracture front position (implicitly obtained with the outer iterative loop).

Maerten et al. (2010) have solved numerically this problem and they have validated their numerical results by comparing them with numerical results obtained with other numerical solvers (see Maerten et al. (2010) for more details). Albeit the available solution is not analytical, it can be used to verify our numerical results.

We solve numerically this problem by discretizing the whole branched fault with 5000 straight elements (notably 3000 straight elements for the main branch of length $4a$, and 2000 straight elements for

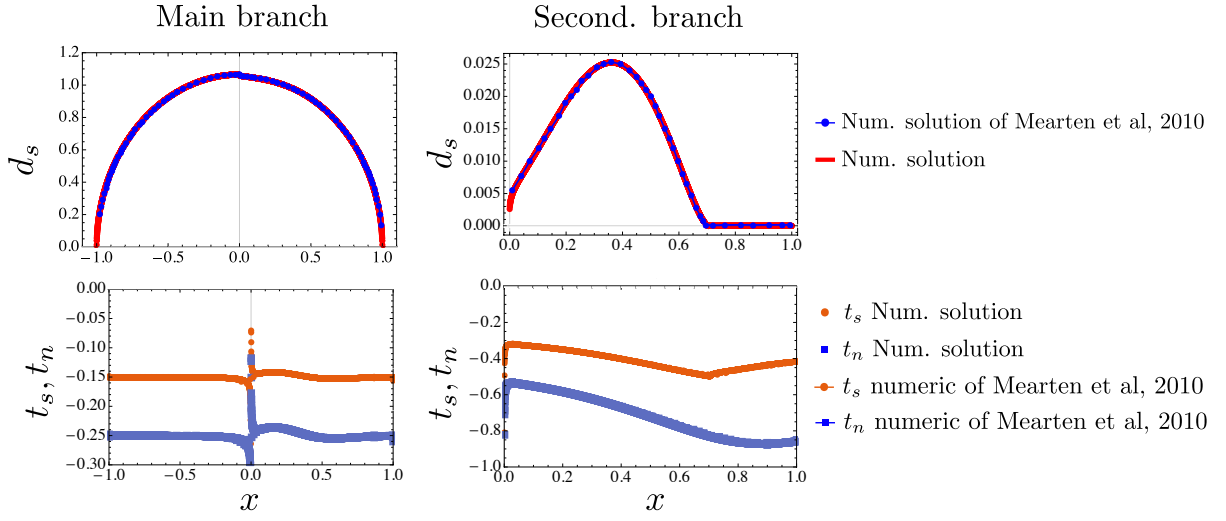


Figure 4.5: Comparison between numerical results in terms of slip d_s and tractions t_i distribution along the branched fault obtained with our one-way coupled HM solver and the ones of Maerten et al. (2010).

the secondary branch of length $2a$). The hierarchical elasticity matrix adopted for this problem has been obtained with the following input data

$$\eta_{\mathcal{H}} = 3, \quad \epsilon_{ACA} = 10^{-6}, \quad N_{leaf} = 10^3,$$

obtaining a compression ratio of

$$T(\mathbb{E}_{\mathcal{H}}) \approx 0.341$$

Figure 4.5 shows the comparison between our numerical results and the ones of Maerten et al. (2010). More precisely, the two plots on the left column represent the numerical solution in terms of slip (top) and tractions (bottom) along the main fault branch of length $4a$, whereas the corresponding numerical results related to the secondary branch of length $2a$ are reported in the plots on the right column. As one can see, a good match between our numerical results and the ones of Maerten et al. (2010) is obtained. The position of the shear crack tip on the secondary fault branch is accurately captured, as well as the tractions distribution along it.

4.2.2 Test #2 : Fluid injection into a frictional weakening planar fault

The second validation test has been performed in order to check whether the frictional non-linearity during crack propagation is well captured by our numerical solver. Fluid is injected into an infinite planar fault with weakening frictional properties, activating ultimately a shear crack (see Figure 4.6). The fault is embedded in an homogenous, isotropic and linear elastic infinite material, whose permeability is supposed to be considerably smaller than the fault longitudinal permeability. Fluid flow only occurs along the fault plane from a source injection located at the middle of the fault in the 2D space - more precisely a line-source in the out-of-plane direction to satisfy plane-strain conditions. Prior fluid injection, the fault is subjected to a uniform initial in-situ stress and pore pressure field. Note that, since we do not account for fault dilatant behaviour, the fluid flow problem is not affected by the mechanical problem, i.e. the problem is only one-way coupled.

This specific problem has been deeply investigated by Garagash & Germanovich (2012) (we refer to their paper for full details about the problem formulation and scaling analysis). Their semi-analytical solution can thus be used to benchmark the numerical solution obtained with our one-way coupled HM solver.

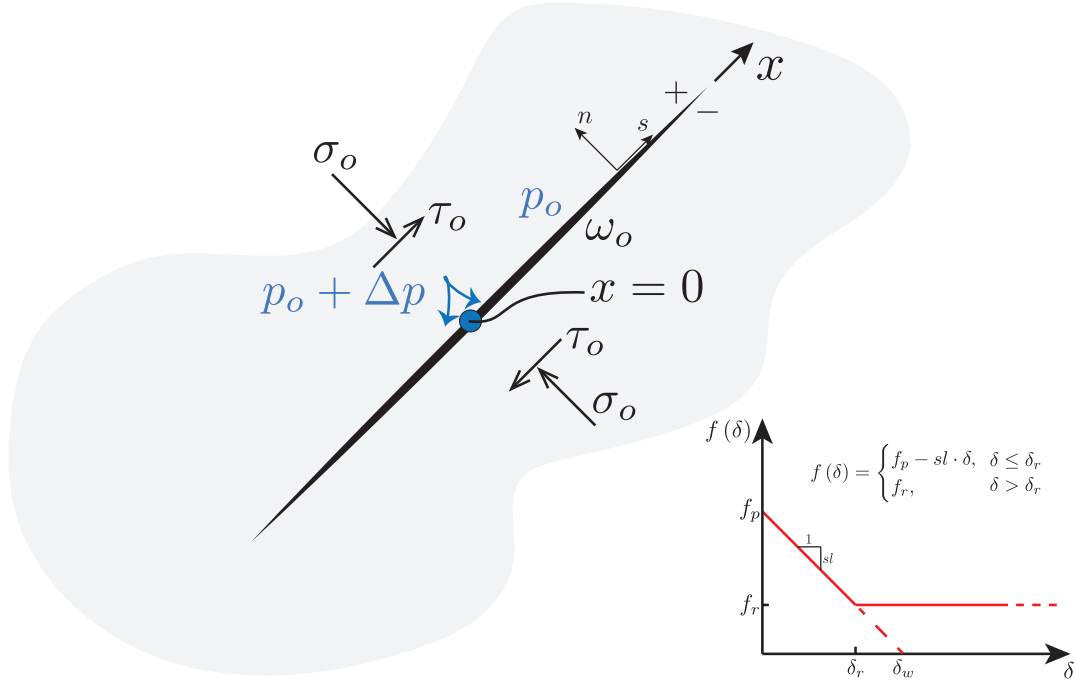


Figure 4.6: Sketch of validation test 2: injection of fluid in a frictional weakening planar fault. The fault is embedded in an infinite, isotropic, homogenous and linear elastic material and it is subjected to a uniform stress distribution, denoted by $\sigma_o = t_{n,o}$ and $\tau_o = t_{s,o}$. The friction coefficient is supposed to weaken during shear deformations, from its peak value f_p to its residual value f_r over a characteristic slip distance δ_r . This problem has been deeply investigated by Garagash & Germanovich (2012). We refer to their paper for full details.

Although the problem is only one-way coupled and pore pressure evolution can be analytically obtained from the solution of the linear diffusion equation in a fault characterized by constant hydraulic diffusivity α

$$p(x, t) = p_o + \Delta P \cdot \text{Erfc} \left| \frac{x}{\sqrt{4\alpha t}} \right|,$$

in our numerical solutions the fluid flow problem is solved numerically via a finite volume scheme. The fault has been discretized with 1000 straight equal-sized elements and the fully populated elasticity matrix is considered (i.e. $\eta_H = 0$).

In Figure 4.7 we report the benchmark of our numerical results against the semi-analytical ones of Garagash & Germanovich (2012), both in terms of dimensionless half-crack length a/a_w (left) and dimensionless peak slip accumulated in the middle of the fault $\delta_{|x=0|}/\delta_w$ (right). Notably, we report only the benchmark for the case of an ultimately stable fault characterized by a stress criticality of $\tau_o/\tau_p = 0.55$, subjected to a moderate overpressure $\Delta P/\sigma'_o = 0.5$. This allows to verify both the aseismic crack propagation and the dynamic event followed by an arrest that necessarily occur due to frictional weakening nature of the fault. As one can see from Figure 4.7, our numerical results match very well the semi-analytical results of Garagash & Germanovich (2012) both in terms of half-crack length and peak slip at the middle of the fault. The nucleation time of the dynamic rupture is accurately hit as well as its arrest that occur when the shear crack catches up with the fluid front.

4.2.3 Test #3 : Loading/Unloading test

We report here an ad-hoc test we have performed in order to check all the possible constraints related to a mixed mode dry fracture propagation along a weakening cohesive interface. Notably, during the time

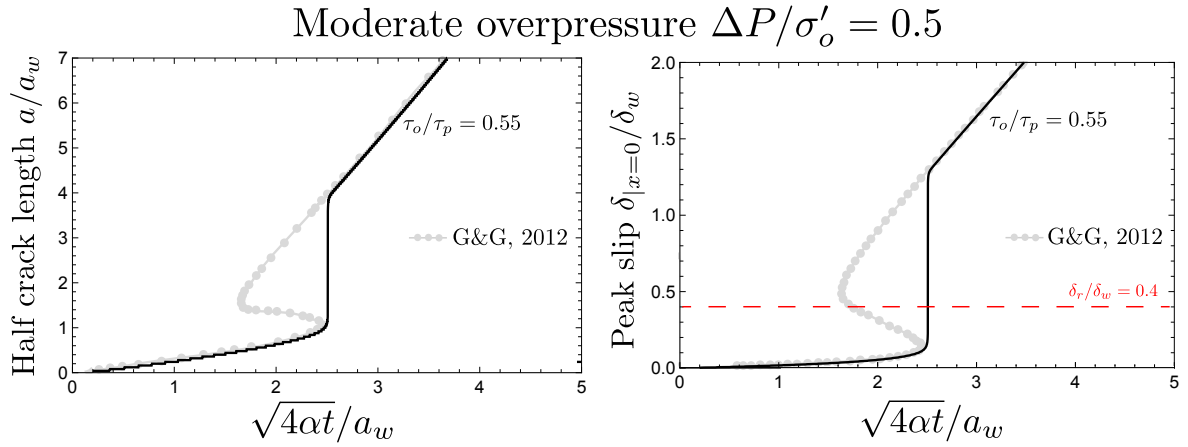


Figure 4.7: Benchmark of numerical results obtained with one-way coupled HM solver (black curve) against semi-analytical ones of Garagash & Germanovich (2012) (light grey curve), in terms of time evolution of normalized half crack length a/a_w (left) and normalized peak slip δ/δ_w at the center of the planar fault $x = 0$ (right). The fault is an ultimately stable fault characterized by a stress criticality of $\tau_o/\tau_p = 0.55$, subjected to a moderate overpressure $\Delta P/\sigma'_o = 0.5$. The friction weakening ratio is $f_r/f_p = 0.6$, so that $\delta_r/\delta_w = 0.4$.

evolution of this test, all the possible constraints related to tractions or deformation are activated. The numerical solution therefore should be in agreement with what we expect a priori.

A planar fracture is embedded in an infinite, homogeneous, isotropic and linear elastic material. Normal and shear tractions are applied on the fracture plane due to the far field stress state defined by the components σ_{yy} and σ_{xy} (see Figure 4.8). The frictional strength along the fracture weakens with shear deformation, except along a finite small patch over which the friction coefficient is at its residual value 0.6 and the cohesion is null. A mechanical force is then applied over a finite length along the fracture, such that its length of application is slightly larger than the frictional weak layer (see Figure 4.8). At time $t_o = 0$, the mechanical force is null, then it increases for $t > 0$ (in tension), up to reach a critical time t_c after which it turns into a compression mechanical force (change of sign). This mechanical force is thus the driving force of a mixed mode fracture propagation.

At initial time $t_o = 0$, a small (central) portion of the fracture is not in equilibrium with far field stress state, due to the lower shear strength associated with lower friction coefficient (with respect to the rest of the fracture- see ‘weak layer’ in Figure 4.8) and null cohesion. Therefore, a shear crack starts to propagate driven by the tensile force (loading process - see time snapshots of slip distribution in Figure 4.9-top). Since in this test dilatancy is considered during the shear crack propagation (with a constant dilatant angle $\tan(\psi) = 0.3$), the normal displacement discontinuities induced by dilatancy are always a fixed fraction of the shear displacement discontinuities. It is worth mentioning that the displacement discontinuities profiles are symmetric with respect to $x = 0$ due to the symmetry of mechanical properties and loading conditions with respect to fracture centre.

As time increases, the tensile mechanical force reduces the compressive normal stress applied in the fracture, up to induce at time $t \simeq 1.15$ a tensile opening (which is embedded within the shear crack). As expected, the normal tractions within the opening mode crack vanish (see Figure 4.10-left), whereas the corresponding slip keep accumulating locally on the fracture (see Figure 4.10-right). When time t reaches $t_c = 1.5$, then the force turns into compressive (unloading) and crack closure is expected followed by an arrest of shear crack. From Figure 4.10, one can notice that the contact condition upon closure is reached at $t \simeq 1.95$, after which the normal tractions in the fracture centre start to build up linearly (as the mechanical force evolves linearly) and the corresponding displacement discontinuities is set to the minimum value 0.04 (satisfying thus the inter-penetrability constraint - see Figure 4.9-bottom).

All the constraints previously discussed are enforced correctly.

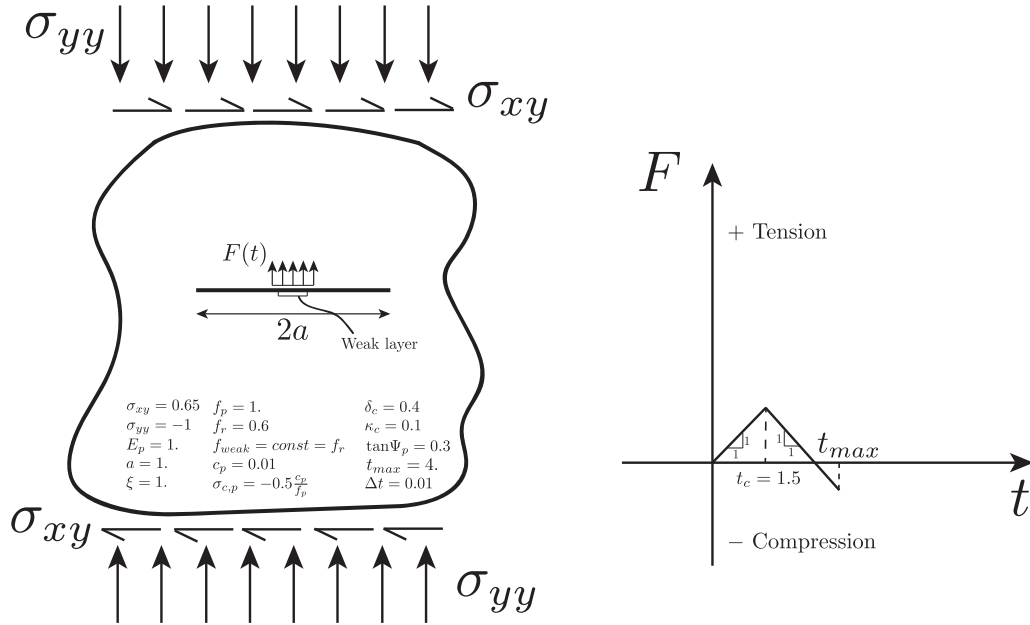


Figure 4.8: Sketch of validation test 3: a planar dry fracture is embedded in an infinite, homogenous, isotropic and linear elastic medium, subjected to a stress state denoted by σ_{yy} and σ_{xy} . The fracture is characterized by frictional weakening properties, except in a small weak zone near its centre where the friction coefficient is constant ($f_{weak} = 0.6$). A time dependent mechanical force is applied to a given fracture zone such that during the loading process a mixed mode fracture propagation is induced. After $t_c = 1.5$ (unloading), the mechanical force tends close back the fracture.

4.3 Fluid injection into a Discrete Fracture Network: critically stressed vs marginally pressurized case

Wellbore images at depth typically show the presence of pre-existing fractures (Zoback 2010). Further analysis shows that fracture lengths are typically spread out over several length scales (from microns to hundreds of kilometers) and fracture length statistics can be modelled by power-law distribution Bonnet et al. (2001).

In the context of deep geothermal energy, pre-existing fractures/faults at depth represent the only pathway for fluid circulation between injection and extraction well. Generally, the stimulation of deep fractured reservoirs can be achieved by injecting fluid at high pressure and thus creating new opening mode fractures (hydraulic fracturing), or by re-activating the pre-existing fractures at depth via hydro-shearing stimulation. In the latter case, fluid is injected at pressure below the minimum principal effective stress at depth with the ultimately purpose of re-activating mode II cracks. A combination of shear-induced dilatancy and linkage between different fractures is responsible for permeability enhancement, allowing thus the circulating fluid to sweep a larger volume.

In this respect, our HM numerical solver is able to simulate hydro-shearing stimulation of a fractured rock mass. In this section, we describe how we generate the pre-existing fracture network at depth, the governing dimensionless parameters and two demonstrative examples.

4.3.1 Discrete Fracture Network generation

Quantitatively, a DFN can be defined with the following mathematical expression (restricting to the 2-dimensional case) (Davy et al. 2006)

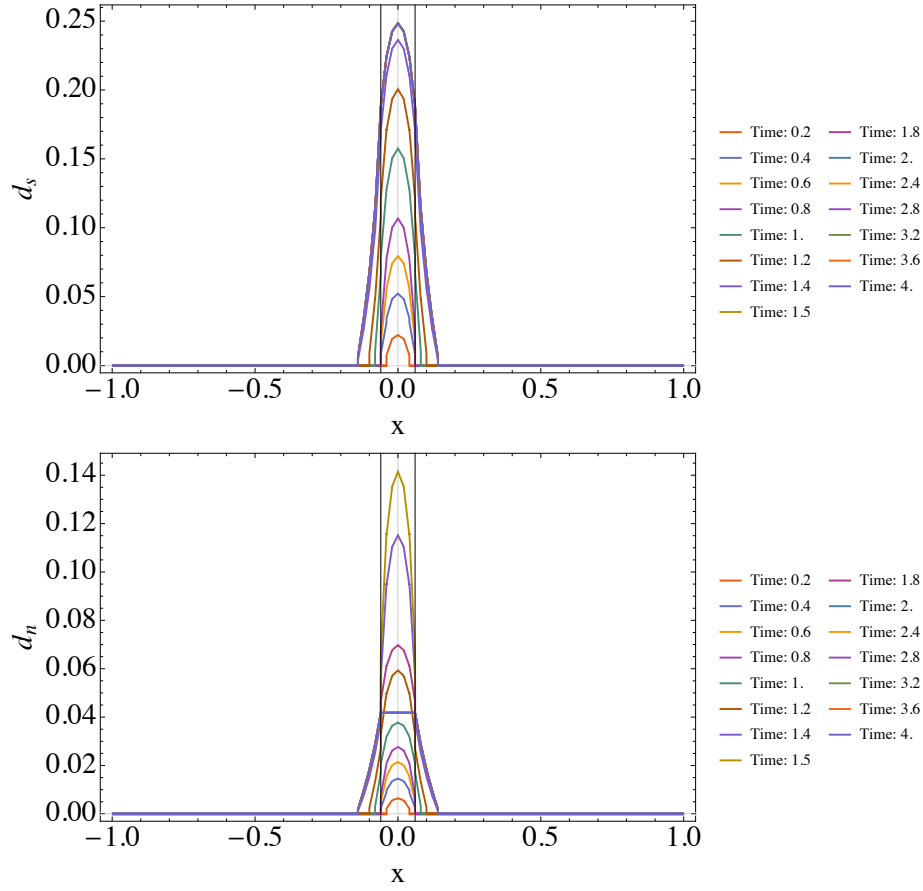


Figure 4.9: Time evolution of slip d_s (top) and opening d_n (bottom) along the fracture during loading and unloading process. The vertical black lines delineate the application zone of the mechanical force.

$$N_{2d}(L, l, \theta, \phi \dots) dl d\theta \dots,$$

which represents the number of fractures contained in an area of typical size L , with length between l and $l + dl$, orientations in θ and $d\theta$, positions in ϕ and $d\phi$, and a set of other properties (denoted by dots \dots). Several fracture distribution models have been introduced in literature (lognormal distribution, gamma law, exponential, power law among others - see Bonnet et al. (2001), Lei et al. (2017) for well done reviews), leading to a not unique choice of the expression for N_{2d} . Each distribution model, however, must contain scaling relations that enable to capture appropriately the multi-scale nature of the problem. In this contribution, we adopt a distribution model that contains two scaling laws: the fractal density (given by the fractal dimension D_{2d}) and a power-law distribution for fracture length generation (exponent a) with cut-off for minimum and maximum fracture lengths (denoted by l_{min} and l_{max} respectively). This choice has been demonstrated in numerous studies at different scales and in different tectonic settings (Hatton et al. 1994, Sornette et al. 1993, Anders & Wiltchko 1994, Kranz 1983, Walmann et al. 1996).

Assuming fracture lengths, positions (or density) and orientations independent entities, we can write the fracture distribution model as

$$N_{2d}(L, l, \theta, \phi) = \alpha(\theta, \phi) L^{D_{2d}} l^{-a}, \quad \text{for } l \in [l_{min}, l_{max}]$$

where $\alpha(\theta, \phi)$ is the fracture density term, which depends on their orientations and positions. Note that the only intrinsic characteristic length scales in this model are the smallest l_{min} and the largest l_{max} fracture lengths. The exponents D_{2d} and a quantify the scaling aspects of the DFN (Lei & Wang 2016, Lei & Gao 2018): the former govern the fracture density, whereas the latter govern the length distribution.

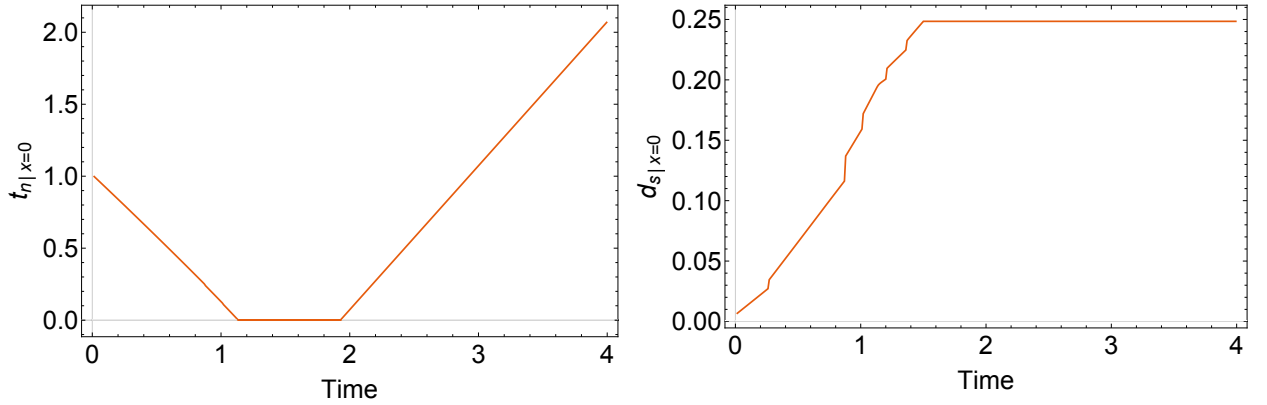


Figure 4.10: Time evolution of normal traction t_n (left) and slip d_s (right) at the fracture centre, i.e. at $x = 0$.

According to extensive outcrop data, D_{2d} typically varies between 1.5 and 2.0, whereas a ranges between 1.2 and 3.5 (Bonnet et al. 2001). In this preliminary investigation, we assume that fractures are uniformly distributed within the region of interest $L \times L^4$ (with random locations and orientations). This assumption implies that the fractal dimension D_{2d} equals the Euclidean dimension, i.e. $D_{2d} = 2$ (homogenous and isotropic case).

By removing the system-size effect, the density distribution model reduces to

$$n_{2d}(l, \theta, \phi) = \frac{N_{2d}(L, l, \theta, \phi)}{L^{D_{2d}}}, \quad \text{for } l \in [l_{min}, l_{max}]$$

which can be scaled by $\frac{l_{min}^{1-a}}{-1+a}$ to obtain the probability density function (pdf)

$$f_{2d}(l) = \frac{-1+a}{l_{min}^{1-a}} l^{-a}, \quad \text{for } l \in [l_{min}, l_{max}] \quad (4.25)$$

This probability density function represents the scaling law for fracture lengths for a given DFN. Typically, this law must be spanned at least for two order of magnitudes.

In order to generate the set of pre-existing fractures, we use ADFNE, an open source library (written in Matlab) for DFN generation (Alghalandis 2017), replacing the original exponential distribution for fracture lengths with power law distribution of type 4.25. For a given set of DFN properties, initial and end coordinates of each fracture are obtained. A pre-processing script written in Mathematica is then used to mesh all the generated fractures, with the possibility of i) controlling the mesh element size per fracture, ii) inserting automatically a mesh node at each fracture intersection and finally iii) set a minimum number of elements per fracture.

4.3.2 Scaling & dimensionless governing parameters

The unknowns of the problem are i) distribution of tractions $t_i(x, t)$, ii) distribution of displacement discontinuities $d_i(x, t)$ and iii) pore pressure evolution $p(x, t)$ or equivalently the over-pressure evolution $\Delta p(x, t) = p(x, t) - p_o$ along the DFN.

Upon fluid injection into a DFN and activation of a shear crack, the shear stress within the slipping patch must equal the frictional shear resistance ($F_2(\mathbf{t}_s^{n+1}, \mathbf{t}_n^{n+1}) = 0$). If we consider a cohesionless DFN with a constant friction coefficient, this constraint reads

$$t_s(x, t) = f \cdot t'_n = f \cdot (t_n(x, t) - p_o - \Delta p(x, t)), \quad |x| < a,$$

⁴Note that this assumption may not reflect most of the real cases, in which discrete set of joints of fracture with given orientations are observed. However, it can be easily relaxed to account for more complex configurations.



where a is half length of the slipping patch for a given fracture of the DFN. Under this conditions, the quasi-static equilibrium equation related only to the shear degrees of freedom reads in the most general case

$$t_{s,p}^k - f\Delta p(x, t) - t_{s,o}^k = -\frac{E'}{4\pi} \sum_k \int_{-a_k(t)}^{a_k(t)} \frac{\partial d_s(s, t)}{\partial s} \frac{ds}{x-s}, \quad k = 1, \dots, N_{fracs},$$

where $t_{s,p}^k = f \cdot t_{n,o}^{\prime,k} = f(t_n^k - p_o)$ is the (peak) shear strength of each pre-existing fracture k at ambient condition (i.e. prior pressurization), f is the friction coefficient, $t_{s,o}^k$ is the ambient shear stress of each fracture and E' is the plane-strain elastic modulus. Note the subscript k refers to distinct fractures in the DFN. Using $t_{s,p}^k$ and $d_{s,w} = \frac{t_{s,p}^k}{E'} L$ to normalize the stress and the slip respectively, we rewrite the condition of elastic equilibrium in the normalized form as

$$\left(1 - \frac{t_{s,o}^k}{t_{s,p}^k}\right) - \frac{\Delta p(x, t)}{t_{n,o}^{\prime,k}} = -\frac{1}{2\pi(a_k/L)} \sum_k \int_{-1}^{+1} \frac{\partial d_s(a_k x + x_{o,k}, t)/d_{s,w}}{\partial q} \frac{dq}{z-q}, \quad k = 1, \dots, N_{fracs} \quad (4.26)$$

where $a_k = (a_{k+} - a_{k-})/2$ and $x_{o,k} = (a_{k+} + a_{k-})/2$. Note that the integral in equation 4.26 has been mapped to the interval $[-1, 1]$ via the transformation $x = a_k z + x_{o,k}$ and $s = a_k q + x_{o,k}$.

In equation (4.26), we can identify the stress criticality ratio $\Lambda = \frac{t_{s,o}^k}{t_{s,p}^k}$, which denotes how far a given fracture k , with a certain orientation with respect to far field stress, is from failure prior the fluid injection. The dimensionless ratio $\mathbb{T} = (1 - \Lambda)$ represents thus the understress of each fracture.

As far as the fluid flow is concerned, upon introduction of the following characteristic scales for spatial coordinate, time and increment of pore pressure respectively

$$x = \frac{L}{2} X, \quad t = \frac{L^2}{4\alpha} \Theta \quad (p - p_o) = t_{n,o}^{\prime,k_{inj}} \Pi, \quad (4.27)$$

the normalized fluid mass conservation equation (4.1) (in absence of dilatancy term) reads

$$\frac{\partial \Pi}{\partial \Theta} - \frac{\partial^2 \Pi}{\partial X^2} = 0 \quad (4.28)$$

In equation (4.27), $t_{n,o}^{\prime,k_{inj}}$ is the effective normal stress at ambient condition of the fracture in which fluid is injected.

The normalized injection condition, instead, reads

$$\Pi = \frac{\Delta P}{t_{n,o}^{\prime,k_{inj}}} \quad (4.29)$$

From this scaling analysis, we can deduce that the equations (4.26), (4.28) and (4.29) govern the solution for the normalized slip $d_s/d_{s,w}$, shear stress $t_s/t_{s,p}$, fluid over-pressure $\Delta p/t_{n,o}'$ and crack length a/L for each fracture k of the DFN. These quantities are function of normalized coordinate $2x/L$, stress criticality Λ (or equivalently fracture understress \mathbb{T}) and normalized maximum overpressure $\Delta P/t_{n,o}^{\prime,k_{inj}}$ at the fracture in which fluid is injected.

Since we are dealing with a discrete set of pre-existing fracture, each of them characterized univocally by a given orientation θ with respect to far field stress, the stress criticality Λ is not an unique parameter for the DFN. Actually, it can be expressed as a function of fracture orientation θ as well as effective stress anisotropy parameter $\kappa = \sigma'_{xx}/\sigma'_{yy}$ (being σ'_{xx} and σ'_{yy} the far field effective principle stresses). By expressing the effective tractions at ambient condition as

$$t_{n,o}' = n_x^2 \sigma'_{xx} + (n_x n_y + n_y n_x) \sigma'_{xy} + n_y^2 \sigma'_{yy}, \quad t_{s,o}' = s_x n_x \sigma'_{xx} + (s_x n_y + s_y n_x) \sigma'_{xy} + s_y n_y \sigma'_{yy},$$

where $n = (n_x, n_y)$ and $s = (s_x, s_y)$ are the orthonormal vectors of each mesh element, the stress criticality Λ reduces to

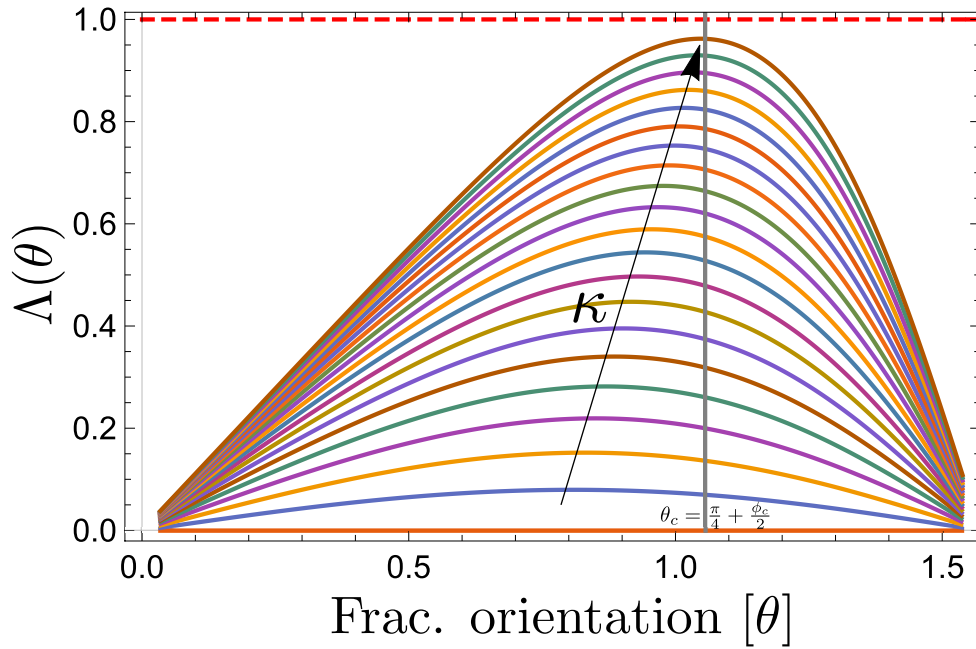


Figure 4.11: Stress criticality evolution as a function of fracture orientation θ and increasing values of effective stress anisotropy ratio κ , for a fixed value of friction coefficient $f = 0.6$ (or critical internal friction angle $\phi_c \simeq 0.54$ radians). The grey vertical line corresponds to the critical fracture orientation $\theta_c = \pi/4 + \frac{\phi_c}{2}$.

$$\Lambda = \frac{(\kappa - 1)}{f} \frac{\text{Cot}(\theta)}{(\kappa \text{Cot}(\theta)^2 + 1)}$$

In Figure 4.11, we can see the evolution of stress criticality Λ in function of fracture orientation θ (expressed in radians) and increasing effective stress anisotropy κ (denoted by the arrow), for a given value of friction coefficient f (specifically $f = 0.6$).

As expected, for the limiting value of $\kappa = 1$ all the fractures in the DFN are far from being critically stressed, i.e. their criticality is null regardless their orientation with respect to the far field stress. Interestingly, for increasing value of κ , the critical fracture orientation θ_c (value at which the stress criticality is maximum) migrates from $\theta = \pi/4$ to $\theta = \pi/4 + \frac{\phi}{2}$ (see grey vertical line), ϕ is the internal friction angle whose value is given by

$$\phi = \arctan(f)$$

Although it is well known in geotechnical engineering that the critical orientation for a Mohr-Coulomb type of soil is $\theta_c = \pi/4 + \frac{\phi}{2}$ (Knappett & Craig 2012, Lancellotta 2012), when dealing with stress criticality of a DFN the picture slightly change. This is strictly related to its definition, which is the ratio of shear stress and peak shear strength of each fracture. The migration of critical fracture orientation (which is somehow related to the skewness of each curve in Figure 4.11) is thus governed by the following dimensionless parameter

$$\Upsilon = \frac{(k - 1)}{f} = \frac{(\sigma'_{xx} - \sigma'_{yy})}{f \sigma'_{yy}},$$

which quantifies the level of effective stress anisotropy with respect to the frictional strength of the DFN. The higher is Υ , the more we expect that the critically stressed fractures are oriented at $\theta = \pi/4 + \frac{\phi}{2}$.

In the next two sections, we report two illustrative examples of fluid injection into a DFN, in which the pre-existing fractures are characterized by a way larger permeability compared to the one of the host

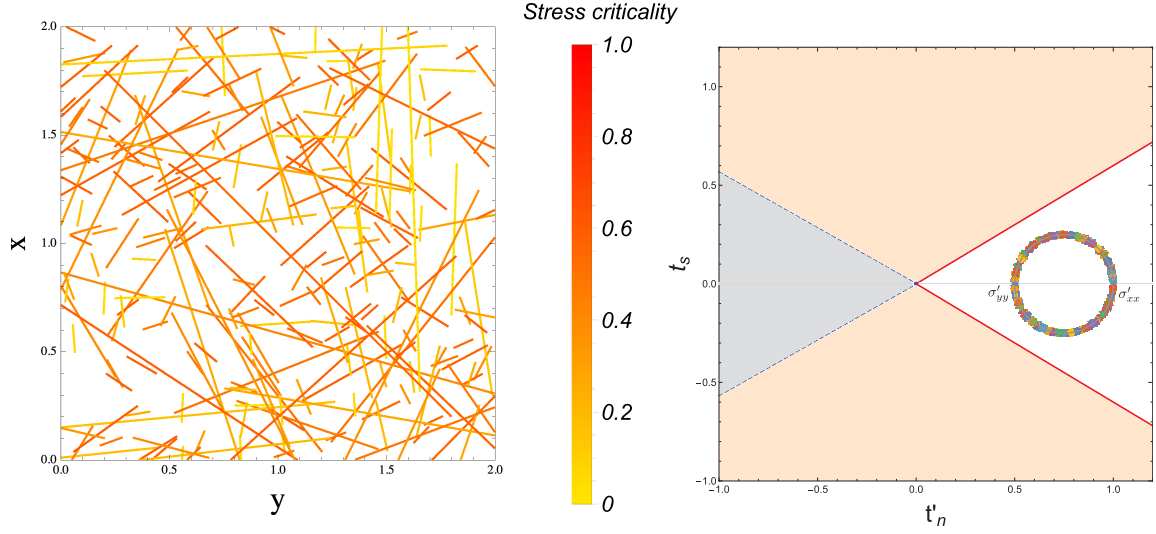


Figure 4.12: Stress criticality Δ of each fracture composing the DFN (left). On the right, all the uniform tractions distribution of each fracture are reported in the Mohr-Coulomb plane. Because of the relative low value of effective stress anisotropy ratio $\kappa = \sigma'_{xx}/\sigma'_{yy} = 2$, the Mohr circle is not closed to the yielding surface (red lines), leading thus to a marginally pressurized type of DFN. The light red area of the plot on the right corresponds to the (inadmissible) zone in which a mode II type of failure is reached, whereas the light grey zone corresponds to the mode I failure zone. The dashed blue lines correspond to the function $h(t_s, t_n)$ defined in equation X.

elastic medium. For a given value of friction coefficient f (here supposed to be constant during DFN pressurization) and a given value of normalized injection over-pressure $\Delta P/t_{n,o}^{l,k_{inj}} = 0.5$, we vary κ such that the pre-existing fractures at ambient conditions are either critically stressed (large κ) or marginally pressurized (relatively low κ), depending on their orientations with respect to far field stress.

4.3.3 Fluid injection into a marginally pressurized DFN

We consider a DFN composed of 251 fractures whose positions and orientations are uniformly distributed within the elementary area of characteristic size $L = 2$ (see Figure 4.12). The lengths of the fractures have been obtained through the power law distribution introduced in section 4.3.1, with the following input data

$$a = 1.2, \quad D_{2d} = 2, \quad l_{min} = 0.1, \quad l_{max} = 10$$

The DFN is subjected to a compressive far field stress (see Figure 4.12-right), whose components are

$$\sigma = \begin{bmatrix} \sigma'_{xx} & \sigma'_{xy} \\ \sigma'_{yx} & \sigma'_{yy} \end{bmatrix} = \begin{bmatrix} 1 & 0 \\ 0 & 0.5 \end{bmatrix}, \quad (4.30)$$

such that the effective stress anisotropy ratio is $\kappa = 2$. We suppose that the friction coefficient remains constant during the shear crack propagation ($f = 0.6$), which implies that slipping patch along the DFN propagates always a-seismically, regardless the local stress criticality of each fracture. Fluid is injected in the middle of the elementary area, i.e. at $(x_{inj}, y_{inj}) = (1, 1)$ - see Figure 4.12-left, controlling the pressure such that it remains always lower than the minimum principal effective normal stress ($\Delta P/t_{n,o}^{l,k_{inj}} = 0.5$).

Upon discretization of all the fractures with 11376 straight finite elements, we solve this problem with our one-way coupled HM solver. Due the large number of elements in the computational mesh (which implies 91008 degrees of freedom), a hierarchical elasticity matrix is used with the following parameters



$$\eta_{\mathcal{H}} = 5, \quad \epsilon_{ACA} = 10^{-6}, \quad N_{leaf} = 1000,$$

obtaining a compression ratio of (the ratio of the storage of the resulting hierarchical matrix compared to the fully populated original matrix)

$$T(\mathbb{E}_{\mathcal{H}}) = 0.253$$

Thanks to this compression, all the simulations reported in the following have been obtained with a laptop whose specific characteristics are

Processor: 2.9 GHz Intel Core i5, Memory: 8GB 1867 MHz DDR3

In Figure 4.12, we can observe the stress criticality Λ of each fracture as well as the position of the local (uniform) effective stress state at ambient condition (i.e. prior pressurization) of each fracture in the Mohr-Coulomb plane. By only looking at the Mohr circle in Figure 4.12-right, one can have an idea of the 'global' stress criticality of the DFN. Due to a moderate value of stress anisotropy ratio κ , all the fractures are marginally pressurized, even those whose orientations are close to the critical orientation of $\theta_c = \pi/4 + \phi/2$.

Since the fracture orientations are uniformly distributed within the area $L \times L$, the position of the stress state of each fracture along the Mohr circle span all angles.

At time $t = 0$, all the fractures are in equilibrium with the compressive stress state 4.30. Fluid is then injected under constant pressure at time $t > 0$ in order to activate a shear crack. Due to the pore pressure evolution within the pre-existing fractures, the shear crack propagates along them. The ending time of the simulation corresponds to the time at which the over-pressure front reaches the boundary of the elementary area.

In Figure 4.13, we include time snapshots of pore pressure evolution within the DFN. Since these time snapshots are expressed in terms of $\sqrt{4\alpha t}$, their values give an approximate idea of where the fluid over-pressure front is located within the region $L \times L$ (obviously we do not know exactly its position as it strictly depends on the percolation property of the DFN). In Figure 4.14, we report the corresponding snapshots slipping patch, denoted by the red color. As expected, the slipping patch lays always within the pressurized region as a result of relatively low stress criticality of each fracture. Notably, when the fluid front reaches the boundary of domain, the slipping patch remains small and is located close to the injection point. It is interesting to note that the upper evolution of the slipping patch is stopped by a fracture with very low stress criticality (nearly horizontal fracture - see Figure 4.14). On the other hand, the lower evolution of the slipping patch is followed by a branching out into another fracture with relatively large stress criticality.

4.3.4 Fluid injection into a critically stressed DFN

We show here the numerical results of fluid injection into a critically stressed DFN. The computational mesh as well as the input parameters are exactly the same as the ones of the previous case. However, the DFN in this case is subjected to a compressive stress state which reads

$$\underset{\sim}{\sigma} = \begin{bmatrix} \sigma'_{xx} & \sigma'_{xy} \\ \sigma'_{yx} & \sigma'_{yy} \end{bmatrix} = \begin{bmatrix} 1.541 & 0 \\ 0 & 0.5 \end{bmatrix},$$

leading to an effective stress anisotropy ratio of $\kappa = 3.082$. As one can notice from Figure 4.15, all the fractures whose orientation with respect to the compressive stress state tends to the critical value $\theta_c = \pi/4 + \phi/2$ are critically stressed, else they are marginally pressurized, i.e. their initial effective stress state is far from Mohr-Coulomb yielding surface. The injection point is the same as the one of the previous example (see Figure 4.15-left). As a large number of fracture are critically stressed, we thus expect that a small pore pressure perturbation will lead to a fast growth of the slipping patch (way faster than fluid diffusion front).

As one can see from the comparison of Figures 4.16 and 4.17, right after fluid injection, the slipping patch evolves rapidly, much faster than fluid diffusion front. As the slipping patch propagates, the stress state changes within the elementary area, activating remotely other fractures. At $\sqrt{4\alpha t} \simeq 0.37$, the pressurized zone is still confined near the injection point, while the slipping patch is way ahead. The slipping



patch evolution is driven by stress interaction between fractures. It is worth noting that all the fractures activated are characterized by a high stress criticality Δ . The relative position between the slipping patch and the fluid front position is, therefore, reversed with respect to the case of a marginally pressurized DFN.

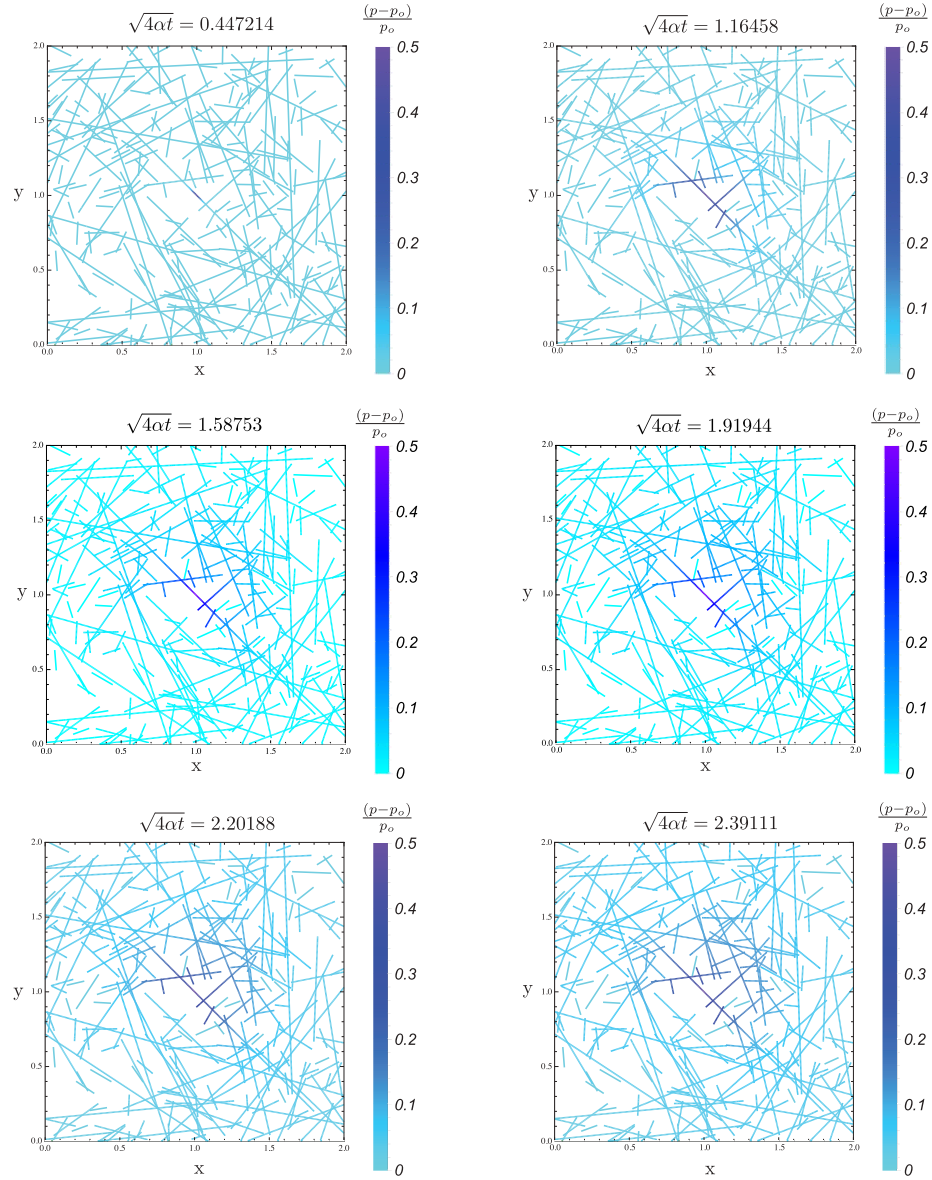


Figure 4.13: Time snapshots of over-pressure evolution in a marginally pressurized DFN ($\kappa = 2$). Fluid is injected into one fracture k_{inj} of the DFN, controlling the pressure at injection point (located at $(x_{inj}, y_{inj}) = (1, 1)$). Notably, fluid is injected at moderate over-pressure $\Delta P / t_{n,o}^{l,k_{inj}} = 0.5$ and it is always lower than the minimum principal effective normal stress. The friction coefficient f is constant and equal to 0.6, as well as the hydraulic conductivity α of all the fractures, i.e. we neglect shear-induced dilatancy or fracture increase of permeability during crack propagation.

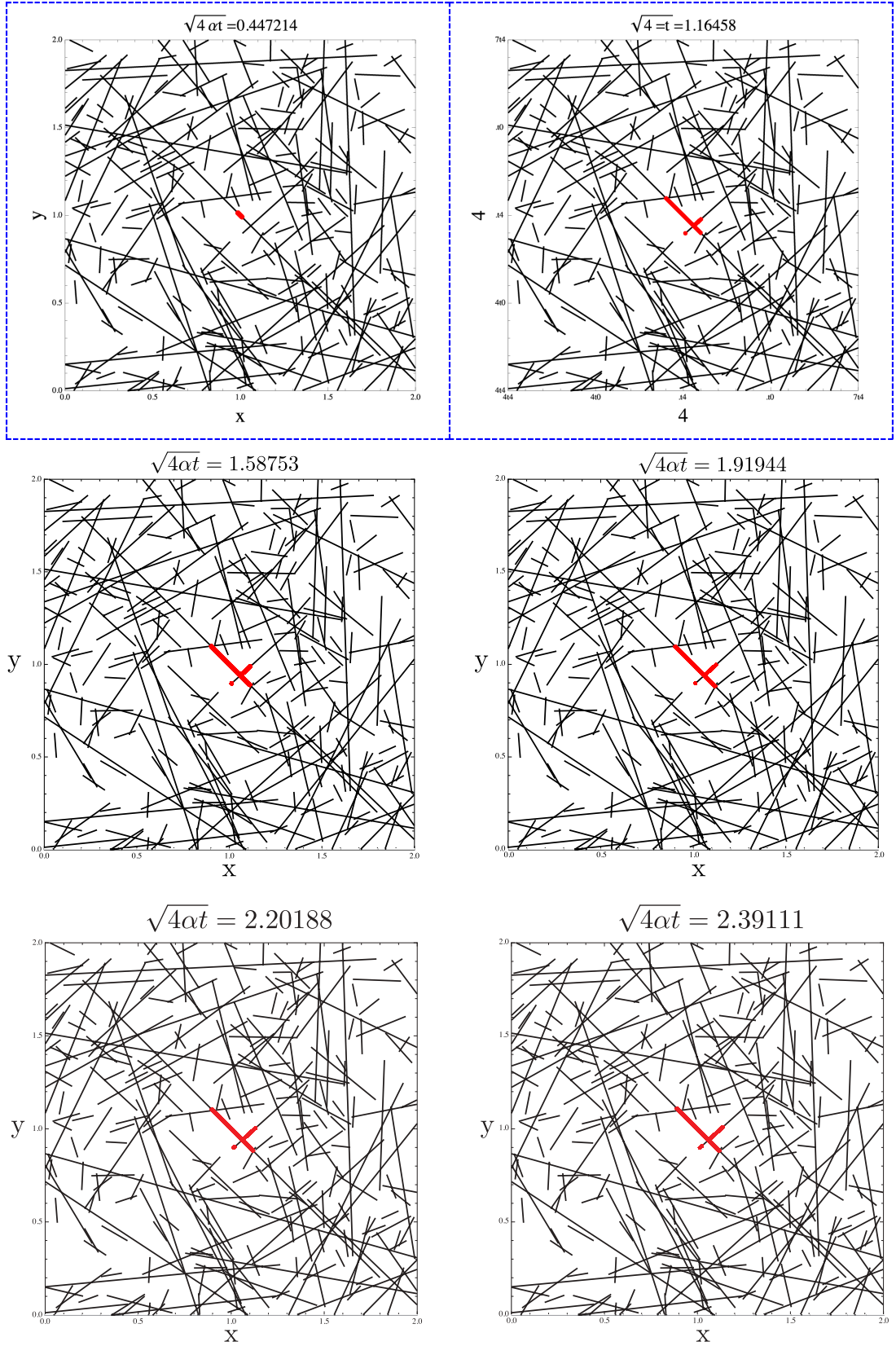


Figure 4.14: Time snapshots of slipping patch evolution (red lines) in a marginally pressurized DFN ($\kappa = 2$). These snapshots correspond to the same of Figure 4.13 for a better comprehension of the relative position between fluid front and slipping patch front.

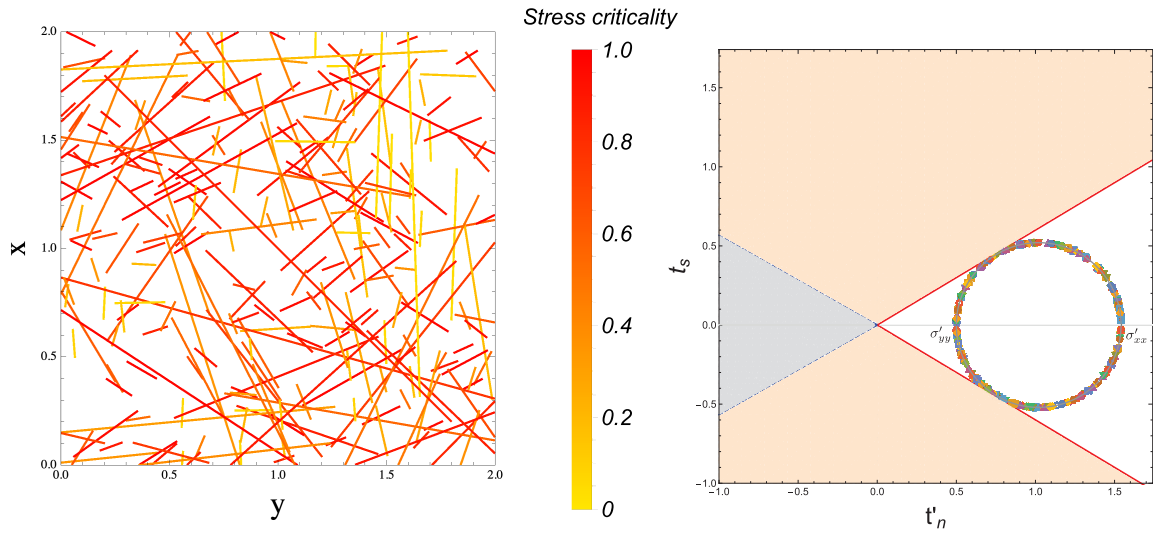


Figure 4.15: Stress criticality Λ of each fracture composing the DFN (left). On the right, all the uniform tractions distribution of each fracture are reported in the Mohr-Coulomb plane. Because of the relative large value of effective stress anisotropy ratio $\kappa = \sigma'_{xx}/\sigma'_{yy} = 3.082$, the Mohr circle is very closed to the yielding surface (red lines), leading thus to a critically stressed type of DFN. The light red area of the plot on the right corresponds to the (inadmissible) zone in which a mode II type of failure is reached, whereas the light grey zone corresponds to the mode I failure zone. The dashed blue lines correspond to the function $h(t'_s, t'_n)$ defined in equation X.

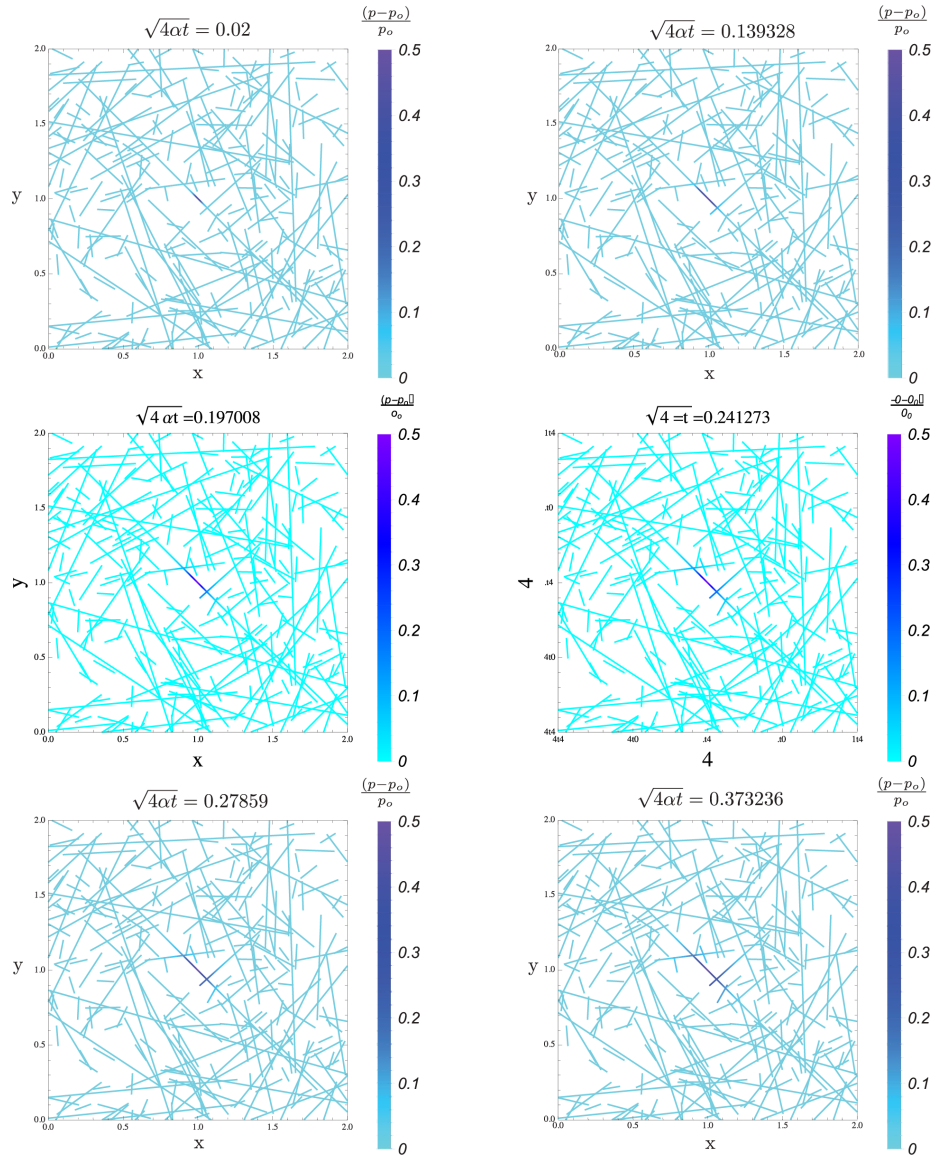


Figure 4.16: Time snapshots of over-pressure evolution in a critically stressed DFN ($\kappa = 3$). Fluid is injected into one fracture k_{inj} of the DFN, controlling the pressure at injection point (located at $(x_{inj}, y_{inj}) = (1, 1)$). Notably, fluid is injected at moderate over-pressure $\Delta P / t_{n,o}^{l,k_{inj}} = 0.5$ and it is always lower than the minimum principal effective normal stress. The friction coefficient f is constant and equal to 0.6, as well as the hydraulic conductivity α of all the fractures, i.e. we neglect shear-induced dilatancy or fracture increase of permeability during crack propagation.

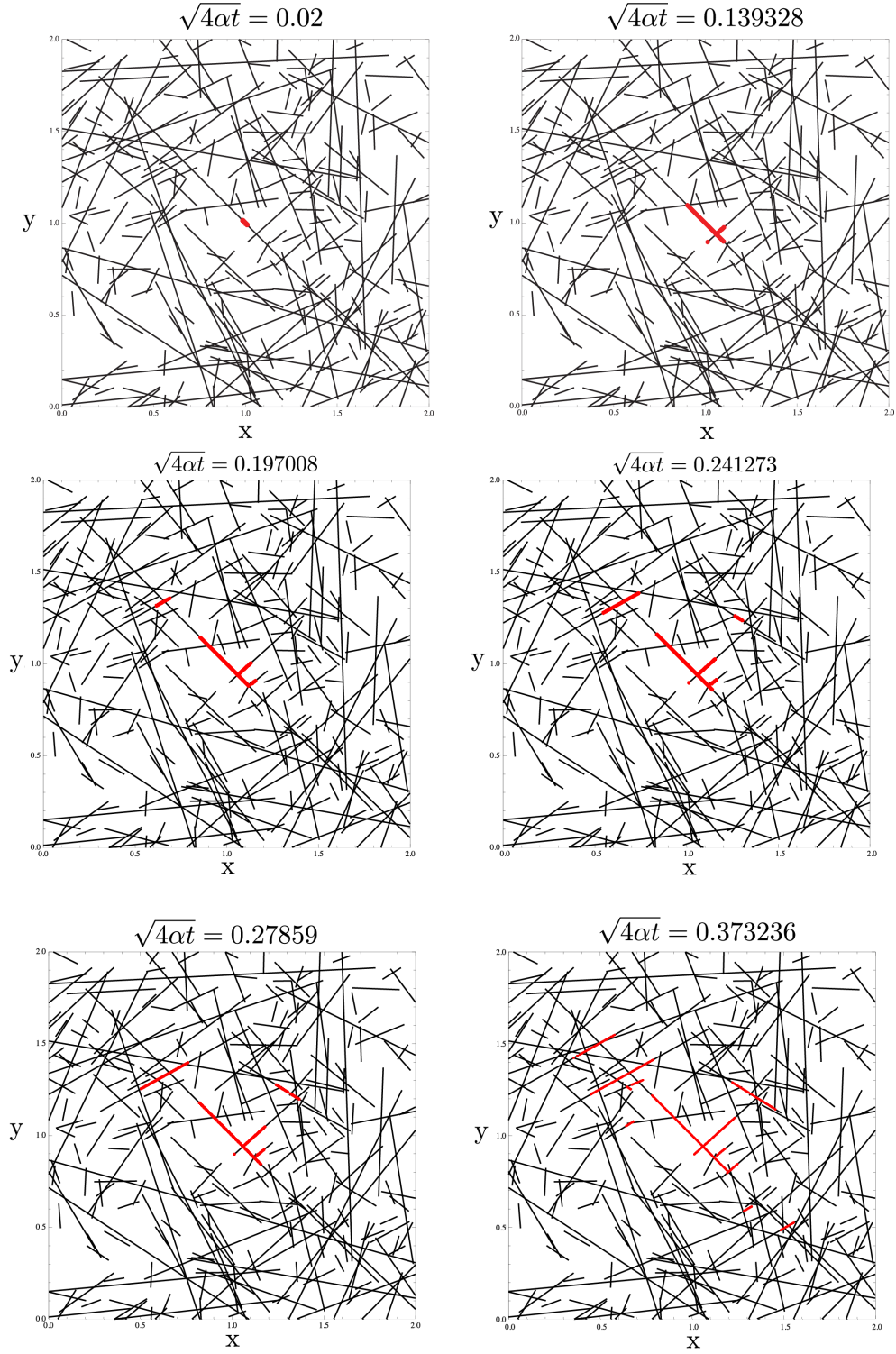


Figure 4.17: Time snapshots of slipping patch evolution (red lines) in a critically stressed DFN ($\kappa = 3$). These snapshots correspond to the same of Figure 4.16 for a better comprehension of the relative position between fluid front and slipping patch front.





Chapter 5

Fully coupled hydro-mechanical solver for planar fault - Effect of dilatancy on the nucleation of dynamic rupture induced by fluid injection



This chapter studies the effect of dilatancy on shear crack propagation along a planar pressurized fault. A pre-existing planar fault is embedded in an infinite, homogeneous, isotropic and linear elastic medium and it is subjected to hydro-shearing stimulation. Fluid is directly injected into the fault at a pressure below the local minimum principal effective normal stress at ambient condition with the specific purpose of activating a shear crack. Aseismic crack growth may or may not lead to the nucleation of a dynamic rupture depending on in-situ conditions, frictional properties of the fault and the value of overpressure. In particular, a fault is coined as unstable if its residual frictional strength τ_r is lower than the in-situ background shear stress τ_o . We study here how fault dilatancy associated with slip affect shear crack propagation due to fluid injection. We use a planar bi-dimensional model with frictional weakening and assume that fluid flow only takes place along the fault (impermeable rock / immature fault). Dilatancy induces an undrained pore-pressure drop during crack acceleration, locally strengthening the fault. We introduce an undrained residual fault shear strength τ_r^u (function of dilatancy) and show theoretically that under the assumption of small scale yielding, an otherwise unstable fault ($\tau_r < \tau_o$) is stabilized when τ_r^u is larger than τ_o . We numerically solve the complete coupled hydro-mechanical problem and confirm this theoretical estimate. It is important to note that the undrained residual strength is fully activated only if residual friction is reached. Dilatancy stabilizes an otherwise unstable fault if the nucleation of an unabated dynamic rupture -without dilatancy- is affected by residual friction, which is the case for sufficiently large injection pressure. We also discuss the effect of fault permeability increase due to slip. Our numerical results show that permeability increases lead to faster aseismic growth but do not impact the stabilizing effect of dilatancy with respect to dynamic rupture.

This chapter is a modified version of a scientific article published in the Journal of Geophysical Research: Solid Earth:

Ciardo, F., & Lecampion, B. (2019). Effect of dilatancy on the transition from aseismic to seismic slip due to fluid injection in a fault. *Journal of Geophysical Research: Solid Earth*, 124, 3724-3743. <https://doi.org/10.1029/2018JB016636>

5.1 Introduction

Seismic and aseismic ruptures associated with anthropogenic fluid injection at depth have been observed in variety of settings (Healy et al. 1968, Hamilton & Meehan 1971, Scotti & Cornet 1994, Cornet et al. 1997, Shapiro et al. 2006, Ellsworth 2013, Skoumal et al. 2015, Bao & Eaton 2016) to cite a few. Industrial applications involved range from waste water disposal to the stimulation of enhanced geothermal systems and hydraulic fracturing.

Injection of fluid into the sub-surface alters the local stress state. Pre-existing fractures/faults or intact rock mass can fail due to the local reduction of effective stresses associated with pore pressure increase. Shear fractures can thus be activated and propagate along favourably oriented planes of weaknesses/faults. In some cases, the aseismic slip may lead to the nucleation of a dynamic rupture (seismic event). A necessary ingredient for such a transition from aseismic to seismic slip is the reduction of fault frictional strength with slip, i.e. when the frictional resistance decreases faster than the elastic unloading associated with slip (Cornet 2015a).

The transition from the activation of aseismic slip to the nucleation of a seismic event due to fluid injection has been discussed theoretically (Garagash & Germanovich 2012) and observed in-situ (Scotti & Cornet 1994, Cornet et al. 1997, Guglielmini et al. 2015, Wei et al. 2015, Cornet 2016). We investigate here the effect of fault/fracture dilatancy associated with slip on the transition from aseismic crack propagation to seismic slip in the context of fluid injection. The physical mechanism of dilatancy associated with sliding over fault's asperities leads to a pore pressure drop under undrained conditions and thus to a fault strengthening denoted as dilatant hardening (Segall & Rice 1995, Segall et al. 2010, Rudnicki & Chen 1988). Strong dilatant behavior has been observed during aseismic crack propagation in scaled laboratory experiments by Lockner & Byerlee (1994), Samuelson et al. (2009) and inferred during field experiment of the stimulation of geothermal reservoir (Batchelor & Stubs 1985) suggesting that dilatancy possibly plays an important role on shear fracture propagation in some cases.

Although the concept of dilatant hardening associated with undrained conditions has been studied on saturated rock masses (Rice 1975) as well as on frictional weakening faults loaded by tectonic strain

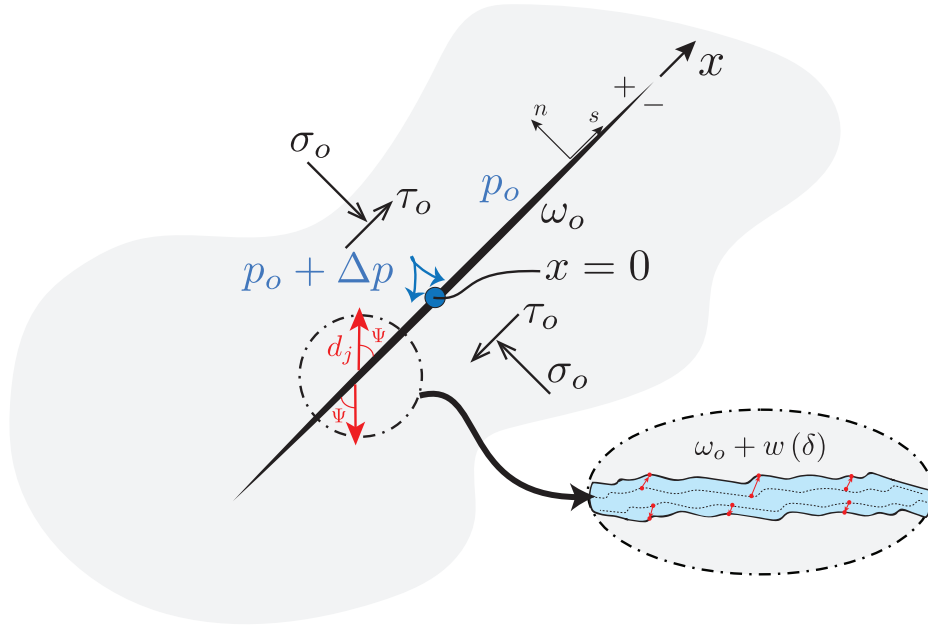


Figure 5.1: Model of frictional weakening dilatant fault & loading conditions. Zoom represents schematically the dilatant process that occur during shear fracture propagation.

(Rudnicki, J. W. 1979, Segall & Rice 1995, Shibasaki 2005, Segall et al. 2010), the quantification of its effect on the transition from aseismic to seismic slip propagation in association with fluid injection remains elusive.

The interplay between fluid injection, in-situ conditions, frictional properties and evolution of the hydraulic properties of fault present a highly coupled problem leading to a wide range of possible behaviour even under 'simple' homogeneous in-situ conditions (Garagash & Germanovich 2012, Viesca & Rice 2012, Zhang et al. 2005). In this paper, we extend previous work to account for fault dilatancy and quantify its impact on the propagation of a shear crack induced by a constant pressure injection. For simplicity, we reduce to a 2D configuration and model the fault / joint as a planar thin strip where both shear slip and fluid flow are localized. We adopt a simple linear weakening slip-dependent friction law Ida (1972) combined with a non-associated flow rule to account for dilatancy, assume isothermal conditions and neglect poroelastic stress changes in the surrounding rock. We pay particular attention to the verification of our numerical solver and discuss the different type of crack propagation (aseismic/seismic) as a function of in-situ and injection conditions. We also put in perspective our results at the light of theoretical arguments under the small-scale yielding approximation (Rice 1968, Palmer & Rice 1973).

5.2 Problem formulation

We consider an infinite planar fault in an infinite homogeneous isotropic elastic medium (see Figure 5.1) under plane-strain conditions. We also assume that the host rock has a much lower permeability than the fault. As a result, the fluid flow only occurs along the fault plane from a source injection located at the middle of the fault in the 2D space - more precisely a line-source in the out-of-plane direction to satisfy plane-strain conditions. Furthermore, we assume a uniform initial in-situ stress and pore pressure field prior to the start of the injection. Such a homogeneous model is obviously only valid for small fault slippage length compared to the background in-situ gradient but it allows to isolate and understand the different type of responses in a clearer way. Although different type of injection conditions, either away or directly on the fault, can be investigated, we restrict here to the case of a constant pressure injection from a point source directly in the fault.



5.2.1 Equilibrium, activation and dilatancy of slip-weakening fault

We consider the occurrence of a mode II shear crack of length $2a$ on the fault plane due to a constant pressure fluid injection. Initially, we assume the fault to be in static equilibrium with the uniform in-situ stress state. Upon activation of slip due to the increase of fluid pressure along the fault, the bi-dimensional quasi-static elastic equilibrium can be written as the following integral equations relating fault tractions and displacement discontinuities in the local normal and tangential frame along the fault plane (using the convention of summation on repeated indices):

$$t_i(x, t) = t_i^o(x) + \int_{-a}^a K_{ij}(\xi, x) d_j(\xi, t) d\xi, \text{ for } i, j = n, s \quad (5.1)$$

where $t_i = \sigma_{ij}n_j$ is the current traction vector acting along the fault, t_i^o its value under the initial in-situ stress and d_j denotes the vector of displacement discontinuities on the fault:

$$d_j = u_j^+ - u_j^- \quad (5.2)$$

The quasi-static fundamental elastic displacement-discontinuity tensor K_{ij} is known in closed-form for a bi-dimensional infinite medium (see e.g. Gebbia (1891), Crouch & Starfield (1983), Hills et al. (1996)). It is worthwhile to recall that for a planar crack, the shear and normal boundary integration uncouples as $K_{sn} = K_{ns} = 0$. As a result, shear slip does not induce any changes in the normal stress along the planar fault. However, if shear slip induces plastic dilatancy, the corresponding normal displacement discontinuity associated with dilatancy modify the normal stress along the fault. We note that the use of a quasi-static approach will obviously overshoot any finite dynamic rupture. Although a quasi-dynamic approximation (Rice 1993) would provide more realistic results without the expense of a complete dynamic simulation, we restrict our-self mostly to the nucleation of a dynamic rupture for which a quasi-static approximation is granted.

We adopt the convention of normal stresses positive in compression. The normal and shear components of the traction vector on the fault plane $t_i = (t_n, t_s)$ (in the local $s - n$ reference system on Figure 5.1) will be noted as $\sigma = -t_n = -(n_i \sigma_{ij} n_j)$ and $\tau = s_i \sigma_{ij} n_j$ for the normal and shear component respectively. We will also write the normal displacement discontinuities as $d_n = w$ (positive for opening) and the shear displacement discontinuities (slip) as $d_s = \delta$ (positive in a clockwise rotation).

5.2.1.1 Activation and plasticity

We assume that the fault obeys a Mohr-Coulomb yield criterion without cohesion, accounting for a slip weakening of friction. The yield criterion is:

$$F(\tau, \sigma') = |\tau| - f(\delta)\sigma' \leq 0, \quad (5.3)$$

where $f(\delta) = \tan(\phi(\delta))$ is the friction coefficient (ϕ the corresponding friction angle), which is supposed to weaken linearly with slip δ , from a peak value f_p to a residual value f_r for slip larger than δ_r (see Figure 5.2-bottom-left). $\sigma' = \sigma - p(x, t) > 0$ is the local effective normal stress acting on the fault plane. We will write the initial in-situ conditions (prior to fluid injection) as $\sigma'_o = \sigma_o - p_o$ and τ_o for the ambient effective normal stress and shear stress respectively.

The fault is activated when the injection overpressure is sufficient to reach the Mohr-Coulomb criterion at peak initial friction (see Figure 5.2-top), and shear slip starts to occur on the fault. We model the fault as rigid plastic and account for a possible dilatant behavior. Using a non-associative flow rule, the rate of displacement discontinuities (denoted with a dot) derive from a plastic potential function of the corresponding effective tractions when the yield criterion is satisfied (i.e. $F = 0$):

$$\dot{d}_i = \lambda \frac{\partial G}{\partial t'_i} \quad (5.4)$$

The (scalar) plastic multiplier λ is either greater than zero as long as the local stress state satisfies the Mohr-Coulomb yield criterion 5.3, or equals to zero for non-yielded stress state (for which $F(\tau, \sigma') < 0$ and the fault is not activated). Plastic slip takes place along the yielding surface (see plastic strain vector

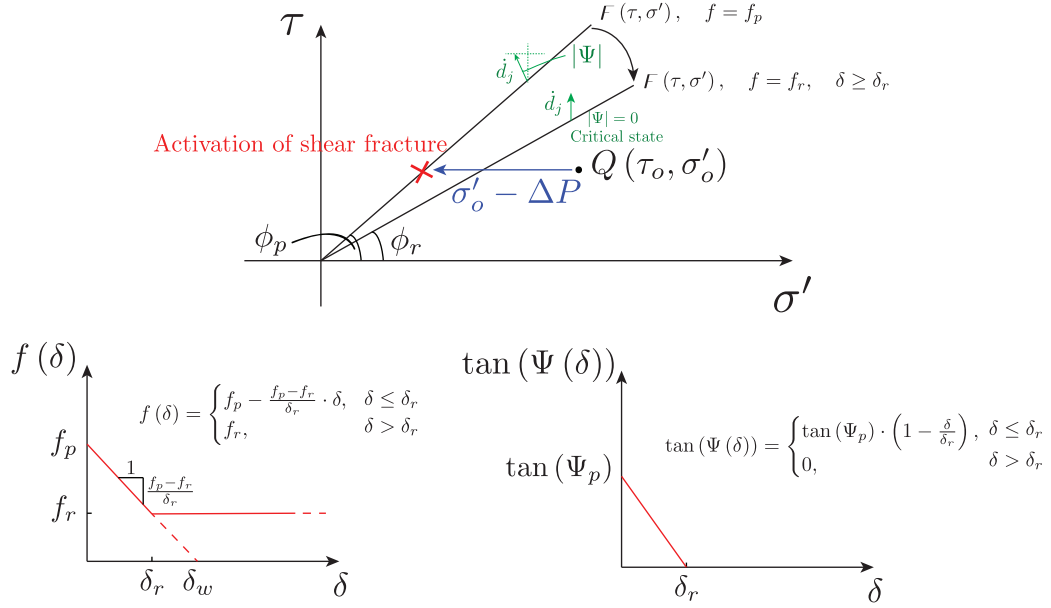


Figure 5.2: The Mohr-Coulomb plot (top) illustrates the evolution of the yielding surface $F(\tau, \sigma')$ with weakening of friction coefficient as well as the evolution of plastic displacement discontinuity vector \dot{d}_j with slip after shear fracture activation due to fluid over-pressure ΔP . The linear evolution of friction coefficient $f = \tan(\phi)$ (left) and dilatancy angle $\tan(\psi)$ (right) with slip δ are displayed in the bottom plots.

in Figure 5.2-top). This can be summarized by the following set of conditions (Lubliner, J. 2005, Maier et al. 1993):

$$\lambda \geq 0, \quad F(\tau, \sigma') \leq 0, \quad \lambda F(\tau, \sigma') = 0 \quad (5.5)$$

In order for plastic flow to occur, the tractions on the fault must persist on the yield surface $F = 0$, while upon unloading plastic flow stops as soon as $F < 0$. This requirement is often denoted as a consistency condition and written as

$$\lambda \dot{F}(\tau, \sigma') = 0, \quad (\text{if } F(\tau, \sigma') = 0) \quad (5.6)$$

It allows to obtain the plastic multiplier λ (see e.g. (Lubliner, J. 2005, Simo & Hughes 1997) for more details).

We use a non-associated Mohr-Coulomb criterion with a dilatancy angle ψ decreasing with accumulated slip δ . We write the plastic potential as

$$G(\tau, \sigma'_n) = |\tau| - \tan(\psi(\delta)) \sigma' \quad (5.7)$$

As a result, the rate of slip and opening displacement discontinuity are related to each other as:

$$\dot{d}_s = \dot{\delta} = \lambda \text{sign}(\tau) \quad (5.8)$$

$$\dot{d}_n = \dot{w} = \lambda \tan(\psi(\delta)) \quad (5.9)$$

We assume that the dilatancy coefficient (tangent of the dilatancy angle ψ) decreases linearly with slip from an initial peak value $\tan \psi_p$ to zero: the fault is assumed to reach a critical state (where the dilatancy angle is zero) over the same slipping distance δ_r at which it reaches residual friction (see Figure 5.2-bottom-right). Such a choice is consistent with experimental observations that a critical state (where no change of volume occur) is reached after sufficient plastic deformation for most rocks and granular material. Integration of 5.8-5.9 provides the following quadratic evolution of fracture width due to the dilatancy induced by slip:

$$w(\delta) = \int_0^\delta \tan(\psi(\delta')) d\delta' = \begin{cases} 2\Delta w \left(\frac{\delta}{\delta_r}\right) - \Delta w \left(\frac{\delta}{\delta_r}\right)^2 & \delta < \delta_r \\ \Delta w & \delta > \delta_r \end{cases} \quad (5.10)$$



where Δw denotes here the maximal / final dilatant opening at residual friction:

$$\Delta w = \int_0^{\delta_r} \tan(\psi(\delta')) d\delta' = \tan(\psi_p) \frac{\delta_r}{2} \quad (5.11)$$

A similar law for the dilatancy evolution with frictional slip has been proposed by Rudnicki & Chen (1988) to model uplift in sliding over asperities of a long homogeneous slab subjected to shear and normal mechanical loadings. Initially, the fault is supposed to have a constant uniform 'hydraulic aperture' ω_o which can be considered as the fault gouge thickness in such a model. The ratio between the maximal dilatant increment of fracture width Δw and this initial aperture ω_o defines a dilatant strain $\epsilon_d = \frac{\Delta w}{\omega_o}$ which can be related to the maximum change of fault porosity due to slip. Such a quantity will directly appear in the hydro-mechanical coupling.

Dilatancy is known to be function of effective normal stress - with lower dilatancy angle typically measured under larger confinement (Matsuki et al. 2010, Barton et al. 1985). Measured value of the peak dilatancy angle (at small slip) ranges from $\sim 40^\circ$ at 5 MPa of confinement to $\sim 6^\circ$ at 30 MPa for Inada granite (Matsuki et al. 2010), leading to values of ϵ_d in a range of $10^{-3} - 10^{-2}$. Laboratory experiments on quartz fault gouge (Samuelson et al. 2009) provides value of ϵ_d in the range $10^{-4} - 10^{-3}$ at effective confinement up to 20 MPa, values which appears of similar order than the one measured at larger confinement (Marone et al. 1990).

In what follows, for sake of simplicity, we do not explicitly account for the complete details of the dependence of dilatancy with normal effective stresses. The peak dilatancy angle can be implicitly taken to be a function of the level of in-situ confinement prior to injection. Moreover, we acknowledge that a relatively large range of possible value of the dilatant strain ϵ_d may exist from 10^{-4} to 10^{-2} .

5.2.1.2 Slip weakening and nucleation length-scale

Following Uenishi & Rice (2003), Garagash & Germanovich (2012), we introduce a characteristic nucleation patch length-scale a_w

$$a_w = \frac{E'}{2\tau_p} \delta_w \quad (5.12)$$

to scale the crack length. This characteristic nucleation length-scale is obtained by normalizing the slip δ and shear stress τ in the elasticity equation 5.1 by $\delta_w = \frac{f_p}{f_p - f_r} \delta_r$ and $\tau_p = f_p \sigma'_o$, respectively. δ_w denotes the amount of slip at which the friction coefficient goes to zero if an unlimited linear slip-weakening friction law is considered (see Figure 5.2-bottom-left). Typically δ_w is of the order the fault's asperities and thus ranges between 0.1 mm to 10 mm. $\tau_p = f_p \sigma'_o$ defines the peak frictional strength at ambient conditions, its difference from the ambient shear stress τ_o quantify the fault stress criticality. Such a peak fault shear strength can vary widely with depth, fault orientation as well as hydrogeological conditions (normally pressurized versus over-pressured formations) and thus can range between a fraction to hundred of MegaPascals. We thus deduce that the range of characteristic patch length-scale a_w (e.g. for a crystalline rock with $E' \sim 60$ GPa) can approximately ranges between tens of centimeters to tens of meters depending on geological conditions.

5.2.2 Fluid flow

Under the assumption of much smaller rock permeability compared to the longitudinal fault permeability, the fluid flow is confined within the fault zone. This case corresponds to an immature fault with little accumulated slip for which the extent of the damage zones around the fault core remains limited. For active and mature fault, the permeability structure around the fault can not be neglected. Much larger permeabilities have indeed been measured in the damage zone (that can have decameters thickness) of active mature fault compared to the fault gouge unit (Lockner et al. 1999). Here, we restrict to the case of an immature / young fault for which the flow is confined in the gouge. Such a hypothesis could also be valid for inactive mature fault that would have exhibited a plugging of their damage zone permeability (e.g. via long term thermo-hydro-chemical effects).



The mass balance equation width-averaged across the fault hydraulic aperture w_h of the gouge layer thus reduces to:

$$\frac{\partial \rho w_h}{\partial t} + \frac{\partial \rho w_h V}{\partial x} = 0, \quad (5.13)$$

where ρ is the fluid density and V is the averaged fluid velocity. The fault hydraulic aperture $w_h = \omega_o + w(\delta)$ is the sum of its initial value ω_o and the additional dilatant aperture function of slip (see eq. 5.10).

By combining fluid compressibility (taken as liquid water) and pore compressibility of the fault gouge in an unique parameter $\beta [M^{-1}TL^2]$, the width averaged fluid mass conservation 5.13 along the fault (x -axis) reduces to

$$w_h \beta \frac{\partial p}{\partial t} + \tan(\psi(\delta)) \frac{\partial \delta}{\partial t} + \frac{\partial q}{\partial x} = 0, \quad (5.14)$$

where $q = w_h V$ is the uni-dimensional local fluid flux given by Darcy's law:

$$q = -\frac{w_h k_f(\delta)}{\mu} \frac{\partial p}{\partial x}, \quad (5.15)$$

with μ the fluid viscosity $[ML^{-1}T^{-1}]$ and $k_f(\delta)$ the fault intrinsic permeability $[L^2]$. The hydraulic diffusivity of the fault $\alpha [L^2/T]$ is defined as:

$$\alpha = \frac{k_f}{\mu \beta} \quad (5.16)$$

In particular, the location of the fluid / pressure front evolves as $\sqrt{4\alpha t}$ for such type of diffusion problem (Carslaw & Jaeger 1959).

In conjunction with the increase of the fault aperture with dilatant slip 5.10, the longitudinal fault permeability may also evolve with shear slip. A number of different models have been proposed in the literature for the evolution of permeability with slip, from using the cubic law for the fault transmissivity (product of permeability $k_f = w_h^2/12$ and hydraulic aperture w_h), to an exponential dependence of permeability with normal stress, or Cozeny-Karman type relations. Here, we first make the assumption of a constant fault permeability $k_f = \omega_o^2/12$ before relaxing such an approximation in section 5.6 in order to properly gauge its effect.

It is important to note that even in the absence of permeability evolution, the changes of hydraulic aperture induced by dilatancy still impact the fluid flow in a non-trivial and non-linear way. This is notably due to the sink term $\tan(\psi(\delta)) \frac{\partial \delta}{\partial t}$ associated with slip induced dilatancy. Fluid flow can not be uncoupled from mechanical equilibrium and fault slip, contrary to the case of zero dilatancy (Garagash & Germanovich 2012), where for a constant pressure injection ΔP , the pore pressure on the fault plane is simply given by $p(x, t) = p_o + \Delta P \text{Erfc} \left[\frac{x}{\sqrt{4\alpha t}} \right]$. No simple analytical solution does exist for this complete non-linear hydro-mechanical coupling.

The effect of slip induced dilatancy leads to a pore-pressure drop under undrained conditions (denoted here as Δp_u). At large slip rate, the change of hydraulic width from its initial value up to its maximum value $\omega_o + \Delta w$ 5.11 will be sudden. In such an undrained limit the fluid has no time to flow and the associated pore pressure change can be directly obtained from mass conservation 5.14:

$$\Delta p_u = -\frac{\Delta w}{\omega_o \beta} = -\frac{\epsilon_d}{\beta} \quad (5.17)$$

This undrained pore-pressure drop will be localized at the crack tips, where frictional slip weakening occurs. From the previously discussed range of the dilatant strain $\epsilon_d \in [10^{-4} - 10^{-2}]$, for a compressibility coefficient β between the one of liquid water and usual pore compressibility ($\beta \in [5 - 100] 10^{-10} \text{Pa}^{-1}$), we obtain a range of values $[0.01 - 20]$ MPa for such an undrained pore-pressure drop. The previous estimate corresponds to the maximum possible amount of undrained pore-pressure drop (sudden slip from zero to δ_r). A re-strengthening of the fault is thus expected as the effective normal stress increase locally as a result of this undrained pore-pressure drop. Similar dilatant hardening is typically observed in fluid-saturated porous medium subject to undrained loading (Rice 1975, Rudnicki, J. W. 1979). It is important to underline that such re-strengthening effect is less pronounced for "mature" faults, for which pore fluid diffusion normal to fault plane (across the permeable units of damaged zone) may prevail against fluid diffusion along the fault gouge unit.



5.2.3 Initial and injection conditions

Initially, the (peak) fault strength $\tau_p = f_p \sigma'_o$ at ambient condition is everywhere larger than the in-situ shear traction on the fault τ_o . In other words, the fault is initially stable (i.e. $F(\tau_o, \sigma'_o) < 0$) and locked before the start of fluid injection. We consider here the case of a constant over-pressure ΔP at the injection point:

$$p(x = 0, t) = p_o + \Delta P, \quad (5.18)$$

We assume that the choice of the injection over-pressure ΔP is such that the minimum principal effective stress σ'_n always remain compressive (positive) such that no hydraulic fracture type failure occurs: i.e. $\Delta P < \sigma'_o$. A constraint often enforced in practice for large scale injection but also sometimes during hydraulic stimulation of geothermal reservoirs. We investigate here the activation of a shear crack that would occur if the overpressure ΔP at the injection point is sufficient to lower the effective normal stress and reach Mohr-Coulomb failure. Such a minimum over-pressure ΔP for activation is directly related to the fault criticality:

$$\frac{\Delta P}{\sigma'_o} \geq 1 - \frac{\tau_o}{\tau_p} \quad (5.19)$$

The ratio τ_o/τ_p represents the stress criticality of the fault at ambient condition (quantifying how far the fault is from failure). For a critically stressed fault ($\tau_o/\tau_p \sim 1$), slip is activated for small over-pressure. On the other hand, a fault whose initial uniform stress state is much lower than its peak frictional strength ($\tau_o/\tau_p \ll 1$) requires a larger over-pressure to activate a shear crack, and is sometimes referred to as a marginally pressurized fault.

5.3 Activation and transition between aseismic and seismic slip

5.3.1 Case of a non-dilatant fault

We first briefly recall the results obtained for the case of a non-dilatant fault by Garagash & Germanovich (2012) using the the same linear frictional weakening model. This summary is required in order to properly put in perspective the effect of a dilatant fault behavior.

After activation of aseismic slip, there exist two ultimate fault stability behaviors depending on the relative value of the residual strength (defined at ambient condition) $\tau_r = f_r \sigma'_o$ compared to the in-situ background shear stress τ_o . Notably, if the residual frictional strength τ_r exceeds the ambient shear stress τ_o , the fault is *ultimately stable*. On the other hand, for a residual frictional strength τ_r lower than τ_o , the fault is unstable. Figure 5.3 summarizes the different behaviors, as a function of the dimensionless fluid over-pressure $\Delta P/\sigma'_o$, stress criticality τ_o/τ_p and relative value of τ_r with respect to the initial shear stress τ_o . Region 1 on Figure 5.3 corresponds to the trivial case of an injection without activation of any slip.

For an ultimately stable fault (for which the residual strength τ_r is larger than the ambient shear stress τ_o), it can be shown that for an over-pressure sufficient to activate slip, at large time / large crack length the shear crack grows quasi-statically (aseismically) as long as the fluid injection continues (regions 2 and 3 on Figure 5.3). However, because of the weakening of its frictional properties, an ultimately stable fault may host an episode of seismic slip followed by an arrest (region 2 on Figure 5.3). Such a 'seismic event' depends on both the stress-criticality and the amount of over-pressure. For a moderate over-pressure (sufficient to activate slip), the shear-crack first lags behind the fluid diffusion front and, due to the interplay between fluid pressurization and frictional weakening, a dynamic event nucleate and grows until it catches up the fluid pressure diffusion front ahead of which the over-pressure is minimal. The subsequent propagation is then a-seismic and tracks the fluid front as long as injection continues. In other words, depending on the value of fluid over-pressure applied in the middle of the fault, the local accumulation of slip during the (aseismic) crack propagation varies. If the fluid over-pressure induces a large local slip accumulation during the aseismic propagation (such that it exceeds the residual slip δ_r), the fault never exhibits a dynamic event (strictly aseismic propagation - region 3), otherwise a nucleation of a dynamic rupture episode occurs (region 2 in Figure 5.3).

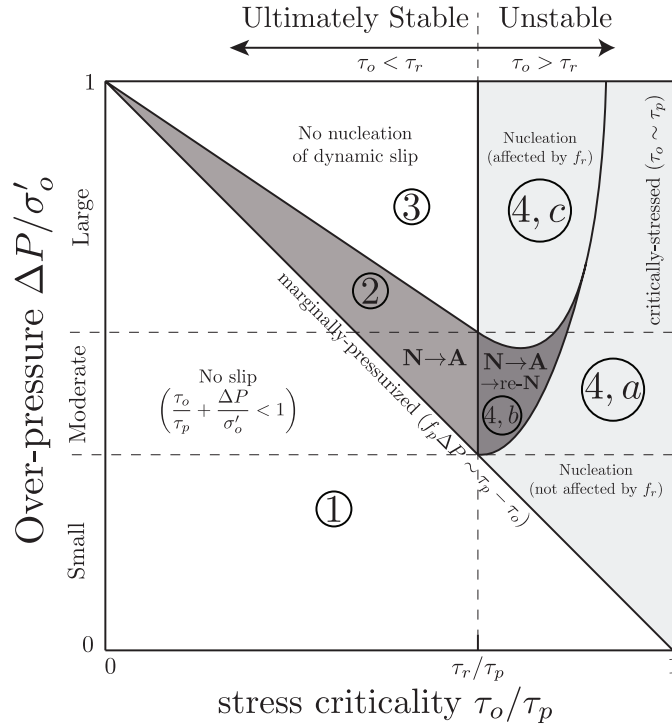


Figure 5.3: Phase diagram of (Garagash & Germanovich 2012) that describes the different regimes of propagation for a non-dilatant fault, as a function of the dimensionless fluid over-pressure $\Delta P/\sigma'_o$ and stress criticality τ_o/τ_p . Region 1 corresponds to the trivial case of an injection without fault re-activation. Regions 4a, b, c corresponds to the unstable fault case for which an unabated dynamic rupture occurs as the residual shear strength (defined at ambient conditions) is lower than the in-situ shear stress ($\tau_r < \tau_o$). Regions 2 and 3 corresponds to the case of ultimately stable faults ($\tau_r > \tau_o$) for which most of the crack growth is aseismic although transient seismic slip may occur (region 2).

The situation is different for unstable fault ($\tau_r < \tau_o$) - regions 4a, b, c on Figure 5.3. It can be proved that an unabated dynamic rupture will always occur when $\tau_r < \tau_o$. The nucleation length (and time of nucleation) depends again on stress criticality, the value of over-pressure and in some cases (region 4c) on the value of the residual friction f_r . For criticality stress fault (region 4a - $\tau_o/\tau_p \sim 1$), the nucleation patch size a_c is independent of the overpressure $a_c = 0.579 a_w$ (Garagash & Germanovich 2012). In these cases, even a small over-pressure is sufficient to nucleate a dynamic rupture and the fluid front lies well within the crack when the unabated instability occurs. For unstable but marginally pressurized fault (moderate stress criticality), subjected to a moderate value of over-pressure, a transient seismic event may occur and then arrest when the crack front catches up with the fluid front. However, here (region 4b in Figure 5.3) a re-nucleation always occurs (affected by residual friction) leading then to an unabated dynamic rupture. For larger of over-pressure, a single nucleation of an unabated dynamic rupture occur (region 4c).

5.3.2 Effect of dilatancy

5.3.2.1 Undrained fault response

At high slip rate, the undrained response associated with dilatancy causes a pore-pressure drop 5.17. Scaling the fluid pressure by effective normal in-situ stress, we express the undrained response via the



following dimensionless undrained pressure change

$$\frac{\Delta p_u}{\sigma'_o} = -\frac{\epsilon_d}{\beta \sigma'_o} \quad (5.20)$$

The dimensionless ratio $\frac{\epsilon_d}{\beta \sigma'_o}$ quantifies the effect of dilatancy in terms of pore pressure drop under undrained conditions with respect to the initial confining stress. For a realistic range of effective in-situ normal stress of [1-200] MPa, whose extremes may represent the case of normally pressurized and over-pressurized fault located approximately between 0.1 and 5 Km below the Earth's surface, and for the previously reported range for undrained pore-pressure drop ϵ_d/β , the dimensionless dilatancy parameter $\frac{\epsilon_d}{\beta \sigma'_o}$ ranges between 0.01 (deeper conditions/low dilatancy) and 20 (shallow conditions / large dilatancy).

Dilatancy is mobilized in the frictional weakening zone. Moreover, its impact on pore-pressure is modulated by the slip rate $\partial \delta / \partial t$ (see eq. 5.14). In proximity of a dynamic event when the slip rate increases rapidly, the undrained pore pressure drop leads to a local strengthening at the crack tip (dilatant hardening). In the case where the slip rate and crack velocity is larger than the fluid flux, the undrained dilatant pore-pressure drops will be at its maximum 5.17 and will persist inside the crack away from the crack tip. We can thus quantify the associated strengthening by adding its effect to the fault residual strength - defining an undrained residual shear strength τ_r^u as:

$$\tau_r^u = \tau_r - f_r \Delta p_u = \tau_r \left(1 + \frac{\epsilon_d}{\beta \sigma'_o} \right) \quad (5.21)$$

From the ranges of value previously discussed, we see that the undrained shear strength can be from 1.01 to 2 times larger than the drained residual strength.

On the other hand, the shear-induced dilation impact (via the non-associated flow rule 5.9) the distribution of normal stress along the fault through the effect of corresponding opening displacement discontinuity in the elasticity equation 5.1. Inside the crack, the opening of the fault leads to an increase of compressive normal stress, whereas ahead the crack tips it induces tensile stresses therefore reducing the fault frictional strength. There is thus an interplay between the non-local stress-induced perturbation due to fault opening and dilatant hardening. The tensile stresses ahead of the tip have however a lower magnitude than the undrained pore-pressure drop. For instance, if we suppose that the weakening region is small compared to the whole crack size (small scale yielding conditions), the mechanical opening is uniform and equal to Δw along the whole crack. We can thus estimate the tensile normal stress ahead of the crack front using the solution for an edge dislocation (e.g. (Hills et al. 1996)) of intensity Δw . Scaling the distance \hat{x} from the dislocation by the nucleation lengthscale a_w , we have

$$\Delta \sigma = -\frac{E'}{4\pi a_w} \frac{\Delta w}{\hat{x}/a_w} \quad (5.22)$$

The corresponding stress intensity for such a singular field is thus $E' \Delta w / (4\pi a_w)$. For a maximum increment of dilatant width Δw of the order of few millimeters and corresponding estimate of the nucleation patch size a_w gives an order of magnitude of about ~ 1 MPa or less for such stress perturbation. Taking the ratio of such stress intensity with the estimate of the undrained pore-pressure drop 5.17, after re-arranging, one obtain $E' \beta \omega_o / (4\pi a_w)$ which will be always smaller than one as $E' \beta \simeq O(10)$ and $\omega_o / a_w \simeq O(10^{-2})$. We therefore conclude that the mechanical effect of dilatancy induced tensile stresses ahead of the crack tip is lower than the undrained pore pressure change Δp_u . The dilatant hardening effect dominates. This is confirmed by our fully coupled numerical simulations (see section 5.5).

5.3.2.2 Small scale yielding & stability condition

Following the work of Garagash & Germanovich (2012), we extend their ultimate stability condition to account for the effect of dilatant hardening. This stability condition can be obtained under the assumption of small scale yielding (s.s.y) which holds when the shear crack of half-length a is sufficiently larger than the characteristic length scale a_w such that all the frictional weakening occurs in a small zone near the crack tip. Such a localization of the frictional weakening in a small zone near the crack tip can be observed



on our numerical results (see section 5.5.1). Under such assumption, the fracture energy G_c (Rice 1968, Palmer & Rice 1973) for the linear frictional weakening model can be estimated as:

$$G_c = \int_0^\delta \tau(\delta) - \tau_r \, d\delta \simeq \frac{\delta_r}{2} (f_p - f_r) \times \sigma'(a) \quad (5.23)$$

under the assumption that the effective normal stress $\sigma'(a)$ is constant within the weakening region. The condition for quasi-static crack growth of such a shear crack reduces to the classical linear elastic fracture mechanics criteria. The driving force for propagation G (the energy release rate) must equal G_c for quasi-static growth to occur. A criteria which for such a shear crack reduce to:

$$G = \frac{K_{II}^2}{E'} = G_c, \quad (5.24)$$

where K_{II} is the stress intensity factor for the given loading and crack size.

As all the crack -besides the small weakening zone at the tips- is at residual frictional strength, the stress intensity factor can be obtained by superposition of the effect of the loading of the crack by i) the residual frictional strength at ambient condition $\tau_r = f_r \sigma'_o$ minus the far-field in-situ shear stress τ_o (which are both uniform along the crack) and ii) the effect of the over-pressure due to the fluid injection on the decrease of shear strength $f_r \Delta p(x, t)$. The stress intensity factor for such a configuration is thus given as (Rice 1968, Tada et al. 2000)

$$K_{II} = (\tau_o - \tau_r) \sqrt{\pi a} + \underbrace{f_r \sqrt{\frac{a}{\pi}} \int_{-a}^{+a} \frac{\Delta p(x, t)}{\sqrt{a^2 - x^2}} dx}_{\Delta K_{II}(a, t)} \quad (5.25)$$

On the contrary to the non-dilatant case, the exact solution for the over-pressure $\Delta p(x, t)$ evolution along the fault is not known analytically. It is the complete solution of the coupled hydro-mechanical problem in the dilatant case. However, in order to obtain an ultimate stability condition for large crack length, it can be approximated as follow. If the shear crack a is much larger than both the slipping patch length scale a_w (which is required for the s.s.y approximation to be valid) and the diffusion length scale $\sqrt{4\alpha t}$, the over-pressure can be approximated as the sum of a point source term of intensity ΔP for the effect of the injection (as $a \gg \sqrt{4\alpha t}$) and the response of the undrained pore-pressure drop. Moreover, if the crack velocity is much larger than the fluid velocity - which would be true in all cases if the crack accelerates - the undrained pore-pressure drop can be assumed to remain constant and equal to Δp_u (eq. 5.17) over the entire crack. Under those conditions, the stress intensity factor reduces to:

$$\begin{aligned} K_{II} &\simeq (\tau_o - \tau_r) \sqrt{\pi a} + \frac{f_r \Delta P}{\sqrt{\pi a}} + \frac{\tau_r \Delta p_u}{\sigma'_o} \sqrt{\pi a} \\ &\simeq (\tau_o - \tau_r^u) \sqrt{\pi a} + f_r \frac{\Delta P}{\sqrt{\pi a}} \end{aligned} \quad (5.26)$$

where the undrained shear strength previously introduced appear. This expression is strictly similar to the one derived in Garagash & Germanovich (2012) pending the replacement of the residual shear strength τ_r by its undrained counterpart $\tau_r^u = \tau_r (1 + \epsilon_d / (\beta \sigma'_o))$ 5.21. As previously anticipated the effect of dilatancy is akin to an increase of the residual shear strength.

The reasoning of Garagash & Germanovich (2012) for the ultimate stability can thus be directly transposed to the dilatant case. In the limit of infinitely large crack $a \rightarrow \infty$, one directly see that the stress intensity factor tends to either $+\infty$ if $\tau^o > \tau_r^u$ and $-\infty$ if $\tau^o < \tau_r^u$. In other words, if the initial shear stress τ^o is larger than the undrained residual strength, the fault is ultimately unstable as the stress intensity factor diverges for large crack length: the nucleation of a dynamic rupture will thus always appear. On the other hand, the fault is ultimately stable when $\tau^o < \tau_r^u$. We therefore see that as the undrained residual shear strength τ_r^u is larger than τ_r , sufficient dilatancy may stabilize a fault that otherwise would be unstable. The minimal/critical amount of dilatancy ϵ_d^c required for such a stabilization to occur is simply given as:

$$\epsilon_d^c = \beta \sigma'_o \left(\frac{\tau_o}{\tau_r} - 1 \right) = \beta \sigma'_o \left(\frac{\tau_o f_p}{\tau_p f_r} - 1 \right) \quad (5.27)$$



It is interesting to note that it directly depends on the residual stress criticality τ_o/τ_r , and the in-situ effective normal stress.

It is important to note that - obviously - in the ultimately stable case ($\tau_r^u > \tau_o$) the stress intensity factor does not tend to $-\infty$ in reality as the propagation can only occur for $G = G_c$. Upon continuous fluid injection, a stable quasi-static growth will occur and will be modulated by the fluid diffusion: i.e the crack will decelerate for large crack length at constant injection. It is actually possible to devise an approximated solution for such a quasi-static growth by hypothesizing that the crack length evolves as a factor of the fluid front: $a = \gamma\sqrt{4\alpha t}$. An approximation of the pore-pressure evolution accounting for the undrained pore-pressure drop at the tip can be obtained and used in eqns. 5.24 and 5.25 to obtain an estimate of γ . Such an approximated solution is detailed and compared to our numerical results in Supporting Information in section 5.8.5. Such a refined (but still largely approximated) solution for the pore-pressure evolution gives the exact same limit for the stability condition at large crack length as well as critical dilatancy than the simpler profile postulated previously.

To conclude, before moving to the complete numerical solution of the problem, a word of caution is required with respect to the stability condition $\tau_o < \tau_r^u$. Such a stability condition holds on the premise that most of the crack is at residual friction pending a small weakening zone (s.s.y approximation). It is valid for sufficiently large crack length compared to a_w and peak slip larger than δ_r . Only under this assumption, the maximum undrained pore-pressure 5.20 can be achieved. If a dynamic rupture nucleates for slip smaller than the residual δ_r , the s.s.y is invalid: the undrained pore-pressure response will not be fully activated and thus not sufficient to quench the nucleation of a dynamic rupture. However, upon reaching larger crack length (and thus residual friction), the complete undrained pore-pressure will ultimately kicks in such that a dynamic rupture should arrest if the ultimate undrained s.s.y stability condition ($\tau_r^u > \tau_o$) is satisfied.

5.4 Numerical scheme description

Although approximation of the complete problem have allowed to highlight the stabilizing effect of dilatancy on the nucleation of a dynamic rupture associated with fluid injection, a full numerical solution is needed to investigate the complete parametric space and test the concept of a critical dilatancy.

The complete problem described in section 5.2 is fully coupled due to the dilatant fault behavior as well as non-linear due to the evolution of the fault hydraulic width (even if the fault permeability remains constant). It also involves the tracking of the moving crack tips. The shear crack evolves in space and time along the fault, paced by pore pressure evolution. Equation 5.1, which links tractions t_i on the fault plane with displacement discontinuities d_j , evolves in time due to the moving crack domain Γ . The developed numerical scheme solve this coupled problem by determining simultaneously the plastic multipliers λ in the 'active' zone of the domain (i.e. where $F(\tau, \sigma'_n) = 0$) through equations 5.1-5.8-5.9 and the increment of pore pressure Δp along the whole fault (through equation 5.14 and Darcy's law 5.15). We then recompute the increment of tractions (due to both increment of slip and the associated increment of hydraulic width) along the rest of the domain via the non-local elasticity equation 5.1. We have chosen a backward-Euler (implicit) time integration scheme for stability and robustness. A choice that stems from the restrictive CFL condition on the time-step for diffusion problem (e.g. (Quarteroni et al. 2000)) - which even deteriorates for strong non-linear variation of permeability similar to the hydraulic fracturing case (Lecampion et al. 2018).

We discretize the elasticity equations using the displacement discontinuity method (Crouch & Starfield 1983, Bonnet M. 1995) with piece-wise linear element (Crawford & Curran 1982). Because of the singular nature of the elastic kernel, the integral equation is collocated at points inside the displacement discontinuity segments. Knowing the effect in terms of traction of a single piece-wise linear displacement discontinuity, the problem reduces to the one of determining the distribution of displacement discontinuities that generates tractions along the fault such that equilibrium with initial tractions and the failure criterion is satisfied (Crouch & Starfield 1983). The fluid flow equation combining fluid mass conservation and Darcy's law is discretized via a vertex centered finite volume scheme. The fluid pore-pressure is assumed to vary continuously and linearly between element vertex.

In all the simulations reported here, the fault is discretized by N straight equal-sized elements (of



size h) - with a total mesh extent of $20 \times a_w$. We therefore have $2N_a$ unknown shear displacement discontinuities (more precisely the plastic multiplier) for the N_a active elements, and $N + 1$ unknowns for pore-pressure for all the element in the grid. After discretization, we obtain a non-linear system of size $2N_a + N + 1$, whose unknowns are composed of the plastic multipliers λ (which are linked to increment of slip $\Delta\delta$ through equation 5.8) in the N_a active yielded elements, and increment of fluid pressure Δp at every nodes of the grid ($N + 1$ unknowns). The size of such a non-linear system evolves with the shear crack propagation as more elements yield mechanically. The non-linearities of such a system are related to shear induced dilatancy and frictional weakening. For a given set of active elements, we use a fixed point iterative scheme to solve for this non-linear system - ending iterations when subsequent estimates of both the increment of slip and pore-pressure are within a relative tolerance of 10^{-6} .

The yielding/active set of element is then re-checked using the Mohr-Coulomb criteria. It is worth noting that an element is at failure when the Mohr-Coulomb criteria is reached for both collocation points in the piece-wise linear displacement discontinuity element.

Over one time-step, such a fully implicit algorithm thus solves the coupled problem by means of two nested loops. The outer loop identify the shear crack position by enforcing implicitly the friction weakening Mohr-Coulomb criterion 5.3 along the whole fault. The inner loop solve the aforementioned coupled non-linear hydro-mechanical system of equations for a trial set of active/yielded elements.

Full details about the numerical solver are included in section 5.8.1.

For numerical efficiency, the time step is adjusted based on the current crack velocity v^n , which is calculated via finite difference:

$$\Delta t^{n+1} = \zeta \frac{h}{v^n}, \quad (5.28)$$

where h is the element size and ζ is a user-defined constant parameter. This allows to better capture the response of the system during high slip rate, and increase time-step size during slow a-seismic growth. However, a constraint is required to avoid a too small time step that would necessarily occur when the shear crack is approaching a dynamic instability, for which the slip rate and crack velocity diverge. Notably, in our simulation, if the variation is such that $\Delta t^{n+1} < 0.8\Delta t^n$, we set $\Delta t^{n+1} = 0.8\Delta t^n$. Similarly, time-step should remain reasonable in order to avoid sampling the pore pressure evolution too coarsely. In our simulations, if $\Delta t^{n+1} > 3\Delta t^n$, then the time step change is constrained to $\Delta t^{n+1} = 3\Delta t^n$, and the initial time-step is taken as a small fraction of the characteristic diffusion time scale.

Thanks to the semi-analytical results of Garagash & Germanovich (2012) for the non-dilatant case, we have performed a thorough benchmarking of this numerical solver. Some of these verifications are described in the Supporting Information together with a mesh convergence study (see sections 5.8.2 and 5.8.3). Notably, our mesh convergence study have shown that the mesh size h must be such that at least 15 elements cover the characteristic lengthscale a_w to obtain accurate results (i.e. $h \leq a_w/15$). All the simulations reported herein have been performed with $h = a_w/25$.

5.4.1 Characteristic scales for dimensionless governing problem

By introducing properly chosen characteristic scales to normalize the governing equations, relevant physical processes can be systematically investigated. As already stated in Section 5.2.1.2, we follow the scaling of Uenishi & Rice (2003) and Garagash & Germanovich (2012) in order to normalize the elasticity equation 5.1 and friction weakening Mohr-Coulomb criterion 5.3. We thus scale the slip δ and the tractions t_i by the slip weakening scale δ_w and the peak fault strength $\tau_p = f_p \sigma'_o$, respectively. By doing so, one can identify the nucleation patch length-scale a_w (see equation 5.12), which is used to scale all the spatial variables: half crack length a and longitudinal spatial coordinate x . We scale the time t by the characteristic fluid diffusion timescale $a_w^2/(4\alpha)$. The characteristic scale for the fluid over-pressure, is taken as the in-situ effective normal stress σ'_o . Upon scaling the governing equations with the previous characteristic scales, the normalized solution is given by δ/δ_w , τ/τ_p , σ/σ'_o , $(p - p_o)/\sigma'_o$ and $2a/a_w$ and is function of only the following four dimensionless parameters (besides space and time):

- normalized injection over-pressure $\Delta P/\sigma'_o$
- dimensionless frictional weakening ratio f_r/f_p
- fault stress criticality τ_o/τ_p at in-situ conditions (prior injection)

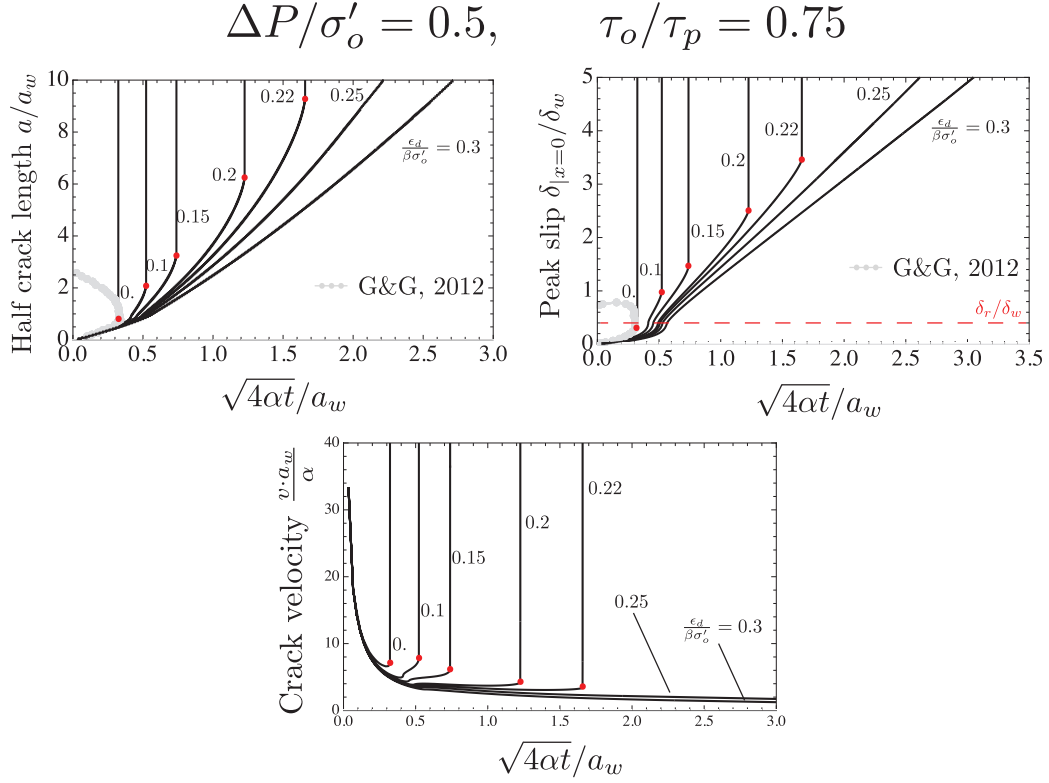


Figure 5.4: Time evolution of normalized half crack length a/a_w (top-left) and normalized peak slip δ/δ_w at the middle of the fault (top-right), i.e. at $x = 0$, for an otherwise unstable fault ($\tau_o/\tau_p = 0.75$), subjected to moderate over-pressure $\Delta P/\sigma'_o = 0.5$. The friction weakening ratio considered here is $f_r/f_p = 0.6$. The corresponding time evolution of normalized crack velocity va_w/α is showed in the plot at the bottom. We vary the dimensionless dilatancy parameter $\frac{\epsilon_d}{\beta\sigma'_o}$ below and above the critical stabilizing value- which is $\epsilon_{d,c}/(\beta\sigma'_o) = 0.25$ in this particular case. Red dots point the onset of unabated dynamic ruptures (color online).

- dimensionless dilatancy coefficient $\epsilon_d/(\beta\sigma'_o)$

All the numerical results of the following sections have been obtained and will be presented in dimensionless form. For all simulations, we fix the dimensionless frictional weakening ratio to $f_r/f_p = 0.6$ and explore the effect of the remaining dimensionless parameters: $\Delta P/\sigma'_o$, τ_o/τ_p and $\epsilon_d/(\beta\sigma'_o)$.

5.5 Dilatant hardening effect on a fault characterized by constant permeability

5.5.1 Case of unstable fault without dilatancy $\tau_o > \tau_r$

We first investigate numerically the effect of dilatancy on otherwise unstable fault, i.e. for which the in-situ shear stress is larger than the residual shear strength and the nucleation of a run-away dynamic rupture is always expected in the absence of dilatancy. We display the time-evolution of the different variables (crack length, maximum slip) using the square root of dimensionless time $\sqrt{4\alpha t}/a_w$ as the x-axis. Such a choice stems from the fact that the injection is diffusion controlled and $\sqrt{4\alpha t}/a_w$ is directly the ratio between the diffusion front over the nucleation lengthscale.



Figures 5.4-top-left and 5.4-top-right display the time evolution of half-crack length and peak slip for different values of the dimensionless dilatancy coefficient $\epsilon_d/(\beta\sigma'_o)$ for the case of a rather critically stressed fault $\tau_o/\tau_p = 0.75$ and a moderate injection over-pressure $\Delta P/\sigma'_o = 0.5$. The theoretical estimate of the critical dilatancy sufficient 5.27 to stabilize the fault is $\epsilon_{d,c}/(\beta\sigma'_o) = 0.25$ in that particular case. We clearly observe that an increase of dilatancy delays the occurrence of a dynamic rupture (highlighted by a red dot on these plots) for values below the critical dilatancy. However, for values of dilatancy equal or larger than the critical one, no nucleation is observed: the propagation is always aseismic. This can be better observed on the time evolution of crack velocity (Figure 5.4-bottom), where we see how dilatancy larger than the critical value kills the acceleration preceding the nucleation of a dynamic rupture.

Figure 5.5 displays the profile along the fault of the fluid over-pressure, friction coefficient, shear slip, effective normal stress and shear fault strength at different times for two distinct values of dilatancy, below and above the critical value. For insufficient dilatancy (left panel on figure 5.5), although an undrained pore-pressure drop can be seen in the weakening zone close to the crack tip, it is not strong enough to stabilize the fault and the last profiles reported in these plots is right before the nucleation of an unabated dynamic rupture. For this particular case without any dilatancy the nucleation occurs early and is not influenced by residual friction. We see that a dilatancy lower than the critical value delays the occurrence of nucleation which is now occurring when a significant part of the crack is at residual friction. For a value of dilatancy larger than the critical one (right panel on figure 5.5), the crack growth is always quasi-static. The undrained pore-pressure drops is now well developed and its minimum reaches the critical value $\Delta p_u/\sigma'_o = -\epsilon_{d,c}/(\beta\sigma'_o) = -0.25$ locally at the tip. The local fault re-strengthening can be observed on the corresponding effective normal stress profiles as well as on the corresponding shear strength versus slip results of our simulation (Figure 5.5). Under undrained conditions, near the crack tips dilatancy leads to a slip hardening phase before the onset of weakening, a response often observed in healed fault rocks. Brantut & Viesca (2015) used a non-monotonic, piecewise linear slip-dependent strength constitutive law (accounting for a strengthening phase followed by a weakening phase) to investigate earthquake nucleation in healed rocks. They solved semi-analytically an uncoupled problem for which stress perturbation is obtained through a mechanical loading whose time and space dependency is known analytically. They notably show that the strengthening phase that occur before the slip weakening phase considerably increases the critical nucleation size. This is in line with our numerical results for increasing values of dilatancy parameter (see Figure 5.5-(e) and the crack length at nucleation time for increasing values of dilatancy in Figure 5.4). We can also observe on these profiles that the weakening zone at the crack tip is small such that the stability condition derived previously under the assumption of small scale yielding is valid.

These simulations confirm the fact that dilatancy can stabilize an otherwise unstable fault if it is above the critical theoretical dilatancy previously derived in section 5.3.2.2. It is worth noting that this would have been difficult to demonstrate solely numerically even with very long simulations.

Effect of the injection over-pressure ΔP For the same value of stress criticality $\tau_o/\tau_p = 0.75$, placing ourselves at critical dilatancy ($\epsilon_{d,c}/(\beta\sigma'_o) = 0.25$ in that case), we test the influence of the amount of over-pressure. Figure 5.6 displays the time evolution of crack length and peak slip for different amount of injection over-pressure ΔP . As expected the larger the injection over-pressure, the faster the crack grows and the propagation remains quasi-static (aseismic). However, an interesting situation occurs for lower value of over-pressures (here $\Delta P/\sigma'_o = 0.4$ and lower) where the nucleation of an unrestricted dynamic rupture is observed. This somehow invalidates the existence of an universal value of stabilizing dilatancy independent of the over-pressure. However, we can clearly see that, for these low over-pressure cases, the peak-slip at the instant of nucleation is lower than the residual slip. In other words, the whole crack is weakening and has not yet reached residual friction. As a result, the undrained pore-pressure is not fully developed and not sufficient to stabilize the fault via dilatant hardening. In these cases, the small scale yielding assumption (small weakening zones at the crack tip) is invalid and the stability condition previously derived for large crack length compared to the characteristic nucleation patch size does not hold. It is worth noting that the nucleation of an unrestricted dynamic rupture is a consequence of the assumption of quasi-static elastic equilibrium. The shear crack velocity at nucleation time diverges instantaneously. Such an unbounded slip rate at nucleation will disappears if inertial terms are accounted for (full elastodynamic or quasi-dynamic formulation): energy dissipation via radiation of elastic waves

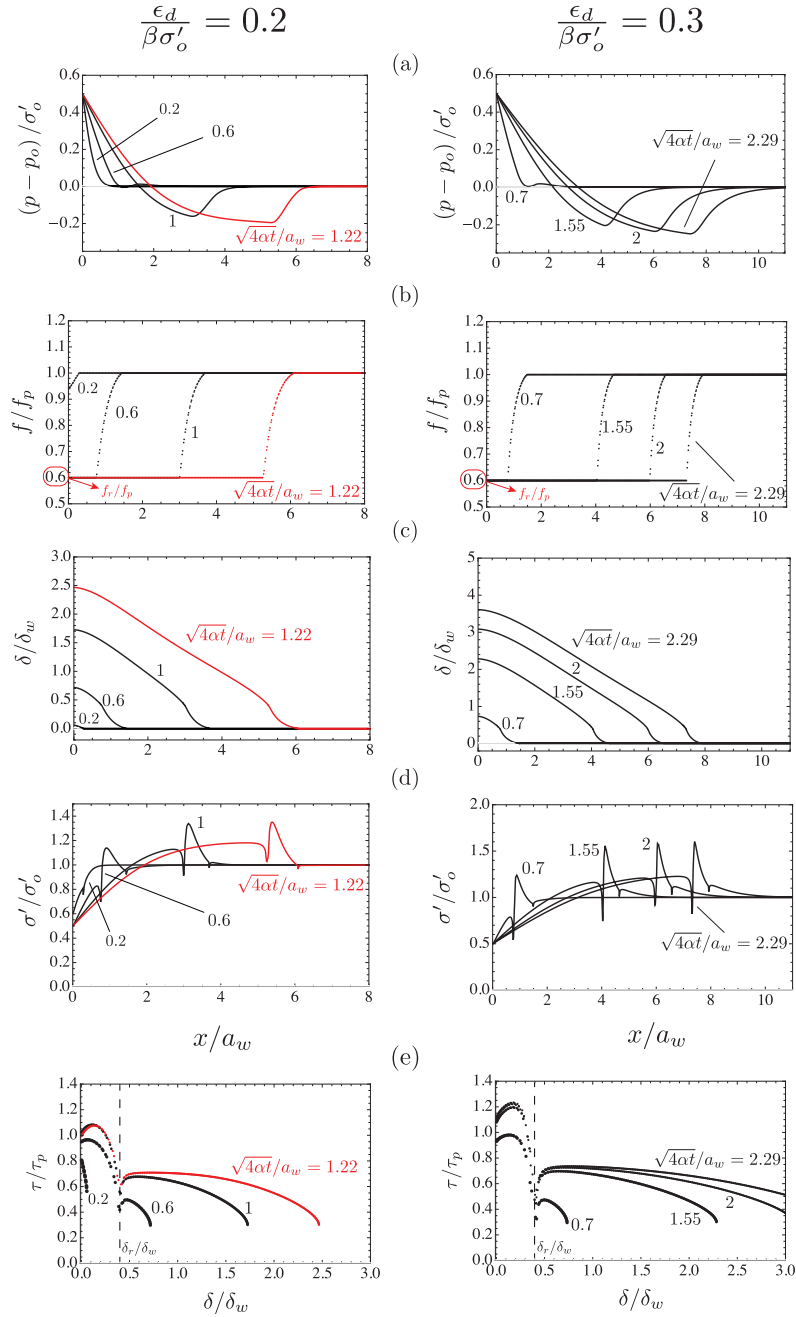


Figure 5.5: Spatial profile of a) dimensionless pore pressure, b) friction coefficient, c) slip, d) effective normal stress for a critically stressed dilatant fault ($\tau_o/\tau_p = 0.75$), subjected to a moderate overpressure $\Delta p/\sigma'_o = 0.5$, at different (normalized) time snapshots. Sub-figures (e) show the evolution of normalized shear strength with slip, at the same time snapshots. Results for two dimensionless dilatancy parameters are reported: left) ultimately unstable fault for which $\epsilon_d/\beta\sigma'_o$ is lower than the critical stabilizing value for that particular set of parameter ($\epsilon_{d,c}/\beta\sigma'_o = 0.25$), right) ultimately stable for a dimensionless dilatancy above the stabilizing value. Red curves (color online) denote the numerical results at nucleation time for the unstable case (left).

always ensure a finite crack velocity. In Figure 5.7, we show that using a quasi-dynamic formulation (with a rather large damping for illustrative purpose) the slip rate remains bounded and the crack propagation eventually slows down at later time compared to the quasi-static formulation where a divergence of the slip rate occurs at nucleation.

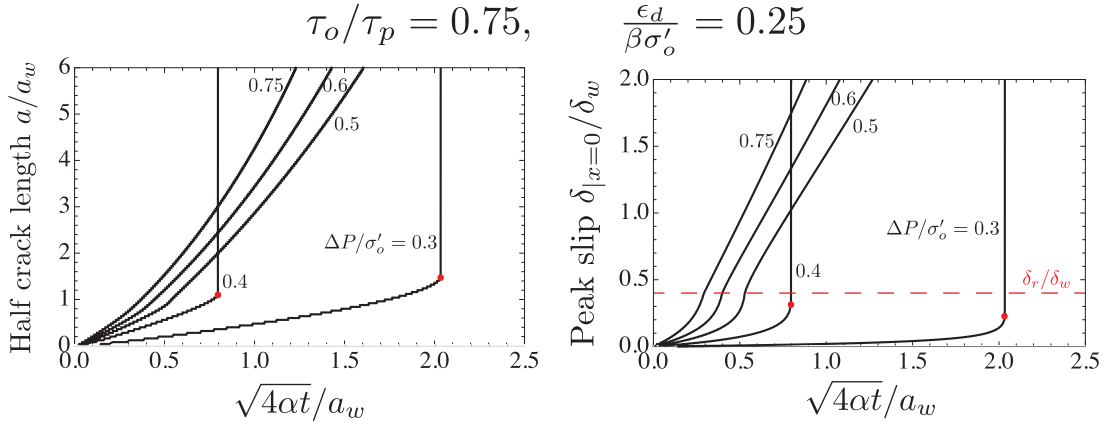


Figure 5.6: Effect of dimensionless overpressure $\Delta P/\sigma'_o$ on a critically stressed dilatant fault ($\tau_o/\tau_p = 0.75$), in terms of time evolution of dimensionless half crack length a/a_w and dimensionless peak slip $\delta/\delta|_{x=0}$. The dimensionless dilatancy parameter equals the critical value for such configuration: $\epsilon_{d,c}/(\beta\sigma'_o) = 0.25$.

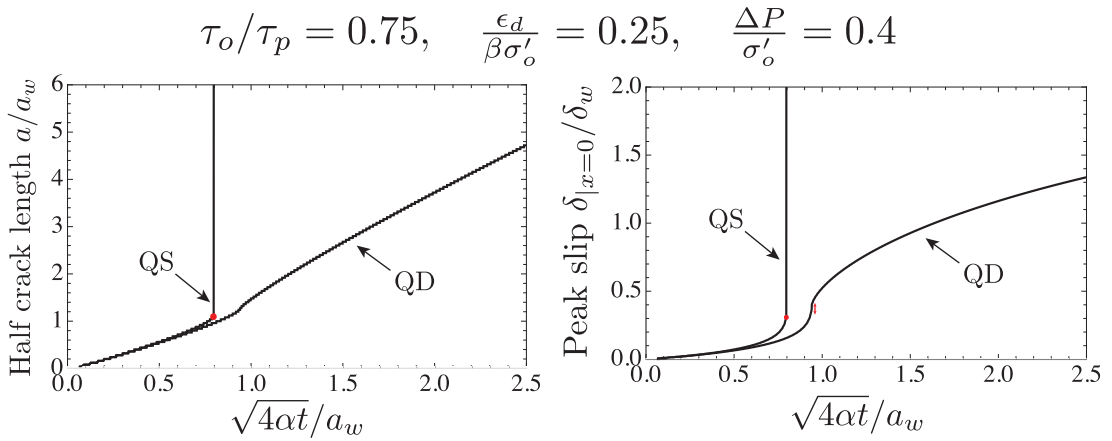


Figure 5.7: Time evolution of normalized half crack length and peak slip under quasi-static (QS) and quasi-dynamic (QD) approximation of elastic equilibrium. The latter is obtained by adding a seismic radiation damping term proportional to slip rate to elasticity equations in order to take into account energy dissipation through seismic waves orthogonal to fault plane during high slip rate (Rice 1993). The radiation damping term in normalized form reads $\frac{G\delta_w 4\alpha}{2c_s \tau_p a_w^2}$, being c_s the shear wave speed and G the shear modulus. We use here a very large value of 40 for such a dimensionless damping term, therefore over-damping the dynamic rupture.

In summary, if residual friction is reached during a-seismic crack propagation, the dilatant hardening effect stabilizes the fault for $\tau_r^u > \tau_o$ and the shear crack always propagates quasi-statically. This always occurs for sufficiently large values of over-pressure ΔP , which promotes larger initial aseismic slip rate thus maximizing the effect of dilatant hardening (i.e. sink term associated with dilatancy in the fluid mass conservation (5.14) is proportional to slip rate - $\tan(\psi(\delta)) \frac{\partial \delta}{\partial t}$). On the contrary, a lower over-pressure significantly slows down the initial aseismic crack growth and the beneficial effect of dilatancy can not develop sufficiently to avoid the nucleation of a dynamic rupture even when $\tau_r^u > \tau_o$. If inertia effects are included during crack acceleration (fully dynamic or quasi-dynamic elastic equilibrium), the slip rate will remain bounded and the full effect of dilatant hardening would eventually kick in for sufficient crack length

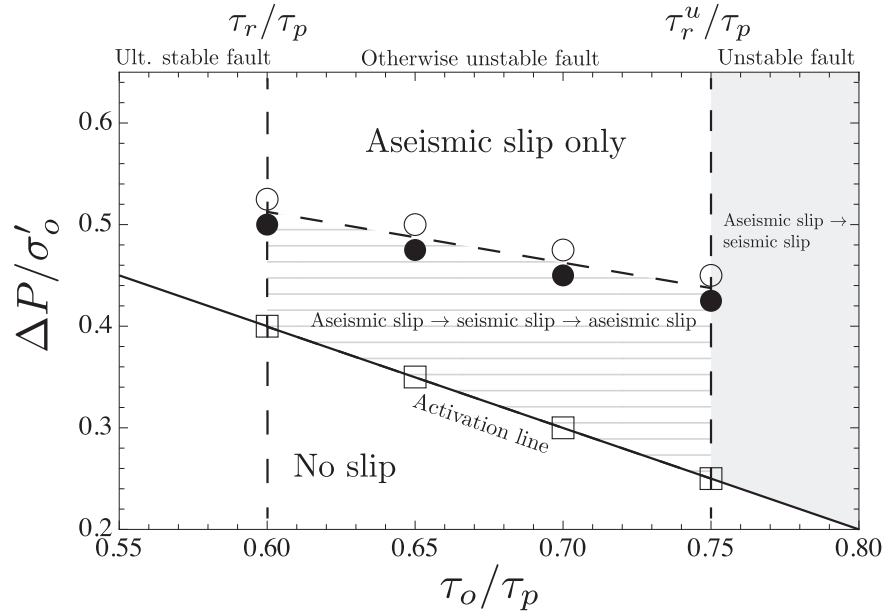


Figure 5.8: Numerical estimation of the minimum amount of over-pressure required to activate the full benefit of dilatant hardening and stabilize an otherwise unstable fault ($\tau_r < \tau_o$) for different stress criticality between the ultimately stable limit ($\tau_r/\tau_p = f_r/f_p = 0.6$ in that case) and the undrained dilatant residual strength ($\tau_r^u/\tau_p = 1.25\tau_r/\tau_p = 0.75$ in that case). The black filled circle denotes the maximum value of over-pressure below which a finite dynamic event always nucleate (for over-pressure above the slip activation limit), while the empty circle corresponds to the minimum normalized over-pressure required to stabilize such a fault (aseismic slip only for larger over-pressure). The minimum over-pressure required for slip activation ($\Delta P/\sigma'_o = 1 - \tau_o/\tau_p$) is also displayed as empty square/continuous line. Stress criticality τ_o/τ_p larger than τ_r^u/τ_p always result in the nucleation of unrestricted dynamic rupture for any value of over-pressure larger than the activation limit.

(larger than a_c) - therefore leading to an arrest of the dynamic rupture due to sufficient dilatancy ($\tau_r^u > \tau_o$). Full elastodynamic simulations would be needed to confirm that the dynamic rupture would indeed arrest upon full activation of dilatant hardening under those conditions of low injection over-pressure and large dilatancy.

For a given set of parameters, the exact minimum value of over-pressure required to fully stabilize the fault can not be estimated analytically, but can be estimated numerically via a series of simulations varying the injection over-pressure. Figure 5.8 displays such an estimation for different stress criticality τ_o/τ_p below or equal to the undrained residual strength - i.e. the domain where dilatant hardening can stabilize an otherwise unstable fault. More precisely, Figure 5.8 displays both the maximum overpressure for which a nucleation of finite dynamic event occur and the minimum over-pressure for which the propagation is solely aseismic (the fault is stabilized). A linear increase of the required over-pressure as the stress criticality decreases can be clearly observed. This can again be understood as a larger driving force is required to reach residual friction for lower stress criticality.

5.5.2 Case of an ultimately stable fault even without dilatancy ($\tau_o < \tau_r$)

We now turn to the case of ultimately stable fault ($\tau_o < \tau_r$), where only a transient seismic episode occurs for moderate over-pressure (region 2 of Figure 5.3) while crack growth is strictly aseismic for large over-pressure (region 3 of Figure 5.3).

For a configuration representative of region 2 in Figure 5.3 ($\tau_o/\tau_p = 0.55$, $\Delta P/\sigma'_o = 0.5$) a transient seismic episode occurs for a low accumulated slip: the residual friction is not yet reached anywhere in the crack. Such a seismic event is directly linked with the crack "catching" up the fluid front in association

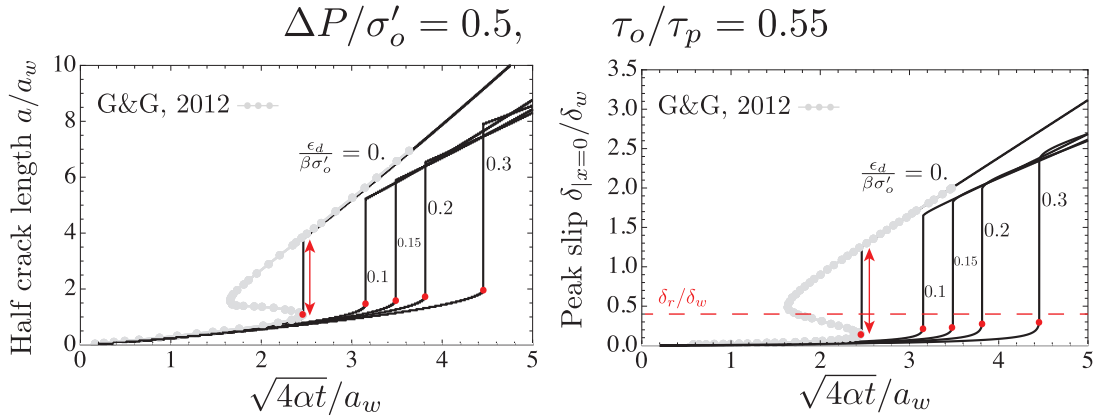


Figure 5.9: Time evolution of normalized half crack length a/a_w and normalized peak slip δ/δ_w at the middle of the fault, i.e. at $x = 0$, for an ultimately stable fault ($\tau_o/\tau_p = 0.55$ and $\tau_o < \tau_r$, for $f_r/f_p = 0.6$), subjected to moderate over-pressure $\Delta P/\sigma'_o = 0.5$. We span several dilatancy cases by varying the dimensionless dilatancy parameter $\epsilon_d/(\beta\sigma'_o)$. Red dots denote the onset of dynamic event, which is always characterized by a nucleation followed by an arrest (red arrow). The run-out distance increases with increase values of dimensionless dilatancy parameter $\epsilon_d/\beta\sigma'_o$.

with frictional weakening. Figure 5.9 displays the crack evolution and peak slip for such configuration for different values of dilatancy. Increasing dilatancy slow down the initial quasi-static crack growth and thus delay the nucleation of this finite seismic slip episode. Interestingly, because with larger dilatancy, the quasi-static crack lags even more behind the fluid diffusion front prior to nucleation, the dynamic run-out increases for larger dilatancy. After this finite seismic slip episode, upon continuous injection, the shear crack propagates quasi-statically on par with the evolution of the diffusion front $a \propto \sqrt{4\alpha t}$. Larger dilatancy slows down the quasi-static crack growth. The corresponding profiles of over-pressure, friction coefficient, slip and effective normal stress along the fault at different time snapshots are reported in Figure 5.10. The finite seismic episode can be clearly seen where we observe that prior to nucleation the weakening zone occupies the whole crack. Because the fault is ultimately stable, beside the seismic episode, the fault propagates quasi-statically: due to the low slip rate, dilatancy does not significantly alter the pore-pressure profile although the effect can be observed on the effective normal stress profiles (see Figure 5.10).

Finally for large over-pressure (region 3 of Figure 5.3), the crack growth is always quasi-static (aseismic). Results for such aseismic growth are reported in section 5.8.6. For similar stress and fault strength conditions, an increase of the fault dilatancy slows down the crack velocity as expected.

5.6 Effect of shear-induced permeability changes

The results presented so far are based on the assumption of a constant fault permeability - although in our numerical results the fault transmissivity $w_h k_f$ is changing in conjunction with the dilatant behavior. Experimental (Makurat et al. 1985, Lee & Cho 2002, Li et al. 2008, e.g.) and field evidences (Evans, Genter & Sausse 2005, Evans, Moriya, Niitsuma, Jones, Phillips, Genter, Sausse, Jung & Baria 2005) have shown that deep fractures under fluid induced slip exhibit an increase of fault permeability (Cornet 2015a, Evans, Genter & Sausse 2005, Evans, Moriya, Niitsuma, Jones, Phillips, Genter, Sausse, Jung & Baria 2005, McClure & Horne 2014). It is important to note that, although possibly significant, the increase of permeability with slip remains small compared to the drastic increase observed when the fracture opens (i.e. when the effective normal stress becomes tensile) such as in hydraulic fracturing. Like previously, we restrict here to the case of compressive effective normal stress, where permeability changes with slip are strictly associated with shear-induced dilatancy.

Several empirical models have been proposed and used in literature for permeability evolution. Some

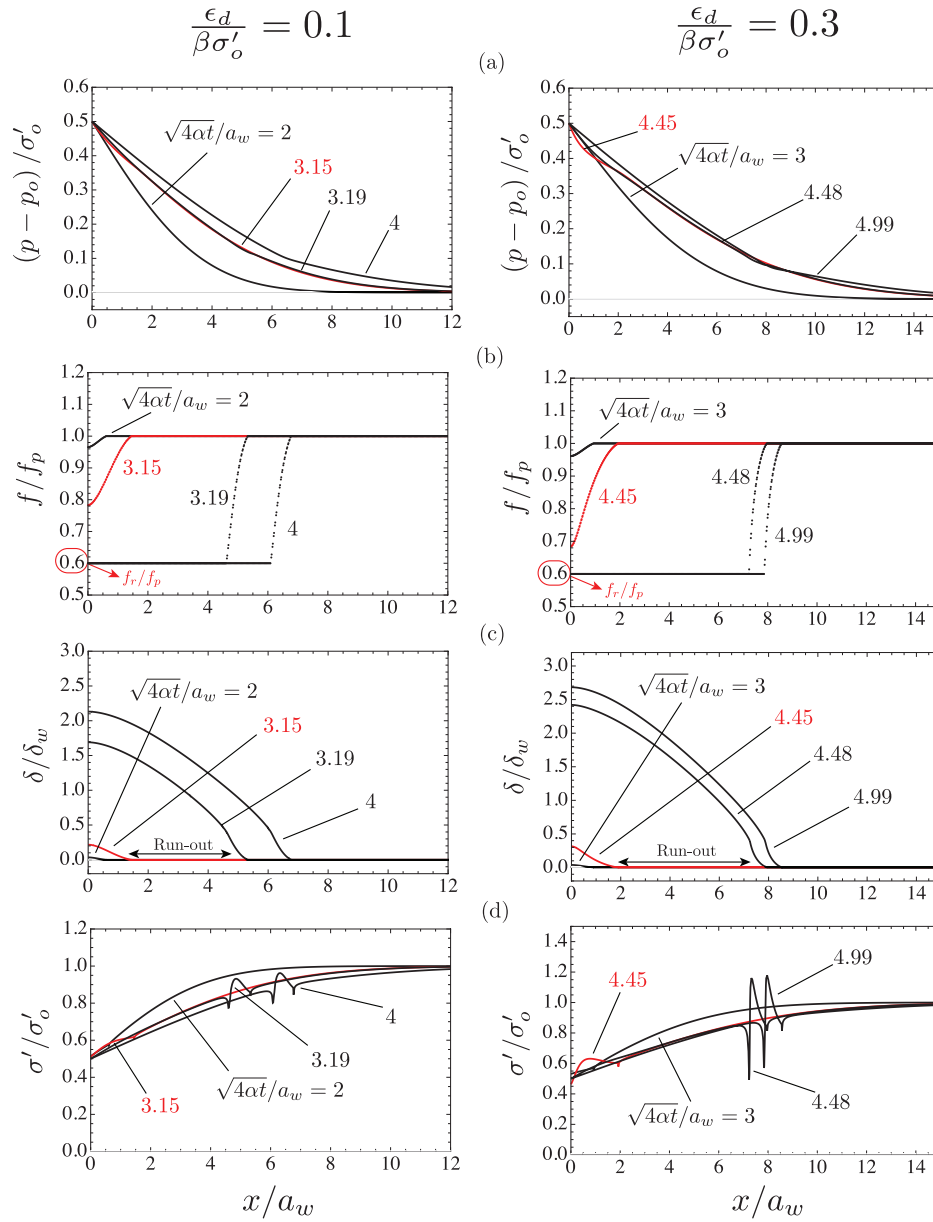


Figure 5.10: Spatial profiles of dimensionless pore pressure (a), friction coefficient (b), slip (c) and effective normal stress (d) at different (normalized) time snapshots, for an otherwise ultimately stable fault ($\tau_o / \tau_p = 0.55$ - $f_r / f_p = 0.6$), subjected to a moderate over-pressure $\frac{\Delta P}{\sigma'_o} = 0.5$. Two dimensionless dilatancy parameters are considered: $\frac{\epsilon_d}{\beta\sigma'_o} = 0.1$ and $\frac{\epsilon_d}{\beta\sigma'_o} = 0.3$. Red lines refer to numerical results at nucleation time of a dynamic rupture. Since the background shear stress τ_o is lower than the residual fault strength τ_r at ambient conditions, the dynamic event is always followed by an arrest.

of them account for porosity changes, while some others include explicit dependency on effect stress changes (see e.g. (Rutqvist & Stephansson 2003) for a review). For example, Rice (1992b) used an effective stress-dependent permeability law, in which the permeability is a non-linearly decreasing function

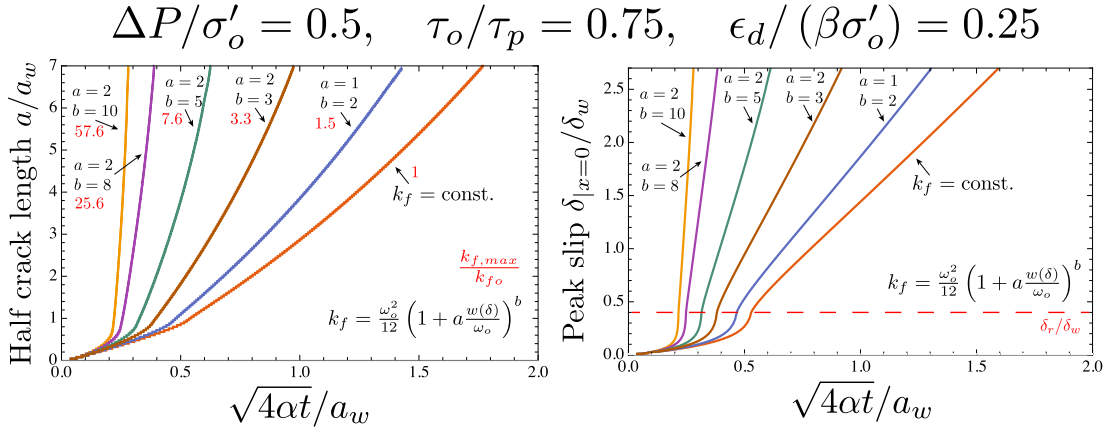


Figure 5.11: Effect of permeability increase on a critically stressed ($\tau_o/\tau_p = 0.75$, $f_r/f_p = 0.6$) dilatant fault under moderate over-pressure ($\Delta P/\sigma'_o = 0.5$): time evolution of normalized half crack length a/a_w and corresponding peak slip $\delta|_{x=0}/\delta_w$. The dimensionless dilatancy parameter $\epsilon_d/(\beta\sigma'_o)$ is set to the corresponding critical stabilizing value (5.27), equal here to 0.25. The effect of permeability evolution following the slip dependent law (5.31) is investigated for five different values of the parameters (a , b) spanning small and large permeability increase from 1.5 to ~ 60 times the initial fault permeability.

of the local (compressive) effective normal stress:

$$k_f = k_* e^{(-\sigma'/\sigma_*)}, \quad (5.29)$$

where k_* is the maximum fault permeability [L^2] and σ_* is a normalizing stress level [$ML^{-1}T^{-2}$] which ranges between 3 to 40 MPa Rice (1992b) - see also (Seront et al. 1998). Another common choice is to use the cubic law for the fault transmissivity ($k_f w_h$), relating the fault permeability directly to the changes of aperture - i.e. a parallel plate idealization of the fluid flow in the fault (Bawden et al. 1980, McClure & Horne 2014, Ucar et al. 2018, e.g.):

$$k_f(\delta) = \frac{w_h(\delta)^2}{12} \quad (5.30)$$

Under this assumption, the maximum constant fault permeability that is exerted when the slip δ is larger than the critical value δ_r is directly function of dilatant strain ϵ_d as $k_{f,max} = \frac{\omega_o^2}{12} (1 + \epsilon_d)^2$. Such a maximum increase of longitudinal permeability with respect to its initial value $\omega_o^2/12$ is actually rather small since the dilatant strain ϵ_d ranges between $10^{-4} - 10^{-2}$. This is clearly in contradiction with experimental and field evidences which mention much larger permeability increase (Makurat et al. 1985, Evans, Genter & Sausse 2005, Evans, Moriya, Niitsuma, Jones, Phillips, Genter, Sausse, Jung & Baria 2005).

In order to investigate cases in which fault dilatancy induces significant increases of fault permeability with inelastic deformations (for instance due to change of fault porosity, for which $\Delta k_f \propto \Delta \varphi^{7-8}$ for dense rocks - see Bernabé et al. (2003)), we generalize the fault permeability evolution law as

$$k_f = \frac{\omega_o^2}{12} \left(1 + a \frac{w(\delta)}{\omega_o}\right)^b, \quad (5.31)$$

where a and b are two constant parameters. Note that when $a = 1$ and $b = 2$, the fault transmissivity obeys the cubic law. By varying these two parameters, one can obtain ten-fold permeability increase associated with shear slip at maximum dilatancy compared to the initial value $\omega_o^2/12$. We use this permeability law 5.31 to gauge the impact of permeability change with slip on the stabilization by dilatancy of an otherwise unstable fault. In particular, our aim is to see if an increase of permeability affect the stabilizing effect of the undrained pore pressure drop associated with dilatancy.

We focus on the case of an otherwise unstable fault $\tau_o/\tau_p = 0.75$ ($f_r/f_p = 0.6$) and a moderate over-pressure case $\Delta P = 0.5$ with a dilatancy equal to the critical stabilizing value $\epsilon_{d,c}/(\beta\sigma'_o) = 0.25$ for



these conditions. Figure 5.11 displays the crack length and peak slip evolution for the case of a constant permeability as well as for different values of a and b for the permeability evolution law 5.31. We span $a = 1$, $b = 2$ (cubic law) and $a = 2$, $b = 3, 5, 8$, and 10 which entails respectively a 1.5 (cubic law), 3.3, 7.6, 25.6 and 57.6 fold increases of permeability at maximum dilatancy.

We observe that although the increase of permeability directly enhance the crack velocity, the propagation always remains aseismic. The permeability increase has a very significant effect on aseismic growth and this effect increases with the value of b as expected. For example, for the strongest permeability variation with dilatancy ($a = 2$, $b = 10$ resulting in $k_{f,max}/k_{fo} \sim 57.6$), we observe a $\sim 550\%$ increase in crack length at $\sqrt{4\alpha t}/a_w = 0.27$ compared to the constant permeability case (see Figure 5.11). A difference that will obviously continue to grow with time. For such a evolution of permeability with slip 5.31, the permeability profile is similar to the dilatancy strain: constant at its maximum value all along the crack except in the weakening zone near the tip - see Figure 5.12. The large permeability increases with slip, however, do not modify the stabilizing effect of undrained dilatant hardening. As the permeability accelerates quasi-static crack growth, the undrained pore-pressure response remains strong at the crack tip (see the pore-pressure profiles in Figure 5.12). Moreover, due to the quasi-static acceleration with increasing permeability, residual friction is reached earlier such that the undrained shear strength is fully mobilized - even possibly for smaller value of over-pressure compared to the constant permeability case. Note that similar results are obtained with other type of permeability evolution (such as the one described by eq. 5.29) as reported in Figures 5.21 and 5.22 of the Supporting Information (see section 5.8.7). In conclusions, in the case of an impermeable surrounding, the increase of permeability with slip along the fault does not affect the ultimate stability condition ($\tau_o < \tau_r^u$).

5.7 Conclusions

We have investigated the effect of dilatancy on the transition from seismic to aseismic slip due to sustained fluid injection regulated at a constant pressure in a fault. Although simple in its nature (planar bi-dimensional fault, uniform in-situ stress and rock properties, linear weakening friction), the model investigated properly couples, via non-associated plasticity, the hydro-mechanical interplay between slip, dilatancy, frictional weakening and fluid flow. We have developed a robust fully implicit numerical scheme - which properly reproduces existing semi-analytical solutions for the case of non-dilatant fault (Garagash & Germanovich 2012). We notably would like to emphasize the necessity of numerical model verification for such type of non-linear fracture propagation problem which -similarly to hydraulic fracturing problem- necessitates to resolve multiple scales (weakening zone and diffusion lengthscale here).

We have shown that dilatant hardening can stabilize an otherwise unstable fault ($\tau_o > \tau_r$), as long as the weakening of friction occurs in a small zone near the tip of the shear crack (small scale yielding). This is captured by an ultimate stability condition defined with an undrained residual strength $\tau_r^u = \tau_r(1 + \epsilon_d/(\beta\sigma_o'))$ function of the dilatant strain of the fault at critical state (when dilatancy saturates). We have demonstrated theoretically that under the assumption of small scale yielding, dilatancy ultimately stabilize the fault if $\tau_o < \tau_r^u$. In other words, for a given fault criticality, there exists a critical dilatancy above which the fault will remain stable and shear slip is solely aseismic. However, the hypothesis behind small scale yielding (small frictional weakening zone near the crack tips) must be satisfied for such a ultimate stability condition to hold. This is the case if and only if the injection over-pressure is sufficient to propagate quasi-statically the shear crack / slipping patch fast enough to reach residual friction and activate the beneficial effect of dilatancy prior to the crack reaching the nucleation length of the non-dilatant case. For injection pressures below a limiting value, the crack propagates too slowly initially. The nucleation of a dynamic rupture occurs prior to reaching residual friction such that the maximum dilatancy is not activated prior to nucleation. For such small injection over-pressure, dilatancy cannot prevent the nucleation of a dynamic rupture for an unstable fault ($\tau_o > \tau_r$) even for large dilatancy $\tau_o < \tau_r^u$ (see Figure 5.8 for the evolution of the minimum overpressure). However, such a dynamic rupture for low over-pressure and a-priori sufficient dilatancy ($\tau_o < \tau_r^u$) - which occurs prior to reaching residual friction - will eventually arrest as the dilatant hardening effect kicks in for sufficient crack length. Although observed with quasi-dynamic damping (see Supplemental Information), a fully elastodynamics simulation would be required to confirm such arrest.



$$\sqrt{4\alpha t}/a_w = 0.27$$

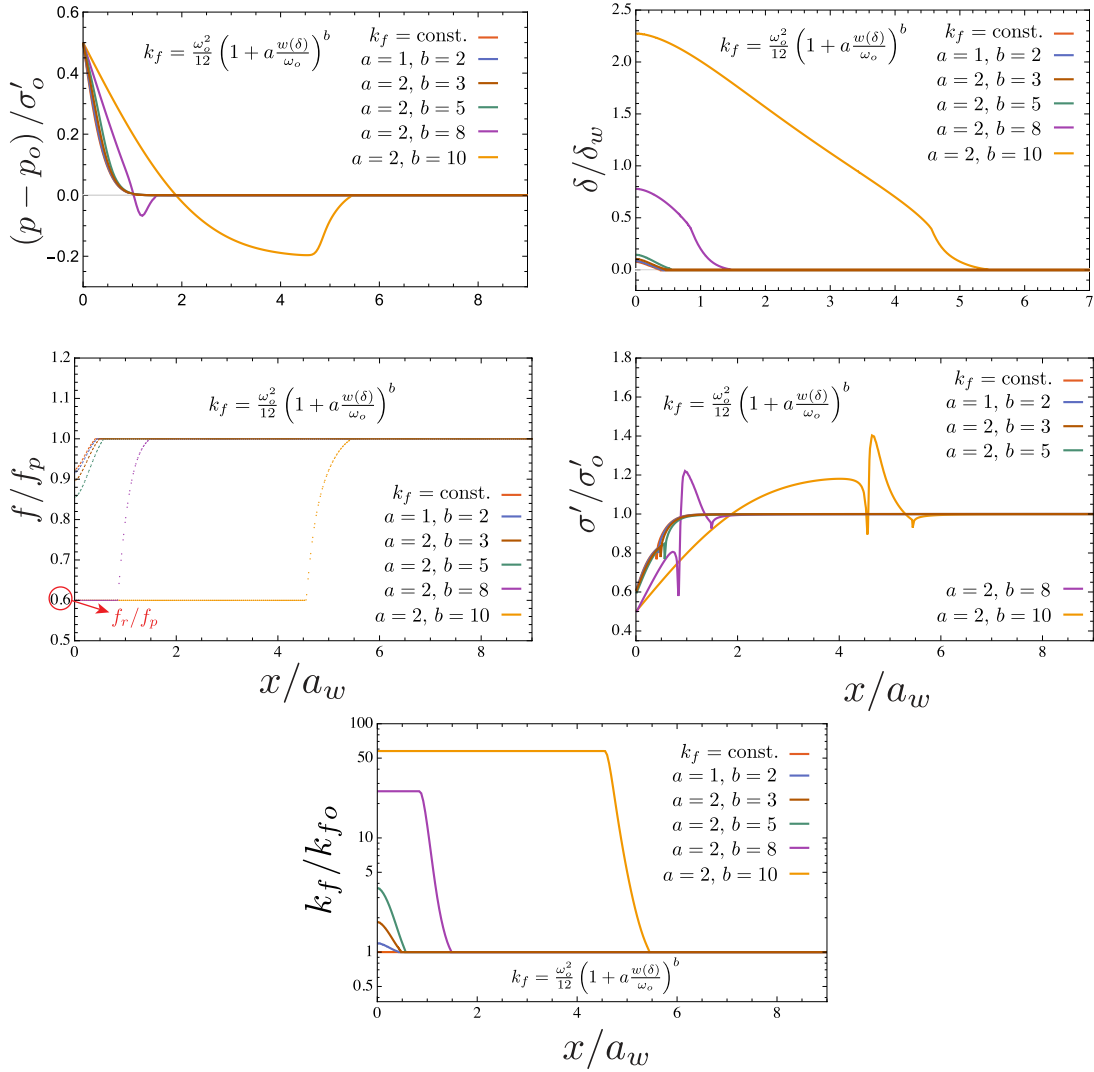


Figure 5.12: Spatial profiles of dimensionless pore pressure, friction coefficient, slip, effective normal stress and fault longitudinal permeability (in linear-log scale) at a given normalized time snapshot $\sqrt{4\alpha t}/a_w = 0.27$, for unstable fault ($\tau_o/\tau_p = 0.75 - f_r/f_p = 0.6$), subjected to a moderate over-pressure $\frac{\Delta P}{\sigma'_o} = 0.5$ and a dimensionless dilatancy parameter equal to the critical value, i.e. $\frac{\epsilon_{d,c}}{\beta\sigma'_o} = 0.25$. The different numerical results are obtained with different fault permeability evolution laws: i) constant permeability $k_f = \frac{\omega_o^2}{12}$, ii) slip-dependent permeability law $k_f = \frac{\omega_o^2}{12} \left(1 + a \frac{w(\delta)}{\omega_o}\right)^b$, with $a = 1$ & $b = 2$ (cubic law for fault transmissivity) and $a = 2$ & $b = 3, 5, 8, 10$.

For an ultimately stable fault ($\tau_o < \tau_r$), our numerical results indicate that dilatancy delays the occurrence of a finite episode of dynamic slip for moderate overpressure. Such a finite seismic event is associated with the abrupt catch up of the diffusion front by the crack front and the fact that the residual friction has not yet reached all along the crack. For large over-pressure and stable fault, an increasing dilatant behavior simply slows down the quasi-static propagation (strictly aseismic slip).

Permeability increases with slip leads to faster aseismic crack growth for the different permeability



evolution tested. However, it does not affect the critical dilatancy stabilizing an otherwise unstable fault. It appears evident that the details of the slip-permeability law greatly influence aseismic growth - a discussion on the most appropriate permeability model clearly require more investigation and necessarily better controlled hydro-mechanical laboratory experiments for sufficient slippage length.

The strengthening effect of dilatancy discussed here must be put perspective with some well-known dynamic weakening mechanisms that may occur as the crack accelerates: notably, thermal pressurization and flash heating of asperities. Although the effect of these weakening mechanisms have been already studied (Garagash & Rudnicki 2003, Segall & Rice 2006, Rice 2006, Garagash & Germanovich 2012) in the scope of earthquake nucleation via remote loading, a complete investigation of such competition would be required in the context of fluid injection. This is out of the scope of this paper. We note however that both of these dynamic weakening mechanisms requires dynamic slip rates (m/s and above) while dilatant hardening is activated quasi-statically. A probably more important point with respect to the stabilizing effect of dilatant hardening is related to the assumption of an impermeable host rock. Although possibly acceptable for young fault/fractures, this is highly doubtful for most mature fault structure. With a permeable surrounding (of say hydraulic diffusivity α_r), the undrained pore-pressure drop associated with the fault dilatant behavior may be short-lived as fluid will be sucked in the fault and repressurize it. The importance of dilatant hardening will directly depend on the ratio between the changes due to dilatancy (which scales with slip rate) and the influx of fluid from the rock mass (which scales as α_r/h_w with $h_w \approx \omega_o$ the gouge thickness). A thorough investigation for the case of injection induced slip is required to clarify that competition further, along the lines of Segall & Rice (1995), Segall et al. (2010) in the context of the seismic cycle. In the sequel, we have also used a simple linear weakening friction law compared to a more elaborate rate-state model. It is nevertheless worthwhile to note that some work (Uenishi & Rice 2003, Viesca 2016b,a) have demonstrated a correspondence between linear weakening friction and rate and state at the onset of nucleation. Investigations of the combined effect of rate and state and dilatancy in the case of fluid injection combined with proper scaling and stability analysis would surely produce a more refined understanding of the mechanisms of induced seismicity.

Finally, we conclude by recalling the decreases of dilatancy with confinement, such that the effect of dilatant hardening is likely to be more prominent mostly at shallow depths. Additional experimental data of fault dilatant behavior in conjunction with frictional properties would enable to further decipher its impact on fluid induced a-seismic and seismic slip with the help of the type of model presented here.

5.8 Supporting Information

5.8.1 Fully implicit hydro-mechanical solver for frictional planar fault: algorithm description

We report here the details of the hydro-mechanical solver developed for purely shear crack propagation along the planar dilatant fault. This solver includes the propagation of a frictional shear crack paced by fluid flow, shear induced-dilatancy and possibility of nucleation of dynamic rupture due weakening nature of friction coefficient along the fault. We use displacement discontinuity method with piece-wise linear displacement discontinuities (see section ??) to discretize elasticity equations 5.1 and a finite volume scheme (see section ??) for discretization of fluid mass conservation equation in the fault 5.14. In this scheme, the fault is discretized with finite sized straight elements (see section ??) and time integration is performed via Backward-Euler scheme¹. Fracture front is tracked by solving for the set of element satisfying the Mohr-Coulomb criterion 5.3, here with zero cohesion. Note that this solver does not include tensile failure, i.e. the injection over-pressure is set such that the effective normal stress remain always compressive.

The algorithm marches in time, from t^n to $t^{n+1} = t^n + \Delta t$. The solution at each time step consists of the set of yielded / active element \mathcal{A}_{elm} (of length N_a), displacement discontinuities on yielded elements and fluid pressure at all N mesh nodes. For sake of compactness, we use the notation of $X^{n+1} = X^n + \Delta X$ for referring to a generic time and space dependent variable $X(x, t)$ at time t^{n+1} (and we denote the initial state with the superscript o). Furthermore, normal and shear displacement discontinuities hereunder are

¹This ensures stability and no restriction given by the Courant-Friedrichs-Lewy condition.



respectively denoted as d_n and d_s (instead of w and δ), whereas normal and shear tractions are denoted as t_n and t_s , respectively (instead of σ and τ).

For a given trial set of active elements, the discretized hydro-mechanical equations at current time read:

- Elasticity (quasi-static formulation):

$$\mathbb{E} \cdot (\mathbf{d}^n + \Delta \mathbf{d}) = \mathbf{t}^n + \Delta \mathbf{t} - \mathbf{t}^o \quad (5.32)$$

or in incremental form

$$\mathbb{E} \cdot \Delta \mathbf{d} = \Delta \mathbf{t} \quad (5.33)$$

- Mohr-Coulomb criterion (with frictional weakening) enforced at collocation points, and the dilatancy relation:

$$\Delta \mathbf{t}_s + \mathbf{t}_s^n = f(\mathbf{d}_s^n + \Delta \mathbf{d}_s) (\mathbf{t}_n^n + \Delta \mathbf{t}_n - \mathbf{p}_{coll}^n - \Delta \mathbf{p}_{coll}) \quad (5.34)$$

$$\Delta \mathbf{d}_n = \Delta \mathbf{d}_s \tan(\psi(\mathbf{d}_s^n + \Delta \mathbf{d}_s)) \quad (5.35)$$

- Discretized fluid flow equation (over the whole mesh) where the pressure unknowns are located at the mesh nodes N :

$$\mathbb{V}_w \left(\frac{\partial \mathbf{d}_n}{\partial \mathbf{d}_s} \right)^{n+1} \cdot \Delta \mathbf{d}_n + \mathbb{V}_p(\mathbf{d}_n^{n+1}) \cdot \Delta \mathbf{p} + \Delta t \times \mathbb{L}(\mathbf{d}_n^{n+1}) \cdot \Delta \mathbf{p} = -\Delta t \times \mathbb{L}(\mathbf{d}_n^{n+1}) \cdot (\mathbf{p}^n - \mathbf{p}^o) \quad (5.36)$$

All the finite volume matrices in equation 5.36 are defined in section ???. Note that, in order to couple the dilatancy term in the fluid mass conservation equation with the elasticity equations related to only shear degrees of freedom, a chain rule must be applied to the time derivative of the opening \mathbf{d}_n , such that

$$\frac{\partial d_n}{\partial t} = d_{n,s} \cdot \frac{\partial d_s}{\partial t} \quad \text{with} \quad d_{n,s} = \frac{\partial d_n}{\partial d_s}, \quad (5.37)$$

The term $d_{n,s}$ can then be obtained analytically from equation 5.10 and, upon integration over each control volume, the dilatancy matrix \mathbb{V}_w can be easily assembled (note again the change of notation, for which $w = d_n$ and $d_s = \delta$).

Since the elasticity equations are collocated at points inside the displacement discontinuity element (see Figure 4.1), whereas fluid pressure is discretized at nodal points, equation 5.35 must be expressed in terms of nodal increment of pore pressure in order to couple it with fluid flow. The pore pressure increment at a collocation point $\Delta p(\xi_j)$ is obtained from the nodal pore pressure increments Δp_i , via the definition of the linear shape functions (see equation ??):

$$\Delta p(\xi_j) = \sum_{i=1,2} N_i(\xi_j) \Delta p_i, \quad (5.38)$$

where Δp_i denotes the value of the over-pressure at node i . Equation 5.38 can be expressed in matrix form as

$$\Delta \mathbf{p}_{coll} = \mathbb{N}_{pc} \Delta \mathbf{p}, \quad (5.39)$$

where \mathbb{N}_{pc} is a $2N_a \times N$ matrix for the transfer of the value of pressure from node to collocation points. The set of discretized equations previously introduced can be re-arranged to yield a non-linear system in terms of the increments of shear displacement discontinuity and increment of pore pressure along the planar fault (for which the elastic equations for shear and normal degree of freedom uncouple):

$$\begin{bmatrix} \mathbb{E}_{ss} & f^{n+1} \times \mathbb{N}_{pc} \\ \mathbb{V}_w(d_{n,s}^{n+1}) \cdot \tan(\psi^{n+1}) & \mathbb{V}_p(\mathbf{d}_n^{n+1}) + \Delta t \times \mathbb{L}(\mathbf{d}_n^{n+1}) \end{bmatrix} \begin{bmatrix} \Delta \mathbf{d}_s \\ \Delta \mathbf{p} \end{bmatrix} = \begin{bmatrix} \text{sign}(\mathbf{t}_s^{n+1}) (f^{n+1} (\mathbf{t}_n^{n+1} - \mathbf{p}^n)) - \mathbf{t}_s^n \\ -\Delta t \times \mathbb{L}(\mathbf{d}_n^{n+1}) \cdot (\mathbf{p}^n - \mathbf{p}^o) \end{bmatrix} \quad (5.40)$$

where $\tan(\psi^{n+1})$ and f^{n+1} are identity matrices containing respectively the current dilatancy angle and current friction coefficient at the nodal points (they are both functions of the current shear slip \mathbf{d}_s^{n+1}), and the current normal stress is simply given by

$$\mathbf{t}_n^{n+1} = \mathbf{t}_n^n + \mathbb{E}_{nn} \tan(\psi^{n+1}) \Delta \mathbf{d}_s \quad (5.41)$$



The system of equations 5.40 is non-linear as both dilatancy, friction and permeability evolves with slip. Starting from a known solution at time n (denote as \mathcal{L}^n) and thus from a given active set of elements \mathcal{A}_{elm}^n , we solve it² via fixed point iterations combined with an under relaxation scheme, upon application of the following boundary condition due to injection condition:

$$\Delta p(x = 0, t) = p_o + \Delta P - p^n(x = 0, t) \quad (5.42)$$

Convergence is reached when the relative difference between successive estimate of slip and fluid pressure increment falls below a fixed tolerance (typically $tol = 10^{-6}$). Upon convergence of this non-linear hydro-mechanical system, we check the Mohr-Coulomb criterion on the full mesh (re-computing shear and effective normal tractions on the full mesh) and modify accordingly the set of active elements. This is done through an iterative checking loop, whose convergence is reached when the set of active elements do not change between two successive iterations or when the current slippage length sl^{n+1} coincides with the length of the fault. The algorithm devised is thus composed of two nested iterative loops. The outer loop allows to determine the current shear crack position by checking the active set of elements (for which $F(t_s, t'_n) = 0$) at current time $n + 1$, whereas the inner one is used to solve the non-linear system of equations 5.40. Upon convergence of the two loops, the new numerical solution \mathcal{L}^{n+1} is obtained and the algorithm move to the next time step.

²Note that the non-linear system 5.40 can be solved equivalently for the plastic multiplier λ , instead of for increment of displacement discontinuities. This can be achieved by replacing the vector $\Delta \mathbf{d}_s$ with the vector $\lambda \cdot \text{sign}(\mathbf{t}_s^{n+1})$ containing all the plastic multiplier of the active elements N_a .



Hereunder, we sum up the algorithm devised for a better comprehension:

Store the primary variable from previous time t^n : $\mathcal{L}^n = (t_i^n, p^n, d_i^n, sl^n, \mathcal{A}_{elm}^n, \Delta t^{n+1}, v^n)$

Set $sl^{n+1} = sl^n$ & $t^{n+1} = t^n$

While ($t^{n+1} \leq t_{max}$ & $sl^{n+1} \leq sl_{max}$)

Set $j = 0$

Set $\mathcal{L}_j^{n+1} = \mathcal{L}^n$

While ($F(t_{s,j}, t'_{n,j})^{n+1} \leq 0$ everywhere & $j < j_{max}$)

$j = j + 1$

Determine $\mathcal{A}_{elm,j}^{n+1}$ from \mathcal{L}_j^{n+1} , i.e. elements for which $F(t_{s,j}, t'_{n,j})^{n+1} \geq 0$

Set $k = 0$, $\Delta d_{i,k} = 0$, $\Delta p_k = 0$

While ($k \leq k_{max}$ & $err_{\Delta d_i} > tol$ & $err_{\Delta p} > tol$)

$k = k + 1$

Determine $d_{i,k}^{n+1} = d_{i,j}^{n+1} + \Delta d_{i,k}$

Build $\mathbb{V}_w, \mathbb{V}_p, \mathbb{L}, \mathbb{N}_{pk}$ with current deformations

Solve the system 5.40 to get $\Delta d_{s,k+1}$ and Δp_{k+1}

Calculate new pressure $p_{k+1}^{n+1} = p_k^{n+1} + \Delta p_{k+1}$

Calculate new increment of opening DD $\Delta d_{n,k+1}$ using flow rule

Calculate new stress state along the fault via elasticity equations and 5.41

Under relaxation:

$$\Delta p_{k+1} = (1 - \omega)\Delta p_k + \omega\Delta p_{k+1} \text{ \& } \Delta d_{i,k+1} = (1 - \omega)\Delta d_{i,k} + \omega\Delta d_{i,k+1}$$

Compute errors on increments

$$err_{\Delta d_i} = \|\Delta d_{i,k+1} - \Delta d_{i,k}\| / \|\Delta d_{i,k+1}\| \text{ and } err_{\Delta p} = \|\Delta p_{k+1} - \Delta p_k\| / \|\Delta p_{k+1}\|$$

Update: $\Delta d_{i,k} = \Delta d_{i,k+1}$ & $\Delta p_k = \Delta p_{k+1}$

End while

Set new trial solution $\mathcal{L}_{j+1}^{n+1} = (t_{i,k}^{n+1}, p_k^{n+1}, d_{i,k}^{n+1}, sl^n, \mathcal{A}_{elm,j}^{n+1}, \Delta t^{n+1}, v^n)$

Determine $\mathcal{A}_{elm,j+1}^{n+1}$ from \mathcal{L}_{j+1}^{n+1}

Determine sl^{n+1} from $\mathcal{A}_{elm,j+1}^{n+1}$

Update $\mathcal{L}_j^{n+1} = \mathcal{L}_{j+1}^{n+1}$

End while

Calculate $v^{n+1} = \frac{sl^{n+1} - sl^n}{\Delta t^{n+1}}$ via finite difference.

Calculate new time step Δt^{n+2}

Update variables, i.e. $\mathcal{L}^n = \mathcal{L}_{j+1}^{n+1}$

End while

Algorithm 1: Fully implicit H-M solver for frictional fluid driven crack.

In the Algorithm 1, sl_{max} is the extension of the whole fault, j_{max} is the maximum number of iterations for the determination of shear crack position and ω is the under-relaxation parameter ($0 \leq \omega \leq 1$).

5.8.2 Verification of the numerical scheme: benchmark for the non-dilatant case

The governing problem is uncoupled when elasticity does not affect fluid flow along the fault and vice-versa. This scenario occurs for a non dilatant fault, i.e. when the fault hydraulic aperture does not change during crack propagation, i.e. $w_h = \omega_o$. The pore pressure evolution in such a case is given by the solution of the linear diffusion equation in a fault characterized by constant hydraulic diffusivity

$$\alpha = \frac{k_f}{\mu\beta} \text{ (Carslaw \& Jaeger 1959):}$$

$$p(x, t) = p_o + \Delta P \cdot \text{Erfc} \left| \frac{x}{\sqrt{4\alpha t}} \right| \quad (5.43)$$

This pore pressure evolution along the fault is linked to elasticity through the shear weakening Mohr-Coulomb criterion (one way coupling): the change of local effective normal stress associated with pore

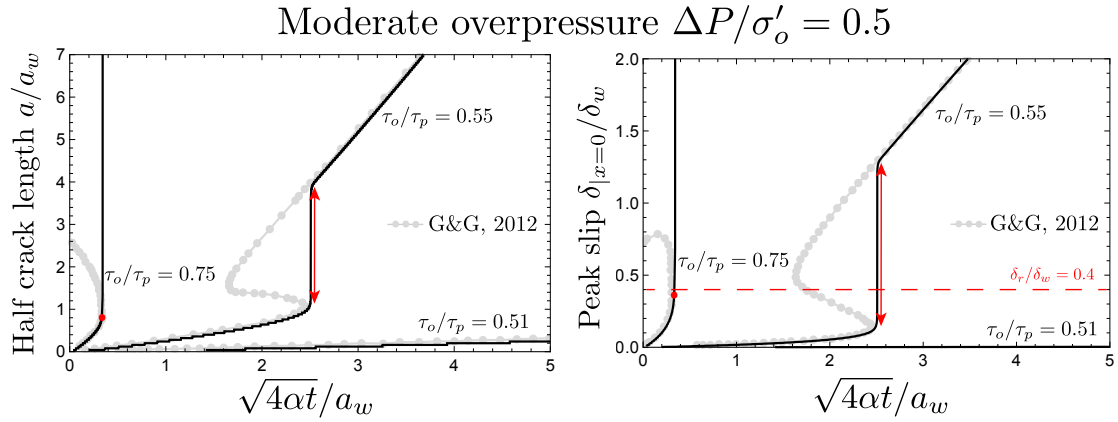


Figure 5.13: Benchmark of numerical results against semi-analytical ones of Garagash & Germanovich (2012) in terms of time evolution of normalized half crack length a/a_w and normalized peak slip $\delta|_{x=0}/\delta_w$ at $x = 0$, for a non-dilatant fault subjected to moderate overpressure $\Delta P/\sigma'_o = 0.5$ and three initial stress conditions: i) $\tau_o/\tau_p = 0.75$ (unstable fault), ii) $\tau_o/\tau_p = 0.55$ (ultimately stable fault) and iii) $\tau_o/\tau_p = 0.51$ (ultimately stable fault). The friction weakening ratio is $\frac{f_r}{f_p} = 0.6$, so that $\frac{\delta_r}{\delta_w} = 0.4$. The red dots denote the nucleation/onset of an unabated dynamic rupture, whereas the red arrows denote the nucleation of dynamic event followed by an arrest.

pressure increment reduces locally the fault frictional strength, affecting in turn elasticity.

Garagash & Germanovich (2012) investigated extensively this particular case. Semi-analytical results are thus available, allowing to verify the numerical scheme. This is of great importance for these kind of non-linear (coupled) problems. Indeed, the dynamic instability that may occur during shear crack propagation due to weakening nature of friction coefficient may lead to numerical errors.

We show in Figure 5.13 the benchmark of our numerical results against the semi-analytical ones of Garagash & Germanovich (2012), both in terms of dimensionless half-crack length a/a_w and dimensionless peak slip accumulated in the middle of the fault $\delta|_{x=0}/\delta_w$. Notably, we chose three scenarios by changing the stress criticality τ_o/τ_p , while keeping a moderate over-pressure $\frac{\Delta P}{\sigma'_o} = 0.5$ and a friction weakening ration of $f_r/f_p = 0.6$, in order to test the numerical solver for different regimes of propagation: i) purely aseismic slip ($\tau_o/\tau_p = 0.51$), ii) aseismic crack propagation with nucleation and arrest of dynamic event ($\tau_o/\tau_p = 0.555$) and iii) aseismic slip followed by an unabated dynamic rupture ($\tau_o/\tau_p = 0.75$). We can observe in Figure 5.13 that our numerical results match perfectly with the semi-analytical ones of Garagash & Germanovich (2012). The discrepancy in terms of half-crack length a/a_w between the numerical solutions and the semi-analytical ones is of the order of the element size h , the latter adopted such to have 25 elements within the frictional weakening zone (i.e. $a_w/h = 25$ - see the mesh convergence study reported in the following pages for relative error estimation). In Figure 5.14, the benchmark in terms of normalized slip δ/δ_w and shear stress τ/τ_p profile is reported (only for the case of aseismic crack propagation with nucleation and arrest of dynamic event). Again, we observe that the numerical results match the semi-analytical results of Garagash & Germanovich (2012) with good accuracy.

All the numerical results in terms of time evolution of half crack length a/a_w show a step-like behaviour. This is intrinsically related to the modeling of the fault as a sum of adjacent finite elements of equal size h . Indeed, in one increment of time, the pore pressure perturbation might not be enough to activate further elements - i.e. to induce $F(\tau, \sigma'_n) = 0$. Time-stepping management as well as mesh resolution play an important role on this kind of step-like crack propagation. For a given increment of time Δt , the finer is the mesh the smaller are these steps. A local dynamic mesh refinement at the crack tips can reduce significantly this behaviour, although the computational cost might considerably increase.

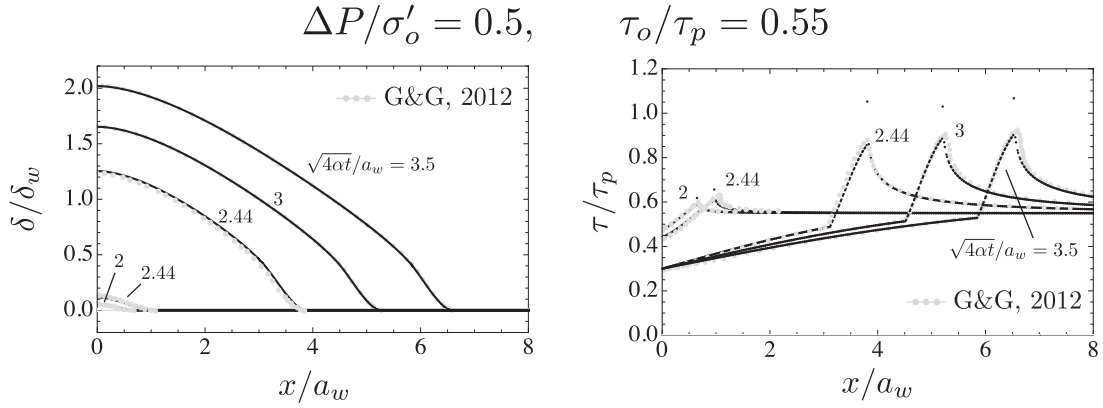


Figure 5.14: Benchmark of numerical results against semi-analytical ones of Garagash & Germanovich (2012) in terms of normalized slip δ/δ_w and shear stress τ/τ_p profiles, for a non-dilatant ultimately stable fault subjected to moderate over-pressure $\Delta P/\sigma'_o = 0.5$. The stress criticality is $\tau_o/\tau_p = 0.55$ and the friction weakening ratio is $f_r/f_p = 0.6$.

5.8.3 Mesh convergence study

In order to check the accuracy of our numerical results, we have performed a mesh convergence study. Similarly to cohesive zone models for fracture propagation, the non linearity of the problem lies in a small zone near the crack tips. As already mentioned in section 5.2.1.2, such a small zone is approximately defined by the characteristic nucleation length-scale a_w , over which the friction coefficient weakens from a peak value to its residual value during crack propagation. It is of great importance, therefore, to have enough mesh resolution within that length-scale so as to be able to capture the non-linearity with good accuracy. A local dynamic mesh refinement at the crack tips can help in doing it, although the computational cost might considerably increase.

Since semi-analytical results of Garagash & Germanovich (2012) for non-dilatant frictional weakening fault are available, we have performed a mesh convergence study for the following test case: ultimately stable fault $\tau_o/\tau_p = 0.55$ (for a friction weakening ratio of $f_r/f_p = 0.6$), subjected to moderate overpressure $\frac{\Delta P}{\sigma'_o} = 0.5$ (and $\frac{\epsilon_d}{\beta\sigma'_o} = 0$ - no dilatancy, uncoupled problem). Notably, we run bunch of simulations with the same initial configuration, while changing the total number of equal-sized elements (of size h) in a given mesh. The nucleation length-scale a_w is thus fixed for all the simulations (as it depends on friction weakening length-scale δ_w , initial stress conditions and elastic property of the medium, which are kept constant for all the simulations), while the element size h varies. In this way, we investigated the fault response in terms of half-crack length a/a_w and peak slip at the middle of the fault $\delta|_{x=0}/\delta_w$ as a function of the ratio a_w/h , which indicates the number of elements within the non-linear length-scale.

Figure 5.15 shows the relative error in terms of normalized peak slip $\delta|_{x=0}/\delta_w$ at a given normalized time $\sqrt{4\alpha t}/a_w = 2$, between the numerical results and the semi-analytical result of Garagash & Germanovich (2012), as a function of the number of elements within the nucleation length-scale a_w . We observe, not surprisingly, that the higher is the number of elements withing a_w , the lower is the relative error. For $a_w/h > 25$, the relative error is below 1%, up to reach 0.1% for $a_w/h = 50$. The non-monotonic decrease of the relative error for increasing values of a_w/h is related to step-like behaviour of the numerical solutions that inevitably appear for low values of a_w/h (already discussed in section 5.8.2). This intrinsic behaviour is, in fact, more pronounced for decreasing values of a_w/h , for which the accuracy deteriorates considerably.

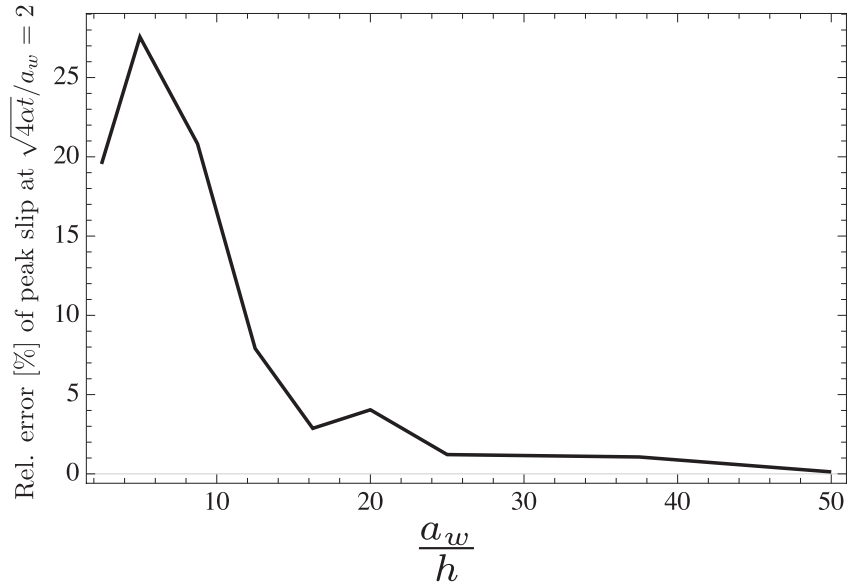


Figure 5.15: Evolution of relative error in terms of normalized peak slip $\delta_{|x=0}/\delta_w$ at normalized time $\sqrt{4\alpha t}/a_w = 2$, as a function of number of elements within the nucleation length scale a_w . The test case investigated is a non-dilatant ultimately stable fault ($\tau_o/\tau_p = 0.55$ and $f_r/f_p = 0.6$), subjected to moderate overpressure $\frac{\Delta P}{\sigma'_o} = 0.5$. Semi-analytical results of Garagash & Germanovich (2012) in terms of normalized half crack length and peak slip at the fault center are available, allowing to calculate the relative error.

5.8.4 Case of otherwise unstable fault $\tau_o > \tau_r$ - Nucleation and Arrest

In the case of zero dilatancy, for unstable fault with relatively low stress criticality, under moderate overpressure (region 4,b in Figure 5.3), a finite seismic episode occurs prior to the nucleation of dynamic rupture. We investigate the effect of different dilatancy in such a configuration ($\tau_o/\tau_p = 0.65$, $\Delta P/\sigma'_o = 0.5$, $f_r/f_p = 0.6$). Figure 5.16 displays the time evolution of crack length and peak slip for different level of dilatancy.

Interestingly, the 'transient' seismic episode which is linked to the fact that the fluid front is initially ahead of the slipping patch (see Figure 5.17 - comparison between pore pressure and slip profile at $\sqrt{4\alpha t}/a_w = 0.5$) does not disappear even for a dilatancy larger than the theoretical critical value $\epsilon_{d,c}/\beta\sigma'_o = 1/12$ in this case. Indeed such a seismic episode occurs with little accumulated slip and its nucleation is not influenced by residual friction: in such cases, the maximum dilatancy is not mobilized and no undrained strengthening of the fault occur. This can well be grasped by looking at the pore pressure profiles in Figure 5.17 at dimensionless time $\sqrt{4\alpha t}/a_w = 1$, i.e. at a given time after the arrest of the seismic episode. The pore pressure drop is not fully developed due to the limited slip rate associated with crack propagation. However, the subsequent re-nucleation is increasingly delayed as the dilatancy increases (see Figure 5.16 for $\frac{\epsilon_d}{\beta\sigma'_o} = 0.05$) and do not occur for values of dilatancy equal of above the critical value (case of $\frac{\epsilon_d}{\beta\sigma'_o} = 1/10$). Note that for such configurations, the nucleation of the unabated dynamic rupture occurs when a significant portion of the crack size is at residual friction, the weakening zone is small and confined near the tip (see friction coefficient profile in Figure 5.17 at $\sqrt{4\alpha t}/a_w = 2.2$ - case of $\frac{\epsilon_d}{\beta\sigma'_o} = 0.05$). In such cases, the s.s.y assumption is valid, the maximum dilatancy is active and the theoretical estimate for the critical dilatancy / undrained shear strength is valid.

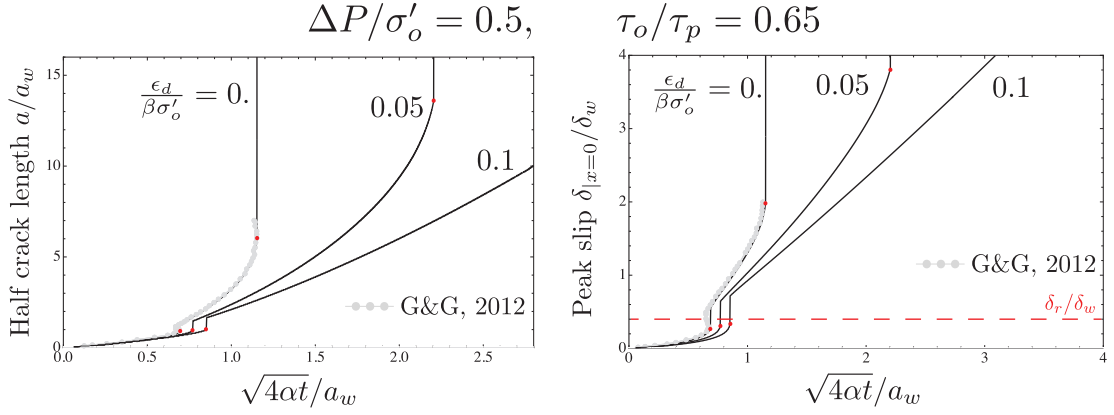


Figure 5.16: Evolution of normalized half crack length a/a_w and normalized peak slip $\delta_{|x=0}/\delta_w$ with normalized time $\sqrt{4\alpha t}/a_w$ for a frictional weakening dilatant fault. The fault is subjected to an initial uniform background shear stress $\tau_o/\tau_p = 0.65$ (unstable fault in the non-dilatant case for a friction weakening ratio of $f_r/f_p = 0.6$ - with relative low stress criticality though) and a moderate constant over-pressure $\Delta P/\sigma'_o = 0.5$ applied in the middle of the fault. Two dimensionless dilatancy parameters are considered: $\frac{\epsilon_d}{\beta\sigma'_o} = 0.05 < \frac{\tau_o}{\tau_r} - 1 = \frac{\epsilon_{d,c}}{\beta\sigma'_o}$ and $\frac{\epsilon_d}{\beta\sigma'_o} = 0.1 > \frac{\tau_o}{\tau_r} - 1 = \frac{\epsilon_{d,c}}{\beta\sigma'_o}$. Grey dotted lines denote semi-analytical results of Garagash & Germanovich (2012), whereas red dots denote nucleation of dynamic rupture.

5.8.5 Approximated solution for quasi-static growth assuming $a \propto \sqrt{4\alpha t}$

The numerical results showed in section 5.5.1 and 5.5.2 suggest that when the shear crack propagation is stable for large crack length, it appears to be synchronized with the fluid front position: i.e. $a = \gamma\sqrt{4\alpha t}$ for $a \gg a_w$ - at least for the constant permeability case. Following the approximated small scale yielding solution obtained for the non-dilatant case (Garagash & Germanovich 2012), we make some further assumptions in order to extend it to account for dilatancy. The main difficulty lies in the determination of the pore-pressure changes in the dilatant case. With an approximated pore-pressure perturbation solution in hand, we can use the small scale yielding approximation of the fracture energy 5.23 and the expression of the stress intensity factor 5.25 to estimate γ from the quasi-static propagation condition.

We make from the onset the hypothesis that $a = \gamma\sqrt{4\alpha t}$, and that the permeability remains constant with slip. We further assume that the increment of hydraulic width with dilatancy is rather small such that $wk_f \approx w_o k_f$. In other words, we assume the fault hydraulic conductivity to remain constant. Under the small scale yielding approximation, we approximate the sink term due to dilatancy by two moving sink of intensity ϵ_d at the crack tips.

By scaling the variables of equation 5.14 with the following characteristic scales

$$\Pi = \frac{p(x,t)}{\Delta P}, \quad \xi = \frac{x}{\ell_d(t)}, \quad \gamma = \frac{a}{\ell_d(t)}$$

where $\ell_d = \sqrt{4\alpha t}$, the fluid flow equation reduces to the following ODE when γ is assumed to remain constant

$$-\frac{1}{4} \frac{\partial^2 \Pi}{\partial \xi^2} - \frac{1}{2} \xi \frac{\partial \Pi}{\partial \xi} + \frac{1}{2} \xi \cdot \frac{\epsilon_d}{\beta \cdot \Delta P} \cdot (\delta_{dirac}(\xi - \gamma) + \delta_{dirac}(\xi + \gamma)) = 0 \quad (5.44)$$

We note in the previous equation 5.44 the presence of two moving sink terms that represent the undrained fault response occurring at small end zone of crack tips. With the following dimensionless boundary conditions

$$\Pi(0) = 1, \quad \Pi(\infty) = 0, \quad (5.45)$$

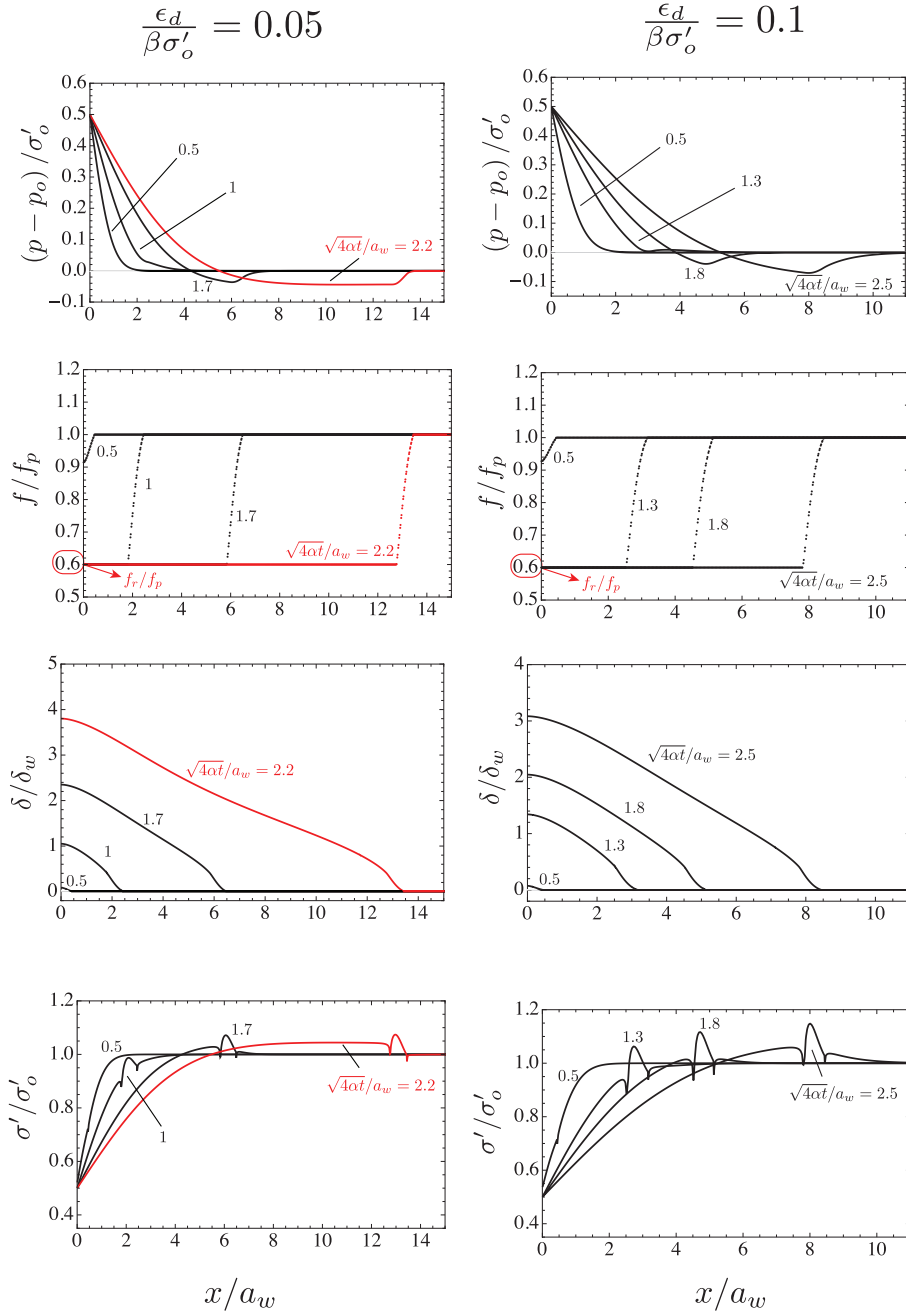


Figure 5.17: Spatial profiles of dimensionless pore pressure (a), friction coefficient (b), slip (c) and effective normal stress (d) at different (normalized) time snapshots, for an otherwise unstable fault ($\tau_o/\tau_p = 0.65$ - relative low stress criticality for $f_r/f_p = 0.6$), subjected to a moderate over-pressure $\frac{\Delta P}{\sigma'_o} = 0.5$. Two dimensionless dilatancy parameters are considered: $\frac{\epsilon_d}{\beta\sigma'_o} = 0.05 < \frac{\tau_o}{\tau_r} - 1 = \frac{\epsilon_{d,c}}{\beta\sigma'_o}$ and $\frac{\epsilon_d}{\beta\sigma'_o} = 0.1 > \frac{\tau_o}{\tau_r} - 1 = \frac{\epsilon_{d,c}}{\beta\sigma'_o}$. Red lines refer to numerical results at nucleation time of an unabated dynamic rupture. equation 5.44 can be solved analytically:

$$\Pi(\xi, \gamma) = 1 - \text{Erf}(\xi) - e^{\gamma^2} \sqrt{\pi} \gamma \Gamma_d \cdot (-\text{Erf}(\gamma) (1 + \text{Erf}(\xi)) + (\text{Erf}(\gamma) - \text{Erf}(\xi)) \cdot H(-\gamma + \xi) + (\text{Erf}(\gamma) + \text{Erf}(\xi)) \cdot H(\gamma + \xi)), \quad (5.46)$$

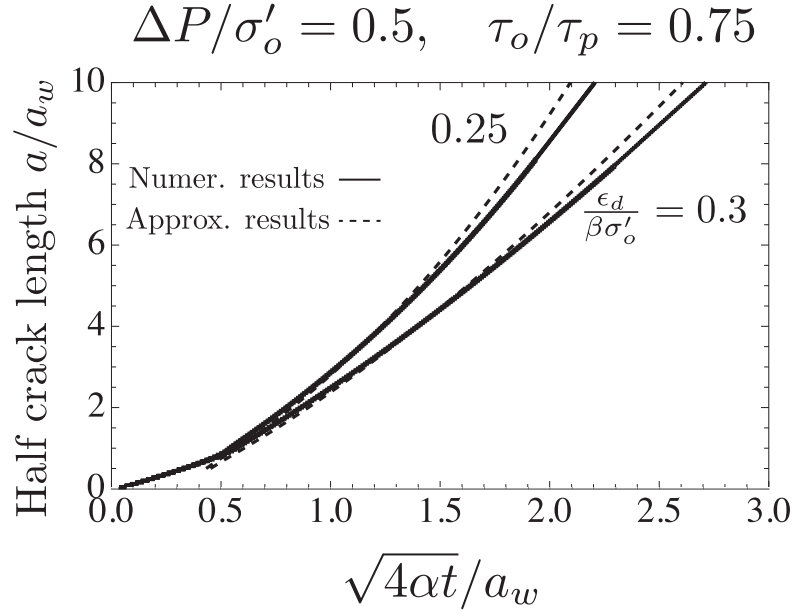


Figure 5.18: Comparison between numerical results and results associated with approximated solution for quasi-static crack growth ($a \propto \sqrt{4\alpha t}$) in terms of time evolution of normalized half-crack length a/a_w . The case investigated is a critically stressed fault ($\tau_o/\tau_p = 0.75$), subjected to moderate over-pressure $\Delta P/\sigma'_o = 0.5$ and two values of dimensionless dilatancy parameter $\frac{\epsilon_d}{\beta\sigma'_o} = 0.25 - 0.3$.

where H is the Heaviside step function and $\Gamma_d = \frac{\epsilon_d}{\beta \cdot \Delta P} = \frac{\epsilon_d}{\beta\sigma'_o} \frac{\sigma'_o}{\Delta P}$ is a dimensionless parameter capturing the effect of the undrained pore pressure drop with respect to the injection fluid over-pressure. Note that the dimensionless over-pressure at the tip simplify to:

$$\Pi(\gamma, \gamma) = \text{Erfc}(\gamma) \left(1 - \gamma\sqrt{\pi} e^{\gamma^2} \Gamma_D \text{Erf}(\gamma) \right) \quad (5.47)$$

Equation 5.46 thus allows to calculate analytically the SIF (through equation 5.25):

$$K_{II} = \tau_p \sqrt{\ell_d} \times \left(\sqrt{\pi} \left(\frac{\tau_o}{\tau_p} - \frac{f_r}{f_p} \right) + \frac{f_r}{f_p} \frac{\Delta P}{\sigma'_o} \Delta k_{II}(\gamma, \Gamma_d) \right) \quad (5.48)$$

$$\Delta k_{II}(\gamma, \Gamma_d) = \sqrt{\pi} - \frac{4\gamma}{\pi} \left(1 + \gamma\sqrt{\pi} e^{\gamma^2} \Gamma_D \text{Erfc}(\gamma) \right) {}_pF_q(\{1/2, 1\}, \{3/2, 3/2\}, -\gamma^2) \quad (5.49)$$

where ${}_pF_q$ denotes the generalized hypergeometric function. Note that interestingly, in the limit of large crack length (i.e. large $\gamma\ell_d$), we recover the exact same limit than the simpler approximation of the superposition of a point source with an uniform undrained pore-pressure drop used in section 5.3.2.2:

$$\lim_{a \rightarrow \infty} K_{II} = \infty \left(\tau_o - \frac{\epsilon_d}{\beta\sigma'_o} f_r - \tau_r \right) = \infty (\tau_o - \tau_r^u), \quad (5.50)$$

and therefore the same critical value of dilatancy 5.27 required to stabilize an otherwise unstable fault.

Under such a small scale yielding approximation, assuming that the over-pressure is uniform in the weakening zone and equal to its value at the crack tip, the fracture energy G_c (see eq. 5.23) can be approximated as

$$G_c = (f_p - f_r) \frac{\delta_r \sigma'_o}{2} \left(1 - \frac{\Delta P}{\sigma'_o} \times \Pi(\gamma, \gamma) \right) \quad (5.51)$$

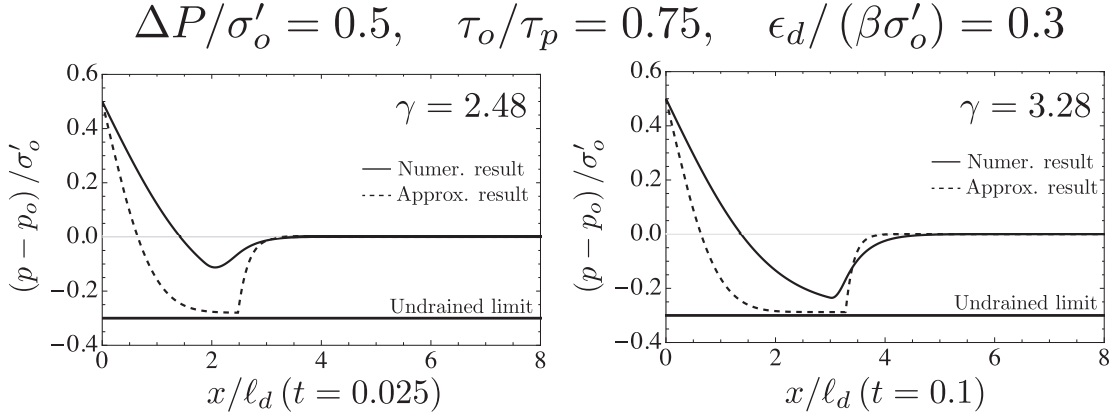


Figure 5.19: Comparison between numerical results and results associated with approximated solution for quasi-static crack growth ($a \propto \sqrt{4\alpha t}$) in terms of pore pressure profiles. The case investigated is a critically stressed fault ($\tau_o/\tau_p = 0.75$), subjected to moderate over-pressure $\Delta P/\sigma'_o = 0.5$ and a dimensionless dilatancy parameter $\frac{\epsilon_d}{\beta\sigma'_o} = 0.3$. The relative (and constant) position between crack tip and fluid front ($\gamma = \frac{a}{\ell_d(t)}$) is 2.48 and 3, which correspond to a dimensionless time of $\sqrt{4\alpha t}/a_w = 1$ and $\sqrt{4\alpha t}/a_w = 2$, respectively.

The quasi static propagation condition (24) can thus be re-written as:

$$\frac{a_w}{\ell_d} \left(\frac{f_p - f_r}{f_p} \right)^2 \left(1 - \frac{\Delta P}{\sigma'_o} \times \Pi(\gamma, \gamma) \right) = \left\{ \sqrt{\pi} \left(\frac{\tau_o}{\tau_p} - \frac{f_r}{f_p} \right) + \frac{f_r}{f_p} \frac{\Delta P}{\sigma'_o} \Delta k_{ii}(\gamma, \Gamma_d) \right\}^2 \quad (5.52)$$

The previous equation can be solved for γ for a given set of problem parameters (τ_o/τ_p , f_r/f_p , $\Delta P/\sigma'_o$, $\epsilon_d/(\beta\sigma'_o)$) and a given value of a_w/ℓ_d . Although, we made the assumption of a time-independent γ to obtain the pore-pressure profile, we can relax it to see its evolution with a_w/ℓ_d . The obtained approximated solution captures the order of magnitude of the aseismic shear crack propagation as can be seen on Figure 5.18. However, it is not precise enough essentially due to i) the impact of the change of hydraulic conductivity with slip which prevent to properly captured the pore-pressure profile (as can be seen on Figure 5.19) and ii) the fact that the pore-pressure is clearly not uniform in the weakening zone which impact the estimation of the fracture energy in the small scale assumption.

5.8.6 Dilatancy effect on purely aseismic crack propagation

In Figure 5.20 we show the numerical results for an ultimately stable dilatant fault ($\tau_o/\tau_p = 0.55$) subjected to large overpressure $\Delta P/\sigma'_o = 0.75$. The dilatancy ratio $\epsilon_d/\beta\sigma'_o$ varies in order to investigate the effect of dilatancy during the aseismic crack propagation. As one can observe from the time evolution of half-crack length a/a_w or from the time evolution of peak slip $\delta_{|x=0|}/\delta_w$, dilatancy slows down the aseismic propagation. Although the undrained fault response is not well pronounced at crack tips due to its aseismic propagation, it is enough to further slow down the crack velocity.

5.8.7 Effect of shear-induced permeability changes: case of effective stress-dependent permeability

We report in Figure 5.21 the numerical results in terms of half crack length a/a_w and peak slip $\delta_{|x=0|}/\delta_w$ at the centre of a critically stressed fault ($\tau_o/\tau_p = 0.75$) as function of normalized time $\sqrt{4\alpha t}/a_w$, both obtained using the effective stress-dependent permeability law 5.29. The normalized dilatancy ratio $\frac{\epsilon_d}{\beta\sigma'_o}$

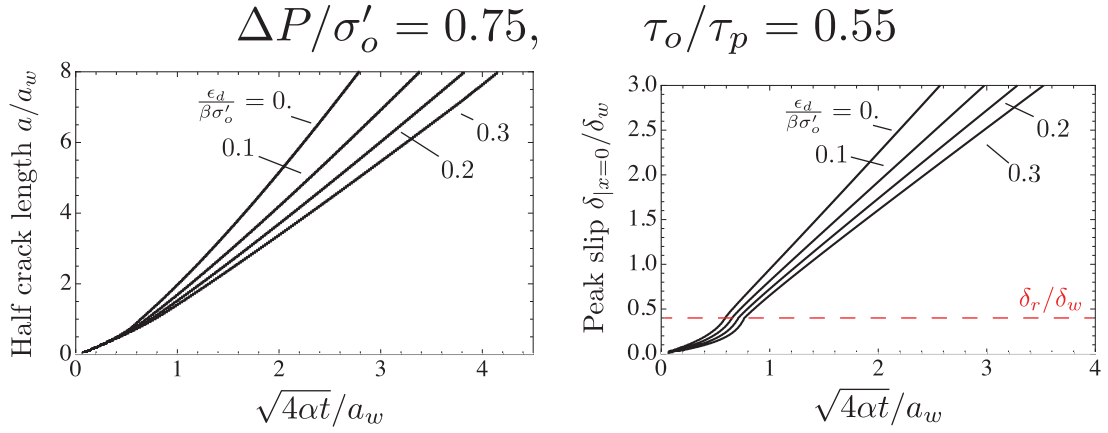


Figure 5.20: Dilatancy effect on normalized crack length a/a_w and peak slip δ/δ_w at $x = 0$ for a frictional weakening fault subjected to large overpressure $\Delta P/\sigma'_o = 0.75$. The fault is ultimately stable in the hypothetical absence of dilatancy as the uniform background shear stress $\tau_o = 0.55 \cdot \tau_p$ is lower than the fault residual strength at ambient conditions τ_r , for a friction weakening ratio of $f_r/f_p = 0.6$. Under such stress criticality and large over-pressure, the fault always exhibits seismic crack propagation (zone 3 of Figure 5.3). However, the crack velocity slows down for increasing values of dimensionless dilatancy parameters.

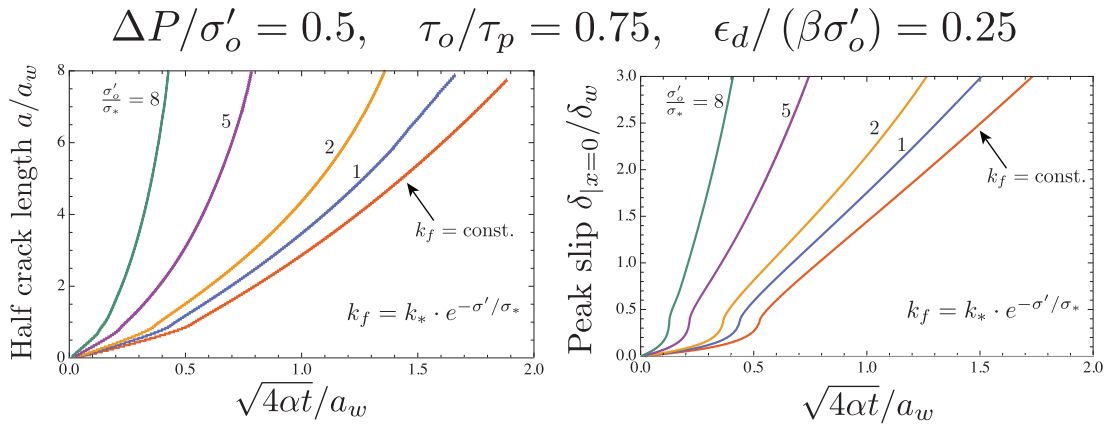


Figure 5.21: Effect of permeability increase on a critically stressed ($\tau_o/\tau_p = 0.75$, $f_r/f_p = 0.6$) dilatant fault in terms of time evolution of normalized half crack length a/a_w and peak slip $\delta|_{x=0}/\delta_w$. The dimensionless dilatancy parameter $\epsilon_d/(\beta\sigma'_o)$ is taken here equal to the critical stabilizing value 0.25. Under such conditions a fault with constant fault permeability $k_f = \omega^2/12$, subjected to moderate overpressure $\Delta P/\sigma'_o = 0.5$, never exhibit seismic slip. An effective stress-dependent permeability law has been considered ($k_f = k_* e^{(-\sigma'/\sigma_*)}$), with four different ratios of σ'_o/σ_* spanning low and large permeability increase.

is kept constant at critical stabilizing value 0.25 as well as the overpressure at injection point $\Delta P/\sigma'_o$ at the moderate value 0.5, whereas the dimensionless ratio σ'_o/σ_* varies in order to span low and large fault permeability increase during shear crack propagation (by calibrating different values of k_*). As already mentioned in section 5.6, these numerical results are qualitatively similar to the ones of Figure 5.11. Large increase of permeability associated with strong reduction of effective normal stress enhance the crack velocity, but the crack propagation always remains quasi-static. The peak slip that the fault can experience is always aseismic even for large increase of fault permeability (see Figure 5.22-right, case $\sigma'_o/\sigma_* = 8$).



In Figure 5.22 the profiles of normalized pore-pressure, slip, friction coefficient, effective normal stress and permeability are reported, all obtained at normalized time snapshot $\sqrt{4\alpha t}/a_w = 0.4$. Although the maximum permeability in the case of $\sigma'_o/\sigma_* = 8$ is nearly two order of magnitude larger than its initial value at ambient conditions, the undrained fault response at crack tips remains strong, preventing the crack velocity from diverging.

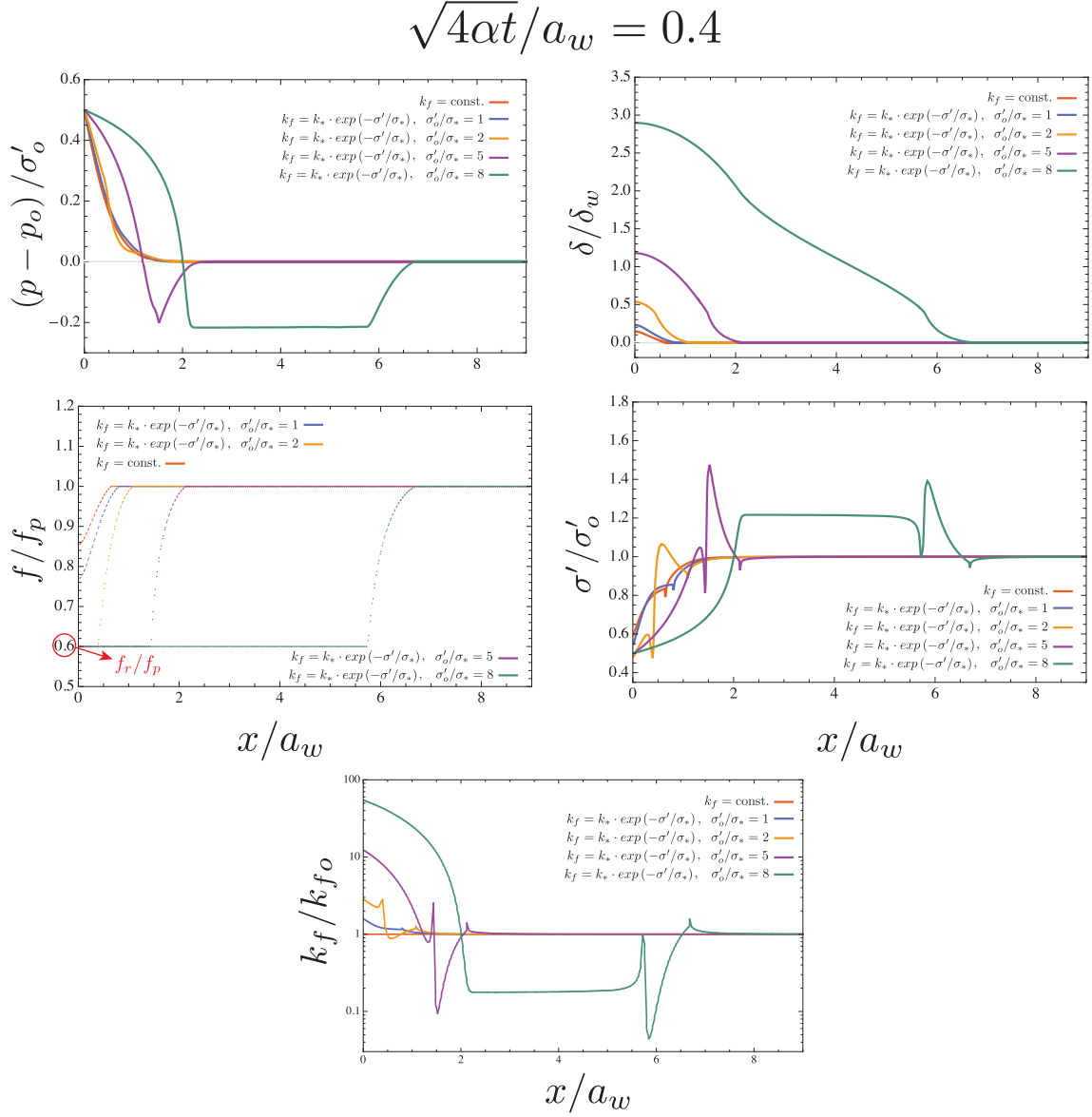


Figure 5.22: Spatial profiles of dimensionless pore pressure, friction coefficient, slip, effective normal stress and fault longitudinal permeability (in linear-log scale) at a given normalized time snapshot $\sqrt{4\alpha t}/a_w = 0.4$, for unstable fault ($\tau_o/\tau_p = 0.75$ - $f_r/f_p = 0.6$), subjected to a moderate over-pressure $\frac{\Delta P}{\sigma'_o} = 0.5$ and a dimensionless dilatancy parameter equal to the critical value, i.e. $\frac{\epsilon_{d,c}}{\beta\sigma'_o} = 0.25$. The different numerical results are obtained with different fault permeability evolution laws: i) constant permeability $k_f = \frac{\omega_o^2}{12}$, ii) effective stress-dependent permeability law $k_f = k_* \cdot e^{(-\sigma'/\sigma_*)}$, with $\sigma'_o/\sigma_* = 1 - 2 - 5 - 8$.





Chapter 6

Conclusions and perspectives

We summarize here the achievements of this project, what remains to be done to achieve the final goals and discuss perspectives with respect to the use of the developed tools.

Achievements

1. 2D and 3D efficient BEM solvers for fracture mechanics problem with an extensive suite of verification tests. The use of hierarchical matrices allows to perform simulation with a large number of unknowns and thus model realistic geological configurations (e.g. with a large number of pre-existing fractures).
2. Finite volume solver for flow in a 2D pre-existing fracture network.
3. 2D hydromechanical solver for the simulation of hydraulic stimulation of a pre-existing fracture networks (with the restriction of no change of permeability during slip). This solver can help testing scenario for the re-activation of a fractured rock mass depending on stress and fracture/joint frictional properties (critically stressed versus marginally pressurized, effect of DFN statistics etc) and directly provide qualitative estimate of micro-seismic activity location. This solver use a fully implicit scheme.
4. 2D fully coupled hydromechanical solver for injection/ pressurization of a planar fault -include the effect of dilatancy on the nucleation of dynamic rupture. This solver use a fully implicit scheme.

Remaining work

1. Development of a solver for flow in a 3D pre-existing fracture network. This implies the development of 2D finite element lubrication type solver with variable fracture flow transmissivity.
2. Finalization of a fully coupled hydromechanical solver for the stimulation of a pre-existing fracture network including permeability changes and further growth of fractures in 2D. Two options are possible to reach this goal and both are worth testing: i) enhance the one-way coupled implicit solver which would results in a large tangent system (and require the development of a specific iterative solver and the corresponding preconditioners), ii) explore the computational efficiency of a fully explicit scheme (which require limited implementation effort but would necessarily need the use of very small time-steps). Additionally, an algorithm for the further propagation of fractures (following the one described in Nikolskiy et al. (2019)) can be then plugged in.
3. Development of a fully coupled hydromechanical solver for the stimulation of a pre-existing fracture network including permeability changes in 3D. Here, the algorithm developed for the 2D one-way coupled solver could be directly extended to 3D once the flow solver is available (point 1 above).



Outlook

The 2D one-way coupled hydromechanical solver (keeping in mind its restriction of constant flow transmissivity) can readily be used to test field injection scenario and also revisit documented field tests. When available, the 3D version will further enhance the possible configurations that can be modelled and open the door to quantitative comparison with laboratory experiments, mid-scale field experiments (such as the ones planned in the Bedretto underground lab) as well as large scale injection (e.g. Haute-Sorne project).



Bibliography

- Adachi, J. I., Siebrits, E., Peirce, A. P. & Desroches, J. (2007), 'Computer simulation of hydraulic fractures', *International Journal of Rock Mechanics and Mining Sciences* **44**(5), 739–757.
- Alghalandis, Y. F. (2017), 'ADFNE: Open source software for discrete fracture network engineering, two and three dimensional applications', *Computers & Geosciences* **102**, 1–11.
- Anders, M. H. & Wiltchko, D. V. (1994), 'Microfracturing, paleostress and the growth of faults', *Journal of Structural Geology* **16**(6), 795–815.
- Asgian, M. (1989), A numerical model of fluid-flow in deformable naturally fractured rock masses, in 'International Journal of Rock Mechanics and Mining Sciences & Geomechanics Abstracts', Vol. 26, Elsevier, pp. 317–328.
- Bandis, S., Lumsden, A. & Barton, N. (1981), Experimental studies of scale effects on the shear behaviour of rock joints, in 'International journal of rock mechanics and mining sciences & geomechanics abstracts', Vol. 18, Elsevier, pp. 1–21.
- Bandis, S., Lumsden, A. & Barton, N. (1983), Fundamentals of rock joint deformation, in 'International Journal of Rock Mechanics and Mining Sciences & Geomechanics Abstracts', Vol. 20, Elsevier, pp. 249–268.
- Bao, X. & Eaton, D. W. (2016), 'Fault activation by hydraulic fracturing in western Canada', *Science*.
- Barber, J. R. (1992), *Elasticity*, Springer.
- Barenblatt, G. I. (1962), 'The mathematical theory of equilibrium cracks in brittle fracture', *Advances in Applied Mechanics* **VII**, 55–129.
- Barton, N., Bandis, S. & Bakhtar, K. (1985), 'Strength, Deformation and Conductivity Coupling of Rock Joints', *Int. J. Rock. Mech. Min. Sci. & Geomech. Abstr.* **22**(3), 121–140.
- Batchelor, A. & Stubs (1985), Hot dry rock reservoir stimulation in the uk an extended summary, in 'International seminar on the results of EC geothermal energy research. 3', European Commission, München, pp. 681–711.
- Bawden, W. F., Curran, J. H. & Roegiers, J.-C. (1980), 'Influence of Fracture Deformation on Secondary - A Numerical Approach', *Int. J. Rock Mech. Min. Sci. & Geom. Abstr.* **17**, 265–279.
- Bebendorf, M. (2005), 'Hierarchical lu decomposition-based preconditioners for bem', *Computing* **74**(3), 225–247.
- Benzi, M. (2002), 'Preconditioning Techniques for Large Linear Systems: A Survey', *Journal of Computational Physics* **182**, 418–477.
- Benzi, M., Golub, G. H. & Liesen, J. (2005), 'Numerical solution of saddle point problems', *Acta Numerica* pp. 1–37.
- Bernabé, Y., Mok, U. & Evans, B. (2003), 'Permeability-porosity relationships in rocks subjected to various evolution processes', *Pure and Applied Geophysics* **160**(5-6), 937–960.



- Bonnet, E., Bour, O., Odling, N. E., Davy, P., Main, I., Cowie, P. & Berkowitz, B. (2001), 'Scaling of fracture systems in geological media', *Reviews of Geophysics* **39**, 347–383.
- Bonnet M. (1995), *Boundary Integral Equation Methods for Solids and Fluids*, John Wiley and Sons Ltd.
- Bonnet, M. (1999), *Boundary integral equation methods for solids and fluids*, John Wiley & Sons.
- Brace, W. F. (1960), 'An Extension of the Griffith Theory of Fracture to Rocks', *Journal of Geophysical Research* **65**(10).
- Brantut, N. & Viesca, R. C. (2015), 'Earthquake nucleation in intact or healed rocks', *Journal of Geophysical Research: Solid Earth* **120**, 191–209.
- Budiansky B. & O'Connell R. (1976), 'Elastic moduli of a cracked solid', *Int. J. Solids Struct.* **12**, 81–97.
- Camacho, G. T. & Ortiz, M. (1996), 'Computational modelling of impact damage in brittle materials', *Int. J. Solids Structures* **33**(20-22), 2899–2938.
- Cao, Z.-H. (2008), 'Augmentation block preconditioners for saddle point-type matrices with singular (1,1) blocks', *Numerical linear algebra with applications* **15**, 515–533.
- Cao, Z.-H. (2009), 'Constraint Schur complement preconditioners for nonsymmetric saddle point problems', *Applied Numerical Mathematics* **59**, 151–169.
- Carol, I., Prat, P. C. & Lopez, C. M. (1997), 'Normal/shear cracking model: application to discrete crack analysis', *Journal of engineering mechanics* **123**(8), 765–773.
- Carslaw, H. & Jaeger, J. (1959), *Conduction of heat in solids*, Oxford Univ Press.
- Cornet, F. (2015a), *Elements of Crustal Geomechanics*, Cambridge University Press.
- Cornet, F. H. (2015b), *Elements of Crustal Geomechanics*, Cambridge University Press.
- Cornet, F. H. (2016), 'Seismic and aseismic motions generated by fluid injections', *Geomechanics for Energy and the Environment* **5**, 42–54.
- Cornet, F. H., Helm, J., Poitrenaud, H. & Etchecopar, A. (1997), 'Seismic and Aseismic Slips Induced by Large-scale Fluid Injections', *Pure and Applied Geophysics* **150**, 563–583.
- Crawford, A. & Curran, J. (1982), 'Higher-order functional variation displacement discontinuity elements', **19**(3), 143–148.
- Crouch, S. L. & Starfield, A. M. (1983), *Boundary element methods in solid mechanics*, George Allen & Unwin.
- Cundall, P. A. (1982), Fluid-rock interaction program (frip) manual, in 'Report of University of Minnesota', Department of Civil and Mineral Engineering.
- Davy, P., Bour, O. & De Dreuzy, J.-R. (2006), Discrete fracture network for the Forsmark site, Technical report, Itasca Consulting Group.
- Dempsey, D., Kelkar, S., Davatzes, N., Hickman, S. & Moos, D. (2015), 'Numerical modeling of injection, stress and permeability enhancement during shear stimulation at the desert peak enhanced geothermal system', *International Journal of Rock Mechanics and Mining Sciences* **78**, 190–206.
- Dugdale, D. S. (1960), 'Yielding of steel sheets containing slits', *Journal of the Mechanics and Physics of Solids* **8**(2), 100–104.
- Ellices, M., Guinea, G. V., Gómez, J. & Planas, J. (2002), 'The cohesive zone model: advantages, limitations and challenges', *Eng. Frac. Mech.* **69**(2), 137–163.
- URL: <http://linkinghub.elsevier.com/retrieve/pii/S0013794401000832>



- Ellsworth, W. L. (2013), 'Injection-induced earthquakes', *Science* **341**.
- Eshelby, J. D. (1973), 'Dislocation theory for geophysical applications', *Philosophical Transactions of the Royal Society of London. Series A, Mathematical and Physical Sciences* **274**(1239), 331–338.
- Evans, K., Genter, A. & Sausse, J. (2005), 'Permeability creation and damage due to massive fluid injections into granite at 3.5 km at soultz: 1. borehole observations', *Journal of Geophysical Research: Solid Earth* **110**(4), 1–19.
- Evans, K., Moriya, H., Niitsuma, H., Jones, R., Phillips, W., Genter, A., Sausse, J., Jung, R. & Baria, R. (2005), 'Microseismicity and permeability enhancement of hydrogeologic structures during massive fluid injections into granite at 3 km depth at the soultz HDR site', *Geophysical Journal International* **160**(1), 388–412.
- Fu, P., Johnson, S. & Carrigan, C. (2013), 'An explicitly coupled hydro-geomechanical model for simulating hydraulic fracturing in arbitrary discrete fracture networks', *International Journal for Numerical and Analytical Methods in Geomechanics* **37**(14), 2278–2300.
- Garagash, D. I. & Germanovich, L. N. (2012), 'Nucleation and arrest of dynamic slip on a pressurized fault', *J. Geophys. Res.* **117**.
- Garagash, D. I. & Rudnicki, J. W. (2003), 'Shear heating of a fluid-saturated slip-weakening dilatant fault zone, 1, limiting regimes', *J. Geophys. Res.* **108**(B2).
- Gebbia, M. (1891), 'Formule fondamentali della statica dei corpi elastici', *Rend. Circ. Mat. di Palermo* **5**, 320–323.
- Ghassemi, A. (2012), 'A review of some rock mechanics issues in geothermal reservoir development', *Geotechnical and Geological Engineering* **30**(3), 647–664.
- Gorbatikh, L., Lomov, S. & Verpoest, I. (2007), 'On stress intensity factors of multiple cracks at small distances in 2-D problems', *International Journal of Fracture* **143**(4), 377–384.
- Gordeliy, E. & Detournay, E. (2011), 'Displacement discontinuity method for modeling axisymmetric cracks in an elastic half-space', *Int. J. Sol. Struct.* **48**(19), 2614–2629.
- Green, A. & Sneddon, I. (1950), 'The distribution of stress in the neighbourhood of a flat elliptic crack in an elastic solid', *Proc. Camb. Philos. Soc.* **46**, 159–163.
- Guglielmini, Y., Cappa, F., Avouac, J.-P., Henry, P. & Elsworth, D. (2015), 'Seismicity triggered by fluid injection-induced aseismic slip', *Science* **348**.
- Hackbusch, W. (2015), *Hierarchical matrices: algorithms and analysis*, Vol. 49, Springer.
- Hackbusch, W. & Nowak, Z. P. (1989), 'On the fast matrix multiplication in the boundary element method by panel clustering', *Numerische Mathematik* **54**(4), 463–491.
- Hadley, K. (1976), 'Comparison of calculated and observed crack densities and seismic velocities in Westerly granite', *Journal of Geophysical Research* **81**(20).
- Hamilton, D. H. & Meehan, R. L. (1971), 'Ground rupture in the Baldwin hills', *Science* **172**(3981), 333–344.
- Hatton, C. G., Main, I. G. & Meredith, P. G. (1994), 'Non-universal scaling of fracture length and opening displacement', *Nature* **367**.
- Hayashi, K., Willis-Richards, J., Hopkirk, R. J. & Niibori, Y. (1999), 'Numerical models of HDR geothermal reservoirs—a review of current thinking and progress', *Geothermics* **28**(4-5), 507–518.
- Healy, J., Rubey, W., Griggs, D. & Raleigh, C. (1968), 'The Denver earthquakes', *Science* **161**(3848), 1301–1310.



- Hills, D. A., Kelly, P. A., Dai, D. N. & Korsunsky, A. M. (1996), *Solution of crack problems: the distributed dislocation technique*, Vol. 44 of *Solid Mechanics and its Applications*, Kluwer Academic Publ., Dordrecht.
- Ida, Y. (1972), 'Cohesive force across the tip of a longitudinal-shear crack and griffith's specific surface energy', *Journal of Geophysical Research* **77**(20), 3796–3805.
- Itasca Consulting Group (2010), *FLAC Constitutive models*, Technical report, Itasca Consulting Group.
- Jung, R. (2013), EGS - Goodbye or Back to the Future, in 'ISRM International Conference for Effective and Sustainable Hydraulic Fracturing', International Society for Rock Mechanics.
- Kamali, A. & Ghassemi, A. (2018), 'Analysis of injection-induced shear slip and fracture propagation in geothermal reservoir stimulation', *Geothermics* **76**, 93–105.
- Knappett, J. A. & Craig, R. F. (2012), *Craig's soil mechanics*, Spon Press.
- Kohl, T. & Mégel, T. (2007), 'Predictive modeling of reservoir response to hydraulic stimulations at the european egs site soultz-sous-forêts', *International Journal of Rock Mechanics and Mining Sciences* **44**(8), 1118–1131.
- Kranz, R. L. (1983), 'Microcracks in rocks: a review', *Tectonophysics* **100**, 449–480.
- Lancellotta, R. (2012), *Geotecnica*, Zanichelli.
- Lecampion, B., Bungler, A. P. & Zhang, X. (2018), 'Numerical methods for hydraulic fracture propagation: A review of recent trends', *Journal of Natural Gas Science and Engineering* **49**, 66–83.
- Lee, H. & Cho, T. (2002), 'Hydraulic characteristics of rough fractures in linear flow under normal and shear load', *Rock Mechanics and Rock Engineering* **35**(4), 299–318.
- Lei, Q. & Gao, K. (2018), 'Correlation between fracture network properties and stress variability in geological media', *Geophysical Research Letters* **45**.
- Lei, Q., Latham, J.-P. & Tsang, C.-F. (2017), 'The use of discrete fracture networks for modelling coupled geomechanical and hydrological behaviour of fractured rocks', *Computers and Geotechnics* **85**, 151–176.
- Lei, Q. & Wang, X. (2016), 'Tectonic interpretation of the connectivity of a multiscale fracture system in limestone', *Geophysical Research Letters* **43**, 1551–1558.
- Li, B., Jiang, Y., Koyama, T., Jing, L. & Tanabashi, Y. (2008), 'Experimental study of the hydro-mechanical behavior of rock joints using a parallel-plate model containing contact areas and artificial fractures', *International Journal of Rock Mechanics and Mining Sciences* **45**(3), 362–375.
- Li, J.-L., Huang, T.-Z. & Li, L. (2010), 'The spectral properties of the preconditioned matrix for nonsymmetric saddle point problems', *Journal of Computational and Applied Mathematics* **235**, 270–285.
- Lockner, D. A. & Byerlee, J. D. (1994), 'Dilatancy in hydraulically isolated faults and the suppression of instability', *Geophysical Research Letters* **21**(22), 2353–2356.
- Lockner, D. and Naka, H., Tanaka, H., Ito, H. & Ikeda, R. (1999), Permeability and Strength of core samples from the Nojima fault of the 1995 Kobe earthquake, in 'Int. workshop on the Nojima fault core and borehole data analysis'.
- Lomize, G. (1951), 'Flow in fractured rocks', *Gosenergoizdat, Moscow* **127**, 197.
- Louis, C. (1969), *A study of groundwater flow in jointed rock and its influence on the stability of rock masses*, Imperial College of Science and Technology.
- Lubliner, J. (2005), *Plasticity Theory*, Dover.



- Maerten, F., Maerten, L. & Cooke, M. (2010), 'Solving 3D boundary element problems using constrained iterative approach', *Computational Geoscience* **14**, 551–564.
- Maier, G., Novati, G. & Cen, Z. (1993), 'Symmetric Galerkin boundary element method for quasi-brittle-fracture and frictional contact problems', *Comp. Mech.* pp. 74–89.
URL: <http://www.springerlink.com/index/P57RK650350X3087.pdf>
- Makurat, A., Neuman, S. & Simpson, E. (1985), 'The effect of shear displacement on the permeability of natural rough joints', *Hydrogeology of rocks of low permeability: International Association of Hydrogeologists Memoir* **17**, 99–106.
- Margonari, M. & Bonnet M. (2005), 'Fast multipole method applied to the coupling of elastostatic bem with fem', *Computers and Structures* **83**, 700–717.
- Marone, C., Raleigh, C. B. & Scholz, C. (1990), 'Frictional behavior and constitutive modeling of simulated fault gouge', *Journal of Geophysical Research: Solid Earth* **95**(B5), 7007–7025.
- Matsuki, K., Kimura, Y., Sakaguchi, K., Kizaki, A. & Giwelli, A. (2010), 'Effect of shear displacement on the hydraulic conductivity of a fracture', *International Journal of Rock Mechanics and Mining Sciences* **47**(3), 436–449.
- McClure, M. & Horne, R. (2011), 'Investigation of injection-induced seismicity using a coupled fluid flow and rate/state friction model', *Geophysics* **76**(6), WC181–WC198.
- McClure, M. W. & Horne, R. N. (2013), *Discrete Fracture Network Modeling of Hydraulic Stimulation: Coupling Flow and Geomechanics*, Springer Briefs in Earth Sciences, Springer, New York.
- McClure, M. W. & Horne, R. N. (2014), 'An investigation of stimulation mechanisms in Enhanced Geothermal Systems', *Int. J. Rock Mech. Min. Sci.* **72**, 242–260.
- Mogilevskaya, S. G. (2014), 'Lost in translation: Crack problems in different languages', *International Journal of Solids and Structures* **51**(25), 4492–4503.
- Mogilevskaya, S. & Nikolskiy, D. (2014), 'The use of complex integral representations for analytical evaluation of three-dimensional bem integrals—potential and elasticity problems', *The Quarterly Journal of Mechanics and Applied Mathematics* **67**(3), 505–523.
- Mura, T. (1982), *Micromechanics of Defects in Solids*, Martinus Nijhoff Publisher.
- Napier, J. & Malan, D. (2007), 'The computational analysis of shallow depth tabular mining problems', *Journal of the Southern African Institute of Mining and Metallurgy* **107**(11), 725–742.
- Needleman, A. (2014), 'Some issues in cohesive surface modeling', *Procedia IUTAM* **10**, 221–246.
- Nemat-Nasser, S. & Hori, M. (1999), *Micromechanics: Overall properties of heterogeneous materials*, 2nd edn, North-Holland.
- Nguyen, T. & Selvadurai, A. (1998), 'A model for coupled mechanical and hydraulic behaviour of a rock joint', *International Journal for Numerical and Analytical Methods in Geomechanics* **22**(1), 29–48.
- Nikolskiy, D., Lecampion, B., Pourpak, H. & Onaisi, A. (2019), Simultaneous initiation and propagation of multiple transverse hydraulic fractures in a horizontal well, in '53rd US Rock Mechanics/ Geomechanics Symposium, June 23-26', New-York, USA. ARMA 19-1617.
- Nikolskiy, D. V., Mogilevskaya, S. G. & Labuz, J. F. (2015), 'Boundary element analysis of non-planar three-dimensional cracks using complex variables', *International Journal of Rock Mechanics and Mining Sciences* **76**, 44–54.
- Nikolskiy, D. V., Zammarchi, M., Mogilevskaya, S. G. & Salvadori, A. (2016), 'Three-dimensional bem analysis of stress state near a crack-borehole system', *Engineering Analysis with Boundary Elements* **73**, 133–143.



- Palmer, A. C. & Rice, J. (1973), The growth of slip surfaces in the progressive failure of over-consolidated clay, in 'Proceedings of the Royal Society of London A: Mathematical, Physical and Engineering Sciences', Vol. 332, The Royal Society, pp. 527–548.
- Pan, E., Yuan, J., Chen, W. & Griffith, W. (2014), 'Elastic deformation due to polygonal dislocations in a transversely isotropic half-space', *Bulletin of the Seismological Society of America*.
- Piva, A. (1982), 'A crack along a circular interface between dissimilar media', *Meccanica* **17**(2), 85–90.
- Plesha, M. E., Ballarini, R. & Parulekar, A. (1989), 'Constitutive model and finite element procedure for dilatant contact problems', *Journal of engineering mechanics* **115**(12), 2649–2668.
- Quarteroni, A., Sacco, R. & Saleri, F. (2000), *Numerical Mathematics*, Texts in applied mathematics, Springer.
- Renshaw, C. (1995), 'On the relationship between mechanical and hydraulic apertures in rough-walled fractures', *Journal of Geophysical Research: Solid Earth (1978–2012)* **100**(B12), 24629–24636.
- Rice, J. R. (1968), *Mathematical analysis in the mechanics of fracture*, Vol. 2, Academic Press, chapter Fracture: An Advanced Treatise, pp. 191–311.
- Rice, J. R. (1975), 'On the stability of dilatant hardening for saturated rock masses', *Journal of Geophysical Research* **80**(11).
- Rice, J. R. (1992a), 'Fault stress states, pore pressure distributions, and the weakness of the san andreas fault', *International Geophysics* **51**(Fault Mechanics and Transport Properties of Rock: A Festschrift in Honor of W. F. Brace), 475–503.
- Rice, J. R. (1992b), 'Fault Stress States, Pore Pressure Distributions, and the Weakness of the San Andreas Fault', *International Geophysics* **51**, 475–503.
- Rice, J. R. (1993), 'Spatio-temporal complexity of slip on a fault', *Journal of Geophysical Research* **98**(B6), 9885–9907.
- Rice, J. R. (2006), 'Heating and weakening on faults during earthquake slip', *J. Geophys. Res* **111**(B05311).
- Rokhlin, V. (1985), 'Rapid solution of integral equations of classical potential theory', *Journal of computational physics* **60**(2), 187–207.
- Rongved, L. (1957), 'Dislocation over a bounded plane area in an infinite solid', *ASME J. Appl. Mech.* **24**, 252–254.
- Rooke, D. P. & Sneddon, I. N. (1969), 'The crack energy and the stress intensity factor for a cruciform crack deformed by internal pressure', *International Journal of Engineering Science* **7**(10), 1079 – 1089.
URL: <http://www.sciencedirect.com/science/article/pii/0020722569900068>
- Rudnicki, J. W. (1979), 'The stabilization of slip on a narrow weakening fault zone by coupled deformation-pore fluid diffusion', *Bull. Seism. Soc. Am.* **69**(4), 1011–1026.
- Rudnicki, J. W. & Chen, C.-H. (1988), 'Stabilization of rapid frictional slip on a weakening fault by dilatant hardening', *Journal of Geophysical Research: Solid Earth* **93**(B5), 4745–4757.
- Rutqvist, J. & Stephansson, O. (2003), 'The role of hydrochemical coupling in fractured rock engineering', *Hydrogeology Journal* **11**(1), 7–40.
- Ryder, J. & Napier, J. A. L. (1985), Error analysis and design of a large-scale tabular mining stress analyzer, in '5th International Conference on Numerical Methods in Geomechanics', pp. 1549–1555.
- Samuelson, J., Elsworth, D. & Marone, C. (2009), 'Shear-induced dilatancy of fluid-saturated faults: Experiment and theory', *Journal of Geophysical Research: Solid Earth* **114**(B12).



- Scotti, O. & Cornet, F. H. (1994), 'In Situ Evidence for Fluid-Induced Aseismic Slip Events Along Fault Zones', *Int. J. Rock Mech. Min. Sci. & Geom. Abstr.* **31**(4), 347–358.
- Seeburger, D. A. & Zoback, M. D. (1982), 'The Distribution of Natural Fractures and Joints at Depth in Crystalline Rock', *Journal of Geophysical Research* **87**(B7), 5517–5534.
- Segall, P. & Rice, J. R. (1995), 'Dilatancy, compaction, and slip instability of a fluid-infiltrated fault', *Journal of Geophysical Research: Solid Earth* **100**(B11), 22155–22171.
- Segall, P. & Rice, J. R. (2006), 'Does shear heating of pore fluid contribute to earthquake nucleation?', *Journal of Geophysical Research: Solid Earth* **111**(B9).
- Segall, P., Rubin, A. M., Bradley, A. M. & Rice, J. R. (2010), 'Dilatant strengthening as a mechanism for slow slip events', *Journal of Geophysical Research: Solid Earth* **115**(B12).
- Seront, B., Wong, T.-F., Caine, J., Forster, C., Bruhn, R. & Fredrich, J. (1998), 'Laboratory characterization of hydromechanical properties of a seismogenic normal fault system', *Journal of Structural Geology* **20**(7), 865–881.
- Shapiro, S. A., Kummerow, J., Dinske, C., Asch, G., Rothert, E., Erzinger, J., Kumpel, H.-J. & Kind, R. (2006), 'Fluid induced seismicity guided by a continental fault: Injection experiment of 2004/2005 at the German Deep Drilling Site (KTB)', *Journal of Geophysical Research* **33**.
- Shibazaki, B. (2005), 'Nucleation process with dilatant hardening on a fluid-infiltrated strike-slip fault model using a rate- and state-dependent friction law', *Journal of Geophysical Research* **110**(B11308).
- Sih, G. C. (1973), *Handbook of Stress-intensity Factors for Researchers and Engineers*.
- Simo, J. C. & Hughes, T. (1997), *Computational Inelasticity*, Vol. 7, Springer.
- Skoumal, R. J., Brudzinski, M. R. & Currie, B. S. (2015), 'Earthquakes induced by hydraulic fracturing in poland township, ohio', *Bulletin of the Seismological Society of America* **105**(1), 189–197.
- Sneddon, I. N. (1946), 'The distribution of stress in the neighbourhood of a crack in an elastic solid', *Proc. Roy. Soc. series A*. **187**(1009), 229–260.
- Snozzi, L. & Molinari, J.-F. (2013), 'A cohesive element model for mixed mode loading with frictional contact capability', *International journal for numerical methods in engineering* **93**(5), 510–526.
- Sornette, A., Davy, P. & Sornette, D. (1993), 'Fault growth in brittle-ductile experiments and the mechanics of continental collisions', *Journal of Geophysical Research* **98**(N7), 12111–12139.
- Stallybrass, M. (1969), 'A cruciform crack deformed by an arbitrary internal pressure', *International Journal of Engineering Science* **7**(11), 1103 – 1116.
URL: <http://www.sciencedirect.com/science/article/pii/0020722569900780>
- Stallybrass, M. P. (1970), 'a pressurized crack in the form of a cross', *The Quarterly Journal of Mechanics and Applied Mathematics* **23**(1), 35–48.
URL: <https://doi.org/10.1093/qjmam/23.1.35>
- Steketee, J. (1958), 'On volterra's dislocations in a semi-infinite elastic medium', *Canadian Journal of Physics* **36**(2), 192–205.
- Stupkiewicz, S. & Mróz, Z. (2001), 'Modeling of friction and dilatancy effects at brittle interfaces for monotonic and cyclic loading', *Journal of Theoretical and Applied Mechanics* **39**, 707–739.
- Szeri, A. Z. (2010), *Fluid Film Lubrication*, Cambridge University Press.
- Tada, H., P.C., P. & Irwin, G. (2000), *The Stress Analysis of Cracks Handbook*, 3rd edn.



- Tao, Q., Ghassemi, A. & Ehlig-Economides, C. A. (2011), 'A fully coupled method to model fracture permeability change in naturally fractured reservoirs', *International Journal of Rock Mechanics and Mining Sciences* **48**(2), 259–268.
- Ucar, E., Berre, I. & Keilegavlen, E. (2017), 'Postinjection normal closure of fractures as a mechanism for induced seismicity', *Geophysical Research Letters* **44**(19), 9598–9606.
- Ucar, E., Berre, I. & Keilegavlen, E. (2018), 'Three-Dimensional Numerical Modeling of Shear Stimulation of Fractured Reservoirs', *Journal of Geophysical Research* **123**, 3891–3908.
- Uenishi, K. & Rice, J. R. (2003), 'Universal nucleation length for slip-weakening rupture instability under nonuniform fault loading', *Journal of Geophysical Research: Solid Earth* **108**(B1).
- Verde, A. & Ghassemi, A. (2015), 'Modeling injection/extraction in a fracture network with mechanically interacting fractures using an efficient displacement discontinuity method', *International Journal of Rock Mechanics and Mining Sciences* **77**, 278–286.
- Viesca, R. C. (2016a), 'Self-similar slip instability on interfaces with rate-and state-dependent friction', *Proc. Roy. Soc. Lond. A* **472**(2192), 20160254.
- Viesca, R. C. (2016b), 'Stable and unstable development of an interfacial sliding instability', *Physical Review E* **93**(6), 060202.
- Viesca, R. & Rice, J. R. (2012), 'Nucleation of slip-weakening rupture instability in landslides by localized increase of pore pressure', *Journal of Geophysical Research* **117**(B03104).
- Walmann, T., Malthé-Sørenssen, A., Feder, J., Jøssang, T. & Maekin, P. (1996), 'Scaling relations for the Lengths and Widths of Fractures', *Phys. Rev. Letters* **77**(27).
- Wei, S., Avouac, J.-P., Hudnut, K. W., Donnellan, A., Parker, J. W., Graves, R. W., Helmberger, D., Fielding, E., Liu, Z., Cappa, F. & Eneva, M. (2015), 'The 2012 Brawley swarm triggering by fluid-induced aseismic slip', *Earth and Planetary Science Letters* **442**, 115–125.
- White, M., Fu, P., McClure, M., Danko, G., Elsworth, D., Sonnenthal, E., Kelkar, S. & Podgorney, R. (2017), 'A suite of benchmark and challenge problems for enhanced geothermal systems', *Geomechanics and Geophysics for Geo-Energy and Geo-Resources* pp. 1–39.
- Witherspoon, P. A. (1980), 'Validity of cubic law for fluid flow in a deformable rock fracture', *Water Resources Res.* **16**(6), 1016–1024.
- Yoon, J. S., Zang, A. & Stephansson, O. (2014), 'Numerical investigation on optimized stimulation of intact and naturally fractured deep geothermal reservoirs using hydro-mechanical coupled discrete particles joints model', *Geothermics* **52**, 165–184.
- Yoshida, K., Nishimura, N. & Kobayashi, S. (2001), 'Application of fast multipole galerkin boundary integral equation method to elastostatic crack problems in 3d', *Int. J. Numer. Meth. Engng* **50**(3), 525–547.
- Zhang, X., Jeffrey, R. G., Llanos, E. & Lecampion, B. (2005), Plane-strain analysis of post-coalescence interaction between fluid-driven cracks and pre-existing fractures, in 'Alaska Rocks, The 40th U.S. Symposium on Rock Mechanics', Anchorage, pp. ARMA/USRMS 05–719.
- Zimmerman, R. W. & Bodvarsson, G. S. (1996), 'Hydraulic conductivity of rock fractures', *Transport in porous media* **23**(1), 1–30.
- Zoback, M. D. (2010), *Reservoir geomechanics*, Cambridge University Press.



Volterra edge dislocation in plane elasticity

We recall the derivation of the solution of a edge dislocation in plane elasticity - see e.g. Nemat-Nasser & Hori (1999) for more details. In the absence of body forces, the balance of momentum in plane elasticity reduces to:

$$\begin{aligned}\sigma_{11,1} + \sigma_{12,2} &= 0 \\ \sigma_{12,1} + \sigma_{22,2} &= 0\end{aligned}$$

For an isotropic material of shear modulus G and Poisson's ratio ν , the constitutive relations reduce to:

$$\begin{aligned}2G\epsilon_{11} &= \frac{\kappa+1}{4}\sigma_{11} + \frac{\kappa-3}{4}\sigma_{22} \\ 2G\epsilon_{22} &= \frac{\kappa-3}{4}\sigma_{11} + \frac{\kappa+1}{4}\sigma_{22} \\ 2G\epsilon_{12} &= \sigma_{12}\end{aligned}$$

where $\kappa = 3 - 4\nu$ is the plane-strain Kolosov constant ($\kappa = (3 - \nu)/(1 + \nu)$ in plane-stress). It is usual to define the Airy's stress function U such that

$$\begin{aligned}\sigma_{11} &= U_{,22} \\ \sigma_{22} &= U_{,11} \\ \sigma_{12} &= -U_{,12}\end{aligned}$$

The elastic Beltrami-Mitchell equations then reduce to:

$$\nabla^4 U = 0$$

It is convenient to use complex variables:

$$\begin{aligned}z &= x_1 + ix_2 \\ \bar{z} &= x_1 - ix_2\end{aligned}$$

such that $x_1 = \frac{z+\bar{z}}{2}$ and $x_2 = -\frac{i}{2}(z - \bar{z})$, and the derivatives become:

$$\begin{aligned}\partial_{x_1} &= \partial_z + \partial_{\bar{z}} \\ \partial_{x_2} &= i(\partial_z - \partial_{\bar{z}}) \\ \partial_{x_1^2} &= \partial_{z^2} + \partial_{\bar{z}^2} + 2\partial_{z\bar{z}} \\ \partial_{x_2^2} &= -\partial_{z^2} - \partial_{\bar{z}^2} + 2\partial_{z\bar{z}} \\ \partial_{x_1 x_2} &= i(\partial_{z^2} - \partial_{\bar{z}^2})\end{aligned}$$



The bi-harmonic function U can thus be expressed in terms of two analytic functions (Muskhelishvili's potentials):

$$U = Re \left\{ \bar{z}\phi(z) + \int^z \psi(z')dz' \right\}$$

such that the stresses components are given by:

$$\begin{aligned} \sigma_{11} + \sigma_{22} &= 4Re \{ \phi'(z) \} \\ \sigma_{22} - \sigma_{11} + 2i\sigma_{12} &= 4(\bar{z}\phi''(z) + \psi'(z)) \end{aligned}$$

while the displacement are given by:

$$2G(u_1 + iu_2) = \kappa\phi(z) - z\bar{\phi}'(z) - \bar{\psi}(z)$$

Moreover the resultant $t = t_1 + it_2$ along an arc AB ($F = \int \sigma_{ij}n_j$) is given by:

$$t = -(\phi + z\bar{\phi}' + \bar{\psi})$$

Setting $\phi = A \ln z$ and $\psi = B \ln z$, the displacement and traction around a loop surrounding the origin gives:

$$\begin{aligned} t_1 + it_2 &= 2\pi(A - \bar{B}) = 2\pi(A_1 - B_1) + 2\pi i(A_2 + B_2) \\ 2G(u_1 + iu_2) &= 2\pi i(-\kappa A_2 + B_2) + 2\pi(\kappa A_1 + B_1) \end{aligned}$$

Note that we can therefore obtain the solution of a dislocation where for such a loop surrounding the origin, $t_1 + it_2 = 0$ and $u_1 + iu_2 = b_1 + ib_2$ as well as the solution for a point force ($t_1 + it_2 = P_1 + iP_2$ and $u_1 + iu_2 = 0$):

- Point force

$$\begin{aligned} A_1 &= \frac{P_1}{2\pi(\kappa + 1)} & A_2 &= \frac{P_2}{2\pi(\kappa + 1)} \\ B_1 &= -\frac{\kappa P_1}{2\pi(\kappa + 1)} & B_2 &= \frac{\kappa P_2}{2\pi(\kappa + 1)} \end{aligned}$$

- Edge dislocation

$$\begin{aligned} A_1 &= \frac{b_2 G}{2\pi(\kappa + 1)} & A_2 &= -\frac{b_1 G}{2\pi(\kappa + 1)} \\ B_1 &= \frac{b_2 G}{2\pi(\kappa + 1)} & B_2 &= \frac{b_1 G}{2\pi(\kappa + 1)} \end{aligned}$$

Dislocation solution

The solution for a dislocation at the origin (dislocation in $[0, \infty[$) with a Burgers vector $b = b_1 + ib_2$ ¹ is given by the following potentials (see e.g. Nemat-Nasser & Hori (1999), Barber (1992)):

$$\phi = -\frac{iGb}{\pi(\kappa + 1)} \log z \quad \psi = \frac{iG\bar{b}}{\pi(\kappa + 1)} \log z$$

The stresses induced by such a dislocation can be schematically written as follow (Hills et al. 1996):

$$\sigma_{ij} = s_{ijk}b_k$$

¹Note that the convention for dislocation is of positive b_1 for an overlap / positive stress in tension.



where e.g. s_{ij1} are the σ_{ij} stresses due to a 'glide' dislocation ($b_2 = 0$, shear dislocation along $x_2 = 0$), and similarly s_{ij2} denotes the stresses due to a 'climb' dislocation ($b_1 = 0$, opening dislocation cut along $x_2 = 0$). The fundamental solution s_{ijk} is given by:

$$s_{ijk} = \frac{2G}{\pi(\kappa + 1)} h_{ijk} = \frac{E'}{4\pi} g_{ijk}$$

$$\begin{aligned} h_{111} &= \frac{-x_2(3x_1^2 + x_2^2)}{r^4} & h_{112} &= \frac{x_1(x_1^2 - x_2^2)}{r^4} \\ h_{221} &= \frac{x_2(x_1^2 - x_2^2)}{r^4} & h_{222} &= \frac{x_1(x_1^2 + 3x_2^2)}{r^4} \\ h_{121} &= \frac{x_1(x_1^2 - x_2^2)}{r^4} & h_{122} &= \frac{x_2(x_1^2 - x_2^2)}{r^4} \end{aligned}$$

$$h_{221} = h_{122} \quad h_{121} = h_{112}$$

The relations between the different components of h_{ijk} can be exploited to reduce computational cost. This dislocation solution is then integrated analytically for a linear variation of displacement discontinuity over a finite segment. We do not list here these integrals - they have been derived using Mathematica analytical capabilities and then coded up in C++.





3D dislocation solutions

Solution in 3D do also exist. Restricting to the elastic full space, the infinitesimal dislocation loop solution can be found in Hills et al. (1996). The solution for a bounded displacement discontinuity over a planar area can be found in Rongved, L. (1957) among others. See also Nikolskiy et al. (2015, 2016), Mogilevskaya & Nikolskiy (2014) for quadratic triangular displacement discontinuity element and references therein. Solutions for the isotropic half-space, transversely isotropic halfspace do also exist (Steketee 1958, Pan et al. 2014, among many others).

Triangular quadratic element We have implement the quadratic triangular displacement discontinuity element described in Mogilevskaya & Nikolskiy (2014), Nikolskiy et al. (2015)